EAST ASIAN SUMMER MONSOON PRECIPITATION SYSTEMS: RAINFALL CHARACTERISTICS, STORM MORPHOLOGIES AND CONVECTIVE PROPERTIES

by

Weixin Xu

A dissertation submitted to the faculty of
The University of Utah
in partial fulfillment of the requirements for the degree of

Doctor of Philosophy

Department of Atmospheric Sciences

The University of Utah

August 2011

The University of Utah Graduate School

STATEMENT OF DISSERTATION APPROVAL

The dissertation of **Weixin Xu**

has been approved by the following supervisory committee members:

Edward J. Zipser	, Chair	**05/16/2011** Date Approved
Yi-Leng Chen	, Member	**05/16/2011** Date Approved
John D. Horel	, Member	**05/16/2011** Date Approved
Steven K. Krueger	, Member	**05/16/2011** Date Approved
Chuntao Liu	, Member	**05/16/2011** Date Approved

and by **W. James Steenburgh** , Chair of

the Department of **Atmospheric Sciences**

and by Charles A. Wight, Dean of The Graduate School.

ABSTRACT

This study attempts to characterize the particular convection type, namely storm morphologies, convective properties, and microphysics, of different weather regimes within the East Asian Summer Monsoon (EASM). Defined rain bands and associated rainfall characteristics are examined in terms of population, location, variability, and rainfall frequency. Though the Mei-Yu rain bands produce a relatively large rain belt over South China and Taiwan during mid-May to mid-June, and over the Yangtze River region during mid-June to mid-July, rainfall maxima and heavy precipitation are most frequent over specific locations.

Generally, the frequency of storms with high echo tops, significant convection, and evident ice scattering signature is greatest in post-Meiyu and break periods, less so during the active Mei-Yu, and least frequent before the monsoon onset. However, preseason, as well as break periods, has a larger fraction of intense convection that behaves more like the classic continental tropical convection with major ice-based rainfall processes. Specifically, preseason and break periods have a larger fraction of rainfall contributed from storms with a 40-dBZ convective core extending above 7-8 km. By comparison, active Mei-Yu convection more closely resembles classic tropical maritime convection with relatively more importance of “warm-rain” collision and coalescence processes with weaker convection but heavy precipitation. Monsoon precipitation over the Yangtze River region, though having similar size and cloud top, differs from its counterpart in South China on convective properties, vertical structures, and rainfall contribution by storm types.

Based on Tropical Rainfall Measuring Mission (TRMM) climatology, the EASM is comparable to other monsoon regimes by having convective properties intermediate between the intense convective systems over continents, and the weaker convective systems found in the classic maritime precipitation regimes.

Analysis based on Terrain-influenced Monsoon Rainfall Experiment (TiMREX) observations indicates that most of the heavy rainfall is associated with Mei-Yu rain bands, strongly influenced by upstream low-level jets, unstable upstream conditions, but a more nearly moist neutral storm environment. A particular long-duration heavy precipitation event is analyzed in detail, and features continuous development of "back-building" new convection under the influence of an extensive precipitation-created cold pool and substantial orography downstream.

TABLE OF CONTENTS

LIST OF TABLES

ACKNOWLEDGEMENTS

First, I would like to thank Dr. Edward Zipser, for his guidance and encouragement, and for giving me great opportunities and freedom in conducting research. This project could not have been completed without his mentoring. Many thanks to Drs. John Horel, Steven Krueger, Yi-Leng Chen, Chuntao Liu, and Yali Luo, for serving as my supervisory committee and their helpful suggestions. Thanks also go to Drs. Ben Jou, Wen-Chau Lee, and other TiMREX scientists for helping me to be involved in the field program and get the data used in this project. I would also like to thank Jon Zawislak, Christy Wall, Adam Varble, Ellen Ramirez, Chie Yokoyama, Michael Petersen, and Sarah Bang in the tropical research group, and all the faculty, staff, and students in the department for their friendship, advice, and assistance. I also owe a debt of gratitude to my parents and families in my home country, China, for their life inspiration, support, and encouragement.

CHAPTER 1

MOTIVATION AND INTRODUCTION

1.1 Scientific Issues and Motivations

The Asian summer monsoon is one of the most important components of the Earth's climate system (Ramage 1971; Chang and Krishnamurti 1987; Trenberth 2000; Chang 2004; Wang 2006). Its monsoon circulation, including winds, air mass, clouds, and precipitation, covers almost the entire tropics and subtropics in the eastern hemisphere, and plays an important role in weather and climate on both regional and global scales. Within the monsoon system, warm and moist air mass is transported from the deep tropics as far as the eastern African coast, producing heavy precipitation, and is subsequently lifted to the upper troposphere by the monsoon deep convection. In the meantime, the dry sinking outflows of the monsoon system affect large areas outside the monsoon region. The strong Asian monsoon circulation is mostly driven by the large thermal contrast between the Eurasian continent and Indo-Pacific Ocean, while the super heat source of the Tibetan Plateau plays an important role in the monsoon onset (He et al. 1987; Yanai et al. 1992; Huang and Sun 1992; Li and Yanai 1996; Wu et al. 1998). The large amount of latent heating released by the condensation of water vapor not only enhances the monsoon circulation but also affects the global climate system. Furthermore, the monsoon system also locally and remotely interacts with the land and ocean surface, hydrosphere, upper troposphere, atmosphere of higher latitudes, and biosphere within the monsoon system (Yasunari and Seki 1992; Kawamura 1998; Wang et al. 2000; Krishnamurti and Goswami 2000).

Over East Asia, the monsoon rainfall tends to be concentrated in rain belts that stretch for a few thousands of kilometers and affect China, Japan, Korea, and the surrounding areas (Chen 1983; Tao and Chen 1987; Ding 1992; Ding and Chan 2005). Major rain belts show stepwise progression toward the north with the first onset over South China, Taiwan, and Okinawa of Japan in mid-May. These rain belts are closely related to a frequently and repeatedly occurring quasi-stationary subtropical front, called the “Mei-Yu” front. The Mei-Yu front produces not only widespread rain but also heavy rainfall, deep convection, and large convective mesoscale systems (Kuo and Chen 1990; Ding 1992; Ninomiya 2000; Chen 2004). These active and persistently occurring monsoonal precipitating cloud systems have significant impacts on both regional and global large scale circulations (Lau and Li 1984; Lau 1992; Chang 2004).

Because of its impacts on the world's largest population and on the global climate system, the East Asian monsoon has received increased attention from all over the world (Tao and Chen 1987; Chang 2004; Ding and Chan 2005). It has been extensively investigated from perspectives including monsoon onset, rainfall distribution and its diurnal cycle, seasonal march of the monsoon and associated rain belts, large-scale dynamics and synoptic setting for heavy rainfall, dynamics and thermodynamics of the Mei-Yu front, island and orographic effects on the Mei-Yu front and rainfall, and interannual and interdecadal variability (summary in Ding and Chan 2005). However, there are limited studies and incomplete understanding of the following issues: 1) convective processes, from perspectives of convection population, diurnal cycle, storm morphology, rainfall contribution, and convective structures; 2) vertical structures of clouds and precipitation, including vertical precipitation profiles and occurrence of precipitating clouds as a function of altitude; 3) microphysical processes of heavy precipitation in terms of vertical occurrence of hydrometeors, drop size distribution, and relative importance of ice-process and warm-rain process. Quantitative solutions to these issues could provide guidelines at least for the validation of model output statistics, physical parameterization in models, rainfall retrievals, regional latent heating calculation, and climate studies.

Firstly, frequent and persistent precipitating systems within the monsoon system have significant feedbacks to the large-scale atmosphere by changing the radiative forcing, releasing latent heat, and transporting momentum (Arakawa 1975; Hartman et al. 1984; Clemens et al. 1991; Trenberth 2000; Wang and Ding 2006), or through a variety of regional and global teleconnections (Horel and Wallace 1981; Hartman et al. 1984). The large-scale atmospheric response depends on the structure of precipitation systems in both the horizontal and vertical dimensions (Tao et al. 1990; Mapes and Houze 1995;

Olson et al. 1999). Secondly, in the modern era, general circulation models or regional climate models are frequently used for future climate projection. These models simulate precipitation and its large-scale effects on the environment through either cumulus parameterizations (summary in Arakawa, 2004) or cloud-resolving "super-parameterizations" (Randall et al. 2003; Grabowski 2004). A major requirement for both parameterization methods is correctly characterizing convection, cloud, and precipitation systems (Yanai et al. 1973; Arakawa and Schubert 1974). Quantification of the populations, characteristics, and organizational structure of cloud and rainfall systems over the tropics on both regional and global scales has a very long history (Simpson 1992; Johnson et al. 1999; Yuter et al. 2005). Similar studies are lacking for Asian monsoon systems over the subtropics and limited to short time statistics of cloud fraction based on IR, microwave, or lidar measurements (Kang et al. 1999; Yu et al. 2001; Luo et al. 2009). Therefore, it is necessary to more directly quantify the occurrence, precipitation characteristics, storm morphologies, and large-scale responses of precipitation systems. The long-term (12 years) Tropical Rainfall Measuring Mission (TRMM) Precipitation Feature (PF) database is in the right position to help to reach this goal. It provides a unique way to connect storm properties with systems of different size, location, precipitation amount, and weather regimes (Nesbitt et al. 2000; Nesbitt et al. 2006; Liu et al. 2008).

A specific question associated with the above problems is what kind of storms, categorized by convective properties, mainly contribute to the rainfall? Generally, many studies on the tropical convective systems have separated the tropical convection into two classic regimes: continental and maritime (Zipser and Lutz 1994; Rosenfeld and Lensky 1998; Petersen and Rutledge 2001; Phillips et al. 2007; Ulbrich and Atlas 2007). Intense convection and strong ice-processes are thought to be the major contribution in precipitation in the continental regime, while maritime precipitation is more contributed by weaker convection but stronger low-level "warm-rain" processes through collision and coalescence. However, convective processes in a particular tropical region may be a combination of processes in these two particular convective regimes with different significance toward each end (Rutledge et al. 1992; Williams et al. 1992; Petersen et al. 2002; Cifelli et al. 2002; Boccippio et al. 2005; May and Ballinger 2007; Lang et al. 2010). The same question should also be answered for the East Asian monsoon system, because of its production of a large amount of precipitation and latent heat. It can be answered through the quantification of rainfall contributed by specific convective proxies, storm intensity, vertical precipitation structure, and major microphysical processes in different regimes within the monsoon region. Statistics of the rainfall contribution and convective structures may offer a roadmap for the model simulations either on mesoscale or climate scale. In addition, it is an important step for improving physical parameterizations and retrieval algorithms, since vertical profiles in these algorithms are mainly derived from certain meteorological regimes and may not be transferable to other regimes.

On the aspect of weather forecasting, despite the increased accuracy of numerical models, there are still significant deficiencies in the heavy precipitation forecasts, especially in regions affected by orography (Smith et al. 1997; Lin et al. 2001). Inadequate knowledge of the upstream conditions, convective processes, microphysics, and their interaction with terrain are the major issues that limit skill in predicting heavy monsoonal or orographic precipitation (Fritsch and Carbone 2004; Chen et al. 2005; Rotunno and Houze 2007). These physical processes need to be better understood and their parameterizations in models improved for better prediction of heavy precipitation and severe weather. To some extent, these processes can be quantified in terms of convection occurrence, convective properties, storm morphology, vertical precipitation structures, and rainfall contribution. This study will address this problem by analyzing the enhanced observations collected during the TiMREX (Terrain-influenced Monsoon Rainfall Experiment). Knowledge learned from the in-situ measurements may help improve understanding of the convective and microphysical processes of heavy precipitation systems in the East Asian monsoon.

1.2 Background and Literature Review

1.2.1 East Asian Monsoon and Mei-Yu System

The giant Asian summer monsoon is one of the strongest atmospheric circulations on the Earth. The strong monsoon circulation carries warm and moist air masses from tropical Indian and Pacific Oceans to Asia and drops about one meter of seasonal rainfall to the monsoon region. The Asian summer monsoon can be further separated into South

Asian (Indian) monsoon, western North Pacific summer monsoon, and East Asian summer monsoon (EASM) (Wang and Lin 2002; Wang et al. 2005). Unlike the other two Asian monsoon components, the EASM is a hybrid of tropical and subtropical monsoons affected by both the warm and moist tropical air mass and midlatitude cold air intrusions or disturbances (Zhang and Tao 1998; Wu 2002; Wang et al. 2005; Chen 2004).

The earliest onset of the Asian summer monsoon occurs in the Indochina Peninsula and South China Sea (SCS). The onset process is very abrupt, with dramatic changes of large-scale circulation and rainfall occurring during a period of about one week. Before the onset, though the low-level westerlies and convection over the tropical East Indian Ocean and Bay of Bengal have already intensified, anticyclonic circulation (the subtropical high) still dominates the Indochina Peninsula and SCS. After the onset of the monsoon, the subtropical anticyclonic circulation is replaced by strong south and southwesterly flow out of the far tropical Indian and Pacific Oceans. In the meantime, the far upstream Somali jet crossing the equator also undergoes a considerable intensification. Monsoon troughs respectively develop over the Bay of Bengal and the SCS, indicated by two cyclonic circulations embedded in the southwesterly low-level jet. With the deepening and extension of the monsoon trough over SCS and the northward progress of the western Pacific Subtropical high, the East Asian monsoon marches stepwise to South China/Southern Japan, Yangtze River/Central Japan, and North China/Korea. The onset timing, location, variability, and physical mechanisms have been studied by many authors and summarized by Ding and Chan (2005).

Before the arrival of summer, the East Asian monsoon is characterized by rain belts associated with quasi-stationary Mei-Yu fronts (Ding 1992; Chen 2004). Regional rainfall peaks at the Mei-Yu period. Usually, the Mei-Yu front establishes its mean position over South China and Taiwan (20-25^{o} N) during the period of mid-May to mid-June and migrates to the Yangtze River Valley (30-35^{o} N) after mid-June (Tao and Chen 1987; Chen 1988). The monsoon flow reaches its peak value when the Mei-Yu front jumps to the Yangtze River Valley and remains there. To avoid confusion, this study defines the Mei-Yu season in South China and Taiwan as “Mei-Yu” while that over Yangtze River as “YZ-Meiyu”. Both the Mei-Yu front and YZ-Meiyu front are affected by tropical and midlatitude air masses and develop in the deformation wind field between a migratory midlatitude high to the north and subtropical high to the south (Chen 1977 and 1983). The Mei-Yu and YZ-Meiyu fronts move southeastward after initiation with an average lifetime of about 8 days, while some extreme cases persist for more than 10 days (Chen 1988; Ding 1992). Heavy rainfall is often produced by long-lived Mesoscale Convective Systems (MCSs) or intense meso-β-scale systems embedded in the Mei-Yu frontal cloud band (Kuo and Chen 1990; Li et al. 1997; Zhang et al. 2003). The presence of southerly or southwesterly low-level-jet (LLJ) (Chen and Yu 1988) to the south-side of the Mei-Yu front significantly helps the development of these heavy rain-bearing systems (Chen et al. 2005), by providing warm and moist tropical air and strong uplifting mechanisms (Chen 1993; Chen et al. 2000).

1.2.2 Monsoon Convection and Storm Morphology

As has been mentioned, the monsoon and Mei-Yu systems have been extensively studied in terms of monsoon onset and seasonal march, rainfall distribution, large-scale dynamics and thermodynamics, and interannual and interdecadal variability (summary in Ding and Chan 2005). Long-term characteristics of convection occurrence, convective properties, and storm morphology of precipitation systems are less studied and are the major motivation of this study. Generally, most of the studies on this perspective are summarized from the observations of several field experiments, short-term satellite measurements, and case studies of weather radar observations.

Luo and Yanai (1983, 1984) pointed out that Mei-Yu rainfall over the Yangtze River, Southern China, and Taiwan is dominated by stratiform precipitation, through the analysis of large scale precipitation, vertical motion, heating, and moistening budgets. Based on the analysiss of measurements of one season from the Taiwan Area Mesoscale Experiment (TAMEX; Kuo and Chen 1990) in 1987, Johnson and Bresch (1990) further reported that Mei-Yu precipitation consists of both deep convective (prefrontal or frontal) and stratiform (postfrontal) components. Mesoscale Convective Systems (MCSs) are often seen to be embedded in the Mei-Yu frontal band-shape clouds from the GMS IR images (Takeda and Iwaski 1987; Ninomiya 2000). Fu et al. (2003) quantified the convective and stratiform rainfall over East Asia during all seasons in 1998 using TRMM Precipitation Radar data and found that the convective precipitation contributes about half of the total rainfall in the monsoon season though covering only about 10% of the total precipitating area. By comparing the occurrence frequency of hydrometeors retrieved from CLOUDSAT/CALIPSO, Luo et al. (2009) pointed out there are more hydrometeors occurring at the upper troposphere in the Indian monsoon than in the East Asian monsoon because of deeper convection in the Indian monsoon systems.

According to the results of TAMEX, the convective properties of the core Mei-Yu precipitation systems over and around Taiwan are closer to those of oceanic regimes and distinct from the continental regime in terms of convective vertical profiles, updrafts, and convection intensity (Jorgensen and LeMone, 1989; Zipser 1994). Though the structures of squall lines during TAMEX are similar to those of fast moving squall lines in the tropical continents, their updraft and downdraft intensities are relatively weaker (Wang et al.1990; and Jorgensen et al. 1991). Zhang et al. (2006) concludes that the main structures of the Mei-Yu frontal convective precipitation systems over the Yangtze River have convection of medium depth, through the analysis 3-year vertical radar reflectivity profiles. The convective properties and vertical structures of systems over land and ocean in the monsoon region are also quite different. For example, a significantly deeper layer is found for land convection given the same surface rainfall rate from profiles of convective rains over land and ocean (Fu and Liu 2003).

Radar case studies using the data collected from the South China Sea Monsoon Experiment (SCSMEX; Lau et al. 2000) in 1998 suggest that convection that occurs during the onset of the South China Sea monsoon has characteristics somewhat different from other tropical oceanic systems because of its significant interaction with a subtropical frontal passages (Wang 2004; Wang and Carey 2005; Johnson et al. 2005). Wang and Carey (2005) found that a MCS near the end of the monsoon onset had very high reflectivities in the convective region but very little stratiform rain production, most likely due to dry air aloft. Johnson et al. (2005) also found that the stratiform rain fraction was generally small during the onset period because of weak instability from low Sea Surface Temperatures (SSTs) and a relatively dry upper troposphere.

1.2.3 Heavy Monsoon Rainfall and Orographic Precipitation

Heavy rainfall and flash floods are major meteorological disasters and remain a challenge for both scientific research and operational forecasts. The Mei-Yu front usually regulates a widespread precipitation rain belt. However, heavy rainfall and rainfall maxima are often produced by Mesoscale Convective Systems (MCSs) embedded in the Mei-Yu frontal cloud band (Kuo and Chen 1990; Zhang 1990; Chen et al. 1995; Ninomiya 2004). Heavy-rain-producing mesoscale or synoptic scale disturbances along the Mei-Yu front may move eastward or stay stationary showing wavelike distribution (Chen et al. 2008). Heavy rainfall is also associated with the low-level vortex developing on the east flank of the Tibetan Plateau and moving into or becoming a cyclone center on the Mei-Yu front (Tao and Ding 1981; Ninomiya and Akiyama 1992; Chang 1998). The presence of a southerly or southwesterly low-level-jet (LLJ) to the south of the disturbances significantly helps the development of heavy-rain-bearing systems (Chen and Yu 1988; Chen et al. 2005, 2006). Locations where the warm and moist southwesterly flows directly and persistently interact with cold air intrusion from behind are also favorable for heavy precipitation (Ding 1992). These and other synoptic settings favorable for the development of heavy rainfall during the monsoon season have been examined and summarized by many authors (Kuo and Chen 1990; Chen and Li 1995; Ding and Chan 2005).

In addition to the large-scale and mesoscale disturbances, the complex terrain over southern China and Taiwan can also produce heavy rainfall and flash floods through the interaction between prevailing monsoon flow and orography-generated local circulations (Li et al. 1997; Li and Chen 1998; Yeh and Chen 1998; Chen et al. 2005). Under the presence of similar southwesterlies or quasi-stationary subtropical fronts, specific locations of heavy precipitation may vary from time to time (Li et al. 1997; Chen 2005; Chen et al. 2007). Heavy rainfall occurs both over mountains, windward slope, and coastal regions during the passage of Mei-Yu fronts (Chen et al. 2007). Mechanisms for orography-enhanced heavy precipitation can be summarized as follows: 1) lifting through forced ascent as the air moves over the slope, or more indirectly, as the airflow is blocked by the mountain, or when mountains act as a high-level heat source (Chen et al. 1991; Akaeda et al. 1995; Chen and Feng 2001); 2) convergence between the prevailing monsoon flow and offshore flow during the night time (Chen and Li 1995; Chen 2005); 3) convergence between monsoon southwesterlies and low-level barrier jets deviated by the terrain or between postfrontal northwesterlies and barrier jets (Chen and Li 1995; Li et al. 1997; Yeh and Chen 2002). 4) stagnation of MCSs or squall lines blocked by the high terrain, leading to extreme rainfall (Reeves and Lin 2006). Theoretically, for a nonrotating conditionally unstable monsoon flow impinging on a mesoscale mountain ridge, the low-level flow may cross the mountain or be blocked and split, depending on the Froude number (Fr=U/Nh where U is the zonal wind component, h is the mesoscale mountain height, N is the Brunt Vaisala frequency) (Chu and Lin 2000; Chen and Lin 2005). For a large Froude number (Fr >1), the flow will cross the mountain and propagate downward. For a small Froude number (Fr <1), the low-level flow will be decelerated, blocked and split around the mountain. The low-level barrier jet observed during TAMEX is produced by Taiwan Island under the prevailing southwesterly monsoon flow with a small Froude number (Li and Chen 1998).

1.2.4 Knowledge Gained from the Tropics

Characterization and parameterization of precipitating convective clouds over the tropics has a long history in tropical research. Riehl and Malkus (1958) first introduced the concept that undilute cumulonimbus towers (or “hot towers”) are necessary to transport the net energy gain at the surface of equatorial regions to higher latitude. Riehl and Simpson (1979) revisited and supported this concept through statistics of radar observations. They quantified the vertical extent of the hot towers and calculated the number of hot towers needed to maintain tropospheric energy balance. Simplified quantifications of convective clouds have also been introduced for the parameterization of convection in larger-scale models (Ooyama 1971; Yanai et al. 1973; and Arakawa and

Schubert 1974). During the past 40 years, a large number of field experiments and satellites have been deployed to quantify the nature of tropical convection and improve the model parameterization of tropical convection.

The Global Atmospheric Research Program Atlantic Tropical Experiment (GATE; Houze and Betts 1981) was the first and largest ever field experiment to characterize the population, dynamics, and properties of tropical convection. The importance of the stratiform precipitation processes in the tropical convective systems was first pointed out in GATE results (Zipser 1977; Houze 1977). About 40% of the total GATE rainfall was accounted for by stratiform rain (Houze and Cheng 1977). Houze (1982, 1989) determined the latent heating profiles associated with convective systems from observations of GATE and other field programs. These profiles are described as being bottom heavy in the convective cores but top heavy in the stratiform regions. Szoke et al. (1986) analyzed the vertical profiles of reflectivity in convective cells and found that most of the tropical convective cells have only modest strength (i.e., a mean of 45 dBZ at the surface and a 20-dBZ echo top at 8.2 km). The vertical profiles vary from the continental regime to the oceanic regime: over land, maximum reflectivity is generally observed near the surface and decreases gradually with height above the 0 °C level while over ocean, maximum reflectivity occurs near the surface and a much sharper decrease is observed above the 0°C level. This finding is based on comparisons among vertical profiles of maximum reflectivity constructed from radar measurements during GATE, TAMEX, and DUNDEE (Zipser and Lutz 1994).

The next most comprehensive tropical field campaign after GATE is the Tropical Oceans Global Atmosphere Coupled Ocean–Atmosphere Response Experiment (TOGA-COARE; Webster and Lucas 1992). Statistics of radar measurements during TOGA-COARE showed that stratiform rain accounts for about 40% of the total rain in active situations, in agreement with the GATE case studies of large MCSs, but far less rain (15%) in inactive situations (Short et al. 1997). Short et al. (1997) also have another important finding about convective systems over tropical oceans: reflectivity profiles increase toward the surface for convective rain below the freezing level, but are nearly constant with height below the freezing level in stratiform rain. Johnson et al. (1999) introduced the trimodal structure of convective cloud occurrence, indicating the coexistence of cumulus congestus, shallow cumulus, and cumulonimbus in the tropics.

There are many other field programs with the goal to observe tropical convection and describe how tropical convective systems relate to the large-scale atmosphere through vertical transports of heat, moisture, and momentum. In addition, the launch of the TRMM satellite also provides an excellent chance to fully compare the satellite observations of the tropical convective clouds with data obtained during field campaigns. Only a few interesting results are listed here. Convective structures shift significantly between the active monsoon and break or westerly regime and easterly regime in the tropics, e.g., Amazon or Australia (Williams et al. 1992; Cifelli and Rutledge 1998; Petersen et al. 2002; Cifelli et al. 2002). Convective systems in the break phase of the Australia monsoon or westerly regime of the Amazon monsoon show higher radar reflectivites in the mixed-phase region. In Asia, premonsoon precipitation systems showed more intense convection than after monsoon onset in terms of higher echo tops and higher lightning possibility (Kodama et al. 2005). Similarly, lightning activity over the Tibetan Plateau and South China Sea peaks in premonsoon and decreases substantially after the monsoon onset (Qie et al. 2003; Yuan and Qie 2008). Stratiform rain fraction was generally small (26%) during the South China Sea monsoon onset period (Johnson et al. 2005).

1.3 Specific Objectives

As mentioned above, extensive research has been conducted to quantify tropical convection and how tropical convective systems relate to the large-scale atmosphere through vertical transports of heat, moisture, and momentum. Similar studies are less common in the subtropical monsoon region, i.e., East Asian monsoon. The study in this dissertation aims to answer the following scientific questions concerning the East Asian monsoon precipitation systems and their seasonal/intraseasonal variability: 1) What is the quantification of convection population, diurnal cycle, storm morphology, rainfall contribution, and convective structures? 2) What is the vertical occurrence of precipitation and vertical precipitation profiles in monsoon clouds and precipitation? 3) What microphysical processes dominate in the monsoon heavy precipitation systems in terms of vertical occurrence of hydrometeors, drop size distribution, and relative importance of the ice-process and the warm-rain process? 4) How different are the convection properties and storm morphologies of precipitation systems among monsoon, continental, and oceanic regimes? 5) What are the storm initiation, evolution, dynamics, and triggering-maintenance mechanisms of extreme events in the orographic monsoon regions?

Long-term (12 years) radar and passive microwave measurements from the TRMM satellite combined with high-resolution in-situ observations during the Terrain-influenced Monsoon Rainfall Experiment (TiMREX) in 2008 provide an excellent opportunity to make progress on the target questions. The TRMM Precipitation Feature (PF) database provides an important link between horizontal and vertical structures of precipitation systems and their rainfall/convective characteristics by combining measurements from the Precipitation Radar, Microwave Imager, and Lightning Sensor together on the storm scale (Nesbitt et al. 2000). The PF database can be used to illustrate spectra and storm morphology of monsoon precipitation systems, highlighting regional and seasonal differences. This database can also provide information on regional rainfall budgets through examining the rainfall contribution by precipitation systems with different horizontal size and proxies for convective intensity (vertical structure).

The U.S.-Taiwan multi-agency field experiment-TiMREX (Lee et al. 2009) provides very high resolution measurements of rainy monsoonal storms. TiMREX included frequent island, ship, and aircraft sondes to collect information on storm environment and upstream conditions. Doppler radars deployed at the coast observed storm initiation and evolution, storm morphology, and kinematic structures of precipitating clouds. In addition, observations of vertical precipitation structures and microphysics were collected from vertically pointing radar, profiler, and drop-size-distribution disdrometers located on the mountain slope. This dataset supplements the TRMM climatology in perspectives of storm initiation, evolution, dynamics, and microphysics of individual monsoon heavy precipitation systems.

The specific objectives of this study include:

- Define the spatial and temporal distribution of Mei-Yu rain bands, heavy rainfall, long-duration rainfall, and corresponding large-scale flows;
- Statistically examine the population, occurrence frequency, spatial distribution, and seasonal variability of precipitation systems with different storm properties (TRMM proxies);
- Quantify the fractions of total rainfall and heavy rainfall contributed by precipitation systems with different storm properties and their regional and seasonal variability;
- Extract statistics of storm properties and vertical precipitation structures in different defined weather regimes and internal relationships between different TRMM-observed storm intensity proxies;
- Compare convection occurrence, intensity, convective properties, vertical structures, and rainfall contribution of precipitation systems among monsoon, continental, and oceanic regimes;

- Describe the diurnal cycles of precipitation, deep convection, and lightning, as well as their diurnal phase propagation, phase differences, vertical structures, and seasonal variability;
- From field program data, perform case studies to obtain quantitative description of storm evolution, dynamics, and possible triggering-maintenance mechanisms for the orography-related long-lived MCSs;
- Assess which microphysical processes mainly contribute to the extremely heavily raining events and statistics of vertical precipitation structures during the field experiment.

CHAPTER 2

DATA AND METHODS

2.1 Data

The primary data sources used in this study are mainly from TRMM satellite observations and retrievals, measurements from the TiMREX field program, and ECMWF ERA-Interim reanalysis. In particular, four datasets are included: 1) TRMM version 6 3B42 dataset derived from TRMM Multisatellite Precipitation Analysis (TMPA; Huffman et al. 2007); 2) TRMM Precipitation Feature (PF) database (Nesbitt et al. 2000; Liu et al. 2008); 3) 2008 TiMREX surface, radar, and sounding data (Lee et al. 2009); 4) ECMWF ERA-Interim reanalysis data (Dee et al. 2011).

2.1.1 TRMM TMPA-3B42 Rainfall Product

The TRMM Multisatellite Precipitation Analysis (TMPA) 3B42 rain product (Huffman et al. 2007) is used to study the rainfall climatology of monsoon rain belts. 3B42 has 3-hourly temporal resolution and 0.25^{o} by 0.25^{o} spatial resolution, covering the globe from 50^{o} S to 50^{o} N, and is available starting from 1998 to the current date. This algorithm uses passive-microwave measurements from low-earth orbiting satellites and infrared radiance measurements from geostationary satellites, as well as land surface precipitation rain gauge analyses when possible. Multiple passive microwave rain estimates are first calibrated to TRMM Precipitation Radar (PR) and Microwave Imager (TMI) estimates (if available) before their combination. IR estimates are generated using the calibrated microwave estimates, and used to fill the passive microwave coverage gaps. 3B42 rain estimates converge to TMI and PR estimates when they are available. 3B42 can approximately reproduce the surface observation–based histogram of precipitation and reasonably detect large daily events. It has lower skill in correctly representing moderate and light event amounts on short time intervals. Statistical results showed that 3B42 has good correspondence with rain gauge data on rainfall amount and rainfall spatial pattern in China (Zhou et al. 2008; Shen et al. 2010).

2.1.2 TRMM Precipitation Feature (PF) Database

There are four sets of instruments on board the TRMM satellite, including the PR, TMI, lightning image sensor (LIS) and visible and IR sensors (VIRS; Kummerow et al. 1998). Figure 2.1 shows an example of a squall line system observed by different sensors of TRMM. Though IR brightness temperature shows a large area of cold cloud tops, measurements of radar reflectivity, microwave brightness temperature, and lightning flashes capture the squall-line's mesoscale features very well. Though these instruments have different footprints, their observations are quite consistent.

A 13-yr (January 1998 through January 2010) precipitation feature database was developed by Liu et al. (2008) based on the TRMM version-6 satellite data. A PF is identified as contiguous raining areas at near surface derived from TRMM Precipitation Radar (PR). More than one PF could be defined relating to one large storm. As shown in Fig. 2.2, the contiguous IR brightness temperature indicates one large cloud system, but 5 PFs are recognized under the same large cloud shield. In this precipitation system, either the old (or larger) or new convective cell (or smaller) is counted as a PF. After a PF is found, measurements from different instruments (with different footprints) are collocated and grouped into its PR pixels with the adjacent-pixel method and parallax collection (Liu et al. 2008). Standard products such as TMI brightness temperature (1B11; Kummerow et al. 1998), storm height and stratiform/convective information of PR (2A23; Awaka et al. 1998), LIS (Christian 1999) orbital data, PR retrieved rainfall (2A25; Iguchi et al. 2000), and TMI retrieved rainfall (2A12; Kummerow et al. 1998) are put into the collocation process. In other words, a PF includes not only three-dimensional radar reflectivity measurements but also ice scattering signature from the TMI, lightning observations, and IR cloud top temperatures. Figure 2.2d shows the cross section of a PF from PR and TMI measurements. Observations from different instruments could indicate different information of a storm, but they are often consistent with each other in the same aspect. For example, the tower of high value radar echoes is corresponding to the depression of brightness temperature from microwave (or ice scattering maximum) as shown in the storm cross-section. PFs have the horizontal resolution of PR, e.g., 4.2 km before the boost and 5.1 km after the boost of the satellite in 2001. As the PR detectable reflectivity is 17~18 dBZ, the PF dataset ignores the very light-raining systems or pixels. But it is still quite reasonable to use this dataset to study precipitation systems in the monsoon regime.

This event-based method condenses the original information of pixel-level measurements from PR, TMI, LIS, and IR into the properties of events. A set of convective proxies has been developed and included in this dataset (Liu et al. 2008). This dataset provides a unique way to connect quantitative storm properties with systems of different size, location, and precipitation amount. Therefore, it is efficient to investigate the convective properties of precipitation systems within different weather regimes by using the PF database.

2.1.3 ERA-Interim Reanalysis

The European Centre for Medium-Range Weather Forecasts (ECMWF) ERA Interim reanalysis data (Berrisford et al. 2009; Dee and Uppala 2009; Dee et al. 2011) between 1998-2008 are used to examine the large-scale flow of different weather regimes within the monsoon system. The ERA Interim dataset is based on a four-dimensional variational data assimilation (4DVAR) system that assimilates a comprehensive suite of data including cloud-track winds, satellite radiances, radio-occultation measurements, and operational radiosonde (wind, temperature, and humidity), and surface observations. It has a horizontal spatial resolution of 1.5^{o} by 1.5^{o} and 6-hourly temporal resolution (at

00Z, 06Z, 12Z, and 18Z). This dataset has 37 vertical levels ranging from 1000 to 1 hPa. Most of the levels are at 25 hPa intervals.

2.1.4 TiMREX Field Measurements

TiMREX was a joint U.S.-Taiwan multi-agency field experiment (Lee et al. 2009) providing very high resolution measurements of monsoon precipitation systems over Southwest Taiwan and the upstream ocean in May and June of 2008. The goal of TiMREX is to improve the understanding and parameterization of physical processes of heavy precipitation systems and their associated environments within the context of active monsoon flow. Details of the experiment's design, motivation, and observations are summarized in Lee et al. (2009). Locations of major facilities are shown in Fig. 2.3.

TiMREX included frequent island, ship, and aircraft sondes to collect information on storm environment and upstream conditions. During the heavy precipitation event during IOP8 (June 14 to June 16) studied herein, soundings are launched every 3 hours from Taiwan Island, and every 6 hours from the upstream small islands and research ship. Four different sonde types (Vaisala RS80, Vaisala RS92, Meisei, and Graw) were used for these upsonde sites. Bias was recognized and corrected using quality control processes, e.g., significant dry bias found in many of the sondes, and contamination of the low-level thermodynamic sonde data by the ship's structure (Ciesielski et al. 2010) are corrected. The corrected sonde data show good agreement with independent estimates.

A set of Doppler radars is deployed at the coast to observe storm initiation and evolution, storm morphology, and kinematic structures of precipitating clouds. Measurements from one of the operational radars (RCCG radar) and the research radar (NCAR's S-Polka radar) are used in this study. Both of the radars send out signals with S-band wavelength and scan simultaneously a full volume in about 7.5 minutes. The S-Polka radar was strategically placed ~70 km from the RCCG radar to form the dual-Doppler radar pair. The S-Polka also executes polarimetric scans when doing the dual-Doppler scans with RCCG. Retrievals of ensemble microphysical properties separating the hydrometeor types based on polarimetric information are included in the TiMREX S-Polka dataset using NCAR PID (Particle Identification) algorithm (Vivekanandan et al., 1999). Quality control of the S-Polka radar reflectivity and radial velocity was conducted by the NCAR TiMREX science group.

During TiMREX, the operational surface network consisted of 25 conventional weather stations, 418 automatic raingauges, 57 GPS integrated water vapor sensors, and a Lightning Location System (LLS). The hourly rain data from the automatic raingauges and lightning observations from LLS are used in this study. The LLS systems can detect only cloud-to-ground lightning events. In addition, observations of vertical precipitation structures and microphysics were collected from vertically pointing radar, profiler, and drop-size-distribution disdrometers located on the mountain slope.

2.2 Methods

This study is focused on the two major regions with quasi-stationary rain belts of the East Asian Monsoon. The first region is South China, Taiwan, and adjacent ocean areas where the major rain belts often occur during mid-May to mid-June. The second region covers the Yangtze River Valley and the surrounding area where peak monsoon rainfall occurs from mid-June to mid-July. Particular methods have been developed for analyzing rainfall and convective precipitating clouds from different perspectives. Only major definitions and methods are described in this section, while more minor and specific ones will be included in each corresponding chapter.

2.2.1 Definition of Mei-Yu Rain Bands and Mei-Yu Periods

Basically, a Mei-Yu front in the Mei-Yu season is defined by the low-level front or wind shear line (Chen 1988). In this study, Mei-Yu “rain bands” associated with Mei-Yu fronts are defined based on the 3B42 daily rainfall and this basic Mei-Yu front definition within the major Mei-Yu region (18^o-36^o N; 105^o-125^o E). Our definition of a Mei-Yu rain band satisfies the following criteria: (1) a continuous band (a gap between major components less than 3^o is allowed) of daily accumulated rainfall >20 mm extending >10 degrees of longitude; (2) lifetime at least 3 days; (3) at least one daily rainfall peak >50 mm; (4) corresponding wind shear line at 925-850 hPa levels. Figure 2.4 presents a classic case of a Mei-Yu front, with frontal rain bands stagnated over South China for more than 3 days. Rainfall accumulation in Fig. 2.5a or Fig. 2.5b is not perfectly contiguous, but with only small gaps, thus considered as Mei-Yu rain band. Cases similar to the one in Fig. 2.5c or Fig. 2.5d, with only scattered rainfall clusters, are rejected as Mei-Yu rain bands.

Statistics of Mei-Yu rain bands indicate that most of the rain bands developed to the south of the Yangtze River after the onset of Mei-Yu over South China but before 25 June (will be shown in Chapter 3). Based on this, May 13-June 23 is selected as the Mei-Yu season in South China and Taiwan. This definition of the Mei-Yu season in South China and Taiwan is about 10 days longer than the one defined by Chen (1988). This definition covers the transition period before the Mei-Yu front stably establishes its position over the Yangtze River region. Four temporal terminologies are specifically defined for the Mei-Yu season in South China and Taiwan: (1) “Mei-Yu”: periods with Mei-Yu rain bands in Mei-Yu season; (2) “Break”: days during the Mei-Yu season but lacking Mei-Yu rain bands; (3) “Pre-Meiyu”: period (10 Apr to 10 May) before the onset of Mei-Yu; (4) “Post-Meiyu”: period (25 June to 15 July) after the Mei-Yu season. In addition, a particular period of June 23-July 23 is used as the Mei-Yu season in Yangtze River Valley, defined as “YZ-Meiyu” in this study.

2.2.2 Selection and Classification of Precipitation Features

Two major sets of precipitation systems are quantified in terms of storm properties in this study: 1) precipitation systems of different periods over South China and Taiwan area; 2) storms during YZ-Meiyu period over Yangtze River Valley region.

The first set of PFs is limited to the region (20 -28 N; 105 -125 E) where most of the Mei-Yu rain bands develop during the first phase of the Mei-Yu season. PFs are collected in different periods (Pre-Meiyu, Mei-Yu, Break and Post-Meiyu) and separated into land and ocean systems. The second set of PFs is selected from the region of (28 -36 N; 105 -125 E), including only land systems during the YZ-Meiyu season. Analysis of these two major sets of PFs are constructed separately and subsequently compared to each other.

PFs smaller than 100 km^2 (about 4 pixels) are removed from the study. Selected PFs are further categorized into convective systems (CSs), thunderstorms (THs), mesoscale convective systems (MCSs), and stratiform systems (STRAs) based on each one's area and the existence of convective pixels. Firstly, PFs with a significant number of convective pixels, i.e., 4 pixels, are defined as CSs. Secondly, THs are defineded as PFs with more than 1 lightning flash. Thirdly, PFs without any convective pixels and with at least 10 stratiform pixels fall into the group of STRAs. Finally, PFs with area $\geqq$ 2000 km^2 and containing at least one convective pixel are defined to be MCSs. The 2000 km^2 criterion is selected to be consistent with the radar echo definition of MCS by Houze (1993).

2.2.3 Interpretation and Selection of Convection Proxies

A suite of PF parameters has been developed for proxies of different convective properties. Several parameters based on PR measurements are used, including areal coverage of PFs, maximum radar reflectivity at each altitude, the maximum height of 30-dBZ radar reflectivity, the maximum radar echo at the height of 6 km. Minimum Polarized Corrected Temperature (PCT) at 37 and 85 GHz frequencies are defined using microwave observations from TMI. Parameters of lightning flash rate or total lightning flash counts are developed based on the LIS measurements.

2.2.3.1 Radar Reflectivity and Associated Proxies

Radar reflectivity responds preferentially to the liquid phase and the largest hydrometeors in the sample volume. Therefore, high values of radar reflectivity above the freezing level suggest the existence of supercooled liquid raindrops or large ice particles. The maximum height of 30dBZ echo is an indicator of how high the updraft can loft large supercooled liquid or ice particles (Demott and Rutledge 1998). Maximum 7-km reflectivity is the greatest reflectivity value at 7 km of a PF. Climatologically, 7 km over the East Asian monsoon region is well above the freezing level and usually in the mixed-phase region with temperature lower than -5 ^{o}C (Table 2.1). Several studies indicate that the presence of radar echoes above a threshold value of 35-40 dBZ in the mixed phase region is a good indicator of charge separation sufficient for lightning (Dye et al. 1989; Williams et al. 1992; Petersen et al. 1996, 1999). A direct way to present the vertical structure of the convective core of precipitation systems is using vertical profiles of radar reflectivity (VPRR) (Donaldson 1961; Zipser and Lutz 1994).

2.2.3.2 Passive Microwave Brightness Temperature

Horizontally and vertically polarized brightness temperature at 85 GHz from TMI is converted into PCT to avoid confusion between low brightness temperatures resulting from low surface emissivity and that from ice scattering (Spencer et al. 1989). The PCT at 85 GHz is defined as $PCT85 = 1.82T85v - 0.82T85_h$. The 85 GHz PCT depends on the scattering of upwelling radiation by the lofted precipitation-sized ice particles. This ice scattering signature responds to the whole column of ice, often expressed as ice water content integrated over depth, or ice water path (IWP) (Vivekanandan et al. 1991). The higher the IWP, the more depressed PCT at 85 GHz tends to be. Thus, 85 GHz PCT is a good proxy indicator of convective intensity or lightning activity (Mohr and Zipser 1996; Cecil and Zipser 1999; Zipser et al. 2006).

2.2.3.3 Measurements from LIS

The LIS is a sensor combining optical and electronic elements including a staring imager capable of locating and detecting lightning radiance from background radiation (Christian 1999). This system can remove the background signal and detect 90% of all lightning strikes. It has an ability to view a 600 km by 600 km area of the earth with the spatial resolution of between 3 and 6 km. Data output from LIS includes the time of a lightning event, its radiant energy, and the lightning location. LIS monitors individual storms for lightning activity for a period of 80 or 90 seconds. Therefore, the total flash counts related to an individual feature record all the lightning flashes that occur in the feature during the LIS viewing time. Lightning flash rate is defined to be total flash counts in the feature divided by LIS viewing time.

Small ice particles colliding with large graupel in the presence of supercooled liquid water is thought to be responsible for the charge separation leading to lightning (Saunders and Peck 1998). A strong updraft is thought to be required to produce significant supercooled liquid water and large graupel in the mixed-phase region (Williams 1989). Therefore, lightning flash rate or total lightning flash counts are good proxies of intense convection (Zipser 1994).

2.2.4 Methods to Characterize Diurnal Variations

2.2.4.1 Definition of Total Rain, MCS, and Deep Convection

Most of the studies on diurnal cycles focus on precipitation, but it is quite important to know the storm type, convection, and three-dimensional structure of precipitation systems contributing to the diurnal peaks. This study provides diurnal information on convection occurrence, structures of storms, and lightning, in addition to precipitation. Five parameters are selected and defined: 1) population of PF; it is defined as number of PFs with area at least 100 km^2; 2) population of MCS; an MCS is defined as a PF with area > 2000 km^2 having at least 1 convective pixel; 3) total rain; it is defined by the total volumetric near surface rainfall of a PF retrieved from the PR 2A25 algorithm (Iguchi et al. 2001); 4) deep convection; it is defined by the area of 20-dBZ radar echo at 12 km ASL (similar to Liu and Zipser 2008); 5) flash counts; it is the total flash counts detected by LIS within any selected PF. These include both intracloud and cloud-to-ground lightning flashes (Nesbitt et al. 2000; Cecil et al. 2005).

2.2.4.2 Methods to Investigate Diurnal Variations

After the onset of the summer monsoon over East Asia, the large-scale circulation and precipitation pattern change significantly from before (Chen 2004; Ding and Chan 2005). However, the westerly steering winds (300-500 hPa) at 20-30 N are diminishing with the progress of the monsoon and vanish by mid-July (Murakami 1958; Murakami and Ding 1982; Chen 1993; Wang et al. 2005). As one of the major purposes of the study is to investigate the seasonal variability of the diurnal cycles and the phase propagation phenomenon, it is essential to consider the seasonal change of the tropospheric flow. Therefore, it is reasonable to define the first time period as "Premeiyu" during April 1-May 11 before the onset of the monsoon, the second as "meiyu" during May 15-June 25 in the monsoon phase with significant steering winds, and third as "midsummer" during July 1–August 10 when steering winds become negligible.

The region of eastern TP and downstream region (23°-36° N; 90°-120° E) is first divided into three strips (dashed boxes in Fig. 2.6): strip1 (32°-36° N), strip2 (28°-32° N), strip3 (23°-28° N). Each strip is further separated into three boxes, except strip3 having only two boxes, at different elevations (solid boxes in Fig. 2.6; A to H): 93°-103° E, 103°-112° E, and 112°-120° E. To describe the seasonal variations of the diurnal cycle, PFs are grouped into different seasons, strips, and regions. The hour-dependent sampling bias of TRMM PR for each box is also calculated and removed in a way similar to that used to correct latitude-dependent sampling bias.

Spatial distribution of diurnal cycles of PFs (or rainfall) over each strip is presented in Hovmöller diagrams similar to those of Carbone et al. (2002), but here done with 2-hourly and 2^{o} longitude bins. Diurnal cycles of occurrence frequency are derived from the summation of each defined parameter in 8 local time bins (3-hour interval) over each selected box during each specific season for 11 years. In both the Hovmöller diagrams and frequency distribution diagrams, the 1:2:1 filter is applied. The 1:2:1 filter is defined as the mean value of values in three consecutive hour/longitude bins with different weight, i.e., $N_i = (N_{i-1} + 2N_i + N_{i+1})/4$. The diurnal cycle of vertical precipitation structures is presented by the time-height CFADs (contour frequency by altitude diagrams; 3-hourly and 1-km interval) of the occurrence frequency of total area of PFs with radar reflectivity ≧20 dBZ in each box. The occurrence frequency is unconditional. It is defined as the fraction of the total area to the total PR sampling area in a specific box.

In the study of nocturnal (23:30-05:30 LT) and afternoon (11:30-17:30 LT) rainfall and convection, the local time (LT) is defined as the UTC plus 7 hours. In the TRMM 3B42 dataset, the 3-hourly data point is defined as the total of the 1.5 hour behind and ahead, e.g., 00 UTC is 22:30-1:30 UTC. Therefore, 23:30-05:30 LT covers both 18 and 21 UTC, while 11:30-17:30 LT covers both 06 and 09 UTC.

Using the ERA Interim dataset, composite wind fields at 850 and 500 hPa during different seasons are generated separately to show the seasonal transition on the large scale. The same ERA Interim dataset is also used to construct vertical profiles of seasonal mean horizontal wind over the region (28-32 N; 105-115 E) showing diurnal phase propagation. Vertical cross-sections of U component at 01 LT (18 UTC) and 13 LT (06 UTC) are further created along the latitude of 30 N. Finally, the anomaly wind field at 01 LT and 13 LT at 850 hPa is defined by the deviation of the 01 and 13 LT wind fields from the daily mean wind field.

2.2.5 Analysis of TiMREX Observations

Two major parts of this study use the data from TiMREX. First, the statistics of convection, precipitation, rainfall contribution, vertical structures, and hydrometeors based on radar retrievals during several heavy precipitation events are examined. Second, one heavily raining long-duration storm is comprehensively investigated from the perspectives of storm evolution, environment, dynamics, triggering-maintenance mechanisms, vertical precipitation structures, and microphysics. All facilities are shown in Fig. 2.3.

2.2.5.1 Quality Control of Radar Data

The NCAR S-Polka radar data quality control process was executed by the NCAR TiMREX data archive office. The RCCG radar were calibrated by the Taiwan Central Weather Bureau and widely used in publications (Chang et al. 2009; Zhang et al.

2009; Liou et al. 2009; Tsai 2010). In this study, noise, ground-clutter contaminated data, and second trip echoes are discarded through the removal of constant echoes and echoes within 1 km from the ground, while aliased Doppler velocities are unfolded. After the quality control, radar volume data from both RCCG and S-Polka are interpolated from the radar spherical coordinate onto a 1.0 km horizontal resolution and a 1.0 km vertical resolution Cartesian coordinate using the NCAR REORDER software package (Oye and Case 1995). A Closest Point weighting function with the effective radius of 1.5 km is used in the interpolating process. The output Cartesian-based radar volume covers 400 by 400 km horizontally and 20 km vertically every 7.5 minutes.

2.2.5.2 Grouping Radar Precipitation Features

Based on the concept of TRMM Precipitation Feature (Nesbitt et al. 2000), contiguous raining pixels (> 18 dBZ) at 2-km of a radar volume scan from the RCCG radar are defined as a radar precipitation feature (RPF; Fig. 2.7). RPFs smaller than 50 km^2 are removed from the dataset. All the information within the column with the 2-km slice as the cross-section is integrated into the RPF. The size of the RPF is defined by the total area of raining pixels at 2-km of the RPF. Maximum radar reflectivity at each level is picked up and defined as a convection intensity proxy. More proxies are defined for the PRF, including maximum height of specific radar reflectivities (e.g., how high the 20-dBZ echo can reach), and convective core size (area of pixels > 40-dBZ). The RPF is also separated into convective and stratiform parts based on the algorithm of Steiner et al.

1995 using radar echoes at 2-km. Large, medium, and small convective cells are also defined. A large convective cell is defined as an RPF with convective core larger than 400-km^2, while a small convective cell is defined as an RPF with convective core smaller than 100-km^2. Accordingly, a medium convective cell is in the size between a large and small cell. The location of a RPF or convective cell is determined by the center of the longest axis of the feature.

2.2.5.3 Dual-Doppler Wind Analysis

Dual-Doppler wind analysis is conducted between S-Polka and RCCG with a separation distance of about 70 km (Fig. 2.3). The wind synthesis and subsequent computations in the dual-Doppler analysis are performed in the NCAR CEDRIC (Custom Editing and Display of Reduced Information in Cartesian Space; Mohr et al. 1986) system. Before processing the dual-Doppler analysis, radar volumes collected at the similar time (at most 2 minutes apart from each other) from both radars are interpolated into the same resolution Cartesian coordinate with S-Polka as the original point. This time, the Cressman filter weighting function is utilized. An average storm movement vector is calculated for each event to perform a differential advection during the dual-Doppler synthesis. The storm motion speed and direction is determined by movement of the convective lines in low-level radar reflectivity evolution. The horizontal wind components (U and V) are calculated directly without setting any boundary conditions. The vertical wind velocity is derived from integrating the mass continuity equation upward from the lowest grid height of 1.0 km, setting the boundary to be a fraction (1.0) of the field in previous level.

The retrieved wind fields from dual-Doppler analysis contain both random and nonrandom errors. Errors can occur due to incorrect storm advection assumptions, boundary conditions, poorly sampled low-level divergence, and temporal sampling difference between two radars (Doviak et al. 1976; Wilson et al. 1984).

2.2.5.4 Analysis of Microphysical Retrievals

The output variables and hydrometeor identification based on the polarimetric measurements from the S-Polka radar are used to investigate the microphysical properties heavy precipitation systems during TiMREX. Polarimetric variables include differential reflectivity, linear depolarization ratio, correlation coefficient, and specific differential phase (detailed information about these variables can be found in Zrnic 1991 and Doviak and Zrnic 1993). Differential reflectivity (Z_{dr}) is derived from the ratio of Z_h (reflectivity factor for horizontally polarized wave) and Z_v (reflectivity factor for vertically polarized wave), relating to the axis ratio and size of hydrometeors. Z_{dr} combined with radar reflectivity is excellent to separate large rain drops and solid hail or large graupel in the mixed phase region. Large rain drops tend to be oblate and thus have high Z_{dr} value, while hail or large graupel present are more nearly spherical and thus have low Z_{dr} value. The linear depolarization ratio (LDR) is the logarithm of the ratio of the cross-polar power received to the copolar power received. Spherical particles such as light rain, cloud droplets, and dry ice particles would reflect a likewise polarized wave, resulting in very low LDR value. In the opposite, nonspherical particles such as hail, melting aggregates, wet graupel would have higher LDR value. Specific differential phase is the difference between propagation constants for horizontally and vertically polarized waves. K_{dp} can be used to discriminate between statistically isotropic and anisotropic hydrometeors. The correlation coefficient (ρ_{hv}) is defined as the relation between copolar returns. ρ_{hv} would have low values for the region with large diversity of hydrometeor orientation and shape, such as the mixed phase region. Typical thresholds of these polarimetric variables for different precipitation types have been determined from numerous observation analysis and modeling studies (Doviak and Zrnic 1993; Carey and Rutledge 1998; Zrnic et al. 2001).

These variables can be combined to obtain information about dominant, bulk hydrometeor types, and amounts in a resolution radar volume (Vivekanandan et al. 1999; Straka et al. 2000; Zrnic et al. 2001). Retrievals of bulk microphysical hydrometeor types based on the NCAR fuzzy logic Particle Identification algorithm (PID) included in the TiMREX S-Polka database are used in this study. In addition to the above-mentioned polarimetric variables, radar reflectivity, and vertical temperature profile are also input into the PID system. The basic working rule of the algorithm is that hydrometeors are delineated by regions of different physical and empirical values of polarimetric variables. There are 17 hydrometeor categories of the PID output, including cloud droplets, drizzle, light rain, moderate rain, heavy rain, hail, hail/rain mix, graupel/small hail, graupel/small hail/rain mix, dry snow, wet snow, irregular ice crystals, horizontally oriented ice crystals, super cooled liquid drops, insects, second trip, and ground clutter. Since the PID system was operated in the radar spherical coordinate system, PID data is interpolated into the Cartesian coordinate using the Closest Point weighting function with the same resolution as the radar reflectivity pixel, i.e., 1 km horizontally and 1 km vertically.

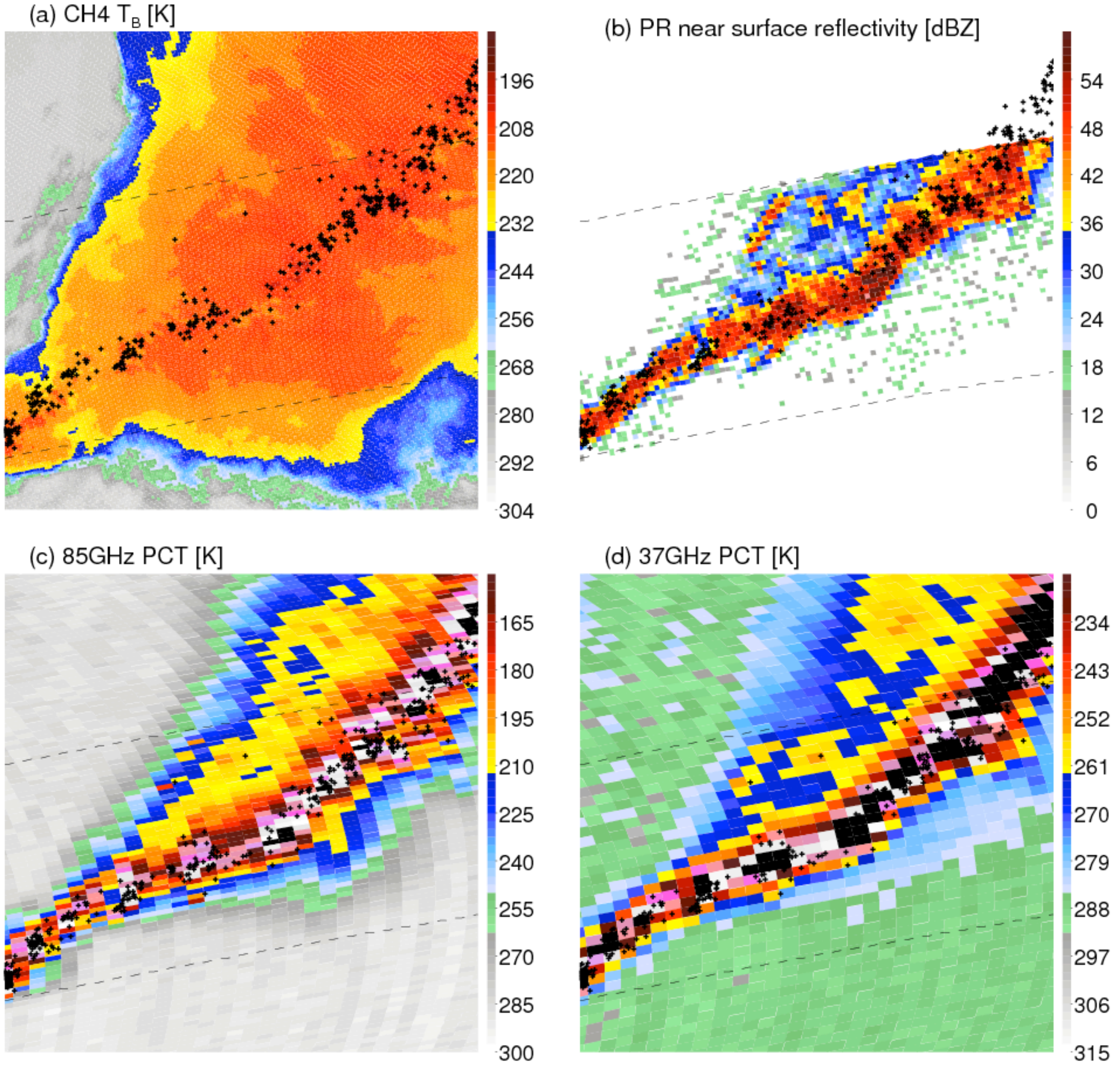

Figure 2.1. Example of a squall line observed by different instruments onboard the TRMM satellite. (a) Brightness temperature (colors) at Channel 4 of IR; (b) Radar reflectivity near the surface; (c) Polarization corrected temperature from the microwave radiometer at the frequency of 85 GHz; (d) Polarization corrected temperature from the microwave radiometer at the frequency of 37 GHz. Lightning Flashes are marked by black dots.

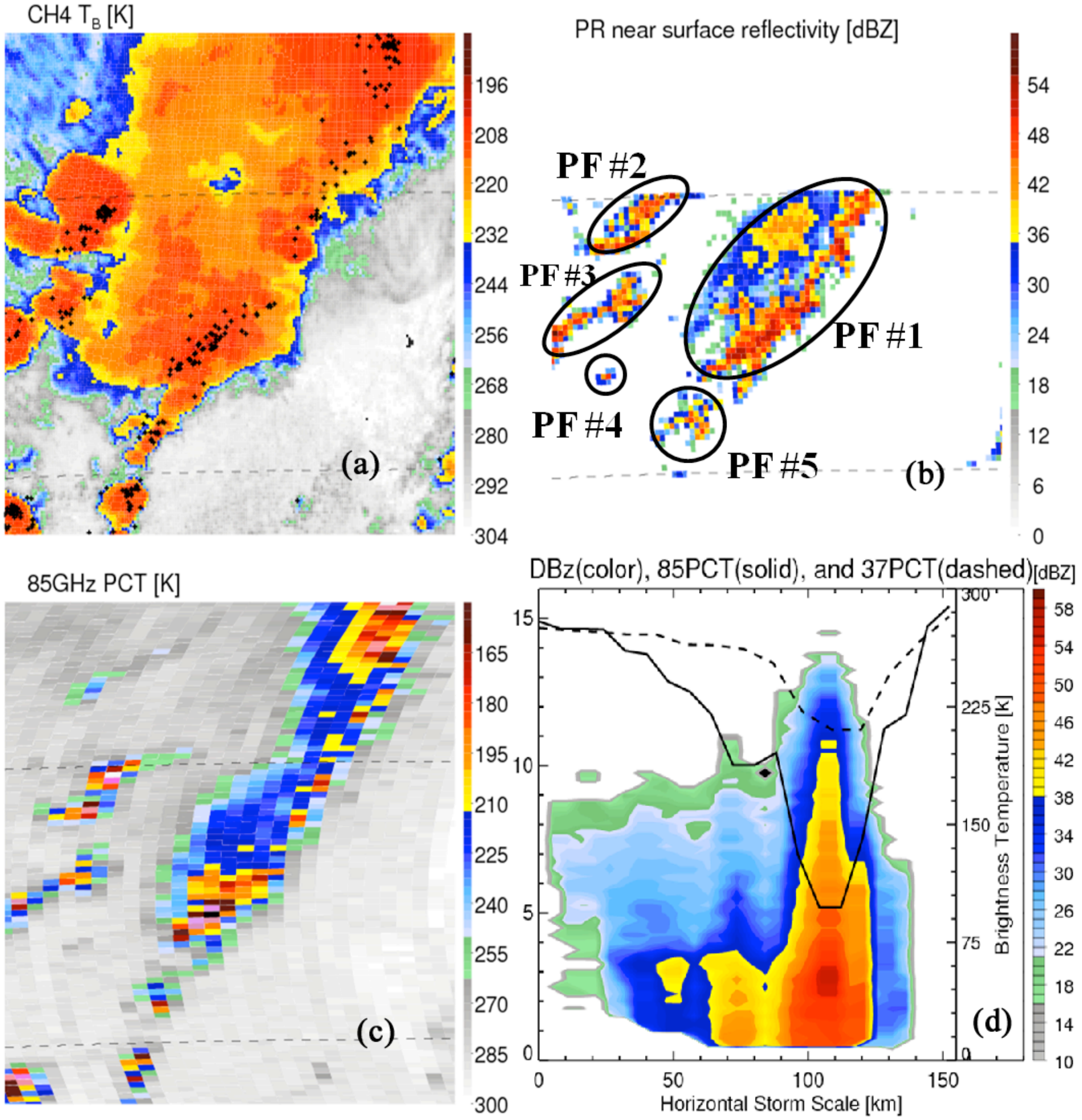

Figure 2.2. An example of precipitation features: (a) Brightness temperature from IR Channel 4, and Lightning Flashes (black dots); (b) Radar reflectivity near surface with PFs marked; (c) Polarization corrected temperature from the microwave radiometer at the frequency of 85 GHz; (d) Cross section of PF #1 in (b) with radar reflectivities contoured and min 37 (85) PCT indicated by dashed (solid) line.

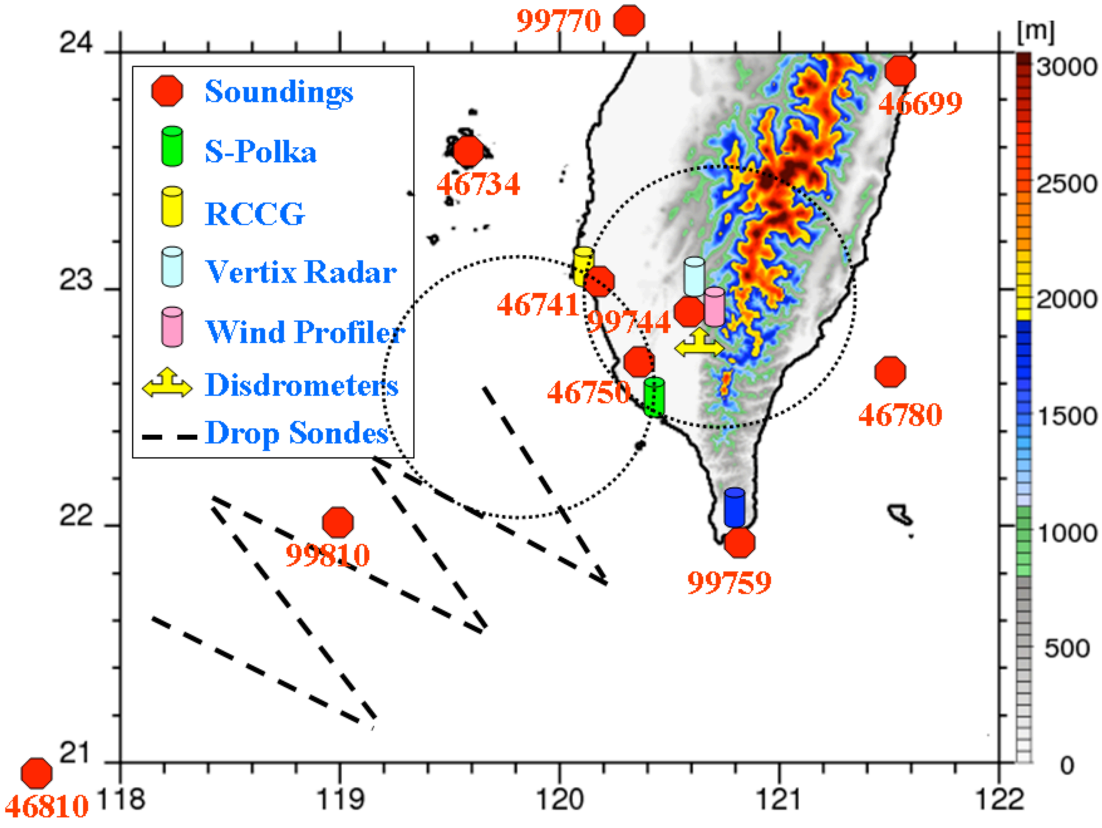

Figure 2.3. Locations of major facilities including sounding sites, NCAR S-Polka radar, operational radar RCCG, vertical pointing radar (vertix), wind profiler, disdrometers, and schematic flight tracks for drop sondes. Terrain elevation is in shaded colors. Dual doppler lobe between RCCG and S-Polka radars is in dashed circle.

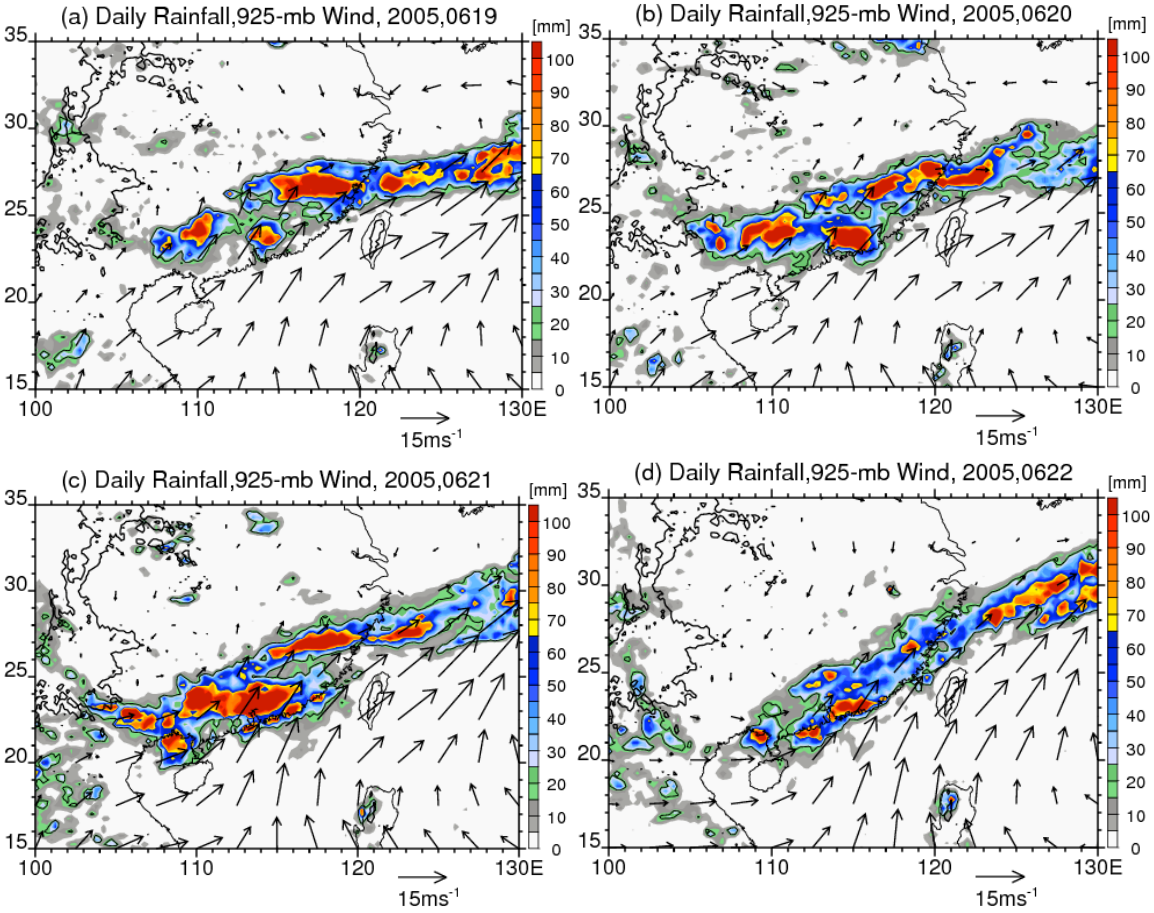

Figure 2.4. Examples of very well organized quasi-stationary Mei-Yu rain bands from June 19-22 in 2005. Rainfall is shaded according to the color bar, and wind arrows show winds at 925 hPa.

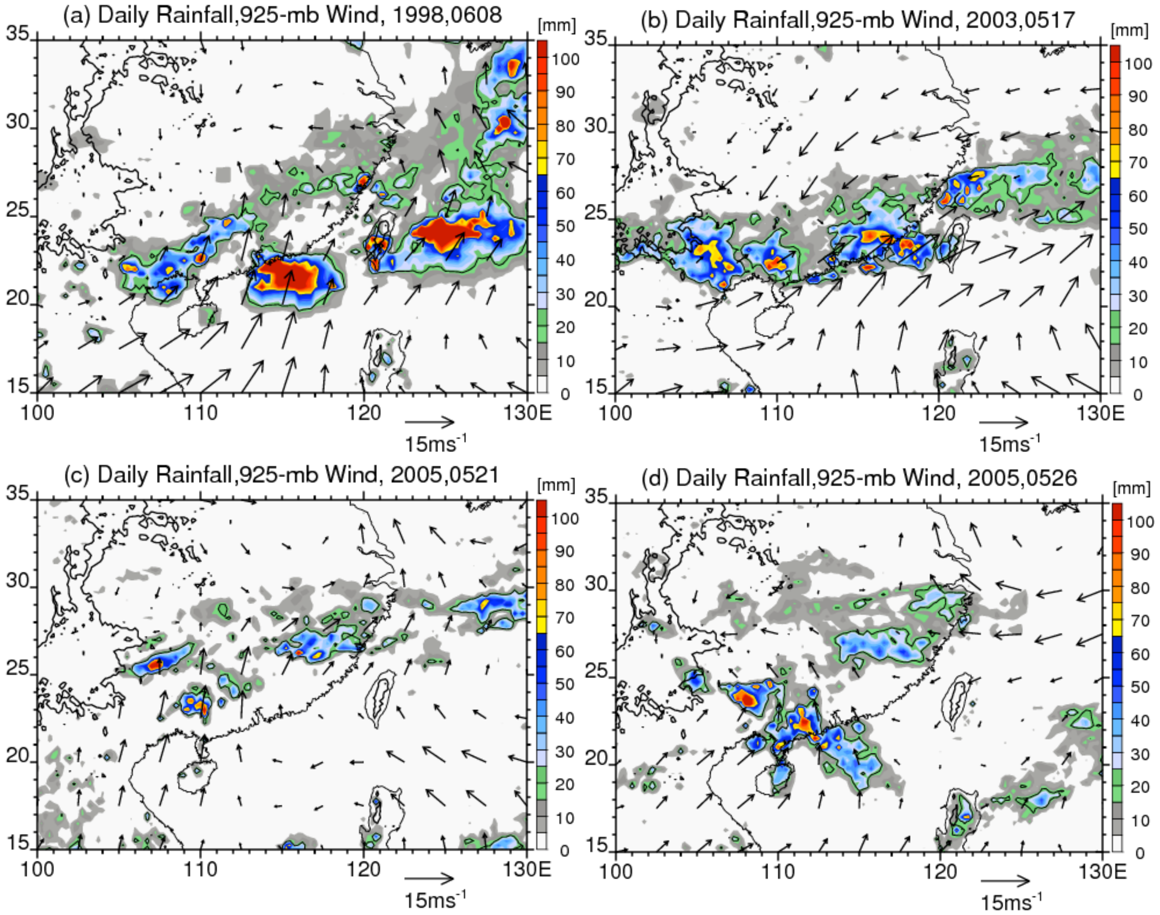
(a) Daily Rainfall,925-mb Wind, 1998,0608

(b) Daily Rainfall,925-mb Wind, 2003,0517

(c) Daily Rainfall,925-mb Wind, 2005,0521

(d) Daily Rainfall,925-mb Wind, 2005,0526

Figure 2.5. Examples of less organized and noncontinuous Mei-Yu rain bands: (a)-(b); and examples of scattered rain clusters not accepted as rain bands: (c)-(d). Rainfall is shaded according to the color bar, and wind arrows show winds at 925 hPa.

Table 2.1. 11-year (1998-2008) mean NCEP atmospheric height (km) at indicated temperatures (^{o}C) within centers of lightning features in Premeiyu and Mei-Yu season over South China.

Temp (^{o}C)	0	-5	-10	-15	-20	-25	-30	-35	-40
Pre-Meiyu Height (km)	4.4	5.4	6.3	7.1	7.8	8.6	9.3	10.0	10.6
Mei-Yu Height (km)	5.0	6.0	6.9	7.7	8.5	9.2	9.9	10.6	11.2

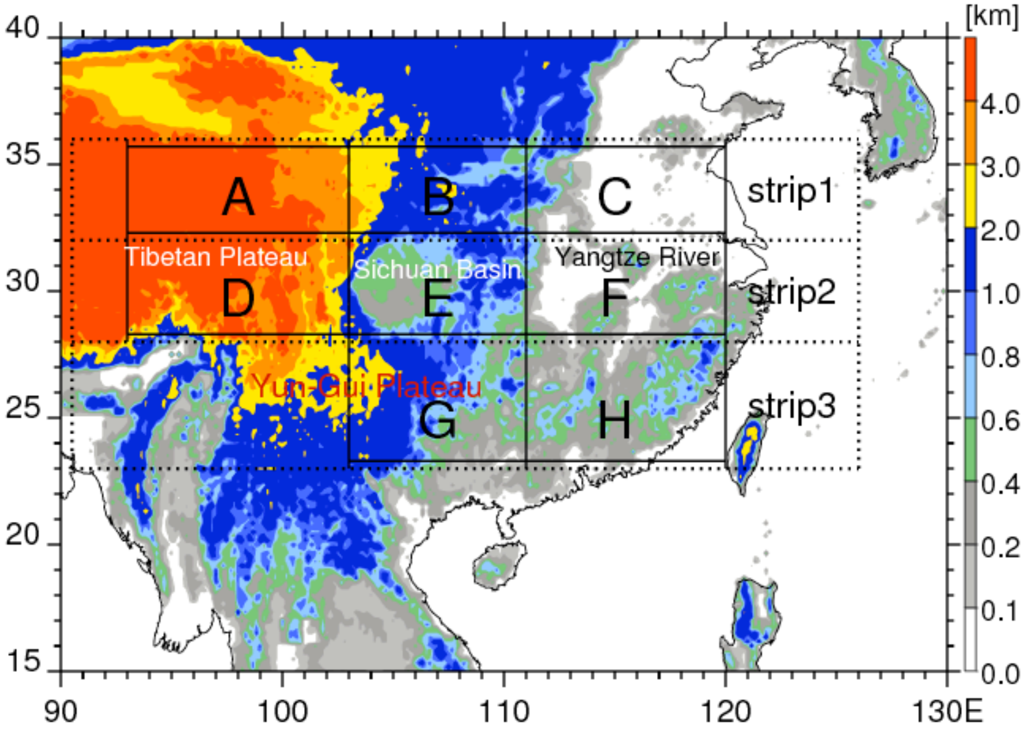

Figure 2.6. Map of the Eastern Tibetan Plateau and downstream. Elevation is given by the color bar. Dashed black boxes are selected strips (from north to south): strip 1, strip 2, and strip 3. Solid black boxes marked by capital characters are different regions for diurnal study. Sichuan Basin, Yangtze River, Tibetan Plateau, and Yun-Gui Plateau are indicated by text.

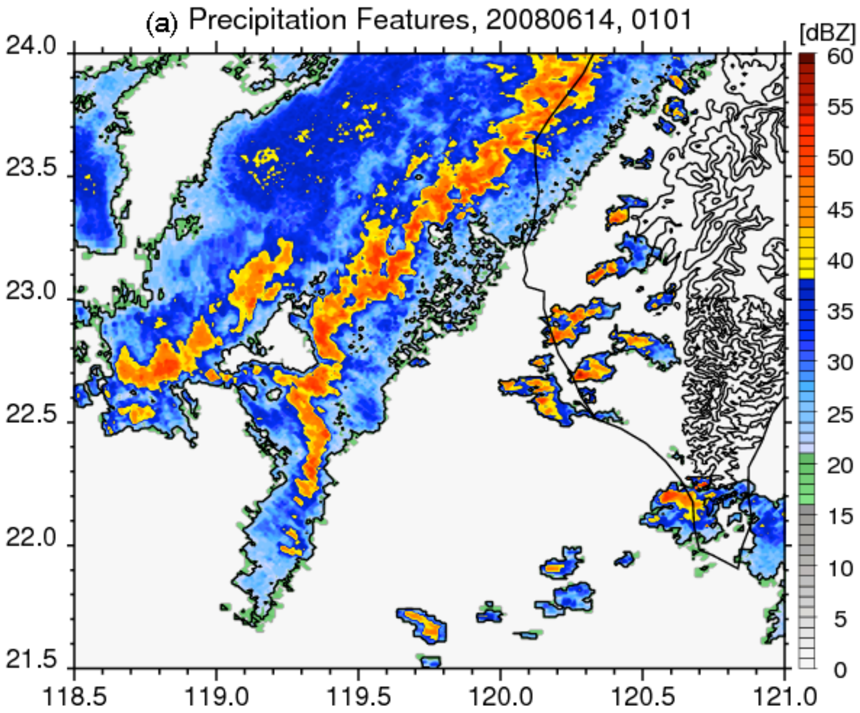

(a) Precipitation Features, 20080614, 0101

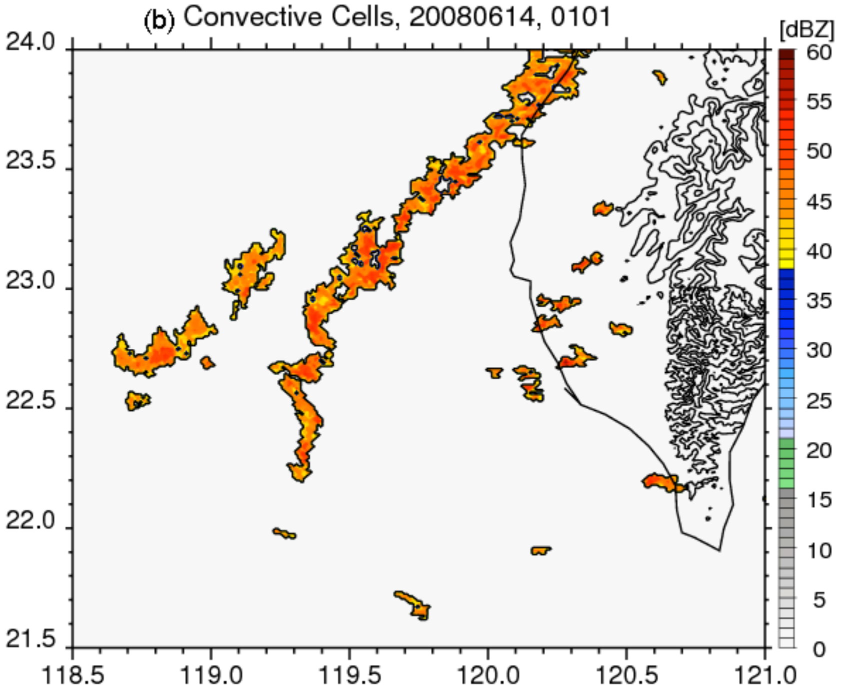

(b) Convective Cells, 20080614, 0101

Figure 2.7. Examples of (a) precipitation features with radar reflectivity > 18 dBZ, and (b) convective cells with radar reflectivity > 40 dBZ.

CHAPTER 3

RAINFALL AND LARGE-SCALE FLOW

As previously mentioned, East Asian monsoon rainfall is characterized by its concentration in rain belts that stretch for a few thousands of kilometers and undergo a stepwise seasonal march toward the north (Ding 1992; Chen 1988; Ding and Chan 2005). This section directly characterizes the population, location, variability, rainfall frequency, and large-scale flow of rain bands compromising the monsoon rain belt. The definition of Mei-Yu rain bands is given in Chapter 2.

3.1 Seasonal and Intraseasonal Changes

3.1.1 Large-scale Flow

Based on the climatology of monsoon onset and seasonal progress, four subseasons are defined: Premonsoon (April 1 to May 10), Mei-Yu (May 13-June 23), YZ-Meiyu (June 23-July 23), and Midsummer (July 25-August 25). During the transition period (about one week) from South China Mei-Yu to Yangtze River Mei-Yu, Mei-Yu fronts still propagate down to South China. Therefore, the definition of Mei-Yu in South China and Taiwan in this study extends one week from that in the literature (Chen 1983; Kuo and Chen 1990). The transition period is not included in the Yangtze River Meiyu.

Figures 3.1-3.3 present the large-scale wind fields at the lower (850 hPa), middle (500 hPa), and upper (300 hPa) troposphere in each period over East Asia. Seasonal transitions of the atmospheric flow are quite evident at all levels. Before the onset of the monsoon, low-level southwesterlies are already prevailing over South China and supported by flow from the Bay of Bengal and Indochina. However, anticyclonic circulation (the subtropical high) dominates the South China Sea, Philippines, and Taiwan at both 850 and 500 hPa levels. The subtropical ridge is located at about 20° N at 850 hPa and 15^{o} N at 500 hPa, and extends from the northwest Pacific Ocean to the eastern Indo-China Peninsula. Strong westerlies prevail throughout East Asia north of 20° N at both middle and upper levels.

3.1.2 Rainfall Distribution

After the onset of the monsoon (Mei-Yu), the subtropical anticyclonic circulation over the South China Sea is replaced by a monsoon trough at 850 hPa. Strong southerly and southwesterly flow comes from the deep tropics and brings a large amount of warm and moist tropical air to the East Asian monsoon region. In addition, the whole giant Asian monsoon circulation, including upstream southwesterlies over the Bay of Bengal, monsoon trough over the Indian Ocean, and the cross equatorial Somali Jet, get strengthened (not shown). The subtropical high ridge migrates to the southeast ocean of Taiwan during the first phase of Mei-Yu season over South China and Taiwan. The Mei-Yu front occurs at the northwest edge of the subtropical high where strong southwesterlies and deformation occur.

The subtropical high ridge (500 hPa) jumps to the north of Taiwan and extends to Southeast China during the Yangtze River Mei-Yu season. The westerlies in the midtroposphere weaken and retreat northward with the progress of the monsoon. By midsummer, westerlies retreat to northern China and the subtropical ridge (500 hPa) progresses up to central China. Though the southwesterly lower troposphere winds over southern China weaken, they extend to northern China during midsummer. During this period, the monsoon flow reaches its northernmost point.

The monsoon rainfall progresses with the same step as the large-scale circulation (Fig. 3.4). During Premonsoon, rainfall is more or less limited to continental South China and its adjacent ocean where relatively warm and moist southwesterlies frequently interact with the intrusion of cold midlatitude air (frontal systems). Since the subtropical high dominates the tropical Indochina and South China Sea, these regions are still very dry with little rainfall. Also in this season, the Bay of Bengal has very limited rainfall, indicating that the monsoon is not onset over East Indian Ocean. After the onset of the monsoon, rainfall over the South China Sea, Bay of Bengal, and foothills of TP increases markedly. Rainfall shows up as an evident rain belt located over southern China, Taiwan, and further northeast during the first phase of the Mei-Yu season. The monsoon rain belt jumps to the Yangtze River Valley region after late June with the northward progress of low-level southwesterly flow. At this period, Taiwan and the adjacent ocean experience a very sharp decrease of rainfall, when controlled by the subtropical high. In midsummer, rainfall spreads out over the whole Chinese monsoon region, with rainfall maxima over the South China Sea, Taiwan, and Philippines where tropical cyclones may contribute a large part of the midsummer rainfall (Chen et al. 2007).

3.2 Mei-Yu Rain Bands over South China

3.2.1 Population of Rain Bands

Generally, rain bands are oriented westsouthwest-eastnortheast (Fig. 3.5) and quite consistent with the 850 hPa wind shift line or front (Fig 2.4). From 1 May – 30 June, about 200 days in 10 years have rain bands, with about 65% in June, and 35% in May, with only 3 rain bands developing before May 10. Specifically, 80% of the rain bands occur during 13 May-23 June, while an evident transition happens around June 25, after which rain bands linger to the north of Yangtze River. The transition is a few days later than the one from “Mei-Yu in South China” to “Mei-Yu in Yangtze River” in Tao and Chen 1987.

Most rain bands are initiated over the region between 25°-30° N, and propagate southeast down to South China, Taiwan, or the South China Sea, with their late stage being quasi-stationary (not shown). Chen (1977, 1983) suggested that the Mei-Yu front develops in the deformation wind field between a migratory midlatitude high to the north and subtropical high to the south. The average lifetime of Mei-Yu rain bands being examined is about 4~5 days, while some extreme cases persisted for more than 10 days. This averaged time span of Mei-Yu rain bands is shorter than the average lifetime of Mei-Yu fronts (8 days) estimated by Chen (1988). The difference is probably due to our definition that excludes dry fronts or less active fronts without well-defined rain bands. On occasion, rain bands associated with decayed Mei-Yu fronts can propagate to the far South China Sea and oceans to the east of Taiwan, but are not counted in this study.

A few “retreat rain bands” (Chen et al. 2006) move northwestward slowly, after they reach the South China Sea (not shown). In this situation, rain bands persist over south China and Taiwan, and lead to extremely heavy rainfall and flash flooding. The coupling between the retrogression of a Mei-Yu front and short-wave trough provide favorable large scale conditions for the production of heavy rainfall in Taiwan (Yeh and Chen 2004; Chen et al. 2006).

The axis of the maximum distribution frequency (Fig. 3.5) is oriented along the south China coast, shifted somewhat south when compared to the Mei-Yu front statistics in Chen (1988). The distribution pattern indicates that the Mei-Yu front is often quasi-stationary in the vicinity of the Pearl River Delta. On average, about 7 rain bands per year (35%) stay over the Pearl River Delta region in South China, while 5 rain bands per year (30%) cross Taiwan.

3.2.2 Rainfall Contribution by Rain Bands

On average, about 18 days per year have Mei-Yu rain bands in South China and Taiwan. In other words, the break period (without rain bands) is just 4 days longer than the Mei-Yu active period (with rain bands) during the 40 days Mei-Yu season defined in this study. Accordingly, Mei-Yu rainfall is defined as accumulated precipitation on these days. Figure 3.6 shows the rainfall in the active periods and breaks. Rainfall contributed by tropical cyclones including tropical depressions and tropical storm have been removed.

As has been shown in Fig. 3.4b, rainfall maximum of the whole Mei-Yu season in South China and Taiwan (40 days) reaches above 500 mm over the Pearl River delta, foothills of Yun-Gui Plateau, Wuyi Mountains, and southwestern Taiwan. The Mei-Yu rainfall pattern matches the seasonal rainfall almost perfectly and has a very well-defined band shape (Fig. 3.6a). Roughly, the rainfall contributed by Mei-Yu rain bands is about 70% of the total rainfall during the Mei-Yu season. In addition, the rainfall is concentrated into a narrow band, with more than 75% of the precipitation falling into a 4 degree wide band (not shown). Speculation is that storms with heavy rainfall are mostly triggered and develop along the convergence line near the low level front, where dynamic forcing is strong and moisture is abundant. The rainfall maxima within the long and narrow rain band should be associated with terrain effects to some degree. Possible effects and mechanisms on the heavy orographic precipitation will be discussed in another section.

On the other hand, break periods occupy more than half of the days but only contribute 30% of the seasonal rainfall, and rainfall during the break is distributed more widely (Fig. 3.6b). During breaks, rainfall maxima show up over the foothills of the Yun-Gui Plateau, Sichuan basin, and Yangtze River valley. Also during breaks, the maximum rainfall center over Taiwan in Mei-Yu period disappears. Moreover, the precipitation center to the west of Canton is oriented southeast-northwest, parallel to the southeasterly flow prevailing during the break (Chen 1994). The weak southwesterly or southeasterly flow during the break (Chen 1994) may also lead to the disappearance of the rainfall maximum in Taiwan. A significant amount of rainfall shows up along oceans to the east of Taiwan and around the Philippines only during the break. It does not mean rainfall over the ocean is preferable for the break. This could be due to the fact that rain bands or rainfall maxima over oceans away from South China and Taiwan are not counted into Mei-Yu rain bands.

3.2.3 Diurnal Cycle of Rainfall

Though the occurrence of Mei-Yu fronts may not show diurnal variability, the associated rainfall has some diurnal features (Fig. 3.7). Viewed from the whole Mei-Yu region, there is less rainfall occurring in the night time and early morning within Mei-Yu rain bands. Diurnal cycles of rainfall in specific regions are significantly different. Rainfall from Mei-Yu fronts over southeast China shows an evident afternoon peak and a minimum at night-time. However, rainfall precipitated from rain bands in the region of the foothills of the Yun-Gui Plateau prefers early morning. Morning and afternoon precipitation contributes the most to Taiwan's Mei-Yu rainfall. Minimum rain falls on the ocean during night time with the passage of Mei-Yu rain bands. Therefore, the rainfall maxima of Mei-Yu rain bands as mentioned previously show different diurnal cycles.

In contrast, rainfall maxima in breaks are mostly in early morning and morning rainfall (Fig. 3.8). For example, the south-northward oriented rainfall maximum along the foothill of the Yun-Gui Plateau is largely early morning rainfall. The early morning rainfall peak also presents as a band along the Yangtze River starting from the Sichuan Basin. The eastward propagation of clouds and rainfall from eastern Tibetan Plateau during early morning has been pointed out by many authors (Wang et al. 2004; Yu et al. 2007a). More specific analysis of the diurnal cycle of convection and storms over the East Asian monsoon region to the east of the Tibetan Plateau is described in Chapter 5.

3.2.4 Large-scale Flow of Active and Break Periods

This section studies the characteristics of large-scale flow associated with active Mei-Yu periods and breaks. Periods with Mei-Yu centers of rain bands passing the key Mei-Yu region are selected as "Active" to construct the composite of the large-scale wind field, while days with only scattered rain (without rain bands) are defined as "Break". Area within (107-120 E; 22-28 N) is defined for the key region of Mei-Yu in South China. The composite wind fields at 850 and 500 hPa for Active and Break periods are shown in Figs. 3.9-3.10.

During both Active and Break periods, components of the East Asian Monsoon are quite evident: monsoon trough over the South China Sea adjacent to eastern Indochina Peninsula, subtropical high over the Pacific oceans to the southeast of Taiwan, significant southwesterlies over South China and the South China Sea, and strong westerly to southwesterly flows over Bay of Bengal. However, there are significant differences between Active and Break periods, mostly on the magnitude of these components. The most evident difference is that low level (850 hPa) southwesterly flows over South China and the South China Sea during Active are much more intense than during Break. The horizontal winds over South China during Break periods are more southerly, especially close to the foothills of the Plateau. Stronger southwesterlies over Indochina and the South China Sea during the Active periods would help to transport more moisture from the tropics to the Mei-Yu region and also help to provide stronger low-level convergence. The difference at the low-level circulation could be related to more intense subtropical high to the southeast of Taiwan. At the midlevel (500 hPa), the Active shows a cyclone over South China and the South China Sea while the Break does not.

3.3 Mei-Yu Rain Bands over Yangtze River

After the monsoon rain belt migrates to the region of the Yangtze River valley, less well-defined rain bands occur there compared to the Mei-Yu season over South

China and Taiwan (Fig 3.11). During 10 YZ-Meiyu seasons (1998-2007), about 100 well-defined daily rain bands show up over the Yangtze River valley region. Most of the rain bands are initiated over the region between 35 ^{o}-40 ^{o} N. During the transition period of June 15-25, many of the rain bands propagate southward down to South China. However, very few rain bands move to South China after June 25 when the monsoon rain belt gets stabilized over the Yangtze River valley. The seasonal migration of the rain belt to the north is associated with the seasonal change of large-scale circulation around mid-June (Ding 1992; Chen et al. 1993; Ding and Chan 2005). After mid-June, the Pacific subtropical high jumps to the north of Taiwan from the South China Sea. In addition, midlatitude disturbances or midlatitude high become weaker and cannot penetrate to south China. The combination of these two factors helps the Mei-Yu front establish its location over the Yangtze River valley being quasi-stationary. At the upper troposphere (300 hPa), the prevailing westerlies over South China retreat to the north of the Yangtze River and become weaker as the monsoon rain belt jumps to the Yangtze River region (not shown).

The maximum distribution frequency (Fig. 3.11b) is located over the Yangtze River basin. Every year, about 4~5 rain bands pass this region, while only one rain band per year crosses the South China Mountain Range. Rain bands during this season extend into the Sichuan Basin just at the foothills of the Tibetan Plateau. Southwest vortices can develop over the Sichuan basin and propagate eastward along the Mei-Yu front (Kuo et al. 1986; Wang et al. 1993).

The rain belt comprised of rain bands extends from the Sichuan Basin and foothills of the eastern Tibetan Plateau through the Yangtze River valley to Korea (Fig. 3.12). YZ-Meiyu rain bands contribute about 75% of the seasonal total rainfall over the Yangtze River region. The rainfall maximum center along the rain belt is directly over the Yangtze River basin. Both during active YZ-Meiyu and breaks, very little precipitation falls on Taiwan and adjacent oceans where the tropical high dominates, except for rain systems of tropical origin. However, convection is frequently pumped up and drops a significant amount of rainfall on the west rim of the subtropical high and foothills of the Plateau. Much less rain falls on the monsoon region during the break and rainfall is more widely distributed. A rainfall maximum at the foothill of the Yun-Gui Plateau is also observed during breaks.

3.4 Extreme and Orographic Rainfall over South China

This study focuses on the Mei-Yu season over South China and Taiwan where heavy precipitation, flash flood, and land sliding occurs frequently. Extreme precipitation is often embedded in the thousand kilometers long and several hundreds kilometers wide daily rain band. South China and Taiwan are also affected by high mountains and complex terrain. Extreme rainfall is studied in terms of heavy rain and long-duration rain.

3.4.1 Heavy Rain and Long-duration Rain

Figure 3.13 shows the frequency function of rainfall contribution by precipitation in different rain rates. More rain is contributed by the precipitation in higher intensity during Premeiyu and active Mei-Yu periods. In this study, heavy rain is defined as 3B42 grid rain rate greater than 8 mm hr^{-1} at the 25 by 25 km grid and 3-hour temporal interval. By this definition, about 35% of the rainfall in Premeiyu and Mei-Yu is contributed by heavy precipitation, while only 25% of the rainfall is heavy in the Break and Postmeiyu. Stronger large-scale forcing and moisture transportation may be related to higher probability of heavy rain in active Mei-Yu than the Break.

Figure 3.14 shows the geographical distribution of heavy rainfall. During Premeiyu, heavy precipitation prefers the location of the Pearl River Delta and the southern part of the Yangtze River basin. The total rainfall maxima in the Sichuan Basin and at foothills of the Yun-Gui Plateau are not accompanied by heavy rainfall maxima. However, heavy rainfall preferential locations in Mei-Yu matches quite well with total Mei-Yu rainfall maxima. Heavy rainfall in these maxima locations contributes more than 40% of the total rainfall. An exception is that the rainfall center in the Wuyi mountain region is missing an evident heavy rainfall maximum. In contrast, spatial distribution of heavy rainfall in the break is more widespread, increasing slightly at foothills of the Yun-Gui Plateau and Yangtze River basin. In summary, heavy precipitation has higher possibility to occur over the river delta, upstream ocean, river basin, and upstream foothills of high terrains, even during the passage of rain bands. Orographic enhancement may play a significant role in this heavy rainfall distribution pattern.

Long-duration rain (> 6 hours) is distributed similarly to heavy rainfall, but has lower rainfall contribution (Fig. 3.15). Generally, the long-duration precipitation contributes only about 15~20% of the total rainfall. For the maximum rainfall centers during Mei-Yu, long-duration rain has about 30% contribution. Evidently, the quasi-stationary Mei-Yu front is favorable for the occurrence of heavy and long-duration precipitation. This could be related to long-lived MCSs embedded in the Mei-Yu front supported by the unstable low-level flow from the south and dynamic forcing in the frontal zone. Persistent interaction between the prevailing monsoon flow and significant orography could also help to enhance the long-lived heavily precipitating mesoscale cloud systems.

3.4.2 Orography-associated Rainfall

Further examination on the distribution of rainfall maxima, prevailing low-level flow, and terrain (Fig. 3.16) indicates that three of the four rainfall maxima during active Mei-Yu periods are located to the windward of mountains, e.g., Pearl River delta, southwest foothills of the Yun-Gui Plateau, and southwestern Taiwan. Basically, during the passage of a Mei-Yu front, warm and moist southwesterly flow or a LLJ impinges on the south China mountain ranges and central Taiwan Mountains, providing forced ascent and abundant moisture for new convection or precipitation enhancement. Different mechanisms for heavy orographic rainfall in Mei-Yu season have been proposed such as barrier jet (Li and Chen 1998), additional lifting by the blocking of mountains (Chen et al. 2005), localized convergence due to the interaction between the prevailing flow and offshore flow in the early morning over southwest Taiwan (Chen et al. 2005), and etc. Interestingly, low mountain ranges (400-1000 m) over central south China seem to play a comparable role in precipitation enhancement to that of the Yun-Gui Plateau and the high mountains (> 2000 m) in Taiwan.

During breaks, the low-level winds are weaker than that in active periods. Wind direction changes from southwesterly to slightly southerly, especially at the western part of South China. The rainfall maxima in the break also vary from the active periods. A rainfall maximum is observed in the mountainous area at foothills of the Plateau, where low-level southerlies impinge.

3.5 Wet and Dry Mei-Yu in South China

3.5.1 Definition of Wet and Dry Mei-Yu

"Wet" and "Dry" Mei-Yu seasons are defined by the occurrence frequency of Mei-Yu rain bands during 1998-2007. Time series of population and rainfall contribution of Mei-Yu rain bands occurring over South China in Mei-Yu season (May 13-June 23) are shown in Fig. 3.17. The population of rain bands evidently varies from one year to another. The year with highest occurrence accounts for about 15% of the total population in 10 years and is three times the lowest occurrence year (5%). The rainfall contribution from rain bands also shows similar variability. We select the years with population and rainfall evidently higher (lower) than the average as Wet (Dry) Mei-Yu years. Based on Fig. 3.17, 1998, 2001 and 2006 are defined as Wet years, while 1999 and 2004 are selected as Dry years.

3.5.2 Rainfall Characteristics

Figure 3.18 shows the averaged rainfall from rain bands in South China and Taiwan Mei-Yu season of Wet years and Dry years. During Wet years, Mei-Yu rain bands are very active and contribute about 400 mm rain fall along the rain belt, with maxima up to 600 mm. However, Mei-Yu rain bands have less than 200 mm rain on average. Very few rain bands propagate down to the South China Sea or Taiwan in Dry years (not shown).

The seasonal rainfall in Dry years is also much less than that in Wet years (Fig. 3.19), indicating population of Mei-Yu rain bands is a good indicator of wet or dry Mei-Yu season. During Wet years, seasonal rainfall maxima at the Pearl River Delta and Southern Taiwan reach about 800 mm. Taiwan and the adjacent ocean experience very sharp decrease of rainfall in Dry years, with averaged seasonal rainfall less than 300 mm. Evidently, characteristics of rainfall in South China and Taiwan change greatly from Wet years to Dry years. One would like to examine the differences between the large-scale flow and environment supporting the particular rainfall pattern in Wet and Dry years.

3.5.3 Large-scale Flow Pattern

Horizontal wind fields composite in Wet years and Dry years at low-level and midlevel are constructed, separately (Figs. 3.20-3.21). Results indicate that low-level southwesterlies over the South China Sea in Wet years are much stronger than those in Dry years. Low-level southwesterly flow in front of the monsoon trough is very important in transporting moisture and energy to the weather systems occurring over South China and Taiwan. The more intense the low-level southwesterly flow, the more active the convection and weather systems in the downstream region. Further examination shows that the stronger low-level southwesterlies in Wet years are associated with the subtropical anticyclone to the south or southeast ocean of Taiwan extending further west and more intense (see the right bottom corner of Fig. 3.20c and 3.21c). Another featured difference between Wet years and Dry years is the stronger flow at midlevel coming from the northwest at midlatitude during Wet years (Fig. 3.21c). This could be related to stronger cold air intrusion to South China from behind the midlatitude trough in Wet years (Chen 1993). Therefore, the combination of stronger cold air intrusion and more intense warm and moist flow from the tropical ocean provides a more favorable environment for convection and precipitation in Wet years. This situation has been pointed out by many authors as the favorable setting for prolonged Mei-Yu fronts and heavy precipitation (Ding 1991; Chen 1994; Wu 2002).

3.6 Summary and Conclusions

Monsoon rain bands during Mei-Yu season (May-June) in South China and Taiwan are first defined and characterized based on TRMM 3B42 rainfall analysis. Mei-Yu rain bands and associated rainfall characteristics are carefully examined in terms of population, location, variability, rainfall frequency, and large-scale flow. Analysis on rain bands are extended to northward monsoon progress in the Yangtze River region. Conclusions and findings are summarized as follows:

(1) During the South China/Taiwan Mei-Yu season, about 5-7 well-defined rain bands pass over the South China and Taiwan region every year, with the maximum frequency at the Pearl River Delta and foothills of the Yun-Gui Plateau;

(2) Most rain bands are initiated over the region between 25 ^{o}-30 ^{o} N, and propagate southeast down to South China, Taiwan, or the South China Sea, with their late stage being quasi-stationary during an averaged life time of about 4-5 days;

(3) More than 70% of Mei-Yu season rainfall is contributed by well-defined rain bands in South China and Taiwan, and the rainfall is concentrated into a narrow band, with maxima located at the Pearl River Delta, foothills of the Yun-Gui Plateau, Wuyi mountain at the southeastern China coast, and Southwest Taiwan;

(4) During breaks, rainfall spreads widely over South China and contributes less than 30% of the total seasonal rain, while the Mei-Yu maximum rainfall center over Taiwan disappears and rainfall in Taiwan has very low occurrence;

(5) The low-level (e.g., 850 hPa) monsoon southwesterly flows over South China and the

South China Sea during active periods are much more intense than during break periods, and they are more southerly during break periods, especially close to the foothills of the Plateau;

(6) About 4-5 rain bands pass the Yangtze River region during the Yangtze River Mei-Yu season from mid-June to mid-July, and very few of them move southward to South China after June 25 when the monsoon rain belt gets stabilized over the Yangtze River valley;

(7) The rain belt comprised of rain bands in the Yangtze River Mei-Yu extends from the Sichuan Basin and foothills of the eastern Tibetan Plateau through the Yangtze River valley to Korea and contributes about 75% for the total seasonal rainfall;

(8) The Mei-Yu rain bands and associated rainfall have very evident interannual variability: during the active years, Mei-Yu rain bands are very active and contribute about twice of the rainfall in dry years when very few rain bands propagate down to the South China Sea or Taiwan;

(9) Stronger low-level southwesterlies associated with the westward extending and more intense subtropical anticyclone to the south or southeast ocean of Taiwan are found in wet years than in dry years, while wet years also experience stronger flow at midlevel coming from the northwest at midlatitude.

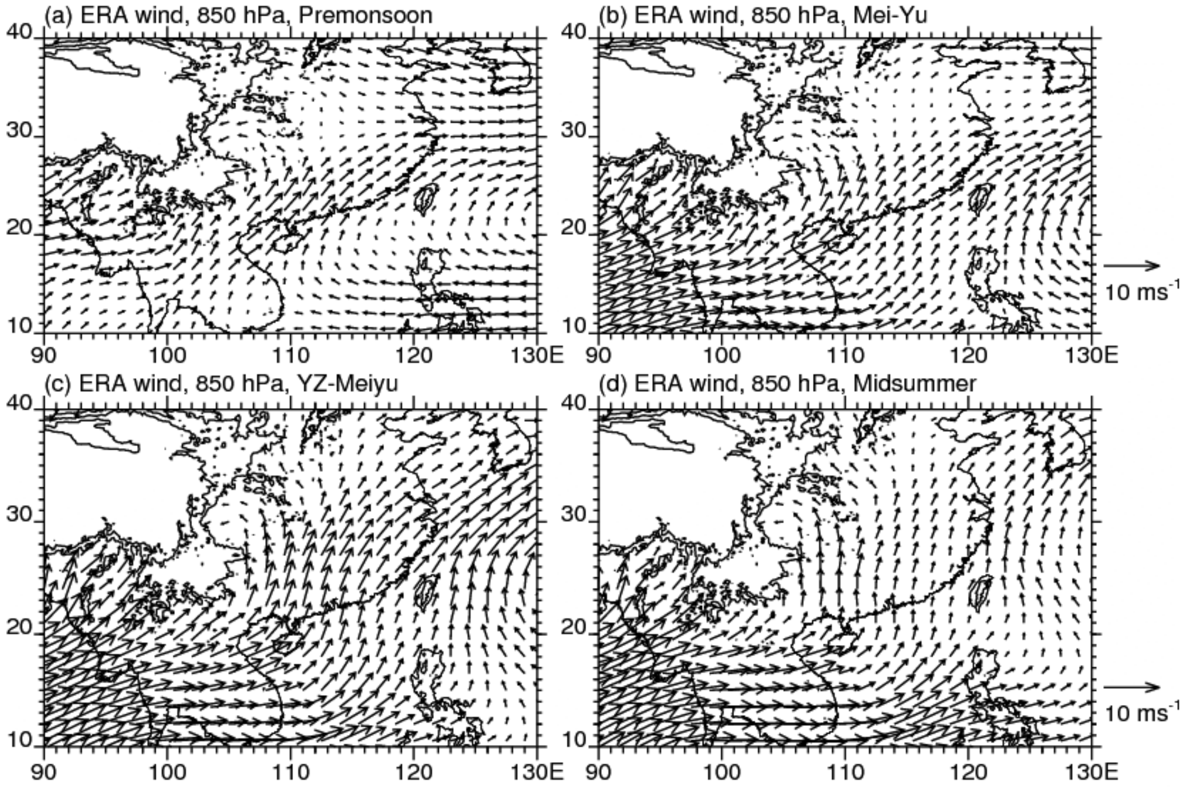

Figure 3.1. Averaged wind field at 850 hPa during 1998-2007 based on ERA-Interim reanalysis. Four different defined periods are included (a) Premonsoon; (b) Mei-Yu; (c) YZ-Meiyu; and (d) Midsummer. Scale of wind arrow is shown on the right side.

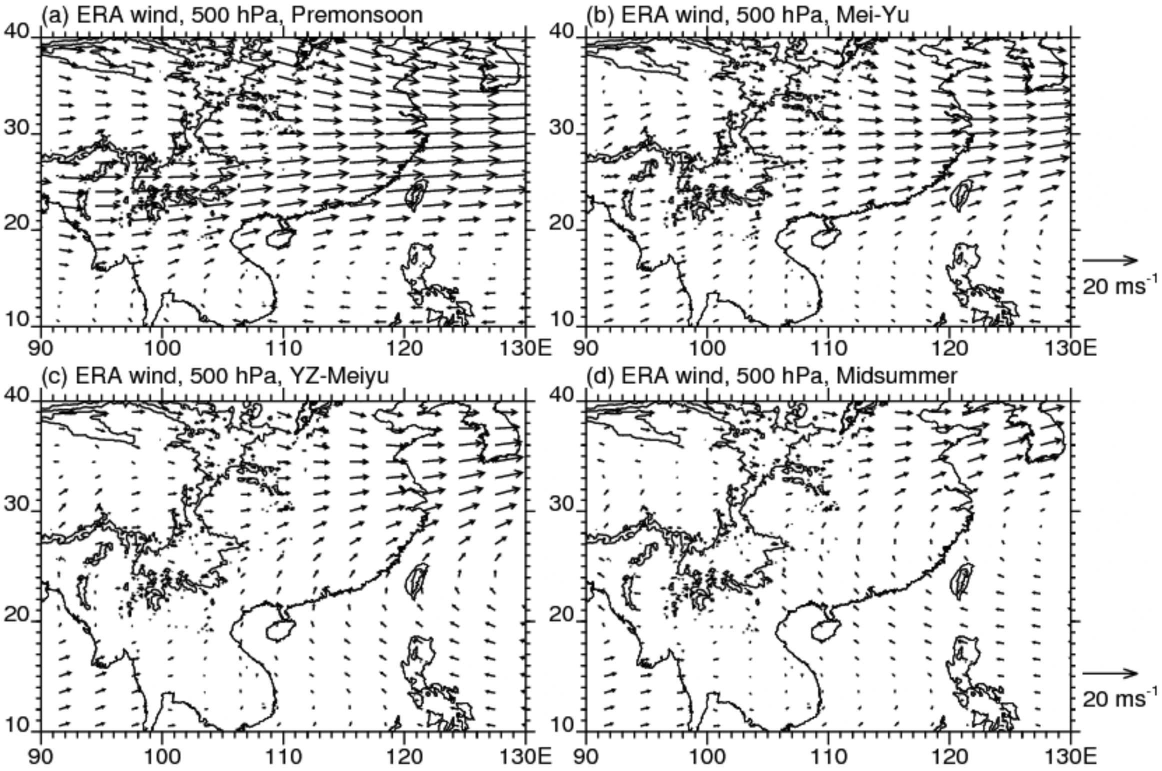

Figure 3.2. Same as Fig. 3.1, but for 500 hPa.

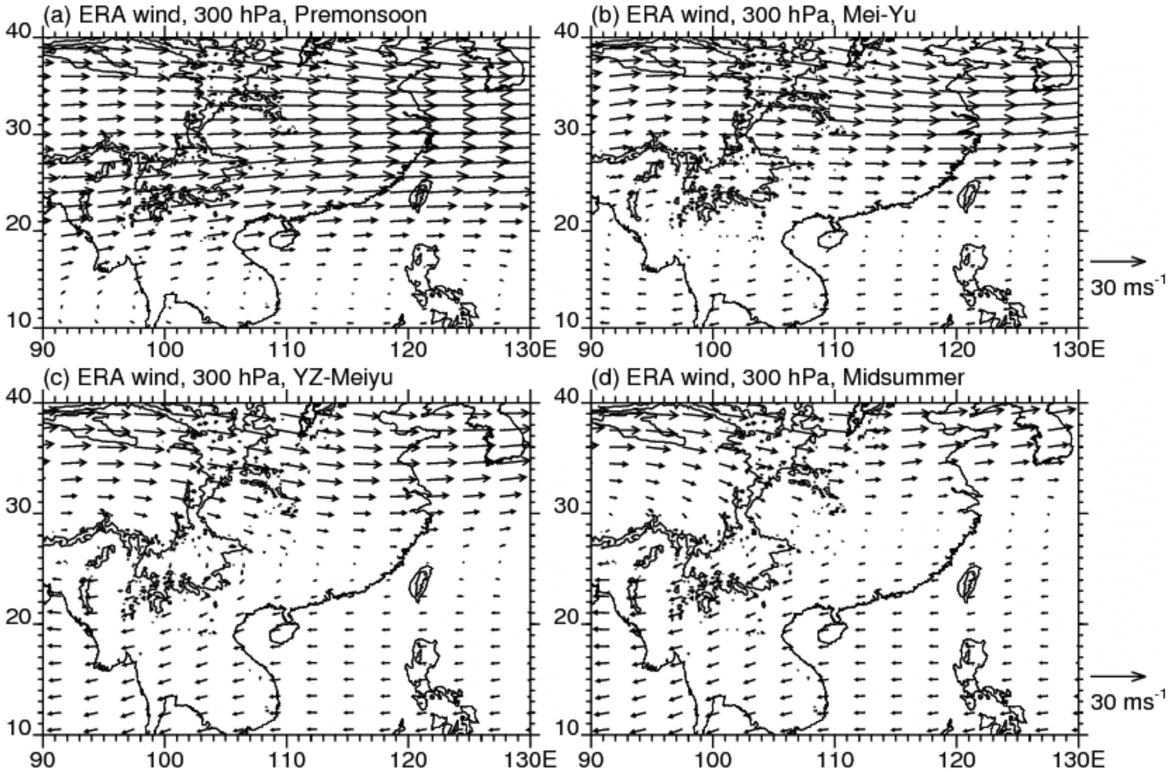

(a) ERA wind, 300 hPa, Premonsoon

(b) ERA wind, 300 hPa, Mei-Yu

(c) ERA wind, 300 hPa, YZ-Meiyu

(d) ERA wind, 300 hPa, Midsummer

Figure 3.3. Same as Fig. 3.1, but for 300 hPa.

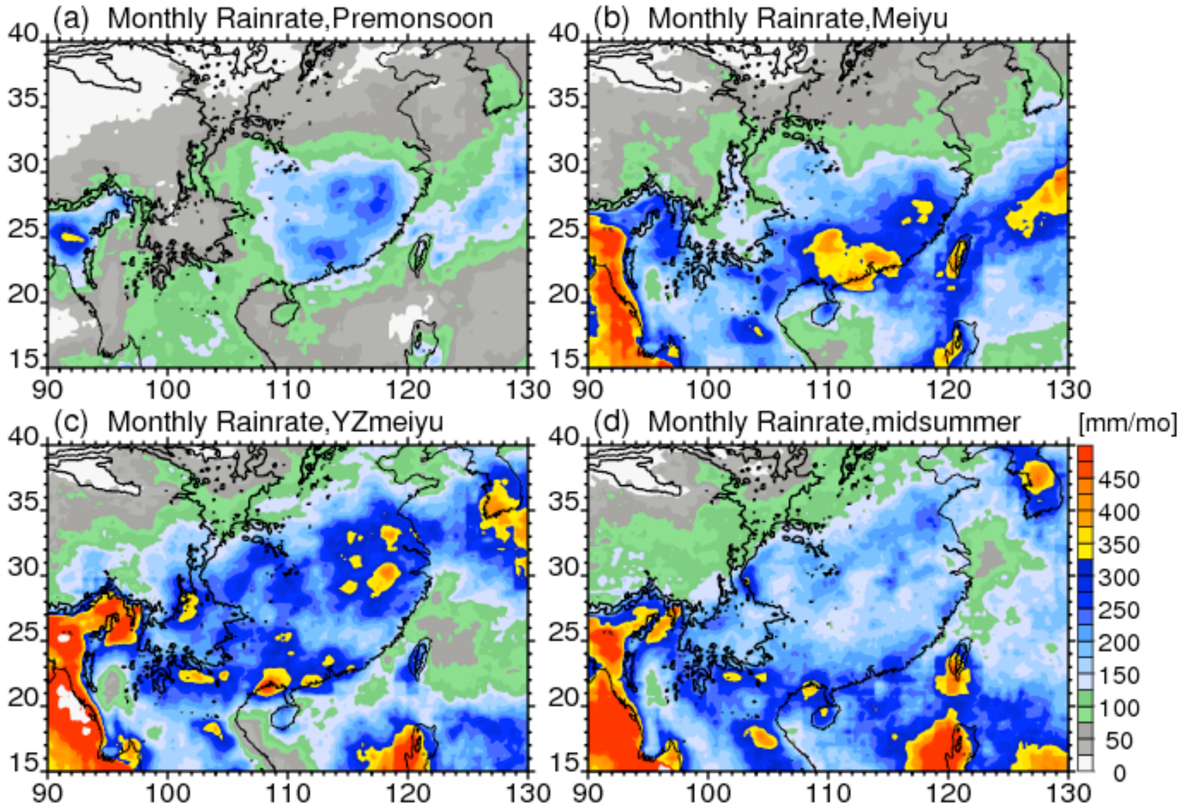

Figure 3.4. Seasonal rainfall distribution in unconditional rainrate (mm/mo) during different periods: (a) Premonsoon; (b) Mei-Yu; (c) YZ-Meiyu; and (d) Midsummer.

(a) Rain bands, 1998-2007,Meiyu

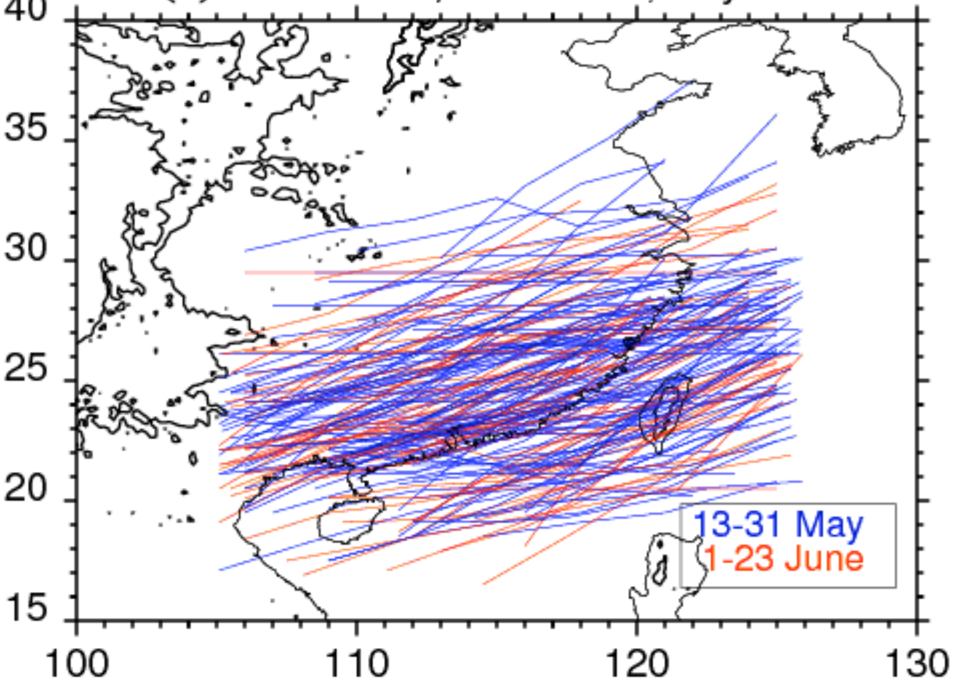

(b) Frequency, 1998-2007,May13-Jun23

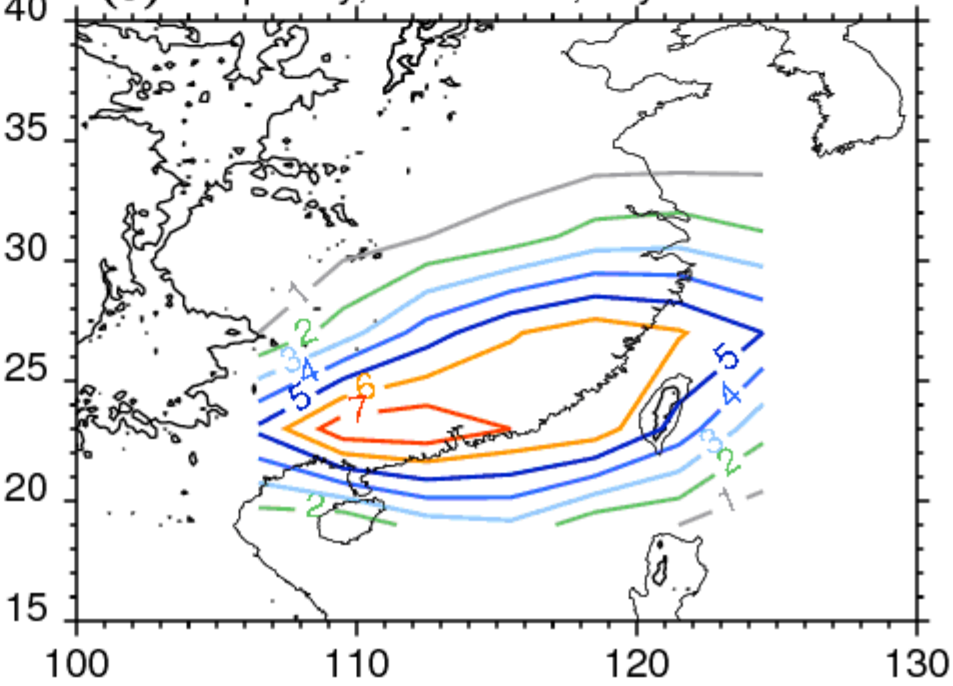

Figure 3.5. Mei-Yu rain bands. (a) Distribution of the central line of Mei-Yu rain bands in May 13-Jun 23 during 1998-2007; (b) Occurrence in a 3 by 2 degree box.

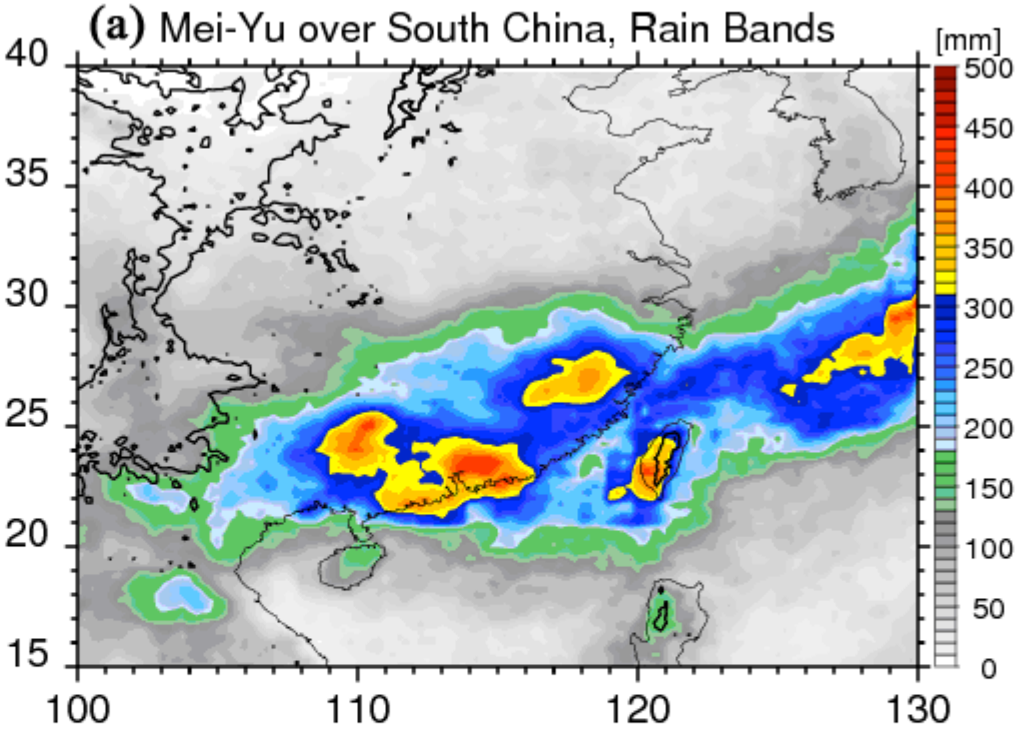

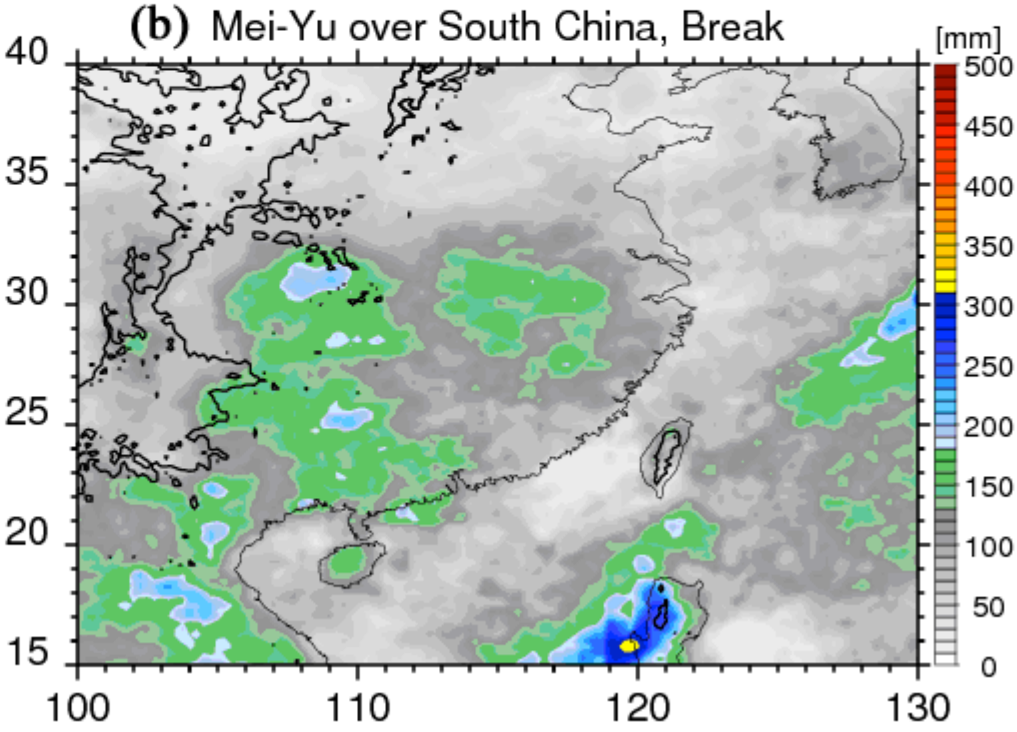

Figure 3.6. Spatial distribution of rainfall contributed by rain bands and in the Break during Mei-Yu season averaged for 10 years (1998-2007).

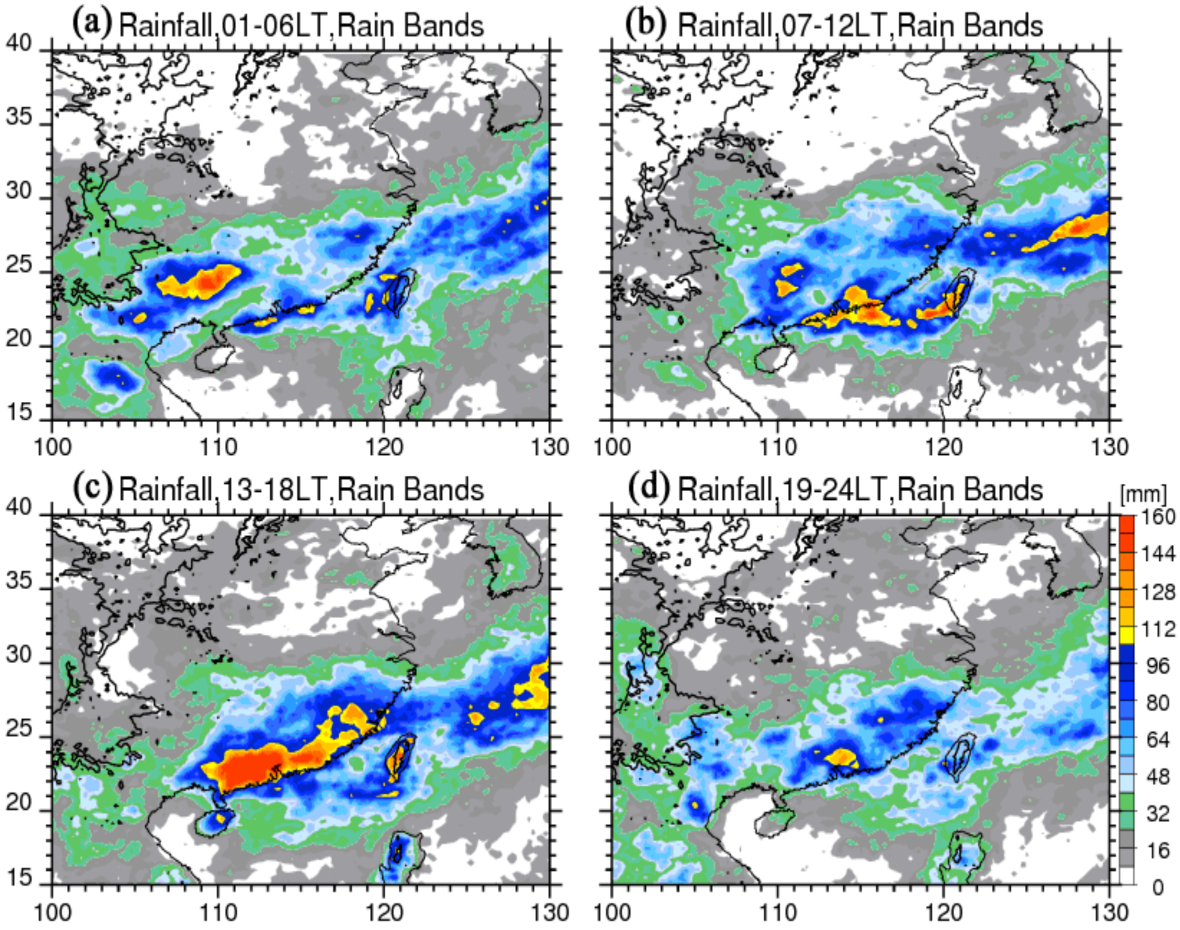

Figure 3.7. Diurnal cycle of averaged rainfall in every 6 hours contributed by rain bands during South China Mei-Yu season.

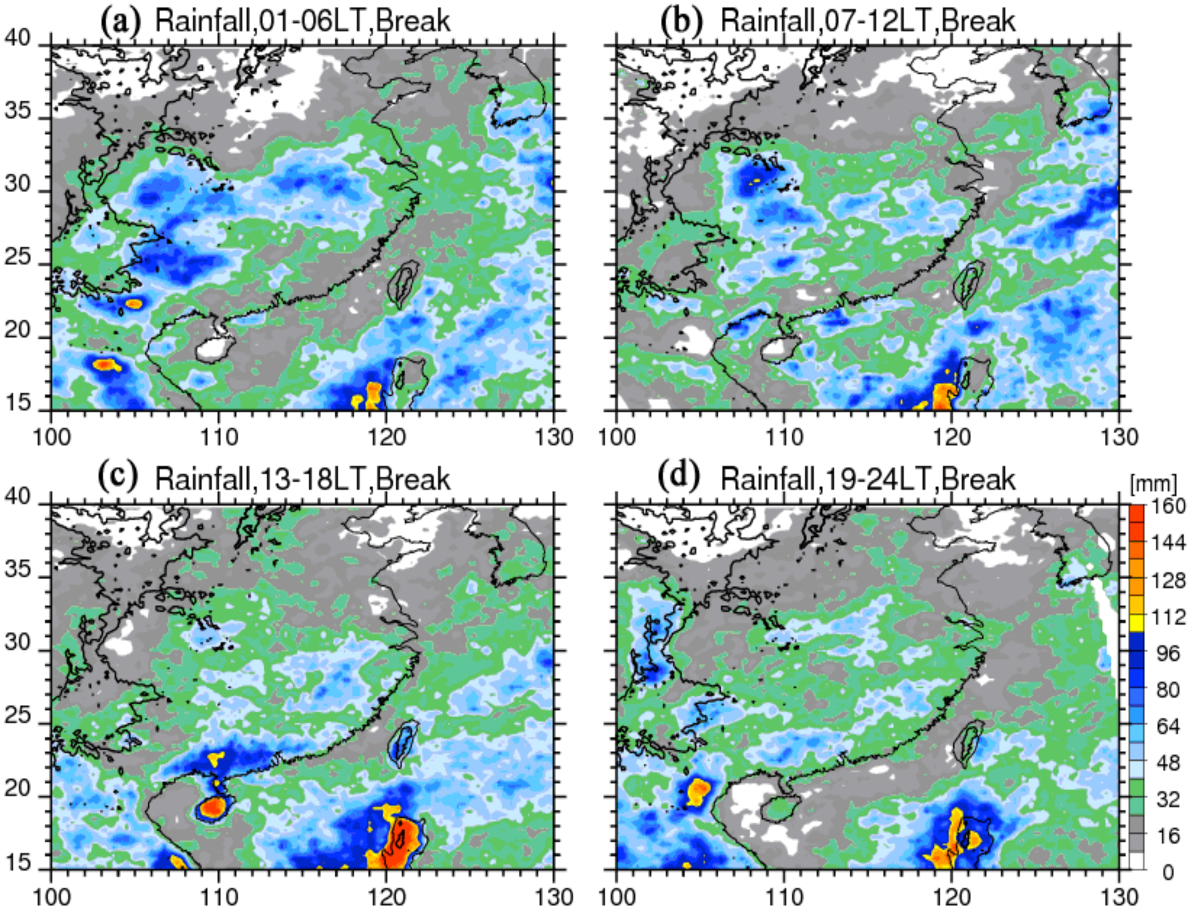

Figure 3.8. Same as Fig. 3.7, but for the break periods.

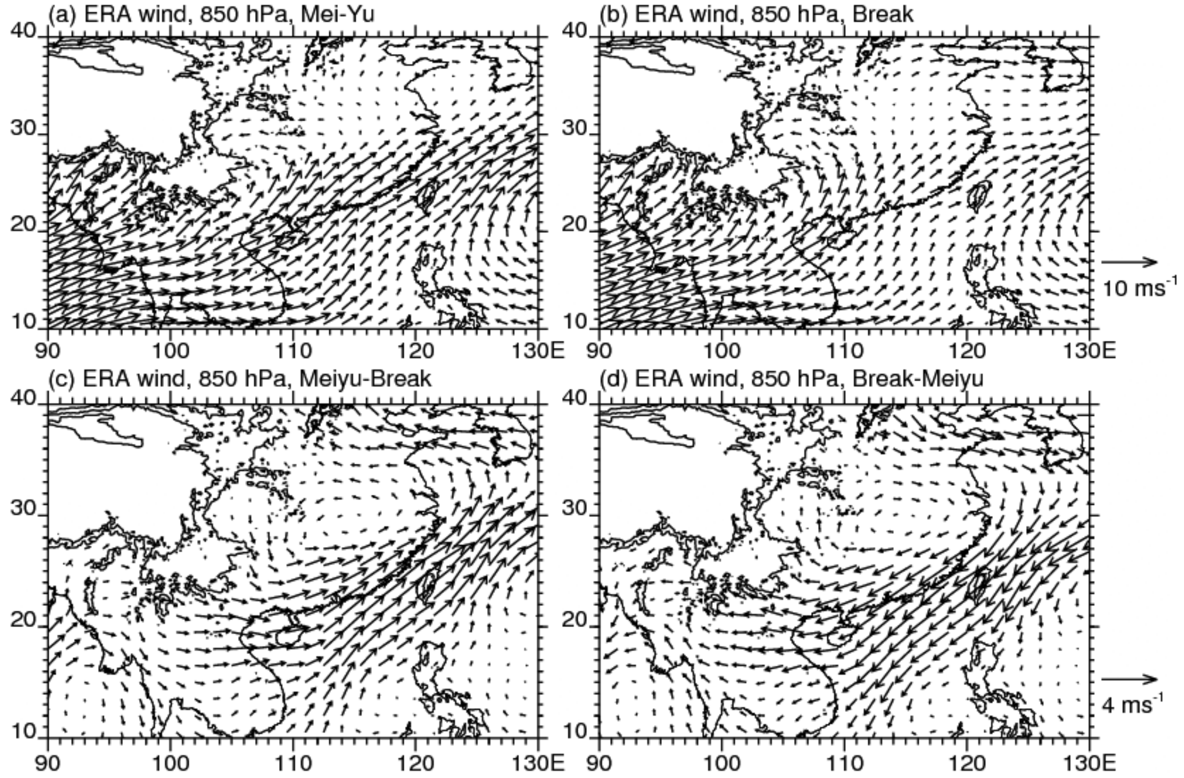

Figure 3.9. Wind field composite at 850 hPa level for (a) Active Mei-Yu periods, (b) Break periods, (c) deviation of active Mei-Yu from Break, and (d) deviation of Breaks from Actives. Wind scale is presented on the right side of the figure.

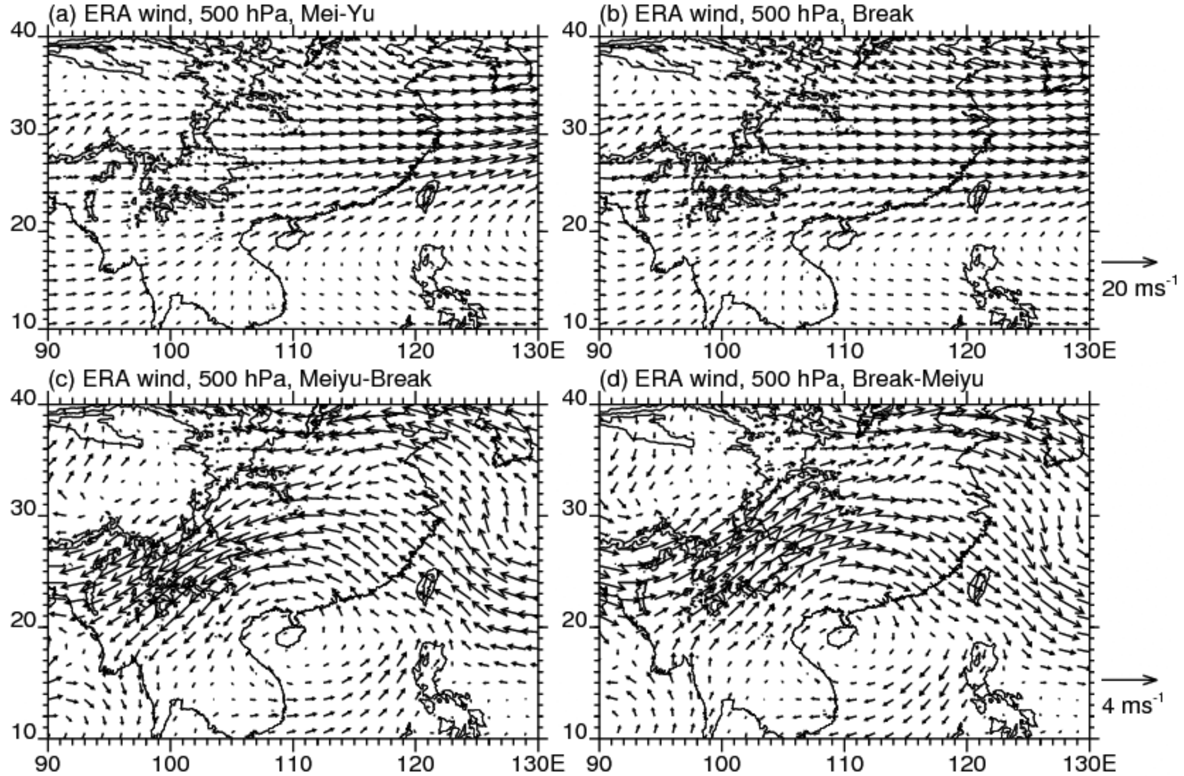

Figure 3.10. Same as Fig. 3.9, but for 500 hPa.

(a) Rain bands, 1998-2007,YZmeiyu

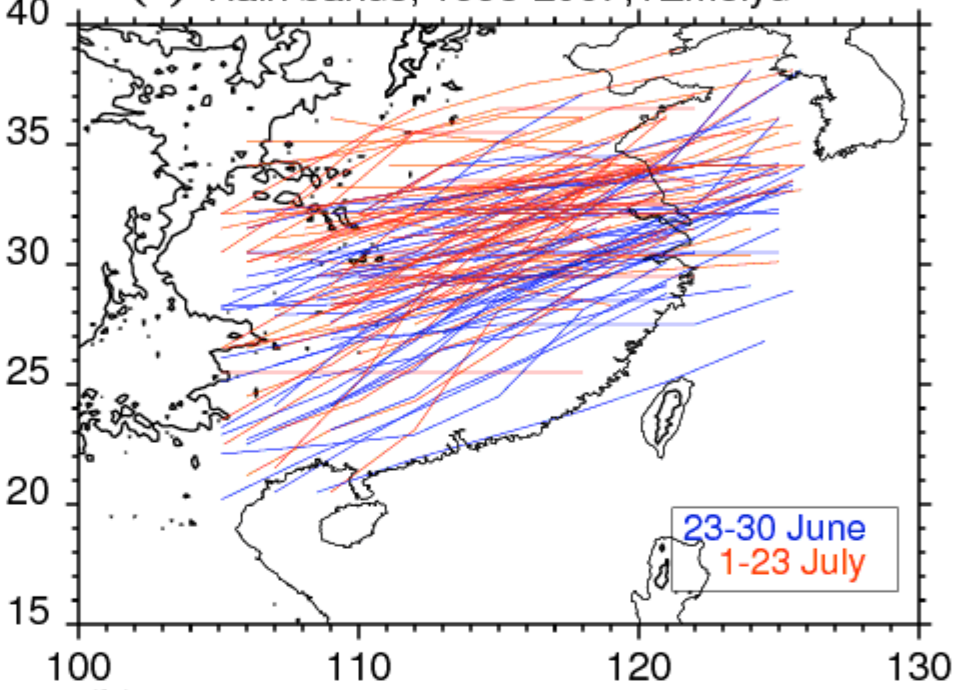

(b) Frequency, 1998-2007,June 23-July 23

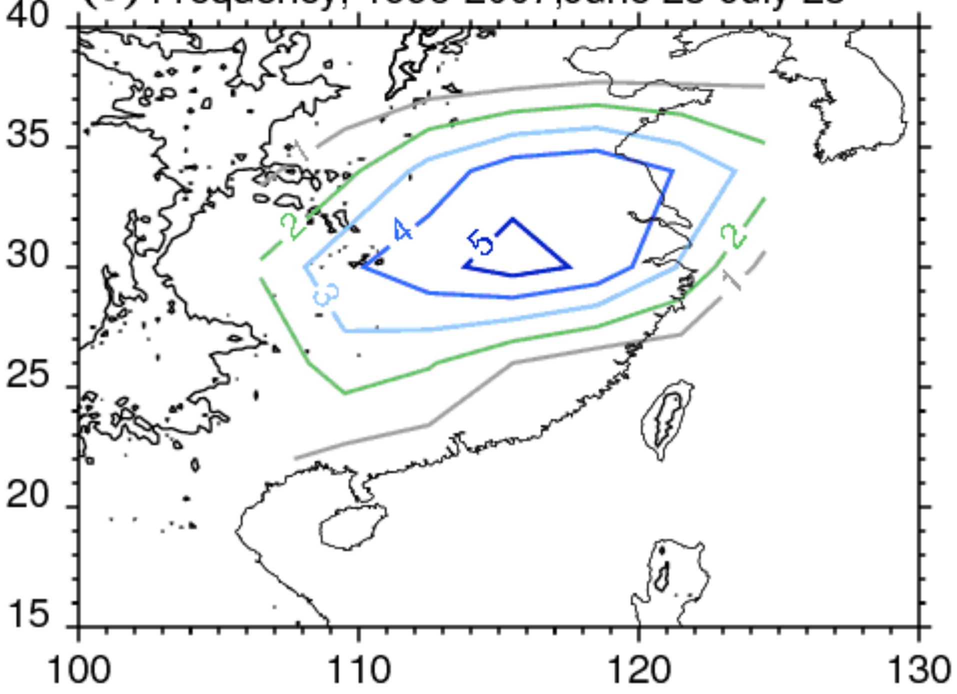

Figure 3.11. Distribution of rain bands. (a) Central lines of rain bands between June 23-July 23 during 1998-2007; (b) Occurrence in a 3 by 2 degree box.

(a) Mei-Yu over Yangtze River, Rain Bands

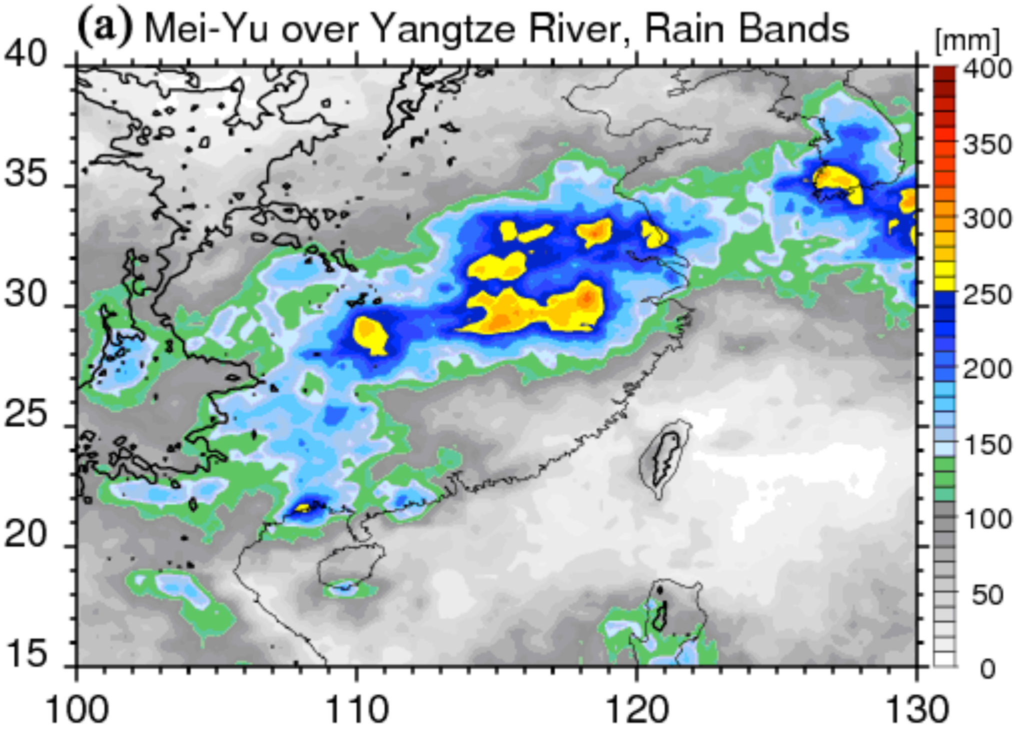

(b) Mei-Yu over Yangtze River, Break

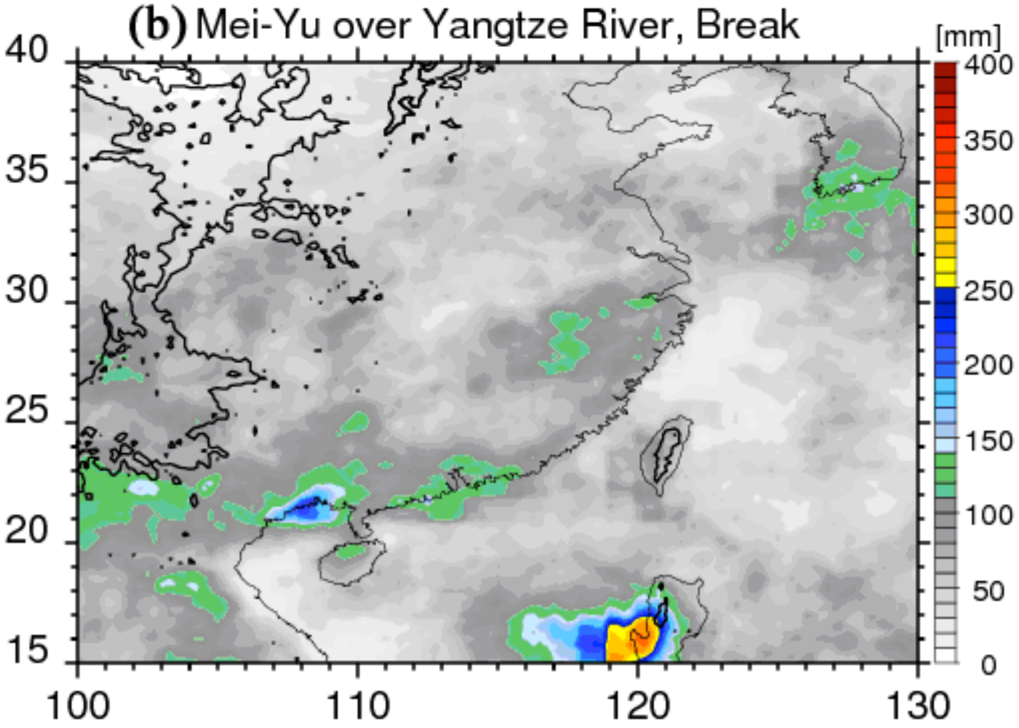

Figure 3.12. Spatial distribution of rainfall contributed by (a) rain bands and (b) in the Break period during YZ-Meiyu season.

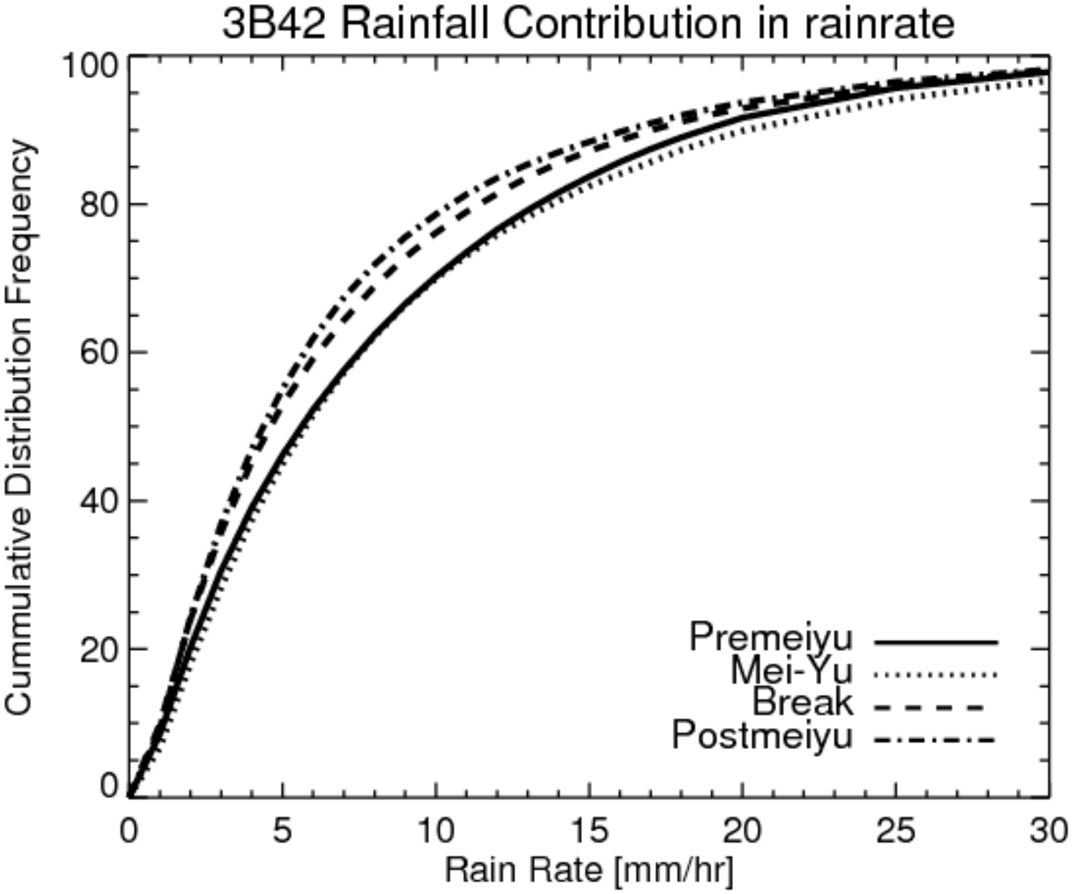

Figure 3.13. Cumulative Distribution Frequency (CDF) of rainfall contribution by different rain rates during different periods in the box of (108-122 E; 20-28 N).

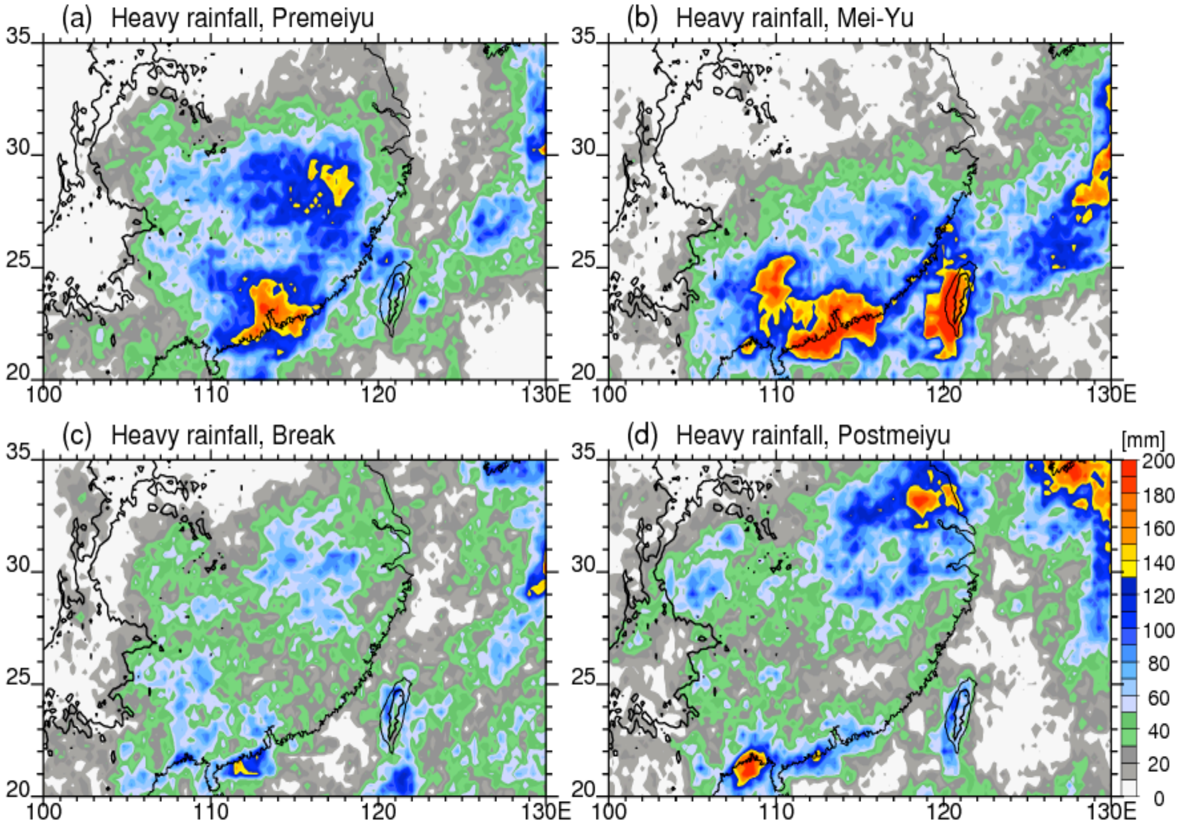

Figure 3.14. Distribution of rainfall contributed by heavy precipitation (> 8 mm hr^{-1}) in different periods.

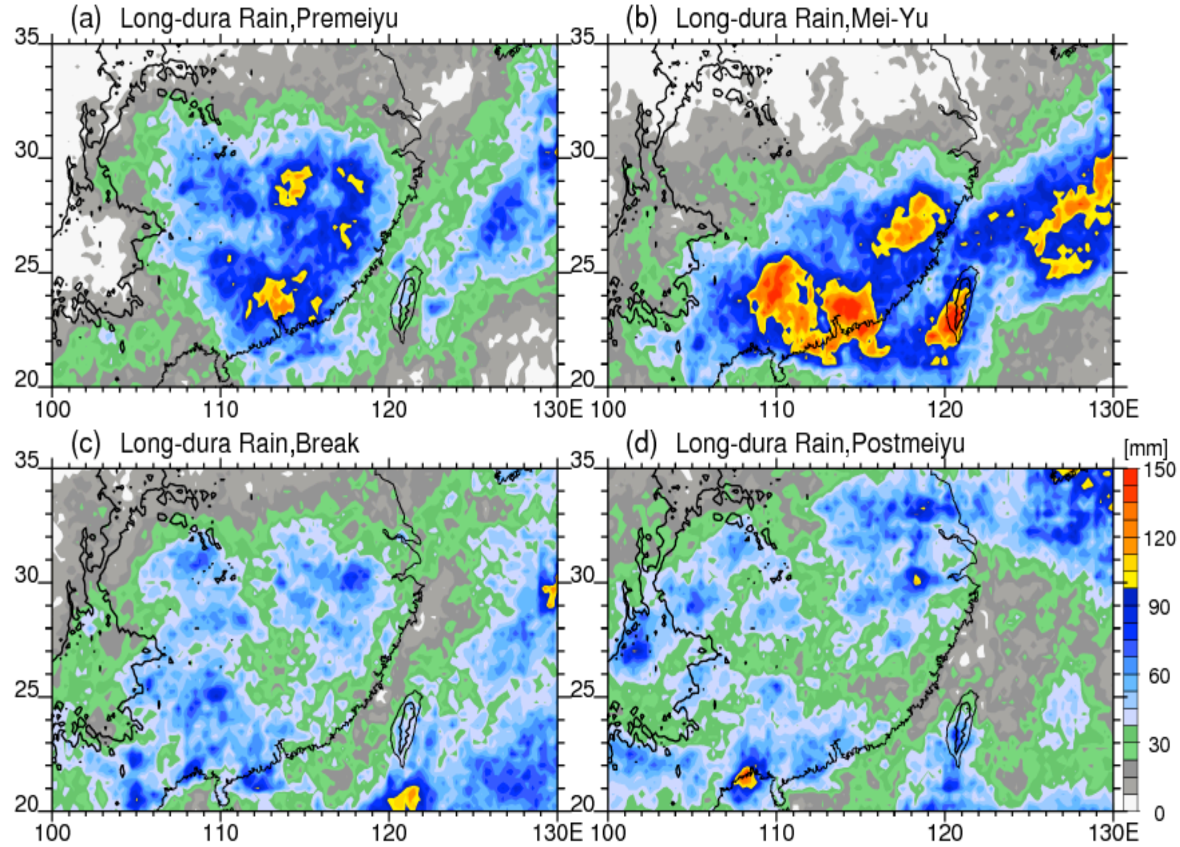

Figure 3.15. Distribution of rainfall contributed by long-duration precipitation (> 6 hrs) in different periods.

(a) Rainfall, Wind, and Terrain, in Active periods

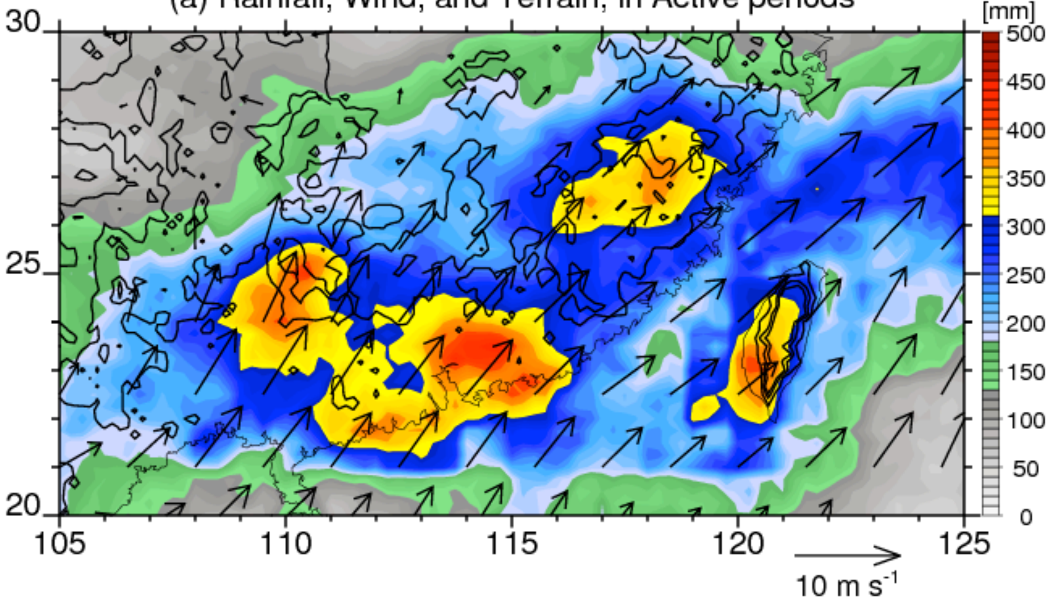

(b) Rainfall, Wind, and Terrain, in Break periods

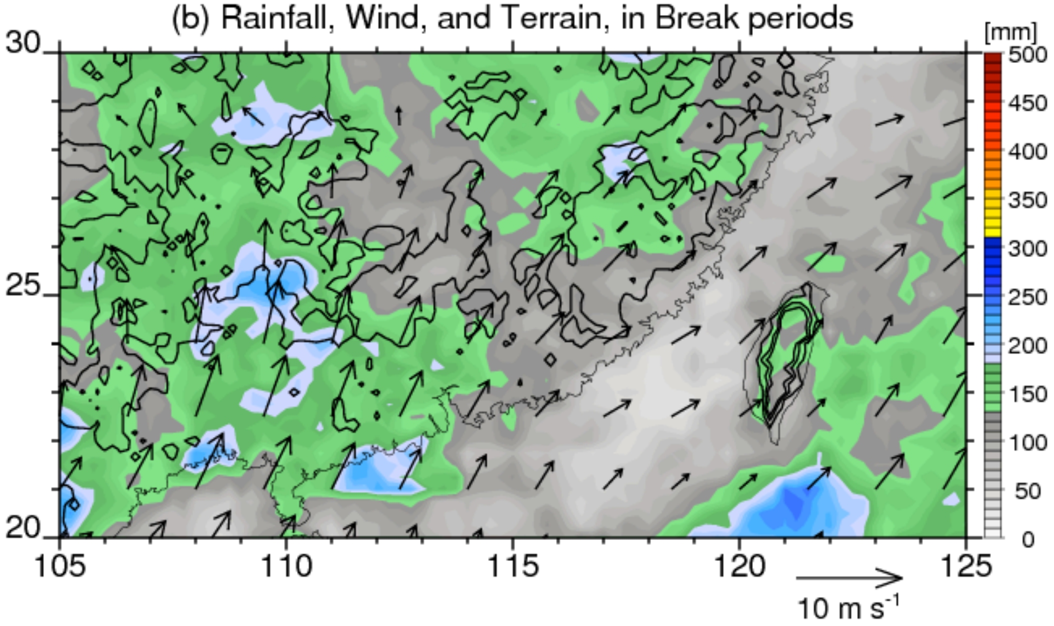

Figure 3.16. Rainfall (shaded), wind at 850 hPa (arrow), and terrain elevation above 500 m (black contours) during Active Mei-Yu and Break.

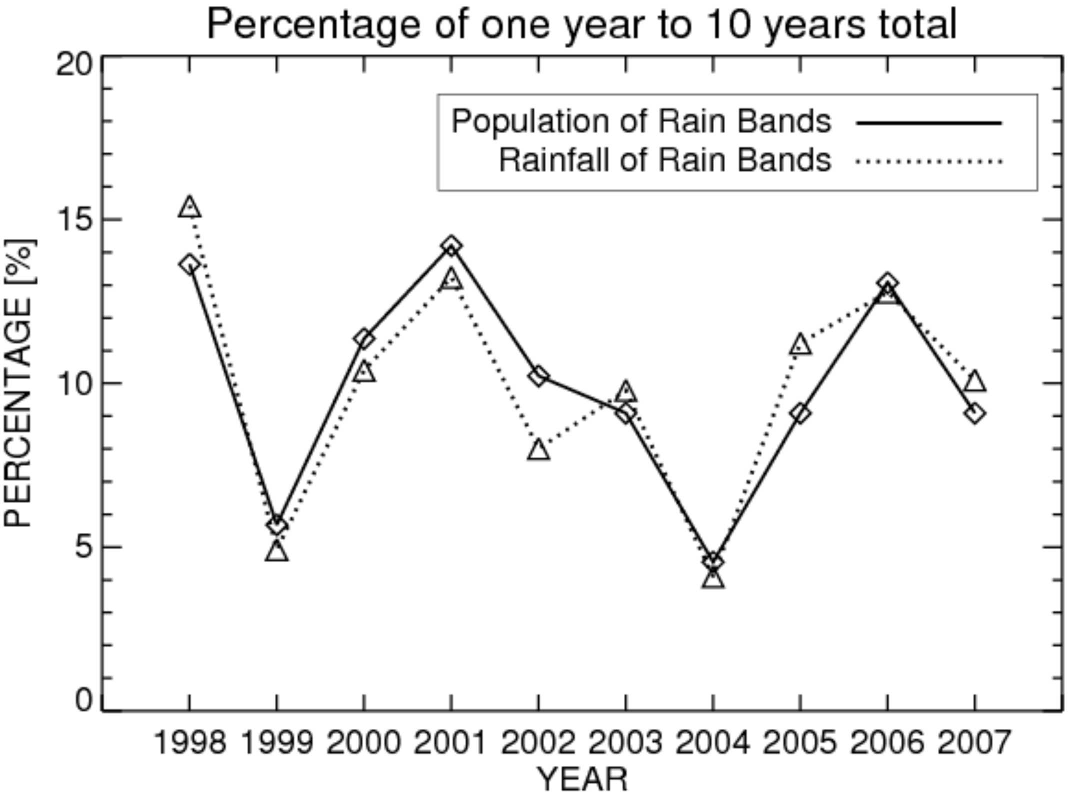

Figure 3.17. Statistics of Mei-Yu rain bands during Mei-Yu season in South China (May 13-June 23). Solid line indicates percentage of rain band population in 1 year to total population in 10 years. Dotted line stands for rain fall contributed by rain bands in the region of (108-122 E; 20-28 N).

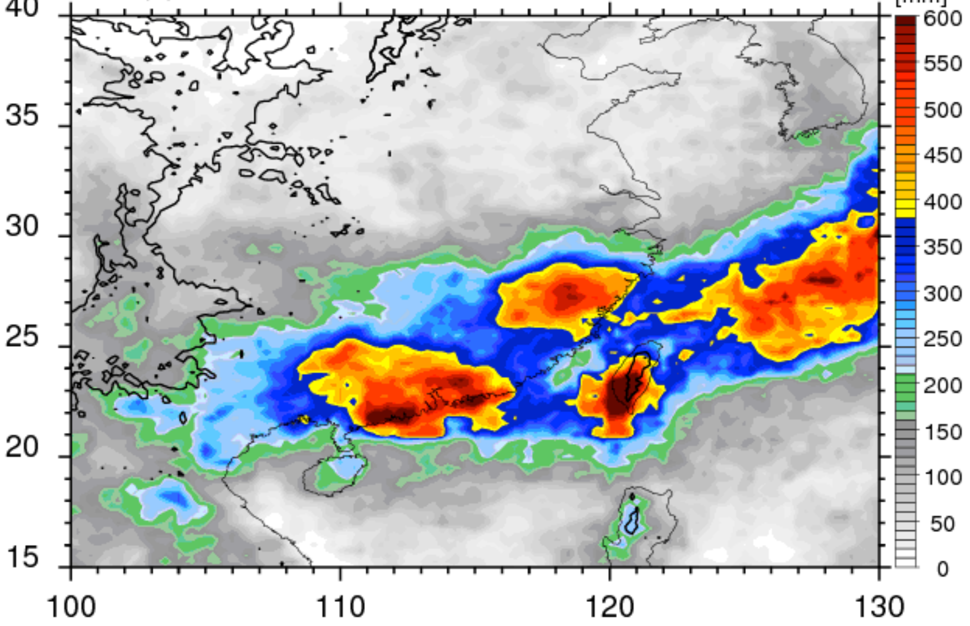

(a) Wet Mei-Yu in South China, Rain Bands

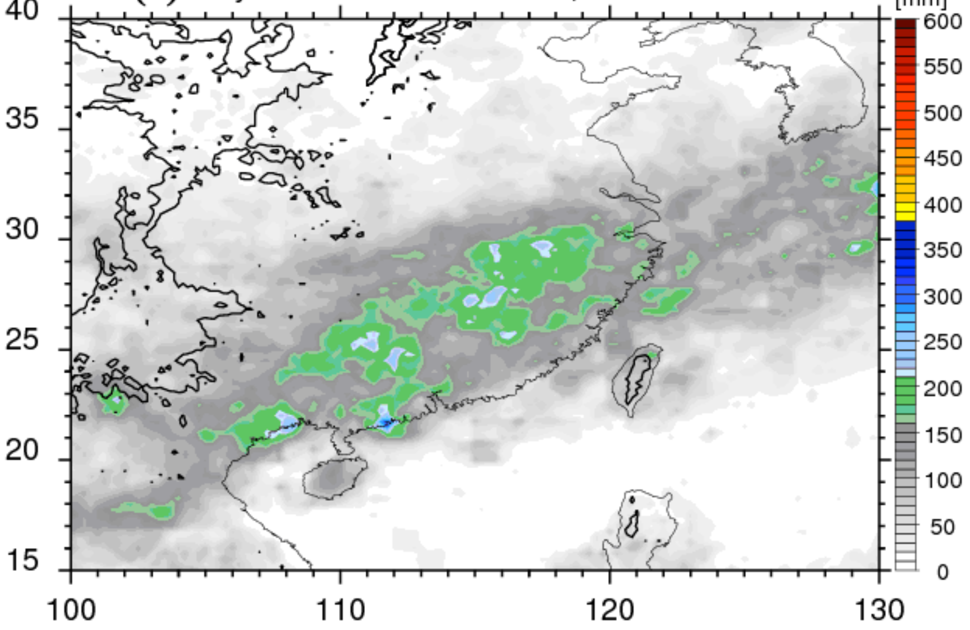

(b) Dry Mei-Yu in South China, Rain Bands

Figure 3.18. Averaged rainfall contributed by Mei-Yu rain bands in the Mei-Yu season of defined Wet and Dry years, respectively.

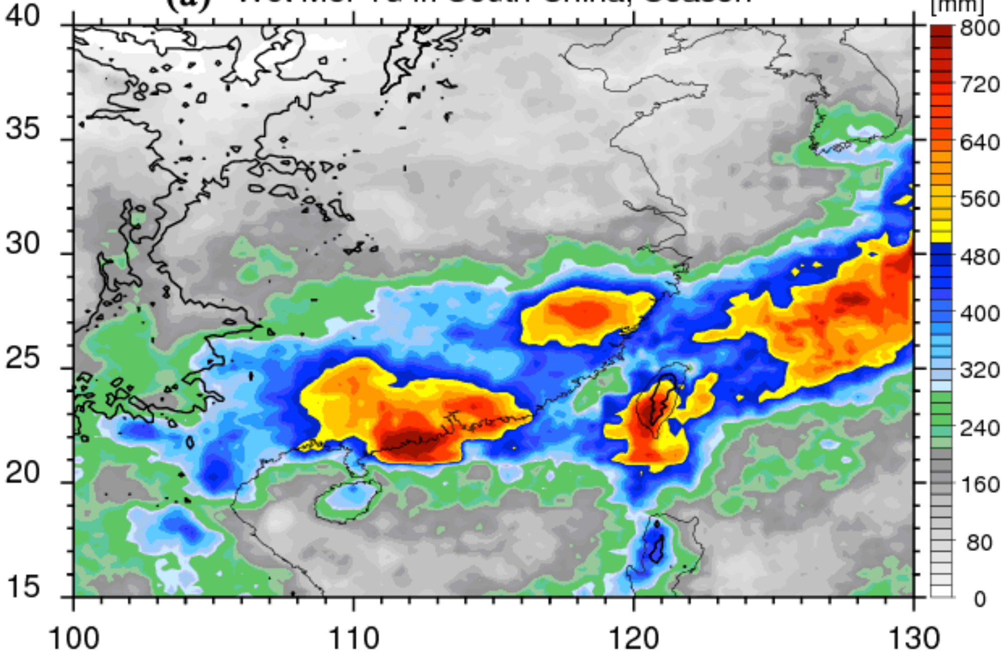

(a) Wet Mei-Yu in South China, Season

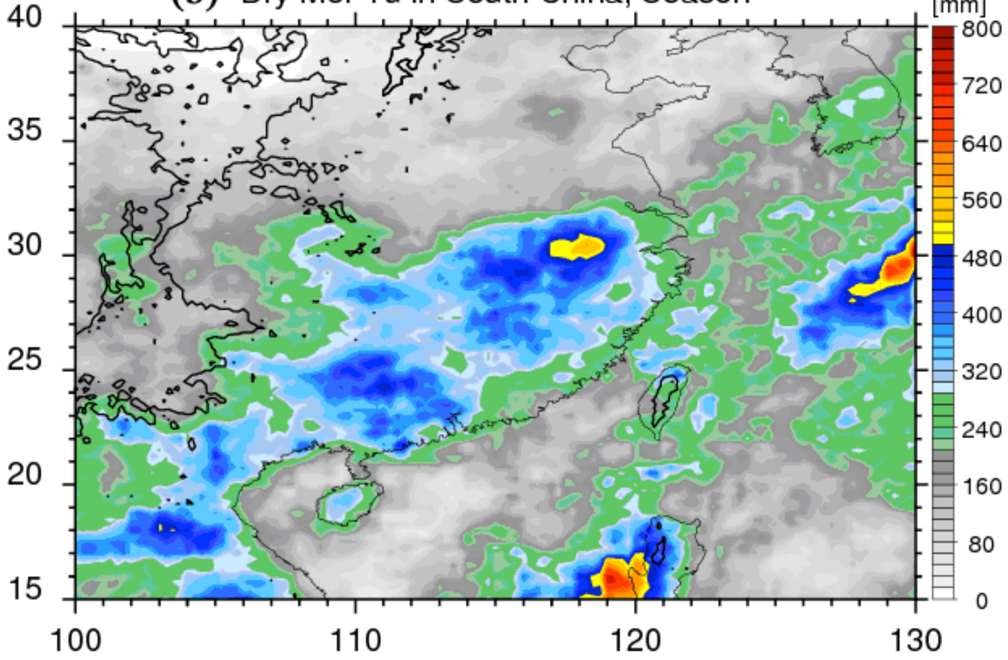

(b) Dry Mei-Yu in South China, Season

Figure 3.19. Averaged total rainfall in Mei-Yu season in South China during Wet and Dry years, respectively.

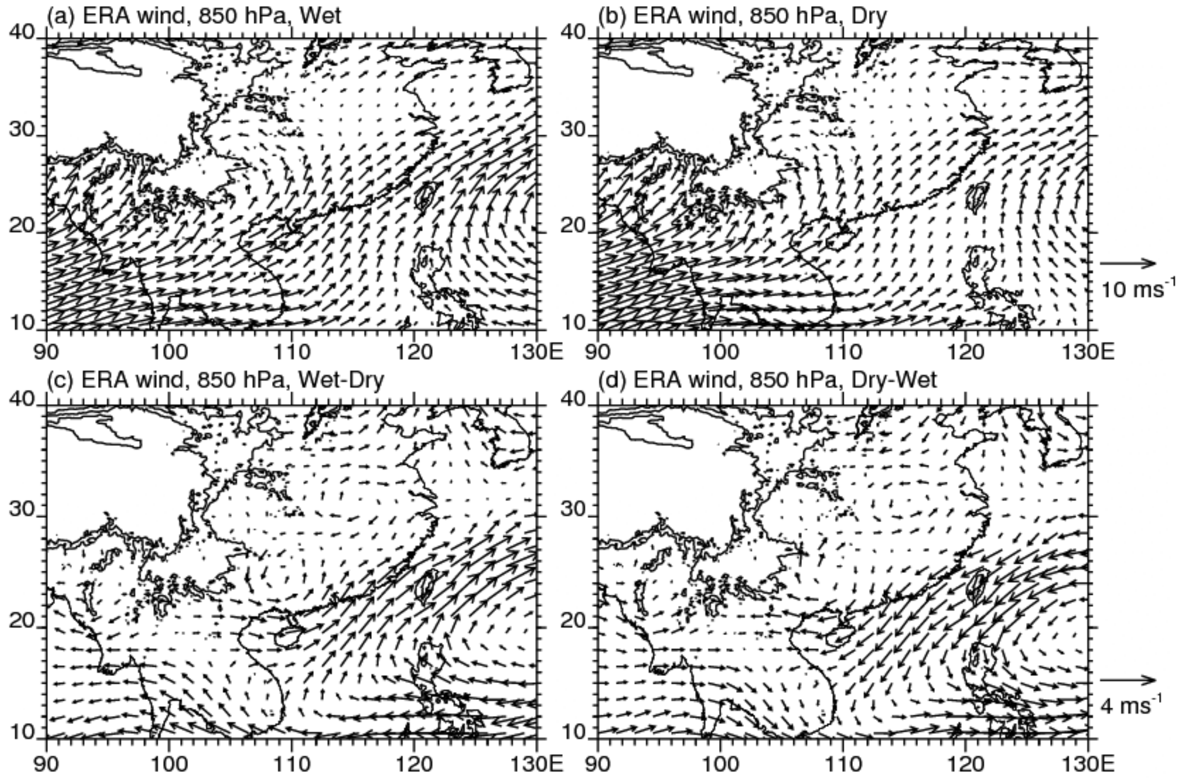

Figure 3.20. Composited wind field at 850 hPa for Mei-Yu seasons in (a) Wet years, (b) Dry years, (c) deviation of Wet years from Dry years, (d) Dry years minus Wet years.

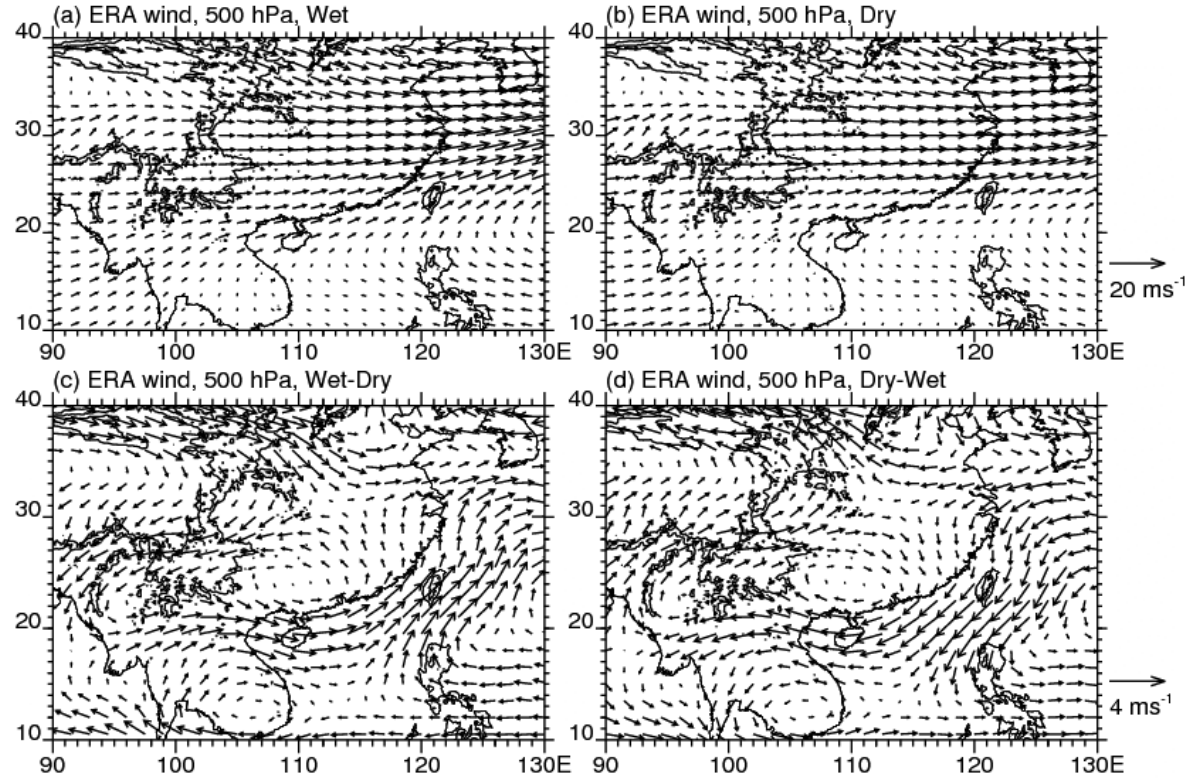

Figure 3.21. Same as Fig. 3.20, but for 500 hPa.

CHAPTER 4

CONVECTION AND STORM MORPHOLOGIES

4.1 Overview

Chapter 3 presents the rainfall characteristics of the monsoon and shows evident seasonal and intraseasonal variations of rainfall amount and spatial distribution pattern. In addition to the horizontal rainfall characteristics, spectra of precipitating system characteristics must also be correctly represented in the calculation of latent heating profiles or parameterization for climate models. Since the relationship between cold cloud detected by IR sensors, precipitation, and latent heating is very weak, quantification of cloud population based on IR or visible remote sensing measurements is not enough. It is necessary to quantify the precipitation systems and rainfall amount as a function of horizontal size, vertical organizational structure, convection intensity, and other storm properties. The TRMM Precipitation Feature database is an excellent tool to separate observed precipitation systems into groups with different storm morphologies and construct the statistics and spatial distribution of each group of storms. This would help to quantify the spectra and three dimensional structures of precipitating systems in different weather regimes within the monsoon systems (e.g., Mei-Yu vs. Break, or Mei-Yu vs. YZ-Meiyu). The convection occurrence, storm properties, vertical structures, and rainfall contribution can then be compared among monsoon, continental, and oceanic regimes within the tropics. Samples of precipitation features of different regimes are quite significant (Tables 4.1, 4.2, 4.3, 4.4, and 4.5).

Quantification of precipitation convective properties is also important in the validation and parameterization for mesoscale or cloud model, and rainfall retrievals. For example, vertical profile of hydrometeors can be estimated from modern cloud resolving models, but validation of microphysics parameterization schemes with real data is rare, and the accuracy of such estimates is unknown. Furthermore, physical parameterization or retrieval algorithms based on convective structures in certain meteorological regimes may not be transferable to other conditions, e.g., Mei-Yu.

4.2 Occurrence Frequency of Convection and Precipitation

There are four sets of instruments on board the TRMM satellite, including the PR, TMI, LIS, and VIRS. Based on the PF database, measurements from different instruments (with different footprints) are collocated and grouped using the adjacent-pixel method and parallax collection (Liu et al. 2008) on to the nearest PR pixels. Therefore, two different kinds of occurrence frequency of convection or precipitation can be determined: unconditional and conditional. Unconditional occurrence is defined as the fraction of PR pixels with certain values (e.g., 20, 30, or 40 dBZ) divided by total PR samples. Conditional occurrence is defined as the occurrence probability of PR pixels with specific properties (e.g., 20-40 dBZ, convective, or lightning) within precipitation features.

4.2.1 Unconditional Occurrence Frequency

The TRMM satellite over-passed the key East Asian Monsoon region (18-36 N; 105-130 E) about 2200-3000 times in each defined seasons (Premeiyu, Mei-Yu, and YZ-Meiyu) during 12 years (1998-2009). In each season, the TRMM PR sampled this region by ~500,000 footprints, on average, in every 2^o by 2^o box, with samples increasing from the tropics toward the north (Fig. 4.1).

Figure 4.2 shows the map of occurrence fraction of PR 20 dBZ pixels at 2 km to the total PR pixel samples. Since the PR 20 dBZ indicates the existence of precipitation-size drops, the occurrence frequency of 20 dBZ can be interpreted as the probability of the occurrence of precipitation-size drops or particles at specific altitudes. In addition, 20 dBZ in the upper troposphere indicates deep convection lifting more or larger ice particles to high altitudes. Therefore, the occurrence frequency of 20 dBZ at high altitudes also suggests the potential of deep convective updrafts to reach upper troposphere. The occurrence frequency of 20 dBZ at 2 km shows a very similar distribution pattern as the seasonal rainfall pattern in Fig. 3.4. In other words, the TRMM PR samples the monsoon region enough and captures the monsoon rainfall features very well. The maximum of occurrence frequency during the South China Mei-Yu season is above 10% (Fig. 4.2b), indicating very frequently occurring and/or large precipitation systems associated with the quasi-stationary Mei-Yu rain bands. Less well-defined band shape occurrence frequency maxima is also found in Mei-Yu season in the Yangtze River (Fig. 4.2c).

Occurrence frequencies of 20 dBZ and higher radar echoes as a function of altitude are further shown in Fig. 4.3. Generally, higher altitudes (reflectivities) have lower occurrence probability. For echoes higher than 20 dBZ and 30 dBZ, the occurrence probability peaks between 1 and 4 km in all seasons. Also for these two parameters, there are evident increases at all the altitudes from Premeiyu season to Mei-Yu season. The difference between Premeiyu and Mei-Yu is almost 1 order of magnitude above 4 km. For example, the occurrence frequency at 6 (10) km for 20 dBZ is 1% (0.1%) in Mei-Yu and YZ-Meiyu, while it is 0.3% (0.02%) in Premieyu. The vertical profiles of occurrence frequency of 20 dBZ after the onset of Mei-Yu are quite similar to those over the tropical land systems from both TRMM PR measurements and CRM simulation presented by Zhang et al. (2008). In contrast, vertical profiles of PR 20 dBZ occurrence frequency before the onset of Mei-Yu are similar to oceanic regimes. For the occurrence frequency of intense radar echoes (e.g., 40 or 45 dBZ), Premeiyu also has lower probability but only at altitudes below 7-km. Above 7 km, Premeiyu has very similar occurrence probability of 40 or 45 dBZ as other seasons. The profiles of occurrence frequency of echoes above 40 dBZ are very close to those over the tropics constructed by CRM in Zhang et al. 2008.

4.2.2 Conditional Occurrence Frequency

This section further examines the occurrence frequency of certain kinds of convection and precipitation when precipitation systems occur. Figure 4.4 shows the population of PFs. Though the distribution of PFs population is less consistent with seasonal rainfall distribution, it still represents the seasonal variation pattern. During SC Mei-Yu season, PF population peaks along a well-defined band with the same location to the Mei-Yu rain belt at this season (Fig. 4.4b). The population maximum to the northwest of this population belt could be associated with the larger PR samples over there and more smaller PFs in the mountains. After the onset of the monsoon, the population of PFs increases dramatically over the edge of the Eastern Tibetan Plateau. This is reasonable, since the combination of strong surface heating over the Tibetan Plateau and abundant moisture along the foothill during the monsoon season could be favorable for daytime convection. Down-slope wind enhanced precipitation is also significant in this region during the night time.

Occurrence frequency (conditional) of certain radar echoes (e.g. 20, 30, 40, 45 dBZ) relative to the PR near surface raining area is presented in Fig. 4.5. Seasonal differences of this conditional occurrence frequency are very similar to the unconditional occurrence frequency discussed in Section 4.3.2. The potential for deep convection (20 dBZ) reaching 10 km is about 1% and 0.1% getting to the tropopause (Fig 4.5a). For the same criteria of 20 or 30 dBZ, Premeiyu season also has lower conditional occurrence probability than the monsoon seasons. However, for the intense convection (40 or 45 dBZ) reaching the mixed-phase region, PFs in SC Mei-Yu season over SC has the lowest conditional occurrence fraction. It implies a higher percentage of extremely intense convection occurring in Premeiyu than in Mei-Yu over SC. The approximate occurrence probability for intense convection reaching above the freezing level is about 0.1% (Fig. 4.5c), similar to that of deep convection getting close to the top of the troposphere (Fig. 4.5a).

4.3 Storm Morphology of Different Regimes in South China

4.3.1 TRMM Proxies and Storm Types

As has been mentioned, measurements from different instruments can yield different kinds of information about a storm. A couple of parameters have been summarized as proxies for storm properties. One of these proxies is the maximum height of radar reflectivity with certain values (e.g., 20, 30, or 40 dBZ). Max height of 20 dBZ indicates the height reached by precipitation, while max height of 40 dBZ indicates the height reached by large particles, and is a good proxy for the intensity of the convective core (Fig. 4.6). Convective cells in Fig. 4.6a and 4.6b are both deep and intense, but cells in Fig. 4.6c and 4.6d are deep but not intense. The difference is that the former convection can lift very large ice particles (signified by strong radar echoes) far above the freezing level, but the latter ones do not lift those large particles to high altitudes, but nonetheless have some precipitation particles at high heights. Another useful proxy is minimum PCT at 37 (min 37PCT) or 85 (min 85PCT) GHz frequency. These proxies are good indicators of ice scattering. As shown in all cross sections of Fig. 4.6, minimum 85PCT (37PCT) usually is near the center of deep (intense) convective towers, while less convective regions of the storm have higher values of 85PCT or 37 PCT. In addition, the lightning flash count of a PF is also a good indicator of convection intensity (Zipser et al. 2006).

Characteristics of horizontal structure is also important and needs to be quantified. One direct way to learn the horizontal structure is examining the size of a PF at different altitudes. For example, PFs in Fig. 4.6a-d have both different storm extents and different heights and sizes of convective cores. Features of 4.6a-c are associated with moderate to large MCSs, while the PF of 4.6d is a small thunderstorm with deep convection. More details of TRMM proxies and storm information are described in Chapter 2.

4.3.2 Storm Occurrence Frequency by Proxies

This section mainly investigates the occurrence frequency of precipitation systems with different properties of proxies discussed above on the storm scale. PFs in different regimes in South China are selected. As described in Chapter 2, PFs in Premeiyu, Mei-Yu, Break, and Postmeiyu over SC (20-28 N; 105-125 E; indicated by the box in Fig. 4.2b) from 1998 to 2009 are selected for the study. This section studies only systems over land. Extremely small PFs (less than 100 km^2 or 4 PR pixels) are removed in this study. Selected PFs are further categorized into convective systems (CSs), thunderstorms (THSs), mesoscale convective systems (MCSs), and stratiform systems

(STRAs) (see definition in Chapter 2). Samples of different systems are listed in Table 4.1.

4.3.2.1 Horizontal Size of Storms

The cumulative distribution frequencies of horizontal size of PFs, MCSs, TSs, and STRAs are shown in Fig. 4.7. Generally, precipitation systems in different periods are comparable in median size when all the PFs are considered (Fig. 4.7a). The whole dataset is dominated by small features, i.e., more than 80% of the systems are smaller than 1000 km^2 and only about 5% of the storms are larger than 2000 km^2. These numbers are similar to that of PFs over the tropics (Nesbitt et al. 2006; Liu et al. 2008). Of the four regimes, Mei-Yu has the largest fraction of extremely large systems. For example, about 4% of the features in Mei-Yu are larger than 10000 km^2, while Break or Postmeiyu has less than 2% of the systems with near-surface area reaching this size. When systems are limited to convective systems or thunderstorms, the area structures are significantly different: Mei-Yu and Premeiyu have the highest fraction of large systems, while Break has less and Postmeiyu has the least. We may speculate that large-scale frontal dynamical forcing combined with a moist environment can help to initiate and maintain large precipitation systems (Houze et al. 2007). About 20-30% (5-10%) of the convective systems are larger than 1000 (10000) km^2. However, more than 60% of the systems with lightning have a horizontal scale of 1000 km^2. During Mei-Yu and Premeiyu, about 30% of the thunderstorms have an area larger than 10000 km^2. Compared to convective systems or thunderstorms, systems with only stratiform precipitation are smaller in size. Stratiform-only systems rarely (less than 1%) have a PR detectable area (> 17 dBZ) larger than 10000 km^2. We cannot know whether echoes < 17 dBZ, thus missed by PR, may compromise a significant part of stratiform systems.

Deep or intense convective systems may extend over large areas (Fig. 4.8). Most of these systems exceed 2000 km^2, with the largest size occurring in the Mei-Yu regime. For the storms with deep convection, e.g., maximum height of 20 dBZ > 12 km or minimum 85-GHz PCT < 225 K, the fraction of systems covering more than 1000 km^2 is 60-70% (Fig. 4.8a-b). Active Mei-Yu has a much smaller fraction of small and intense convective systems (max height of 40 dBZ > 7 km or with more than 5 lightning flashes) than the Break or Postmeiyu (Fig. 4.8c-d).

4.3.2.2 Vertical Extent of Storms

This section examines the vertical extent of precipitation systems, in terms of occurrence frequency of storms categorized by maximum height that certain values of radar reflectivity can reach. Figure 4.9 shows the occurrence frequency of systems with different precipitation tops (max height of 20 dBZ). When all the PFs are considered (Fig. 4.9a), the highest fraction (30%) of all systems have 20 dBZ only reaching to near the freezing level (5 km). There is not any difference among different regimes on the occurrence frequency of systems with echo top lower than 8 km. At levels above 8 km, Premeiyu systems have the least occurrence probability, followed by Mei-Yu, Break, and

Postmeiyu, respectively. About 5% (1%) of all PFs can extend up to 10 km (15 km). Some individual systems (0.1%) even reach 17-18 km. Convective systems show very similar profiles of occurrence frequency, but with higher probability of features reaching the upper troposphere (Fig 4.9b). Cloud tops of thunderstorms peak at a very high altitude, with 15% of monsoonal thunderstorms extending up to 15 km. But Premeiyu thunderstorms peak at a lower altitude (10 km). Systems with only stratiform precipitation rarely (0.1%) extend up to the upper troposphere (12 km). In other words, stratiform systems dectected by PR are significantly shallower and smaller than systems with any convection embedded. The regime differences for occurrence frequency of storms categorized by max height of 30 dBZ (Fig. 4.10) are very similar to that of 20 dBZ.

However, the pattern of regime differences varies when occurrence frequency of the max height of 40 dBZ is considered (Fig. 4.11). Premeiyu regime tends to have a higher occurrence fraction of storms with 40 dBZ reaching above the middle mixed phase region (7-8 km) than Mei-Yu and Break. About 1% (0.1%) of all PFs have 40 dBZ echoes reaching 8 km (10 km). By comparison, the fraction of thunderstorms with 40 dBZ well above the freezing level at 5.5-6.5 km is 30%, and 5% have 40 dBZ reaching 10 km.

4.3.2.3 Ice Scattering Signature of Storms

As has been discussed, the minimum PCT at 85 GHz is a good indicator of ice scattering (Kummorow et al. 1998; Nesbitt et al. 2000). The greater the depression of 85-GHz PCT (min 85PCT), the deeper is the column with ice particles, or putting it differently, the greater is the ice water path. Figure 4.12 shows CDFs of min 85PCT. The whole dataset is dominated by PFs with very weak or nonexistent ice scattering (high PCT values). Specifically, median values of min 85PCT of total features are about 20 K higher than 250 K, a threshold used to delineate systems with just enough ice scattering that rain from melting ice reaches the surface (Spencer et al. 1989). Nesbitt et al. (2000) used this same threshold for the existence of appreciable ice scattering. Less than 10% of total features have even a single pixel with ice scattering signature lower than 225 K, a value that McGaughey et al. (1996) used as a threshold for ice associated with deep convection. Regime differences of ice scattering signature are negligible between Premeiyu, Mei-Yu, and Break, while Postmeiyu systems have slightly stronger ice scattering. Even when features are limited to existence of at least 4 convective PR pixels (defined as convective systems), less than 30% of these systems have significant ice scattering (min 85PCT < 250 K). Almost all the defined thunderstorms and MCSs have min 85PCT lower than 250 K, and 30-40% of them have very strong ice scattering (min 85PCT < 175 K).

CDFs of min 37 GHz PCT are shown in Fig. 4.13. Compared to min PCT at 85 GHz, min PCT at 37 GHz is more sensitive to large ice particles in the column being sensed. For this proxy, the Premeiyu seems to have the highest fraction of features with low min 37 PCT, while Mei-Yu has the least. This result is quite consistent with the fact that Premeiyu has higher occurrence frequency of storms with 40 dBZ in the mixed-phase region than Mei-Yu though having much smaller fraction of high cloud systems. Both results demonstrate a higher probability of large supercooled raindrops or precipitation-size ice particles in the mixed-phase region during Premeiyu than Mei-Yu. Break also has a larger fraction of storms with low values of min 37 PCT and features with 40 dBZ reaching the mixed-phase region, though the difference is not huge.

4.3.2.4 Lightning Frequency of Storms

Lightning activity is another possible proxy for convective intensity (Zipser et al. 2006). Many studies reveal that lightning frequency is higher before monsoon onset than during the monsoon rainfall peak (Qie et al. 2003; Yuan and Qie 2008). Higher lightning occurrence is also reported in the break than in the active monsoon period in other parts of the tropics (Williams et al. 1992; Petersen et al. 2001). The question here is whether variations in lightning flash rate also modulate transitions in convective structures among Premeiyu, Mei-Yu, Break, and Postmeiyu.

On average, about 4-10% of the total PFs produce lightning flashes in the South China monsoon region (Fig. 4.14). The regime-dependent differences are quite evident. For example, the fraction of storms with any lightning activity is 4% for Mei-Yu, 7% for Premeiyu and Break, and 10% for Postmeiyu. Storms producing a moderate to high flash rate, e.g., more than 10 flashes in the viewing time of LIS (80-90s), are less likely during Mei-Yu than in any other time period. Only about 1% of PFs in Mei-Yu have more than 10 lightning flashes, compared with 3% in Premeiyu and Postmeiyu. Premeiyu also has the highest probability of storms with high lightning flash rates. Premeiyu has about 0.8% of PFs or 10% of thunderstorms with more than 50 lightning flashes. Only half of the occurrence frequency occurs in Mei-Yu.

4.3.2.5. Summary of Regime Differences on Convection Intensity

This subsection summarizes regime differences on convection intensity based on results presented in the above sections. Precipitation systems with deep convection or intense convection are defined and their occurrence frequencies in different regimes are calculated. Deep convection is defined by max height of 20 dBZ extending above 12 km, max height of 30 dBZ reaching above 10 km, or min PCT at 85 GHz being lower than 180 K. All these proxies indicate the existence of a very deep column of ice particles (small or large). Intense convection is defined by max height of 40 dBZ extending above 8 km, having more than 20 lightning flashes, or min PCT at 37 GHz being lower than 240 K. Compared to deep convective proxies, these proxies require significant amounts of large ice particles and/or supercooled liquid droplets being aloft in the mixed-phase region (Nesbitt et al. 2000; Toracinta et al. 2002; Cecil et al. 2005; Cecil, 2011).

As shown in Fig. 4.15, regime differences on occurrence of deep convection and intense convection are quite evident. The Break in the SC Mei-Yu season is much more favorable for deep convection than the active phase and period before the onset of Mei-Yu (Fig 4.15a). Active Mei-Yu and Premeiyu have similar occurrence of deep convection, but active Mei-Yu has slightly higher fraction of storms with high cloud tops. However, Premeiyu has much higher probability of intense convection and high flash rates than Mei-Yu (Fig. 4.15b). Postmeiyu is the most favorable for both deep convection and intense convection.

4.3.3 Rainfall Contribution by Different Storm Types

One unique advantage of the TRMM PF database is the ability to connect rainfall and precipitation systems with specific storm properties. The rainfall contribution from different types of storms to the total rainfall is analyzed (Fig. 4.16-4.17). Though systems with area greater than 1000^2 km occupy less than 20% of the total PFs, their contribution to total rainfall is higher than 80% (Fig. 4.16a). This result is very similar to that of PFs in the tropics (Liu et al. 2008). Large systems (e.g., > 10000 km^2) contribute far more rain in Mei-Yu (75%) than in the Break (60%) or Postmeiyu (50%) periods. Premeiyu has a similar fraction (70%) of rainfall produced by the large systems as Mei-Yu. Systems with at least one pixel of 20 dBZ reaching above the freezing level contribute almost all the total rainfall (> 95%). About half of the total rainfall is contributed by storms with max height of 20 dBZ extending to the upper troposphere, e.g., 10 km (Fig. 4.16b). The Premeiyu regime has the least fraction of rainfall coming from storms with high echo tops (max ht of 20 dBZ). About 90% of the total rainfall comes from systems with at least one pixel of 40 dBZ (Fig. 4.16c). Storms with 40 dBZ extending above the freezing level produce about 40% of the total rain. A higher fraction of rain is contributed by systems with intense convection (e.g., 40 dBZ extending above 7-km) before and after the Mei-Yu than during Mei-Yu. Consistently, the Mei-Yu regime has the lowest fraction of rainfall contributed by systems with thunder (Fig. 4.16d). The Premeiyu rain is more like thunderstorm rain (60%), while half of the rainfall in the Break or Postmeiyu comes from lightning systems. In contrast, only 40% of the rainfall in Mei-Yu is associated with lightning flashes. Premeiyu season also has the largest fraction of rainfall produced by systems with high flash rate, e.g., 40% from features with more than 10 flashes and 20% from storms with more than 50 flashes. There is less than 5% of the rainfall coming from storms with more than 50 flashes in other periods.

The rainfall contribution by systems with ice scattering is less different among different periods (Fig. 4.17a-b). More than 80% of the rainfall is produced by systems with significant ice scattering (min 85PCT < 250 K) and 40% by storms with very strong ice scattering (min 85PCT < 175 K). CDFs of rainfall contribution by max dBZ at 7-km (Fig. 4.17c) is very similar to that of max height of 40 dBZ (Fig. 4.16c). Rainfall contribution by convective precipitation varies from regime to regime (Fig. 4.17d). Only 35% of the rainfall in Mei-Yu is convective, while 45% (55%) in the Break (Postmeiyu) or Premeiyu.

4.3.4 Vertical Structures of Radar Echoes

The TRMM PR gives reflectivity of precipitation feature with vertical resolution of 0.25 km. This is one major advantage of the PR vs. ground-based radar measurements for investigation of vertical structures of precipitation systems. In order to study vertical structures, the vertical profile of radar reflectivity (VPRR) as a function of temperature is first constructed for PFs in different periods (Fig. 4.18). We use the same definition of VPRR as Donaldson (1961), where it was designed as the maximum reflectivity of a cell as a function of height. The methodology for determining the VPRR uses the maximum reflectivity at any altitude regardless of whether or not convective cells tilt. VPRR is often a strong indicator of storm intensity or lightning probability (Szoke et al. 1986; Zipser and Lutz 1994; Cecil et al. 2005): the higher the reflectivity in and above the mixed phase region, the more intense the storm tends to be.

Shown in Fig. 4.18 are profiles of VPRR for PFs in the top 1, 5, 10, 20 and 50 %. Generally, differences among regimes are quite evident for profiles within the top 20%. Notable changes on convective structure happen between storms in Premeiyu and Mei-Yu. As illustrated by Fig. 4.18a, profiles in the top 1% and top 5% in the Premeiyu have much stronger radar echo (by about 5 dBZ at -15^{o}) than in Mei-Yu at levels between 0^{o} and -30^{o}. In the region between 0^{o} and -30^{o} is the mixed-phase region, where higher radar reflectivity means larger liquid drops or precipitation-size ice particles, with a higher potential of charge separation (Dye et al. 1989). But intense convective elements in Premeiyu reach somewhat lower heights than in Mei-Yu. Lower echo tops could be a result of a lower tropopause in the premonsoon season. This difference on the convective structure between Mei-Yu and pre-Meiyu is also shown by other proxies such as maxht40 and maxht20 in previous sections.

Dramatic differences were reported on the convective structure between periods with strong monsoon westerly and the break in Darwin (Rutledge et al. 1992; Williams et al. 1992). In this study, VPRRs of top 1% PFs in Mei-Yu and the Break are very close, indicating no significant difference in the convective structure for very intense convection (Fig. 4.18b). However, less intense systems (top 5% or top 10%) during Mei-Yu have weaker radar echoes (2 dBZ at -15^{o}) in the mixed-phase region than their counterparts during the Break, as well as lower echo tops. Deep convective storms in the Break are more like those in Premeiyu in the structures of the mixed-phase region, but have higher echo tops than Premeiyu (Fig. 4.18d).

The VPRR of MCSs over south China and Taiwan indicates convective intensity between the typical oceanic ones and continental examples. For example, reflectivity lapse rate between 0^{o} and -20^{o}C (3-km interval above the freezing level) were documented as 6.0-6.5 dBZ/km for oceans and 2.5-3.5 dBZ/km for continents in Liu et al. (2008) and Zipser and Lutz (1994). Applying the same analysis to the median profile of VPRR of MCSs in this study, we get 4.0-4.5 dBZ/km lapse rate for the 3-km interval above the freezing level. However, the convective structure of Mei-Yu regime based on VPRR is close to that of the tropical South China Sea (Yuan and Qie 2008), with similar reflectivity at low level and the same lapse rate in the mixed-phase region.

In addition to profiles of VPRR, vertical profiles of PFs' horizontal size as a function of altitude are examined (Fig. 4.19). As discussed in Section 4.3.2, more than 80% of the PFs are smaller than 1000 km^2. Only vertical profiles of feature size above the top 20% are presented here. The storm size of PFs reaches the maximum value at 2-3 km and decreases very fast above this level. Below freezing level (5-6 km), Mei-Yu systems have the biggest size, followed by Premeiyu, Break, and Postmeiyu, respectively. The storms in different regimes are similar to each other above the freezing level. For the top 1% largest PFs, maximum storm size is in the range of 30,000-60,000 km^2 for different regimes. But the size decreases to about 4000 km^2 at 8 km for all regimes. Systems in the top 10% of size have areas between 1500-2500 km^2 at 2 km and only cover about 200 km^2 at 10 km.

4.4 Mei-Yu, YZ-Meiyu, and Subtropical Oceanic Systems

After analyzing storm occurrence and morphology of precipitation systems in different periods over South China, this section compares storm morphologies among rainband-associated systems over South China land area (21-28 N; 105-125 E) during SC Mei-Yu, rainband-associated systems over the Yangtze River region (28-36 N; 105-125 E) during YZ-Meiyu season, storms in the Break over the Yangtze River region during YZ-Meiyu season, and oceanic systems over the South China Sea (17-21 N; 111-121 E) during both Mei-Yu periods. Samples are shown in Table. 4.2.

4.4.1 Horizontal and Vertical Structures

Precipitation systems associated with rain bands over both SC and YZ regions are very similar in horizontal size (Fig. 4.20). Similarly, there is also a smaller fraction of large systems in the break period of YZ-Meiyu. Rainband-associated storms even show larger horizontal extent than precipitation systems over the adjacent ocean of SC in the same season. But thunderstorms over the ocean have comparable probability to cover large horizontal area as thunderstorms embedded in Mei-Yu rain bands.

Though the Mei-Yu and YZ-Meiyu systems are very close in the horizontal extent, the YZ-Meiyu systems tend to have much higher probability of intense convection (Fig. 4.21). The whole YZ-Meiyu season is more favorable for convectively intense storms than the Mei-Yu over SC (Fig. 4.21a). Storms above the top 20% in YZ-Meiyu season have 2-3 dBZ higher radar echoes than those in Mei-Yu at both low and middle levels, with stronger convective cores. Compared to systems in the active YZ-Meiyu (Fig. 4.21b), active Mei-Yu systems are closer to those occur over the adjacent subtropical oceans (Fig. 4.21c). Except for systems with extreme convection (top 1%), most of the Mei-Yu systems have very similar vertical profiles as those oceanic storms, especially at the lower and middle levels. By comparison, the oceanic storms have even higher cloud tops than Mei-Yu systems. There are also evident differences between profiles of break periods during the YZ-Meiyu season and active periods (Fig. 4.21d). Similar to Mei-Yu season over SC, systems in active periods show lower radar reflectivities (2-3 dBZ) above the freezing level than storms in break periods. This suggests very different microphysical processes happen in the rainband-associated precipitation systems and storms in the Break.

4.4.2 Storm Properties and Rainfall Contribution

Cumulative distribution frequencies of PF population categorized by different proxies are shown Fig. 4.22. There is not any significant difference between CDFs of PFs categorized by cloud tops or cloud depth with ice particles (Fig. 4.22a and 4.22c) in Mei-Yu and YZ-Meiyu. This is consistent with results shown by vertical profiles (Fig. 22b). However, both active and break periods of YZ-Meiyu have much higher fraction of PFs with 40 dBZ extending above the freezing level and of thunderstorms. Though not comparable to YZ-Meiyu in intense convection, Mei-Yu has a higher fraction of systems with intense convective cores (40 dBZ reaching above 7-8 km) and systems with lightning.

Above-mentioned regime differences on storm properties are more evident with regard to rainfall contribution (Fig. 4.23). Active YZ-Meiyu systems have a slightly higher fraction of rainfall contributed by large-size systems (e.g., > 10000 km^2) than Mei-Yu and oceanic systems, while YZ-Break has the least rainfall coming from those large storms (Fig. 23a). For the rainfall contribution by PFs with high echo top (e.g., 20 dBZ reaching above 12 km), oceanic systems have the highest fraction (70%) and Mei-Yu systems have the least (30%). About 50% of the total rainfall in the whole YZ-Meiyu season is still contributed by systems with high echo top. Also for YZ-Meiyu season, 40% of the total rainfall is produced by systems with intense convection (e.g., 40 dBZ above 7 km) or frequent lightning (e.g., > 10 flashes). But only 20% of the total rainfall in Mei-Yu and oceanic regime is contributed by storms with intense convection and frequent lightning. Therefore, systems in Mei-Yu are significantly distinct from those in YZ-Meiyu in convective properties, vertical structures, and rainfall contribution; they resemble those over the adjacent oceans.

4.5 Monsoonal, Continental, and Oceanic Regimes

4.5.1 Review and Selection of Different Regimes

Many studies have shown that periodic, regional-scale, and global-scale variations in atmospheric forcing (thermodynamic/dynamic) present different patterns of occurrence, intensity, and convective structures of convection (Williams et al. 1992; Zipser 1994; Petersen and Rutledge 1998; Nesbitt et al. 2000; Toracinta and Zipser 2000; Petersen et al. 2001; Cifelli et al. 2002; Liu et al. 2008). Typically, there are three regime-dependent types of convection: oceanic, monsoon, and continental convective regimes. Different regimes correspond to different convective structures, precipitation characteristics, and microphysical processes. Quantification of regime-dependent convective structures, precipitation characteristics, and microphysical processes are important in regional retrievals of latent heat release, evaluation of simulations of regional climate, and testing rainfall retrieval algorithms for specific meteorological regimes. Most of the above-mentioned studies are based on short-term statistics, examination of only one or two individual regions, or analysis combining different seasons of a region. Given 13-year-long measurements from radar, passive microwave, IR, and lightning sensors onboard the TRMM satellite and large samples on the regional and seasonal scales, it is now possible to specifically pursue the identification of regional or regime-dependent variations in convection occurrence, convective vertical structure, and characteristics of rainfall contribution.

Comparisons of precipitation systems that occur in the whole East Asian Summer Monsoon (EASM) and in other monsoon regimes around the world are conducted. Since the EASM is mature in June and July (Wang et al. 2002; Chang et al. 2004), precipitation systems over the land area of the EASM key region (20-35 N; 105-125 E) during June-July are selected for the study. Indian summer monsoon (ISM) and Australia summer monsoon (ASM) are two other major components of the huge Asian-Australian Monsoon systems and peak in June-July and January-February, respectively (Gadgil 2003; Wang et al. 2005; Ding 2007; Suppiah 1992). The EASM is a subtropical type monsoon with low-level wind reversal from northerly in winter to southerly in summer, while the ISM and ASM are tropical monsoons with low-level westerlies as the summer monsoon prevailing winds. We select features over continents of (15-25 N; 75-90 E) and (10-25 S; 125-125 E) for ISM and ASM in their peak periods In addition to the Asian-Australian Monsoon systems, North American Summer Monsoon (NASM) and South American Summer Monsoon (SASM) are also included in the comparisons. The NASM establishes its mature/rainy phase in July and August over Arizona, New Mexico, and northern Mexico (Adams and Comrie 1997). Therefore, precipitation systems over (20-35 N; 100-110 W) in July-August are defined as NASM features. Though there are still controversies on the existence of a SASM (Ramage 1971; Zhou and Lau 1998), we select systems in the wet period (Jan-Feb) over the Amazon (AMAZ; 0-10 S; 50-70 W) for SASM. Locations of all the selected monsoon regimes are shown Fig. 4.24, while samples are shown in Table. 4.3.

It is well known that intense convection, overshooting storms, and high flash rate thunderstorms prefer continents rather than oceans (Nesbitt 2000; Williams and Stanfill 2002; Liu et al. 2005; Zipser et al. 2006). Convective structures and dynamics of oceanic and continental regimes are also quite distinct (Zipser 1994; Petersen et al. 2001; Liu et al. 2008). The continental regimes are most evident in the Congo basin, western central Africa, South America, especially Argentina, Northwest India, and Southeast US. In this study, the EASM is placed among the typical continental regimes. Systems over four regions in their peak warm seasons are selected: Congo (CONG; 10 S-10N; 55-70 W) in April and May; West Africa (WASM; 10-20 N, 10 W-10 E) in July-August; Argentina (ARGE; 20-30 S; 50-60 W) in Jan-Feb; Southeast US (SEUS; 30-35 N; 80-100 W) in June-July. Locations of all the selected continental regimes are shown Fig. 4.24, while samples are shown in Table. 4.4.

A few tropical ocean regions are selected for the comparison with EASM, including oceans adjacent to continents and open oceans. Four oceanic regimes are defined: Bay of Bengal (BOB; 10-20 N, 80-100 E); South China Sea (10-20 N; 110-120

E); Northwest Pacific Ocean (NWPAC; 20-30 N, 125-135 E) all in June-July; Western Tropical Pacific warm pool (WTPAC; 0-10 N, 130-145 E) in May-June. Locations of all the selected oceanic regimes are shown Fig. 4.24, while samples are shown in Table. 4.5.

4.5.2 Comparison between EASM and Other Monsoons

EASM is compared to the other four monsoons, either tropical or subtropical, through analysis of occurrence, convective properties, horizontal and vertical structures, and rainfall contribution of precipitation systems (Fig. 4.25-4.28). EASM is very similar to the other two components of the Asian-Australian monsoon system, i.e., ISM and ASM, in all the analyzed storm morphologies. One might speculate that this is evidence of similar atmospheric forcing within the large monsoon system. Since the occurrence, horizontal and vertical precipitation structures, and convective properties of storms in the whole Asian-Australian monsoon are quite statistically close, the Asian-Australian monsoon may share the same vertical profiles for latent heating, rainfall retrieval algorithm, hydrometeor distribution for model evaluation, and so on.

NASM and AMAZ are quite different regimes from the EASM in storm morphologies. Though NASM and AMAZ also have similar echo tops or depth of significant ice particles (Fig. 4.25a and 4.25c), NASM (AMAZ) has a higher (lower) fraction of systems with intense convection and lightning and rainfall contributed by these systems (Fig. 4.25b, 4.25d, 4.28c, and 4.28d). Compared to EASM, the NASM is a drier regime (with less rainfall but more intense convection), while AMAZ is a wetter regime (with more rainfall but less intense convection). The vertical profiles of horizontal size are quite close, except for that of NASM. Size of NASM systems tends to peak at 3 km and decrease very fast toward the surface, while size of other monsoons slightly increases toward the surface (Fig. 4.26a and 4.26b). In addition, far less rain is contributed by large systems in NASM than in other monsoons (Fig. 4.28a), e.g., only 30% of rain comes from systems larger than 10000 km^2 in NASM compared to 50-60% in other monsoons. These results could be related to drier low-level troposphere of the NASM thus stronger evaporation of the rain drops. However, the storm size decreases slower in NASM than other monsoon regimes above the freezing level. Also associated with more intense convective cores, NASM precipitation systems show much higher radar echoes in the mixed-phase region than other monsoon systems (Fig. 4.27). Radar reflectivity vertical profiles of systems in AMAZ decrease very fast above the freezing level, indicating that updraft is too weak to loft large ice particles or precipitation-size supercooled liquid droplets (Williams et al. 2002; Cifelli et al. 2002).

4.5.3 Comparison between EASM and Continental Regimes

By comparing the occurrence frequency of PFs categorized by different TRMM proxies (Fig. 4.29), it is found that EASM is distinct from those continental regimes. The EASM only has similar occurrence frequency of PFs with deep precipitation top with two of the continental regimes, i.e., SEUS and ARGE (Fig. 4.29a). Otherwise, EASM has a far lower fraction of systems with intense convection (40 dBZ reaching high altitudes), storms with strong ice scattering signature (low PCT of 85 GHz), and frequent lightning (Fig. 4.29b-d). Continental regimes are closer to each other in the above-mentioned storm properties, with CONG and WASM having a slightly higher fraction of intense convection. Continental systems, especially for those in CONG and WASM, show larger horizontal extent at all levels (Fig. 4.30a). But the size of these continental systems decreases very evidently below the altitude of 3 km. Systems in SEUS and ARGE are close to EASM in horizontal size at low levels, but still have a larger size in the middle to upper troposphere.

Based on the above difference of storm properties between continental and EASM regimes, it is not surprising that continental regimes show much stronger vertical profiles of VPRR (Fig. 4.31). Continental storms have higher values of radar echoes from near surface level all the way to the upper troposphere. The maximum difference is located at the mixed-phase levels, indicating very different mixed-phase microphysics between continental regimes and EASM.

CDFs of rainfall contribution by PFs with different storm properties in specific regime are present in Fig. 4.32. EASM shows very similar statistics in rainfall contribution by PFs with large size, e.g., > 1000 km^2 (Fig. 4.32a). Otherwise, EASM has a smaller fraction of rainfall coming from storms with high cloud tops, intense convection, or frequent lightning (Fig. 4.32b-d). The only exception is that SEUS regime has less rainfall contributed by high cloud tops than other continental regimes, but similar to that in EASM. These typical continental regimes have about 60% of total rain produced by storms with high lightning flash rate (> 10) or with intense convective cores (40 dBZ reaching above 7 km), while typical monsoon regimes like EASM only have about 25% of rainfall from those systems.

4.5.4 Comparison between EASM and Tropical Oceanic Regimes

Similar comparisons have also been conducted between EASM and oceanic regimes around the tropics. Though EASM has similar occurrence frequency of PFs categorized by echo top (max height of 20 dBZ) or ice scattering (85-GHz PCT), it has a higher fraction of systems with intense convection and lightning (Fig. 4.33). Among the oceanic regions, oceans adjacent to major continents are closer to EASM in storm properties, while the open oceans including the Tropical Pacific warm pool have a far smaller fraction of PFs with intense convection and lightning. Oceanic systems also have smaller size than the EASM systems except for the top 1% (Fig. 4.34). Compared to the near-constant storm size below 3-4 km of EASM storms, oceanic systems tend to increase their size toward the surface below 3 km, especially for moderate size (500-1000 km^2).

The regime-dependent difference between EASM and Oceanic systems is most evident in the vertical precipitation structures (Fig. 4.35). Though radar echoes at the upper and lower troposphere within systems of EASM, BOB, and SCS are quite similar, EASM systems have much higher radar reflectivities at middle levels than storms of BOB and SCS (Fig. 4.35a-b). In other words, precipitation systems over oceans adjacent to major continents can have similar precipitation tops and near-surface precipitation rate as the monsoon systems over continents, but they have much lower ability to loft precipitation-size ice particles or supercooled liquid droplets than their counterparts in the continental monsoon systems. Storms over open oceans have much weaker profiles of radar echoes, especially within the mixed-phase region (Fig. 4.35c-d).

In terms of rainfall contribution, oceanic storms close to continents have a higher fraction coming from large-size systems and high cloud top storms (Fig. 4.36a-b). This group of oceanic storms has a similar fraction of rainfall from systems with intense convection and frequent lightning (Fig. 4.36c-d). In contrast, systems over open oceans (NWPAC and WTPAC) have similar rainfall contribution by large-size systems and high echo top storms, but a much smaller fraction of rain produced by storms with intense convective cores or lightning flashes.

4.6 Summary and Conclusions

This chapter examines the convection/precipitation occurrence, storm properties, vertical structures, and rainfall contribution by different storm types. Comparisons of above-mentioned quantities are further made among monsoon, continental, and oceanic regimes within the tropics. Major conclusions and results include:

(1) The occurrence probability of 20, 30, 40 dBZ between 1 and 4 km in all periods shows evident intraseasonal changes, while vertical profiles of occurrence frequency of 20 or 40 dBZ after the onset of Mei-Yu are quite similar to those over the Tropical

land systems from RMM PR measurements;

(2) There are significant differences in storm morphologies and convective properties among different weather regimes in the South China Mei-Yu region: Break period in the SC Mei-Yu season is much more favorable for deep convection (high echo top) than the active phase and period before the onset of Mei-Yu, but Premeiyu has much higher probability of intense convection (high radar reflectivity in the mixed-phase region) and lightning flashes than Mei-Yu,

(3) Though precipitation systems associated with rain bands over both SC and YZ regions are very similar in horizontal size, the YZ-Meiyu systems tend to have much higher probability of intense convection and vertical convective structures indicating stronger ice-processes;

(4) Precipitation systems in South China Mei-Yu are significantly distinct from those in YZ-Meiyu in convective properties, vertical structures, and rainfall contribution by storm types, but relatively closer to those over the adjacent oceans;

(5) EASM is comparable to other monsoon regimes around the world on storm morphologies and convective properties, though it is less convective than the drier regime (e.g., NASM) and has stronger convection than the wetter regime (e.g., AMAZ);

(6) Precipitation systems of EASM are intermediate in proxies of convective intensity between the stronger convection over nonmonsoonal continents, and the weaker convection over oceans.

Table 4.1. Population of different precipitation types during different periods over land area of South China (20-28 N; 105-125 E) as shown in Fig. 4.2b.

	Premeiyu	Mei-Yu	Break	Postmeiyu
PFs	10,864	8,385	9,854	14,333
CSs	3,540	2,501	3,415	5,187
THs	675	351	626	1191
STRAs	2,035	1,872	1,934	2,929
MCSs	1,289	955	1,029	1,540

Table 4.2. Population of precipitation features for Mei-Yu over South China, YZ-Meiyu or Break over Yangtze River (28-36N; 105-125 E) as shown in Fig. 4.2c, and South China Sea (17-21 N; 111-121 E).

	Mei-Yu	YZ-Meiyu	YZ-Break	Ocean
PFs	8,385	5,961	13,006	7,673

Table 4.3. Population of precipitation features in different monsoon regions shown in Fig. 4.24 during defined period of 1998-2007.

	EASM	ISM	ASM	NASM	AMAZ
Period	Jun-Jul	Jun-Jul	Jan-Feb	Jul-Aug	Jan-Feb
PFs No.	33,263	32,760	21,955	31,631	24,022

Table 4.4. Population of precipitation features in different continental regions shown in Fig. 4.24 during defined period of 1998-2007.

	SEUS	WASM	CONG	ARGE
Period	Jun-Jul	Jul-Aug	Apr-May	Jan-Feb
PFs	19,548	14,640	38,669	19,162

Table 4.5. Population of precipitation features in different oceanic regions shown in Fig. 4.24 during defined period of 1998-2007.

	BOB	NWPAC	WTPAC	SCS
Period	Jun-Jul	Jun-Jul	May-Jun	Jun-Jul
PFs	11,266	18,043	28,866	15,721

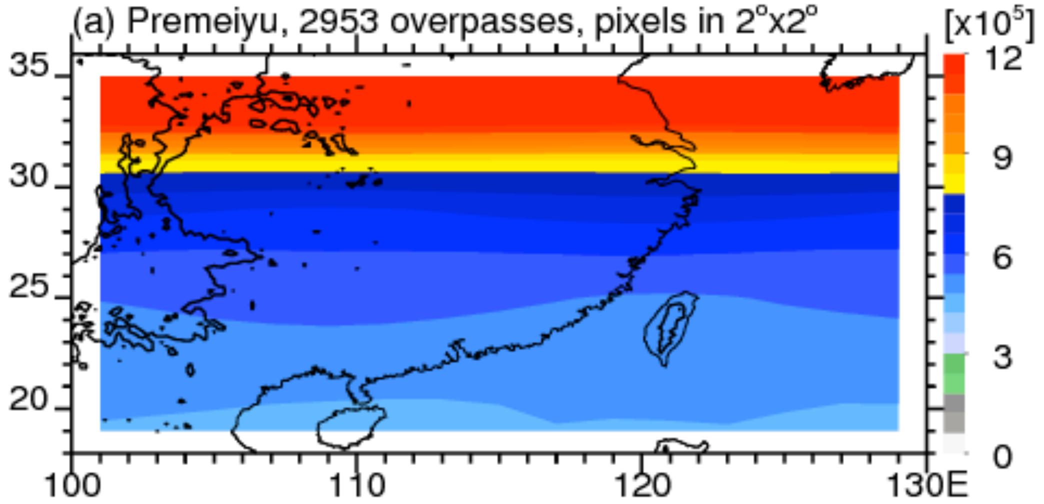

(a) Premeiyu, 2953 overpasses, pixels in 2°x2°

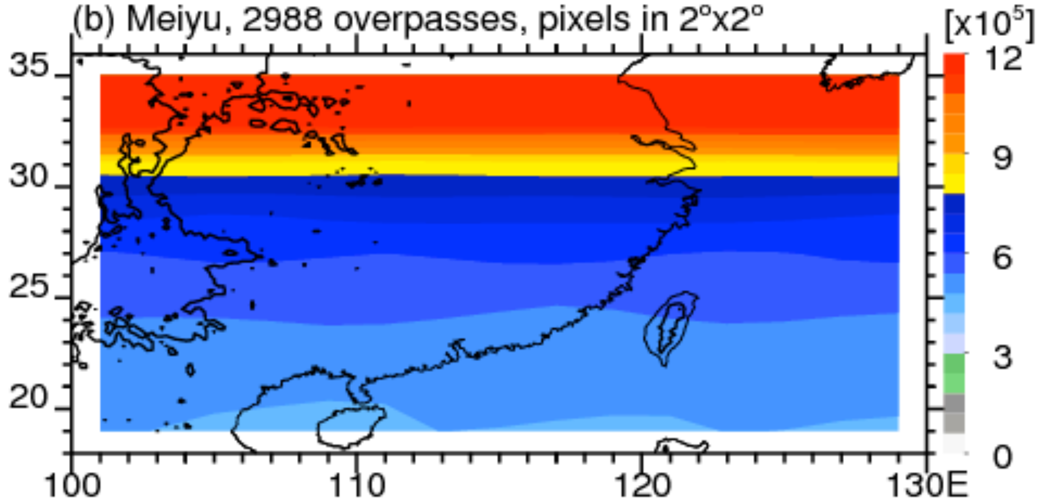

(b) Meiyu, 2988 overpasses, pixels in 2°x2°

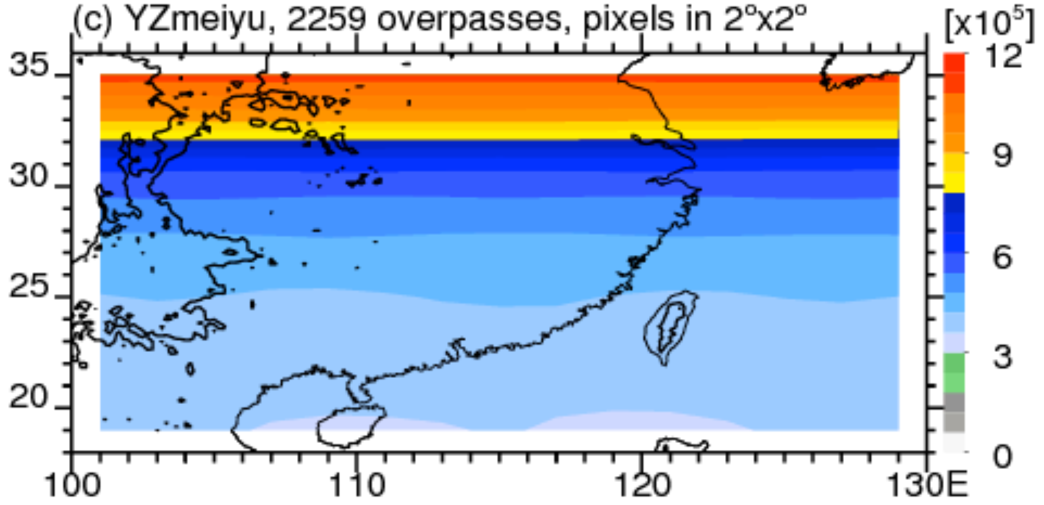

(c) YZmeiyu, 2259 overpasses, pixels in 2°x2°

Figure 4.1. Number of pixel samples of TRMM PR in each 2° by 2° box in different seasons during 1998-2009.

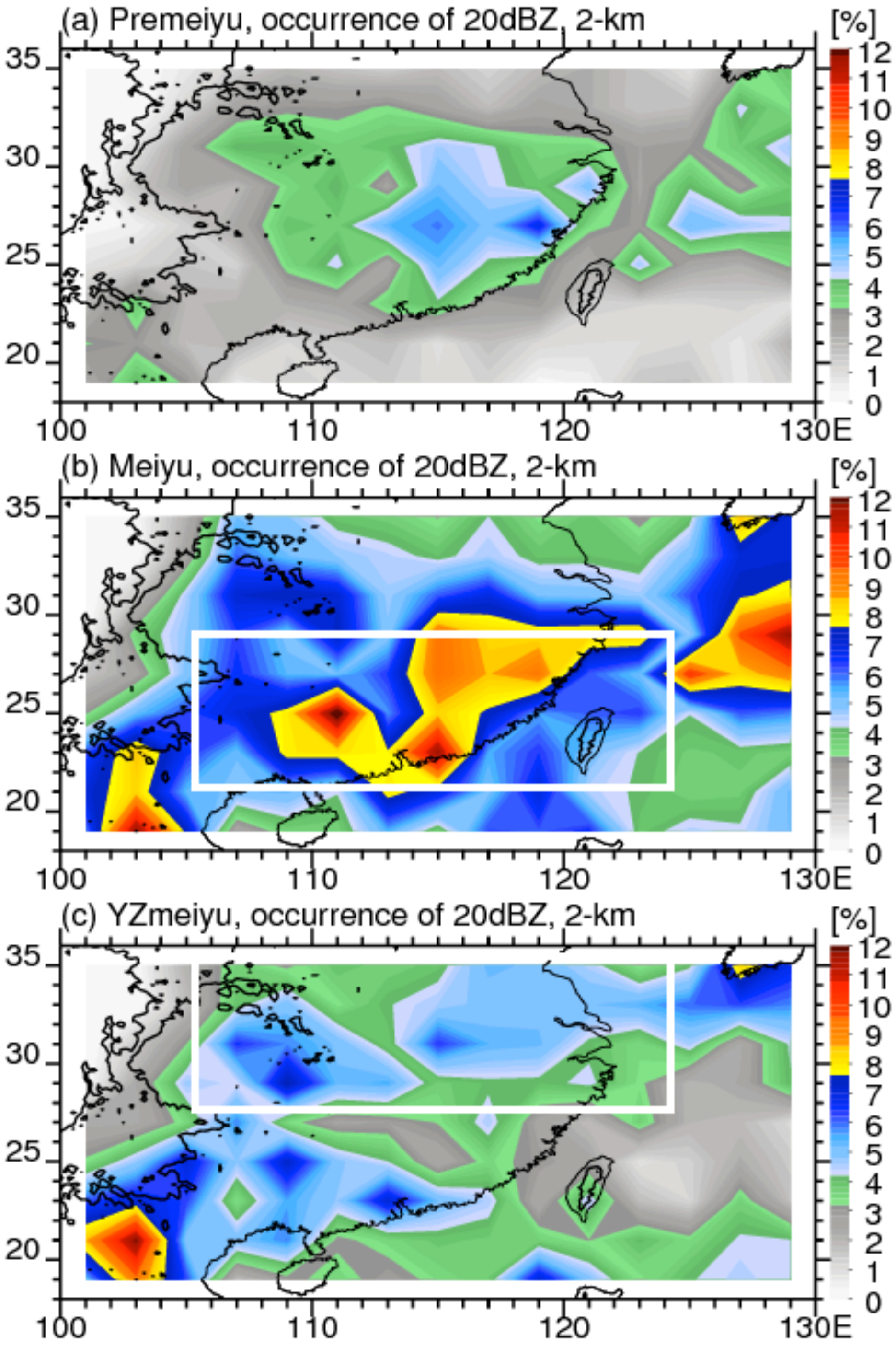

Figure 4.2. Unconditional occurrence frequency (%) of raining pixels (> 20 dBZ) in different seasons during 1998-2009.

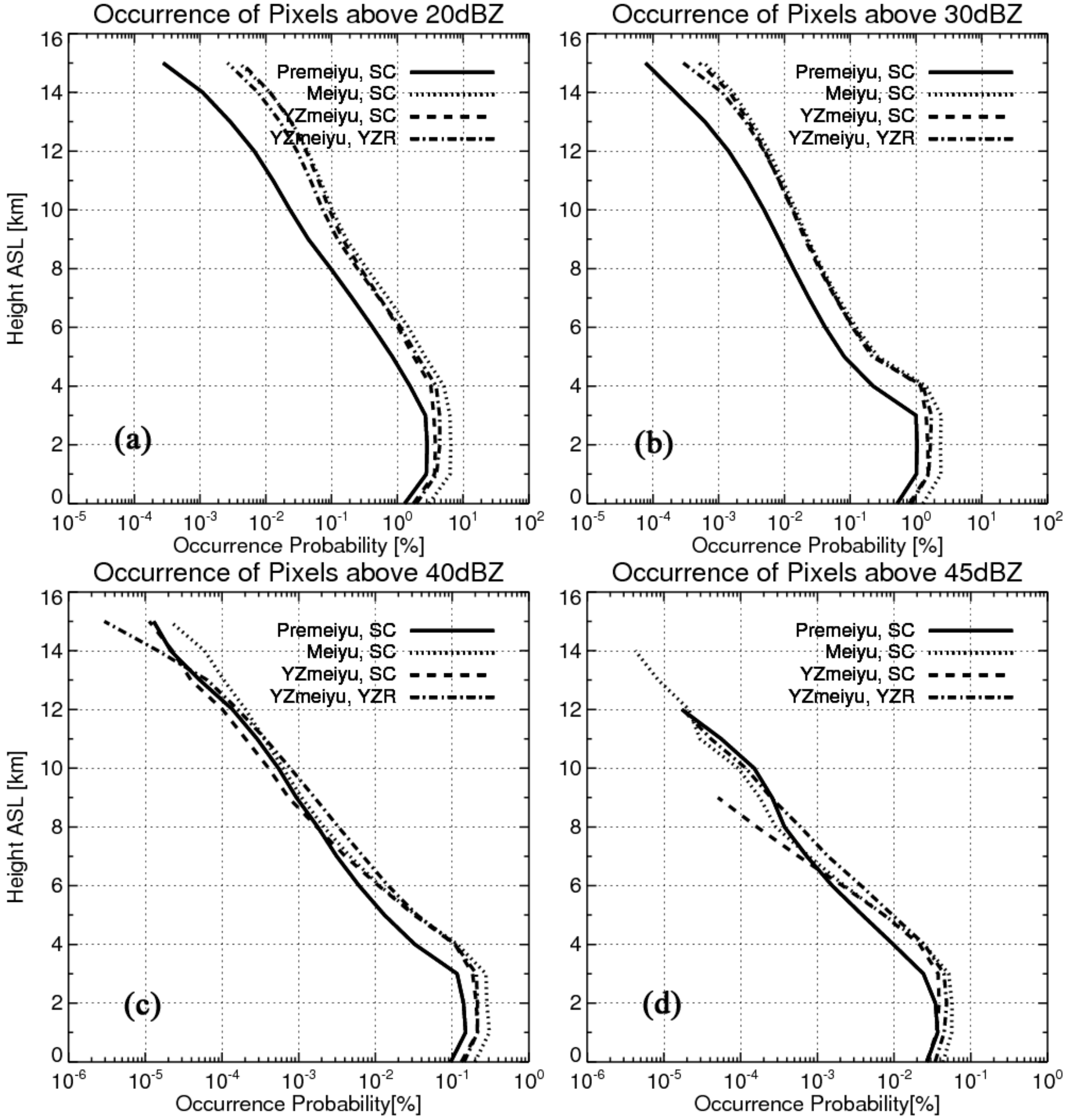

Figure 4.3. Occurrence fraction (in percent) of pixels with reflectivity (a) > 20 dBZ; (b) > 30 dBZ; (c) > 40 dBZ; (d) > 50 dBZ at different altitudes to PR pixels in South China Mei-Yu region (20-28 N; 105-125 E) as indicated in Fig. 4.2b and Yangtze River Mei-Yu region (28-36 N; 105-125 E) as shown in Fig. 4.2c in different seasons.

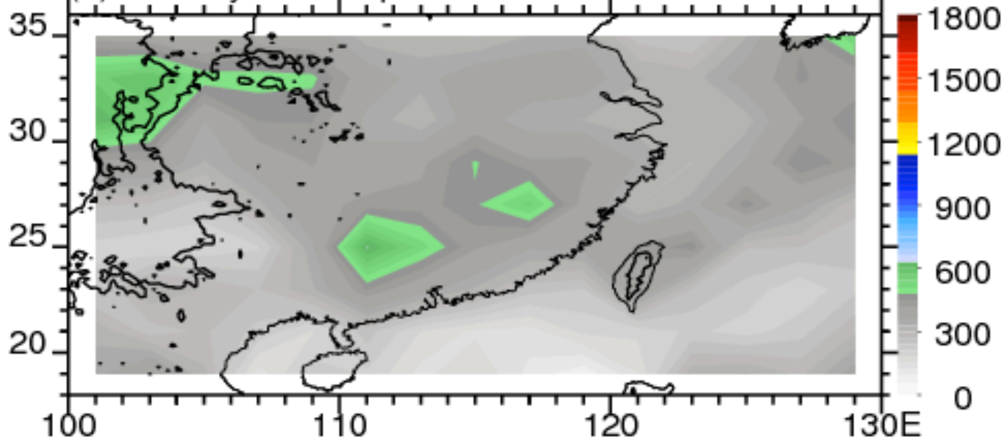

(a) Premeiyu, PF Population in 2^ox2^o

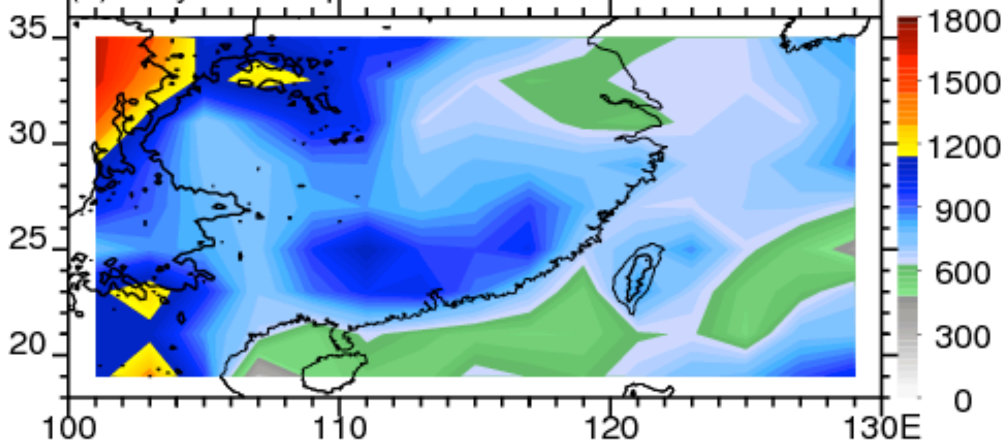

(b) Meiyu, PF Population in 2^ox2^o

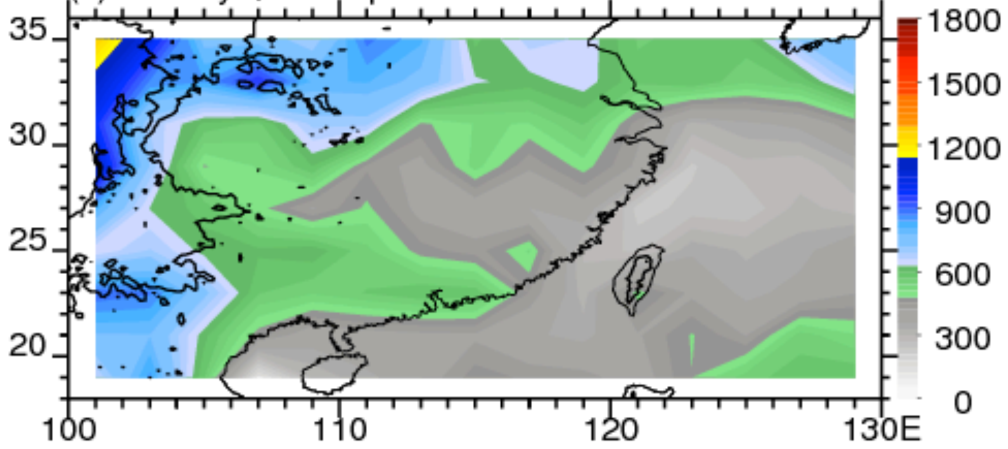

(c) YZmeiyu, PF Population in 2^ox2^o

Figure 4.4. Population of TRMM PFs in each 2^o by 2^o box in different seasons during 1998-2009.

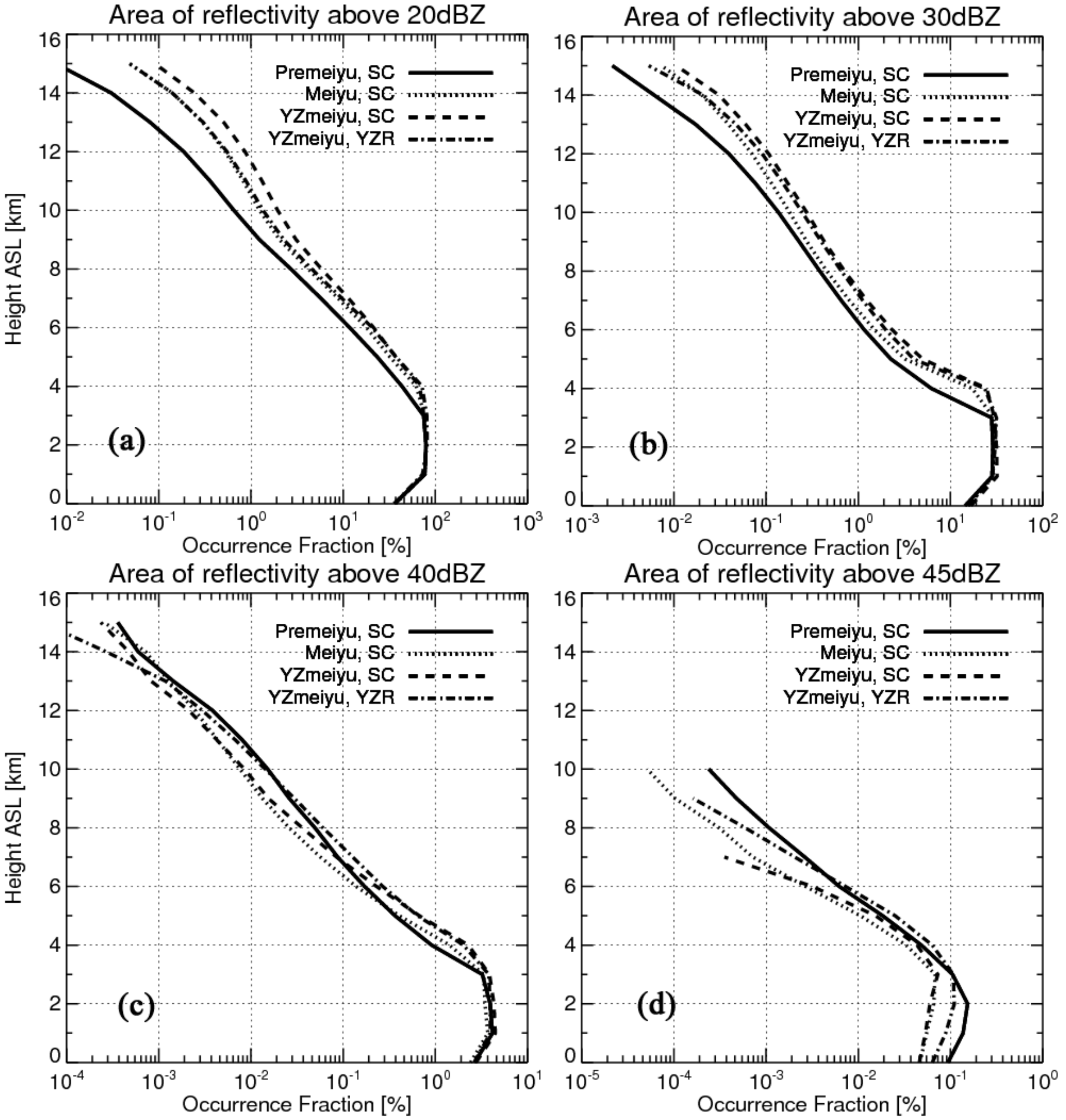

Figure 4.5. Conditional occurrence fraction (in percent) of pixels with reflectivity (a) > 20 dBZ; (b) > 30 dBZ; (c) > 40 dBZ; (d) > 50 dBZ at different altitudes to PF near-surface raining pixels in South China Mei-Yu region (box in Fig. 4.2b) and Yangtze River Mei-Yu region (box in Fig. 4.2c) in different seasons.

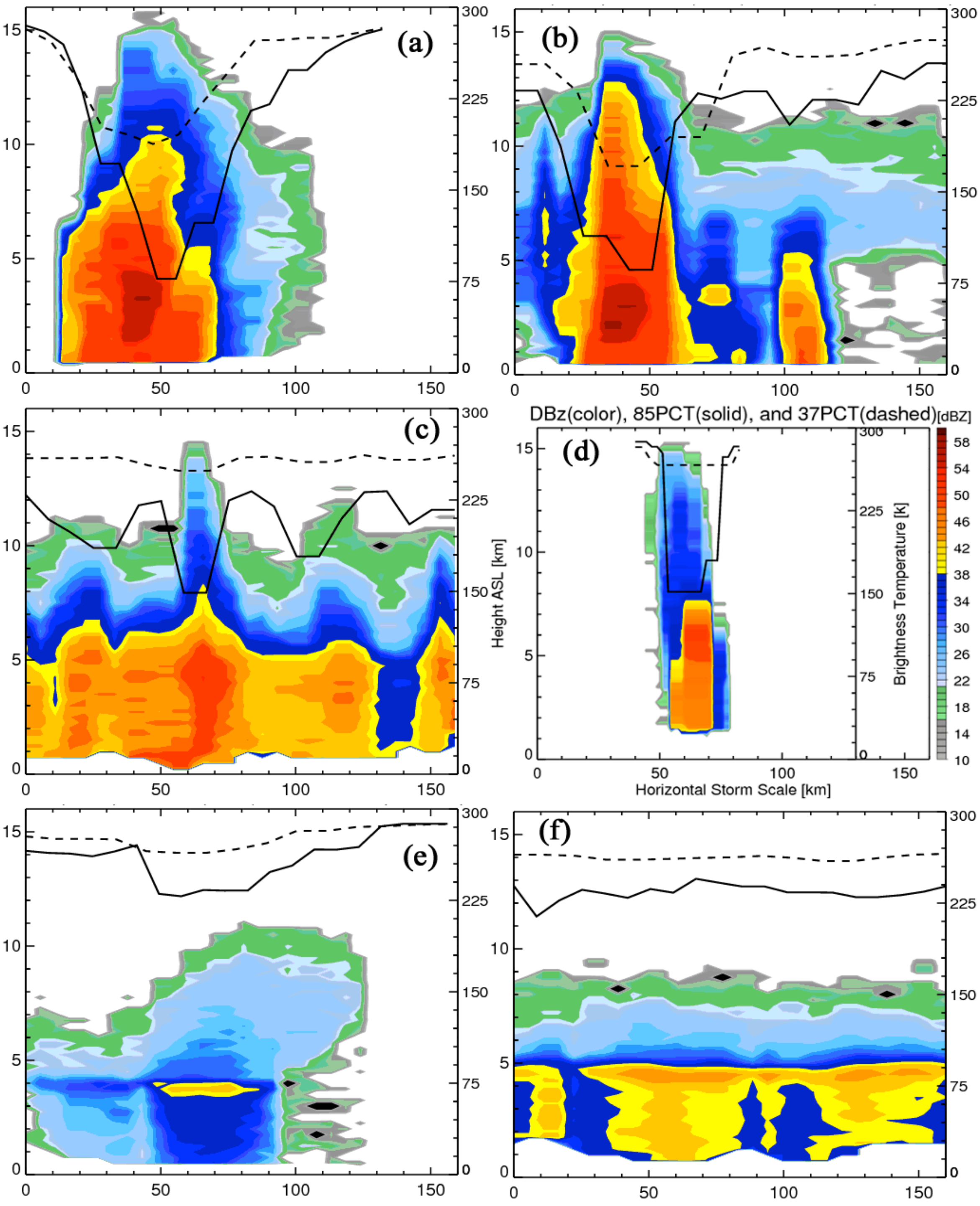

Figure 4.6. Storm cross section: (a) Storm with deep convective core, but no anvil; (b) Storm with deep convective core and anvil; (c) Storm multiple convective cores; (d) Deep but small convective; (e) Small stratiform system; (f) Large stratiform system. Note that all figures share the same y-axis and color bar as (d).

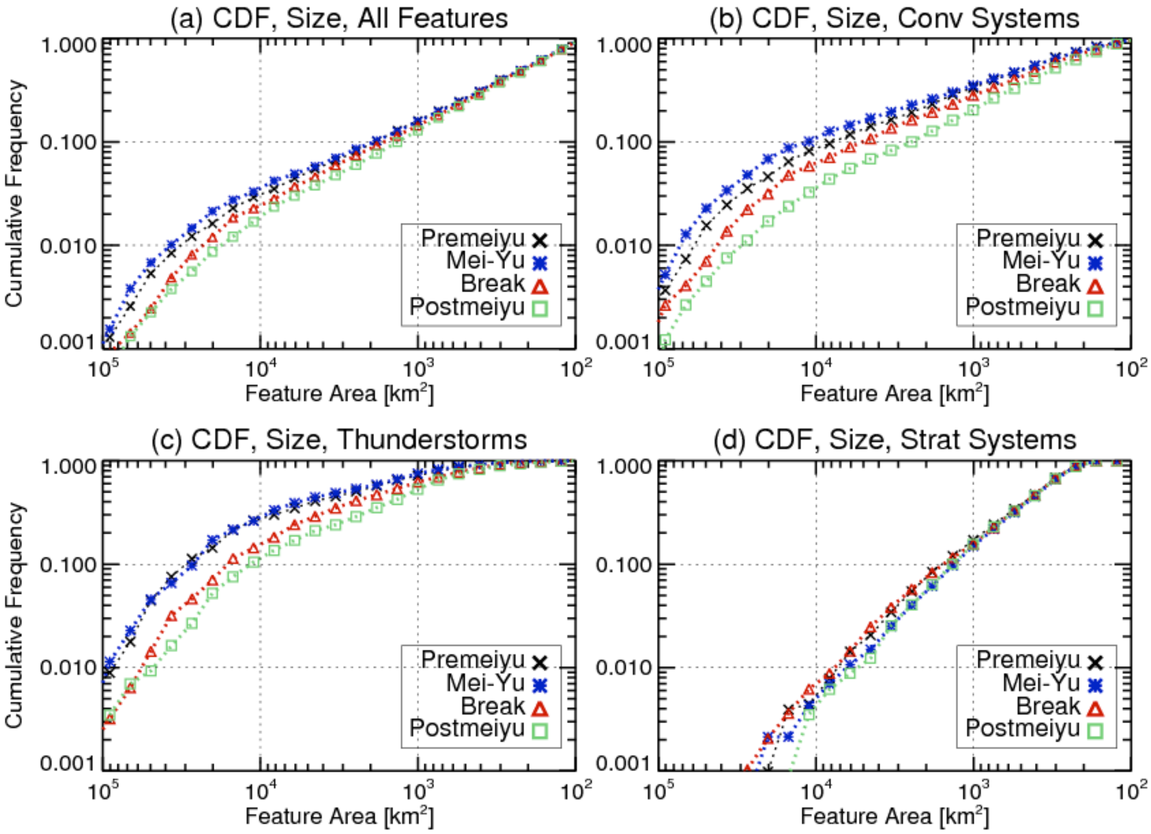

Figure 4.7. Cumulative distribution frequency (CDF) of horizontal storm size at near the surface of different precipitation systems: (a) All the PFs; (b) Convective systems; (c) Thunderstorms; (d) Stratiform systems.

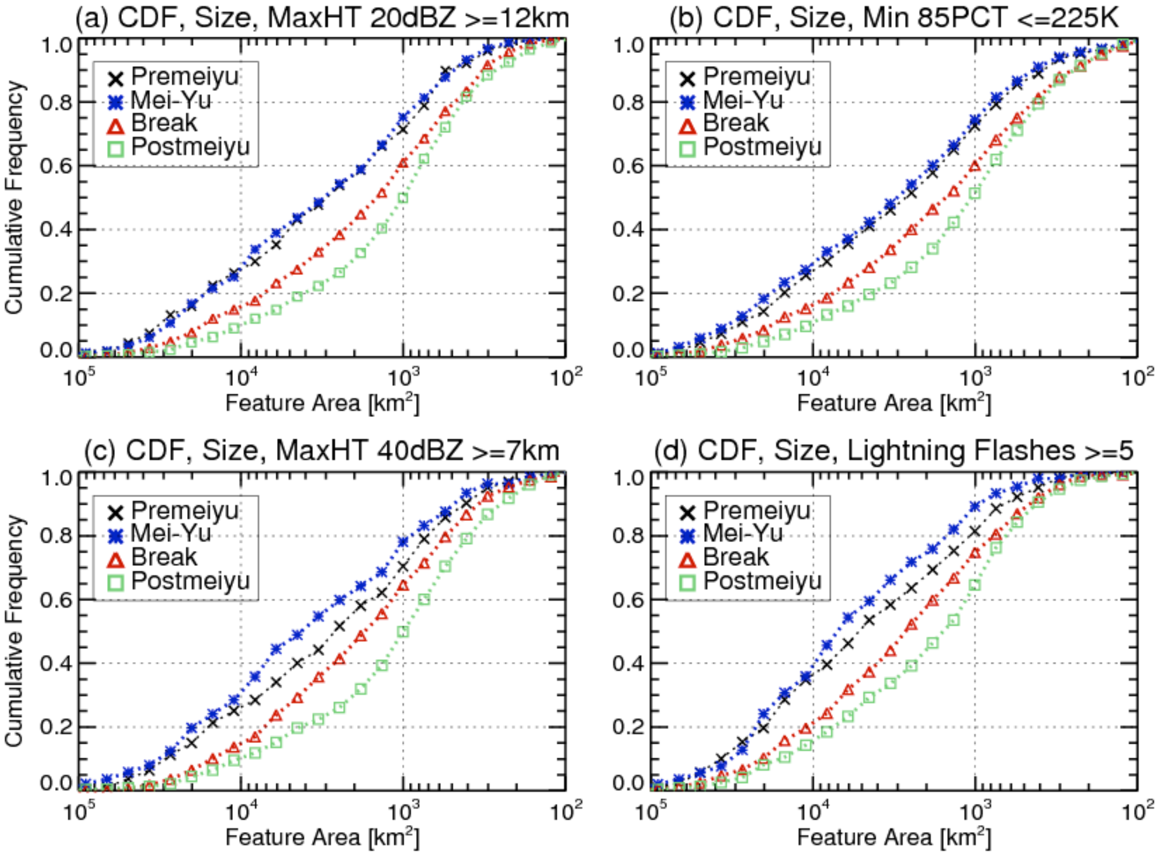

Figure 4.8. CDF of horizontal storm size at near the surface of precipitation systems limited by different criteria: (a) Features with 20 dBZ echo reaching the maximum height of 12 km; (b) Systems with minimum PCT at 85 GHz frequency lower than 225 K; (c) Storms with 40 dBZ radar reflectivity extending a maximum height of 7 km; (d) Thunderstorms with at least 5 lightning flashes.

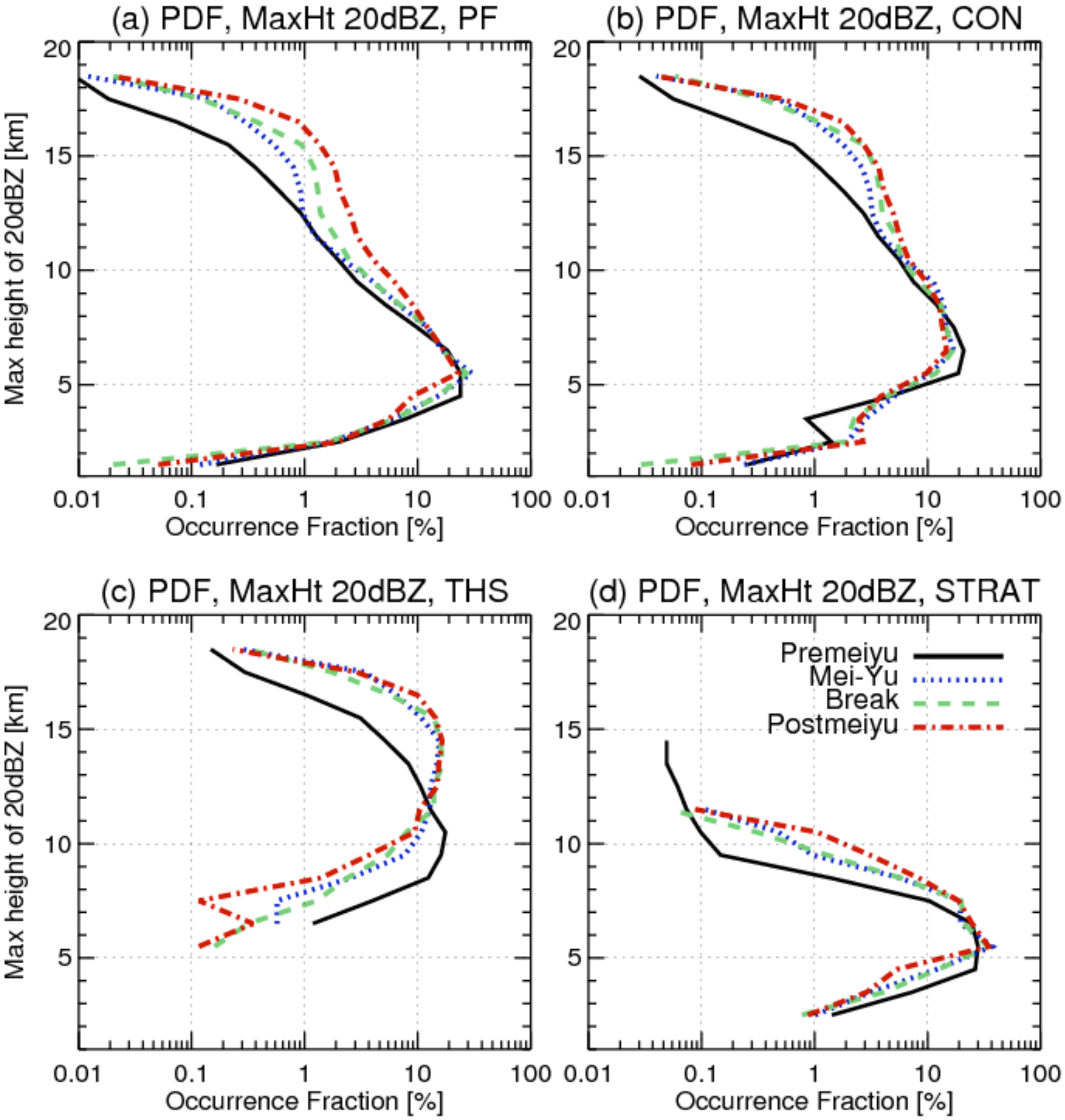

Figure 4.9. Occurrence frequency (in %) of features with 20 dBZ reaching different maximum height for 4 types of storms: (a) All the PFs; (b) Convective systems; (c) Thunderstorms; (d) Stratiform systems.

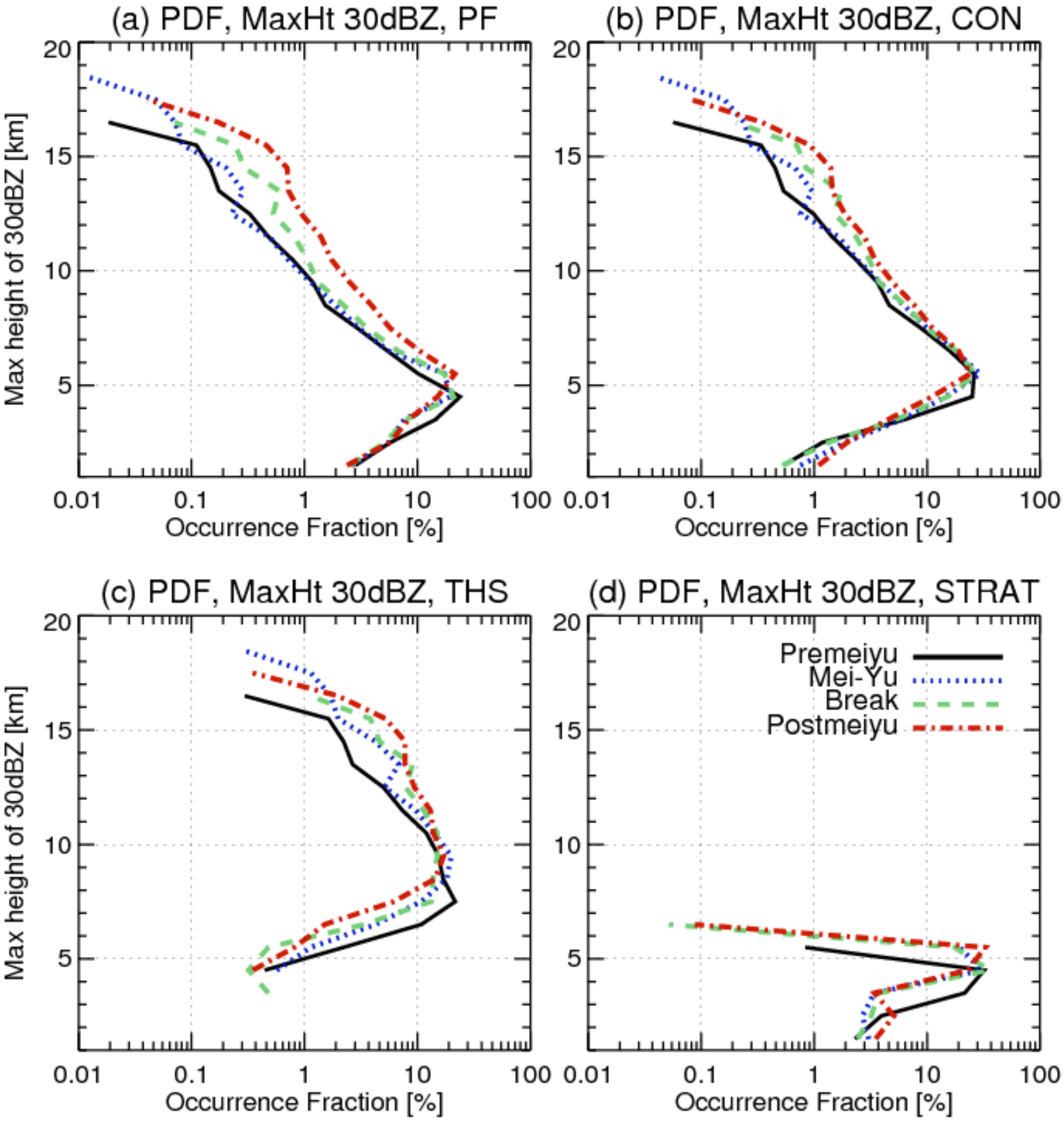

Figure 4.10. Same as Fig. 4.9, but for 30 dBZ.

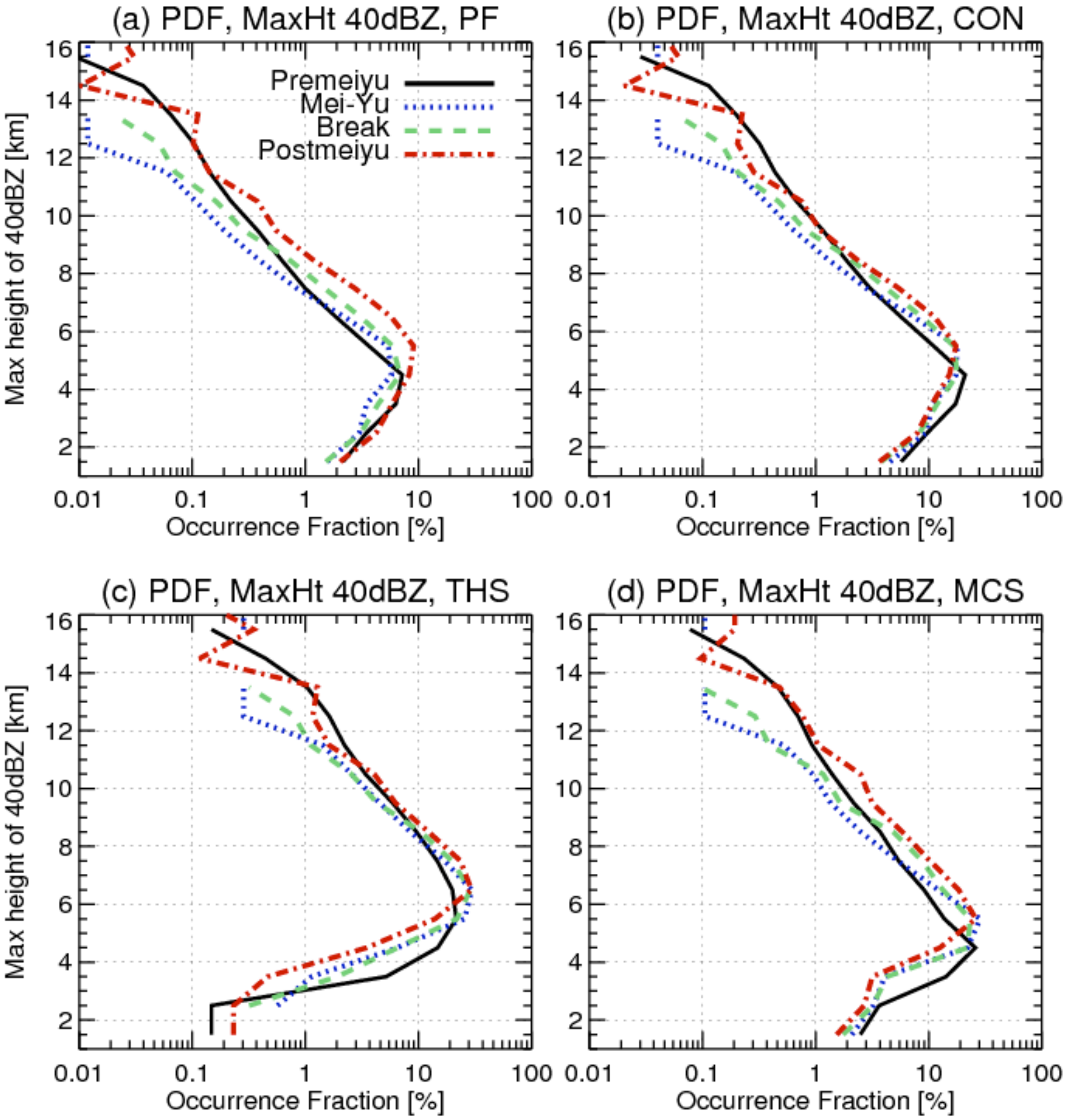

Figure 4.11. Occurrence frequency (in %) of features with 40 dBZ reaching different maximum height for 4 types of storms: (a) All the PFs; (b) Convective systems; (c) Thunderstorms; (d) Mesoscale convective systems (MCSs).

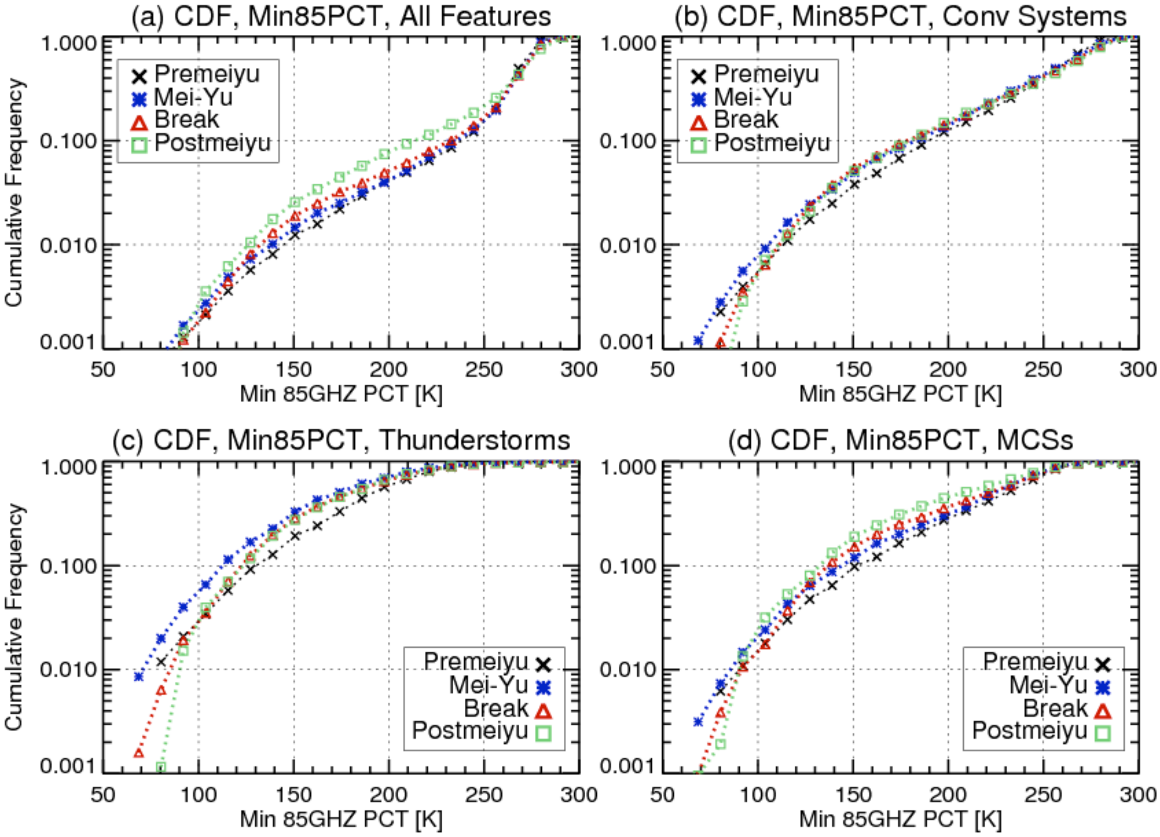

Figure 4.12. Cumulative distribution frequency (CDF) of storm population categorized by values of minimum 85 GHz PCT for different precipitation systems: (a) All the PFs; (b) Convective systems; (c) Thunderstorms; (d) MCSs.

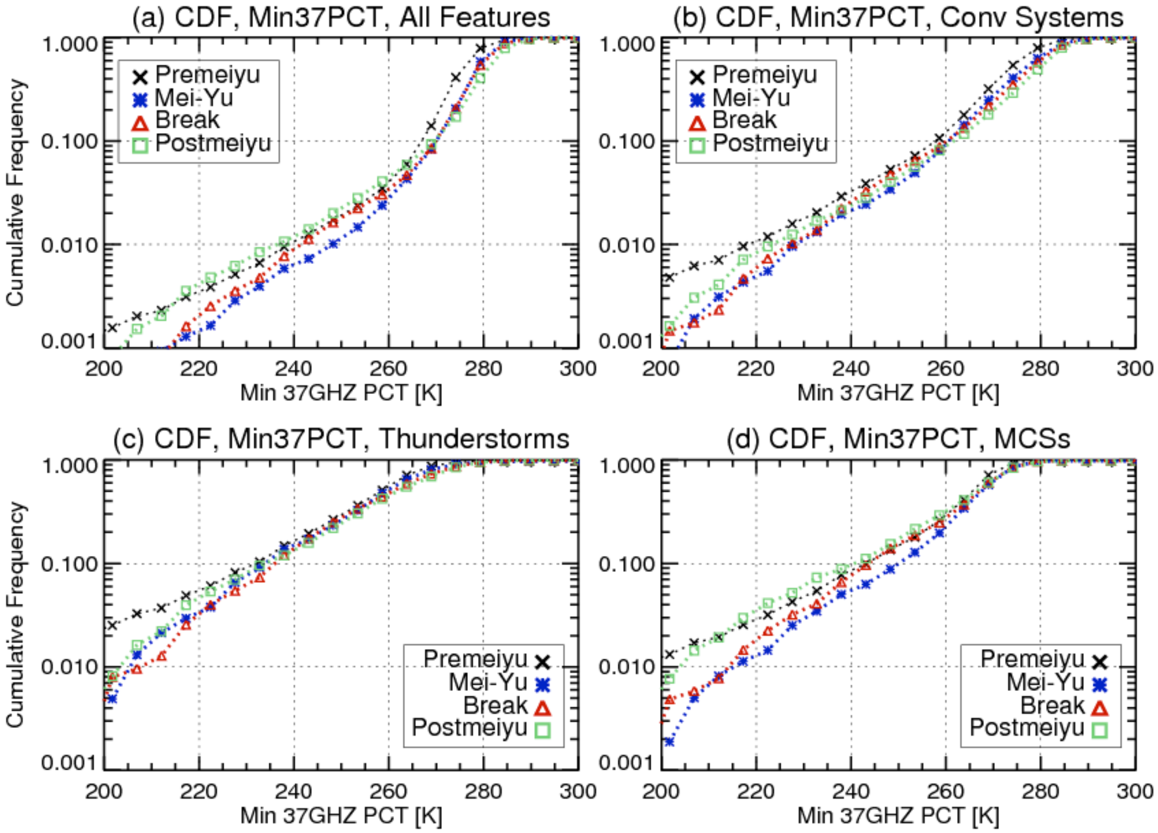

Figure 4.13. Same as Fig. 4.12, but for 37 GHz PCT.

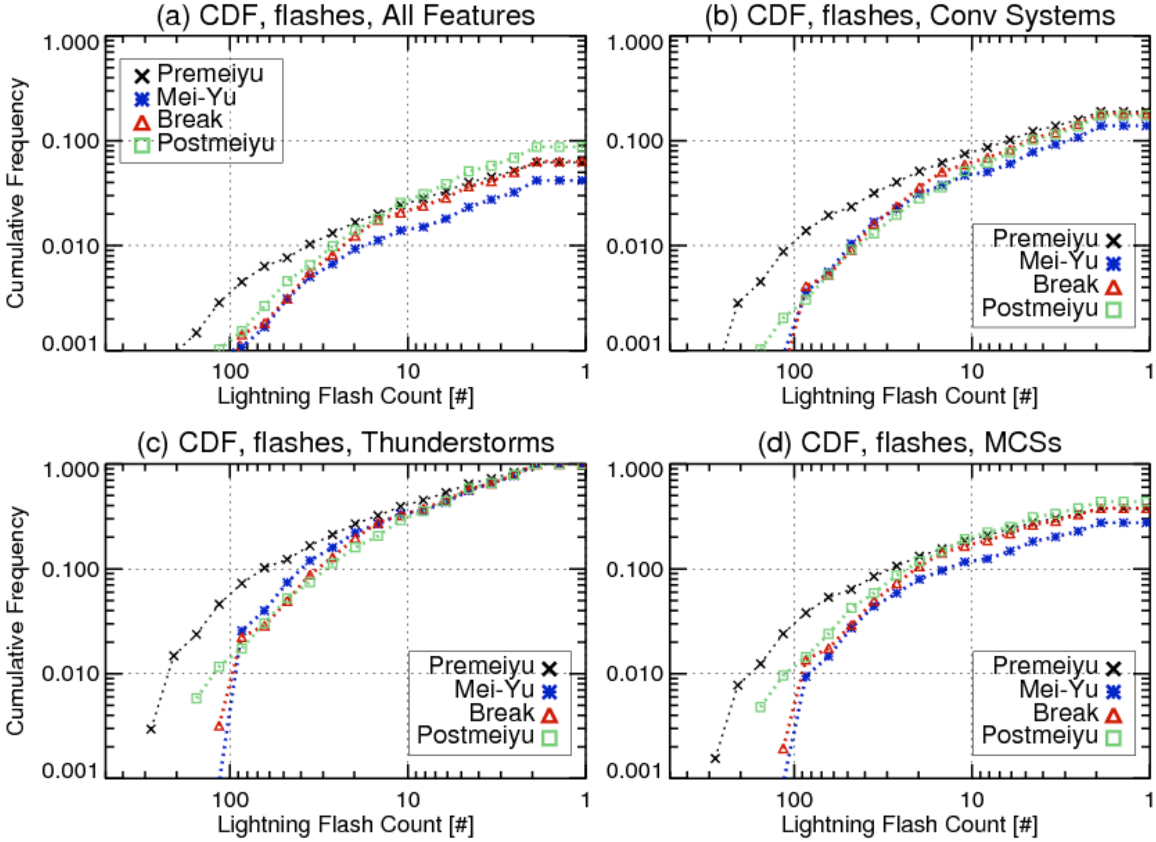

Figure 4.14. Same as Fig. 4.12, but for lightning flash count.

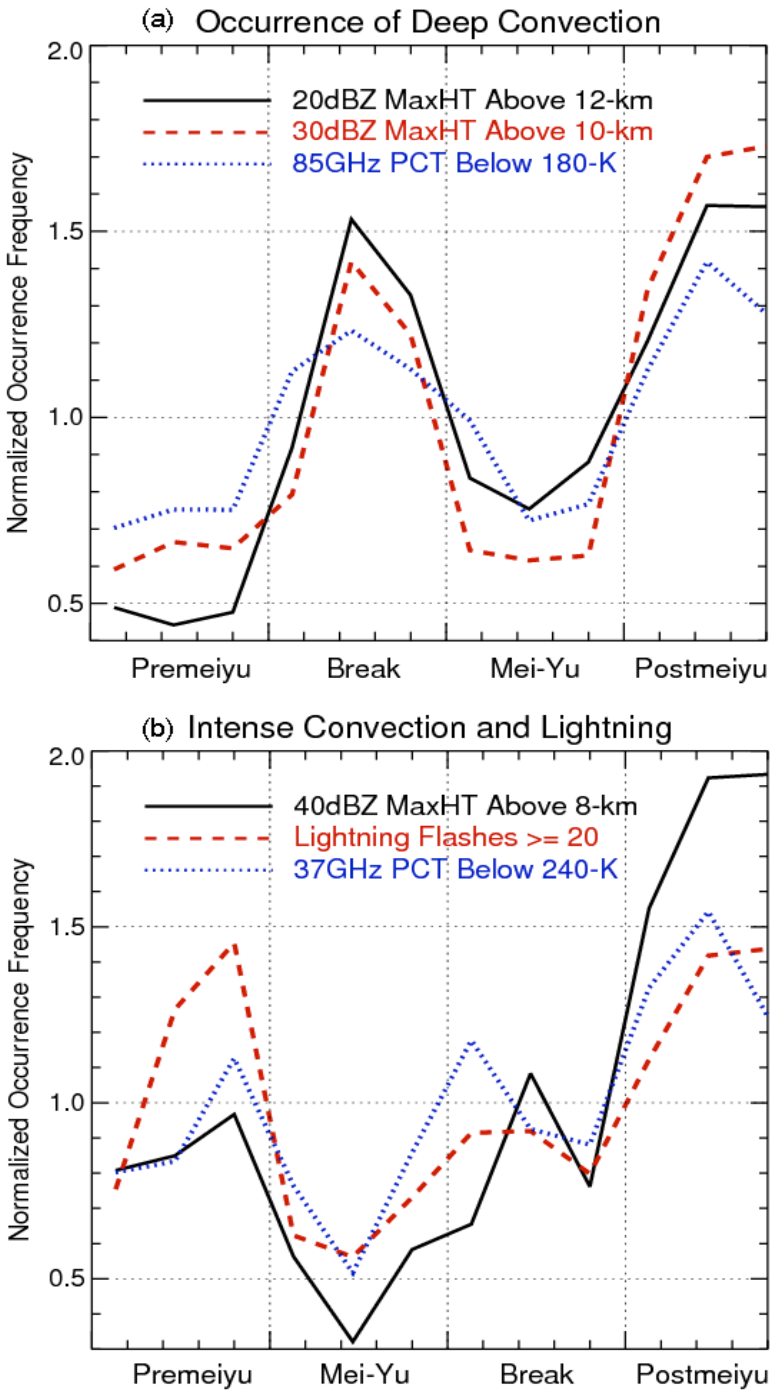

Figure 4.15. Occurrence frequency of PFs with (a) defined deep convection (b) intense convection and lightning, during different periods normalized by the mean of these periods. During each period, data points are from data of every 4 years of the total 12 years.

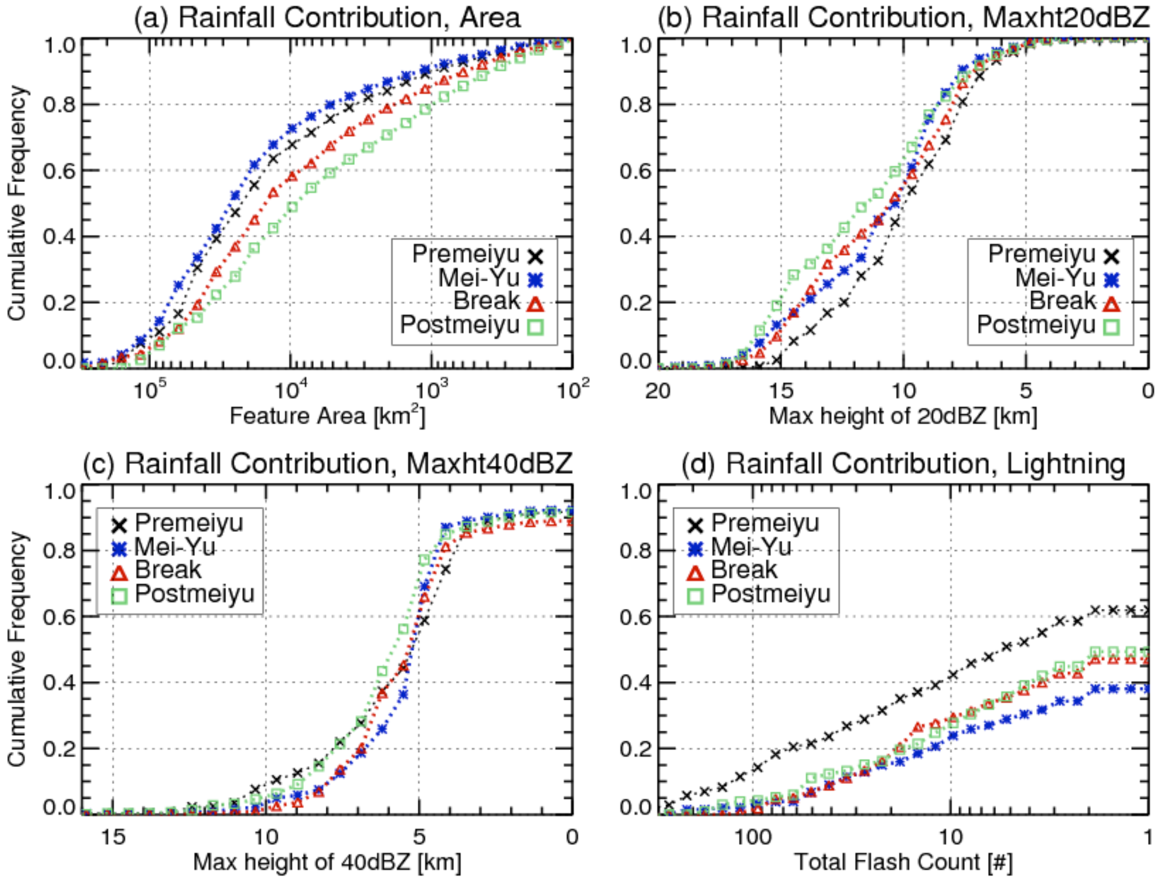

Figure 4.16. Cumulative distribution frequency (CDF) of rainfall fraction contributed by storms categorized by different proxies: (a) Horizontal area; (b) Maximum height of 20 dBZ radar echo; (c) Maximum height of 40 dBZ; (d) Lightning flash count.

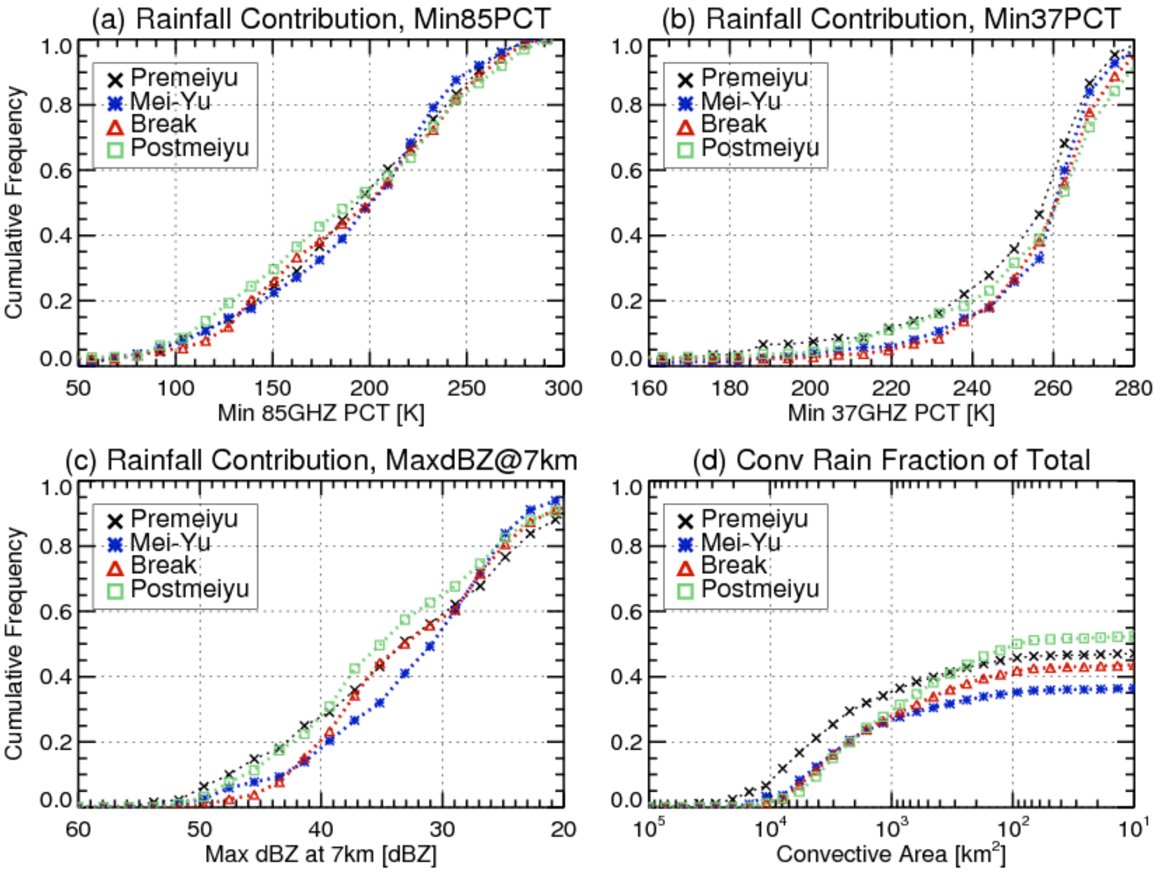

Figure 4.17. Cumulative distribution frequency (CDF) of rainfall fraction contributed by (a) storms categorized by 85 GHz PCT; (b) storms categorized by 37 GHz PCT; (c) storms cauterized by maximum dBZ at 7 km; (d) Convective rainfall from storms categorized by size of convection.

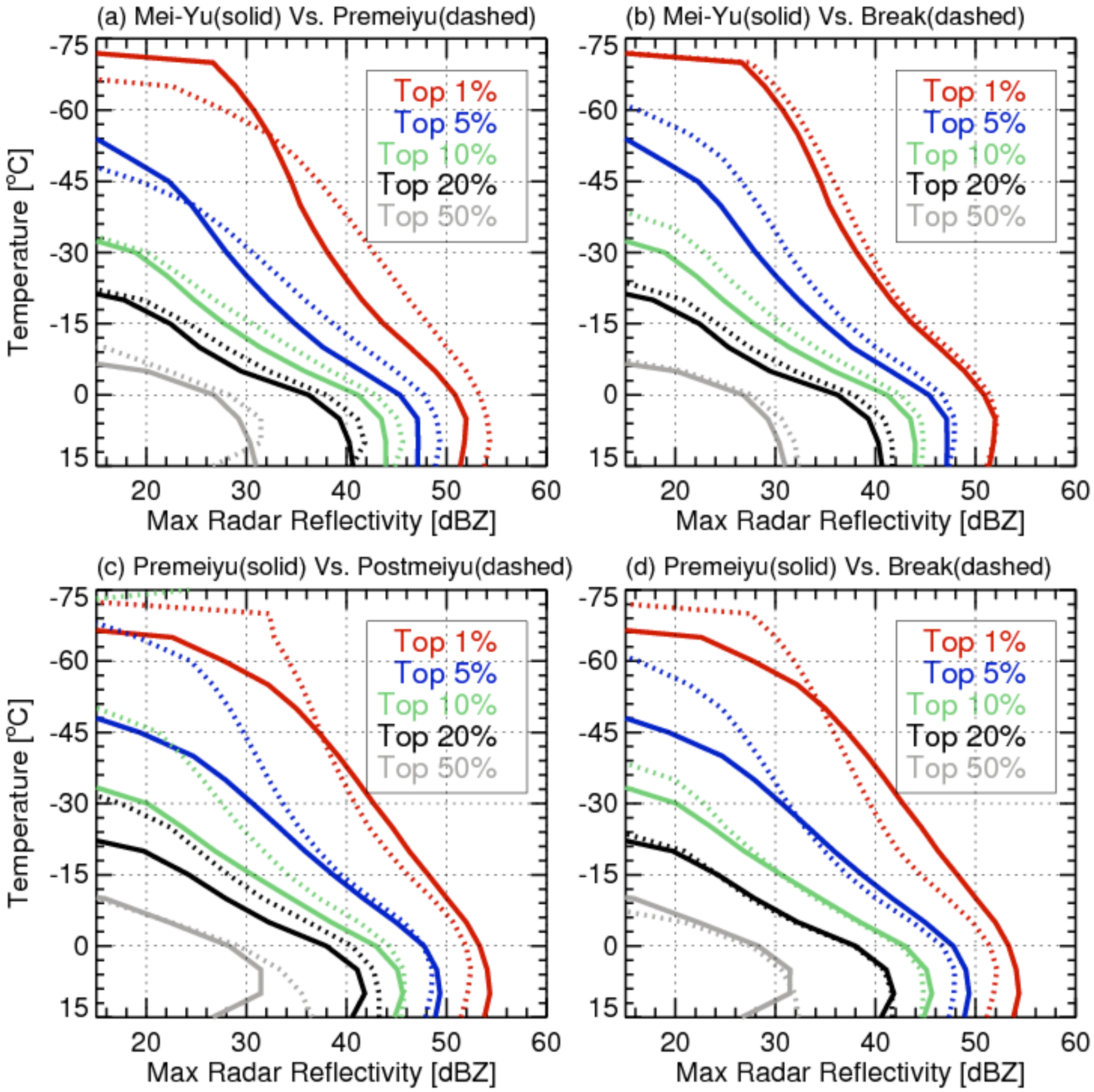

Figure 4.18. Comparisons of vertical profiles of maximum radar reflectivity of PFs as a function of temperature: (a) Mei-Yu vs. Premeiyu, (b) Mei-Yu vs. Break, (c) Premeiyu vs. Postmeiyu, (d) Premeiyu vs. Break.

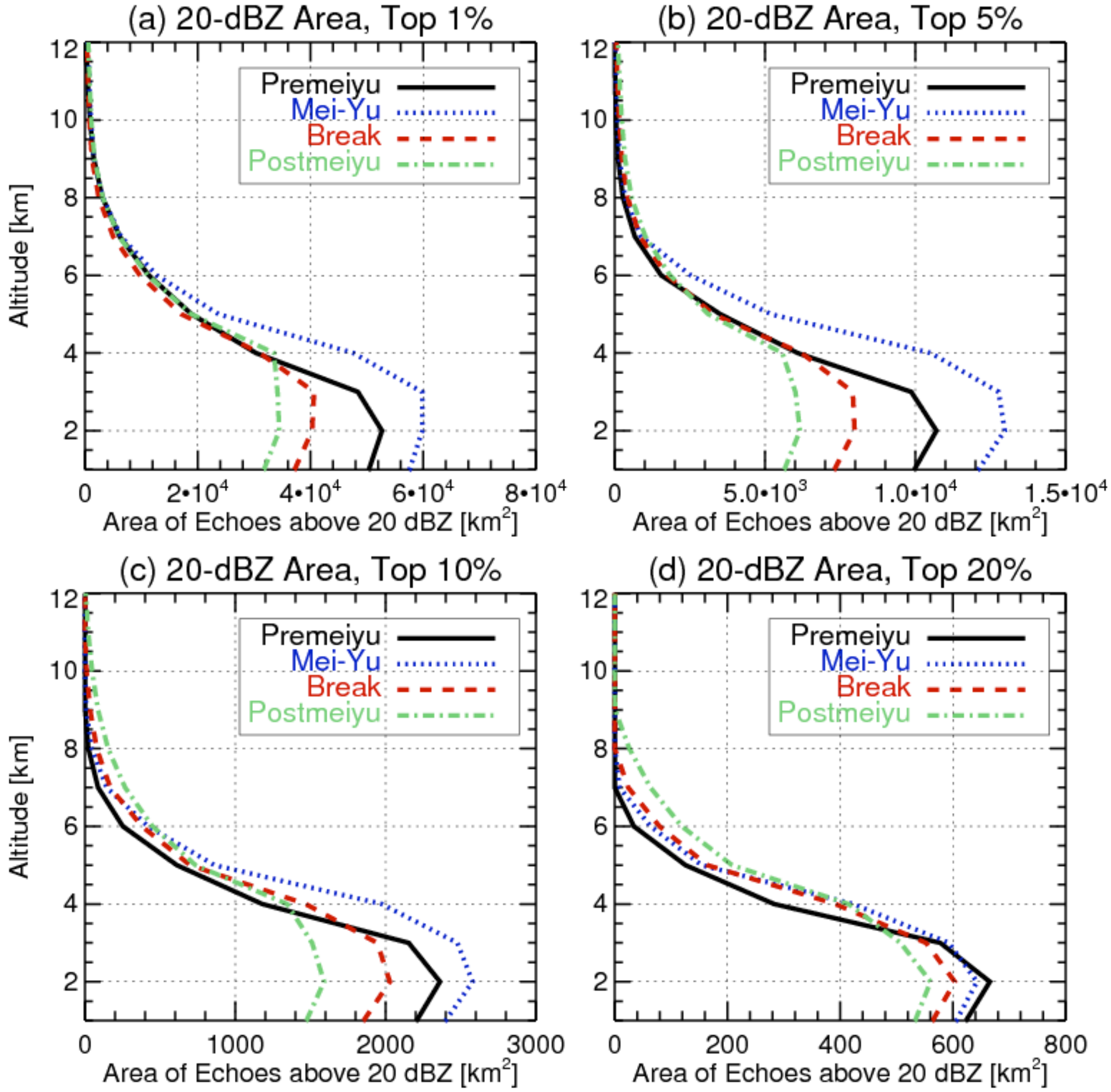

Figure 4.19. Comparisons of vertical profiles of area of radar echoes above 20 dBZ in PFs as a function of altitude: (a) Top 1%, (b) Top 5%, (c) Top 10%, (d) Top 20%.

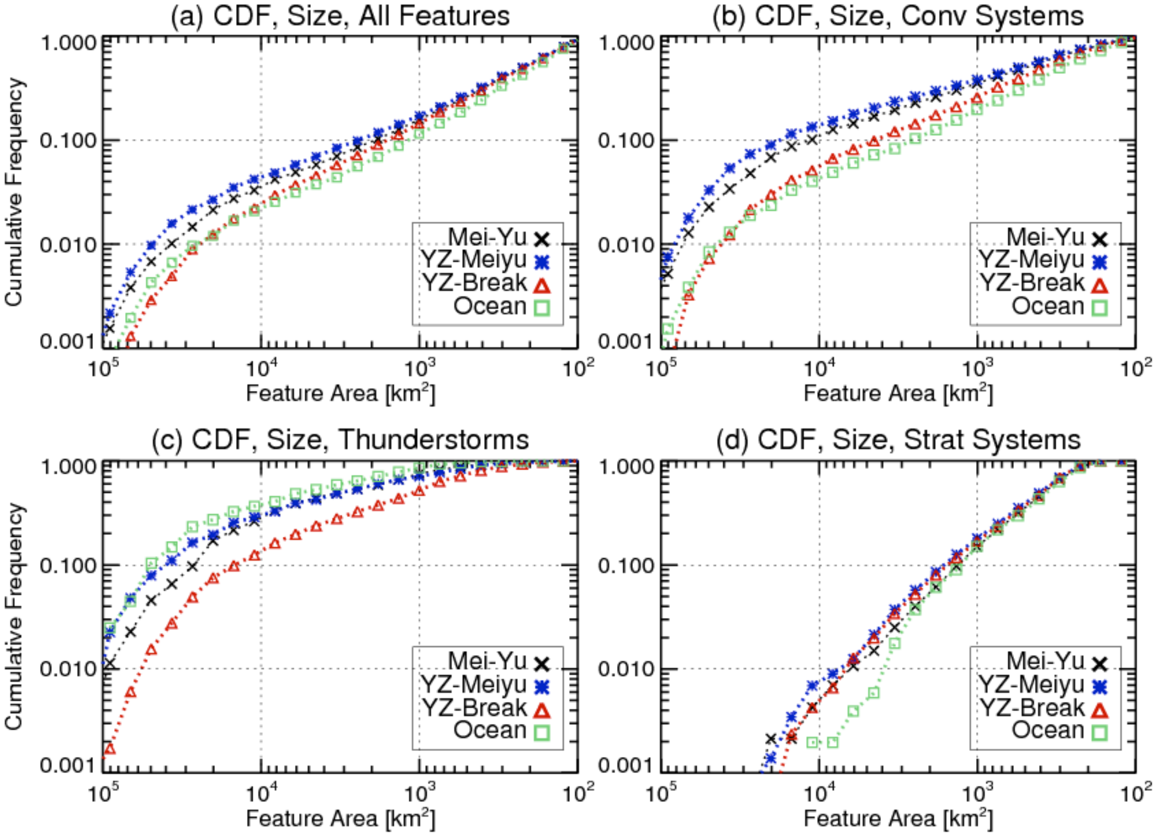

Figure 4.20. Cumulative distribution frequency (CDF) of horizontal storm size at near the surface of different precipitation systems: (a) All the PFs; (b) Convective systems; (c) Thunderstorms; (d) Stratiform systems.

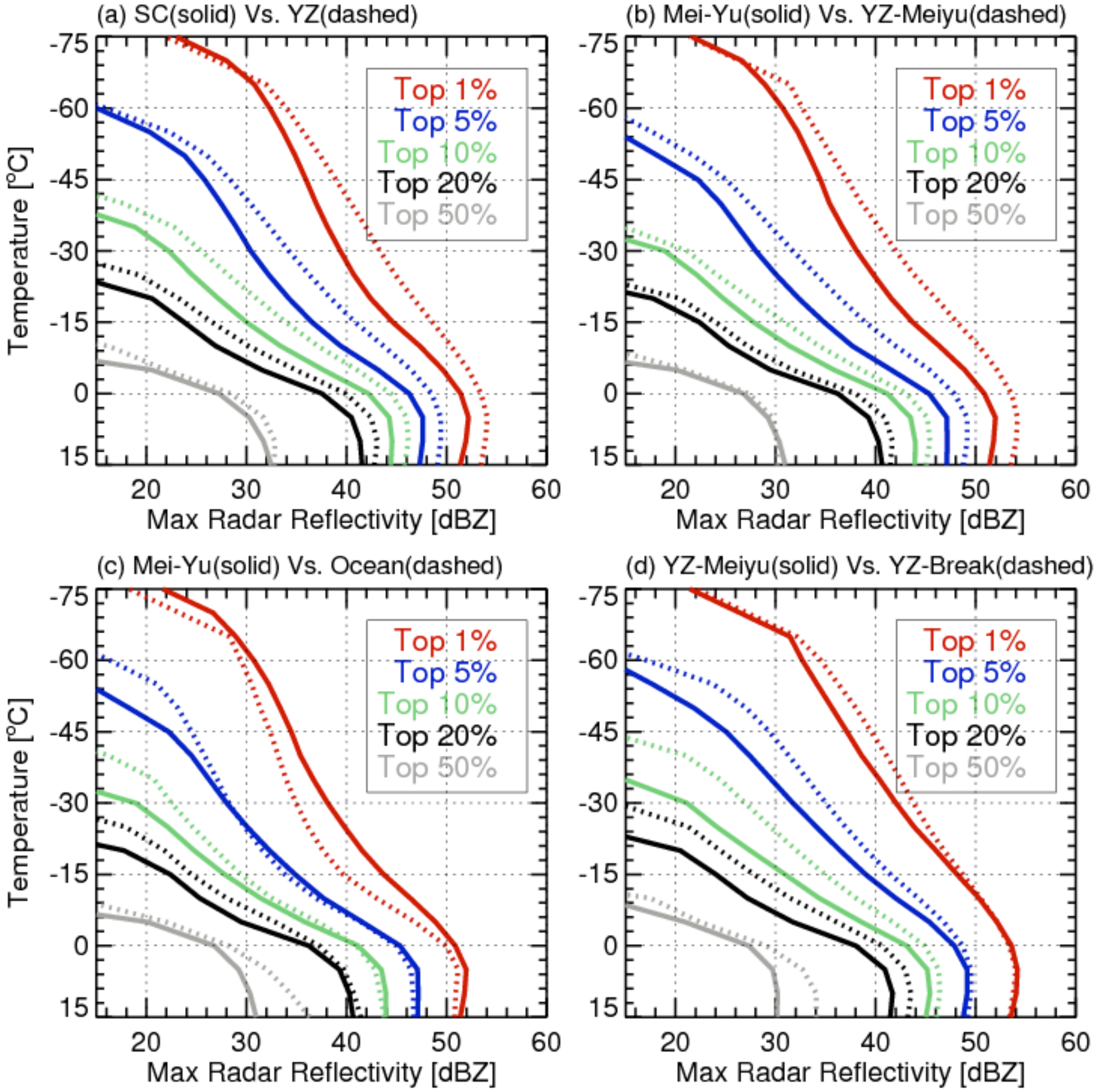

Figure 4.21. Comparisons of vertical profiles of maximum radar reflectivity of PFs as a function of temperature: (a) Meiyu season in South China vs. Meiyu season in Yangtze River, (b) Active Mei-Yu vs. active YZ-Meiyu, (c) Active Mei-Yu vs. Oceanic systems, (d) YZ-Meiyu vs. YZ-Break.

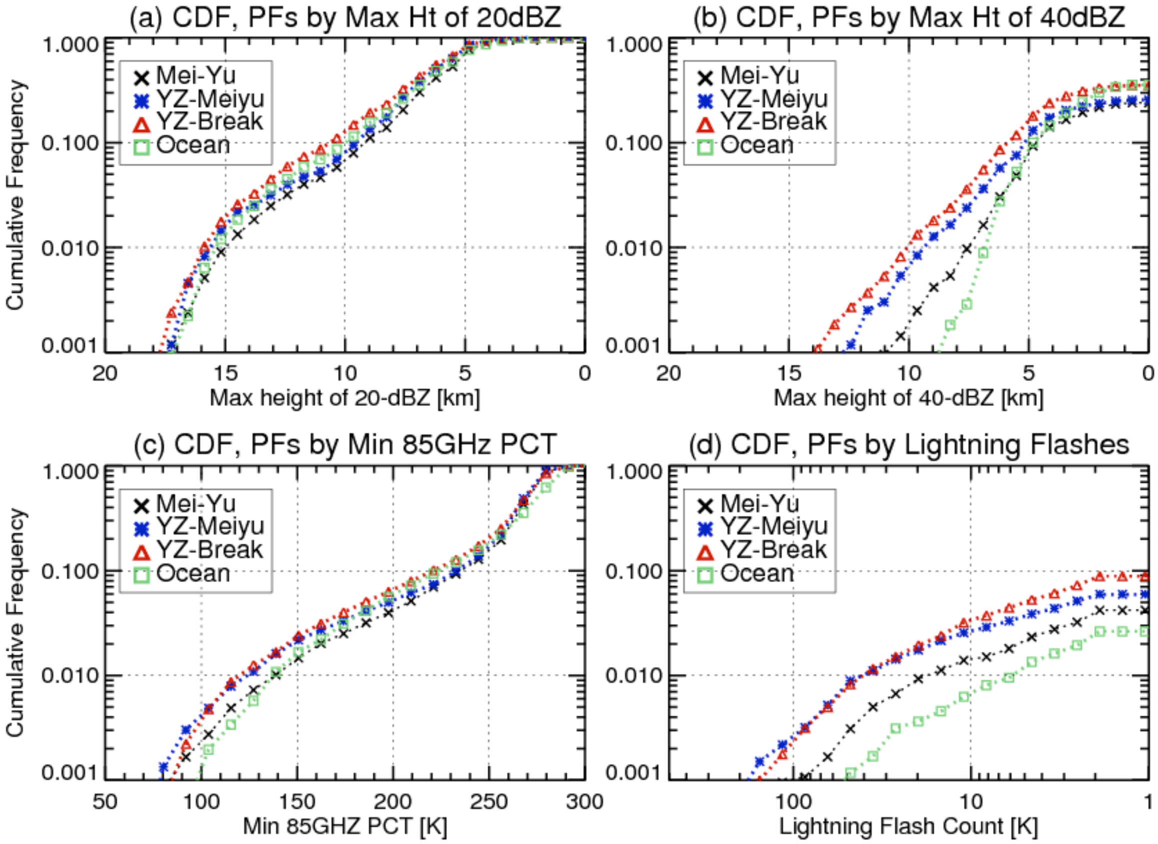

Figure 4.22. Cumulative distribution frequency (CDF) of PF population categorized by (a) Maximum height of 20 dBZ, (b) Maximum height of 40 dBZ, (c) Minimum PCT of microwave at 85GHz, (d) Lightning flash count.

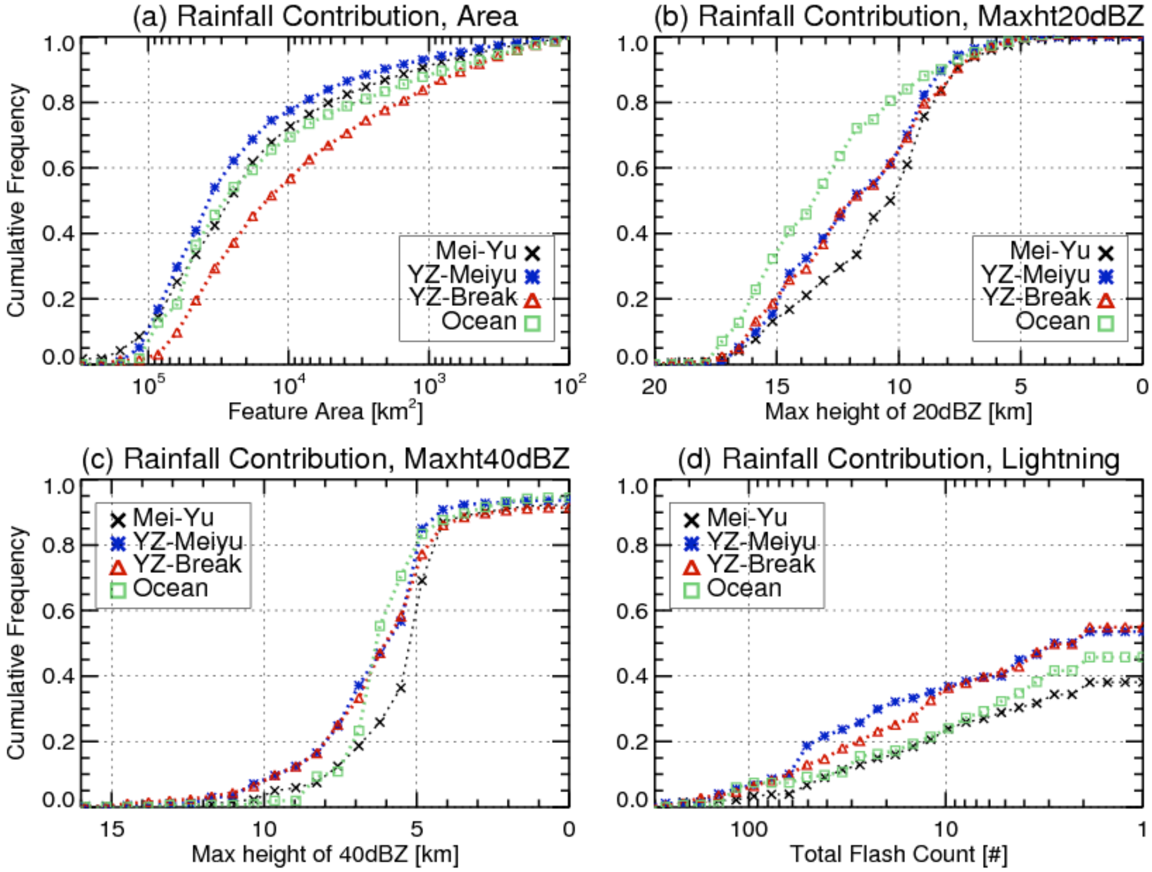

Figure 4.23. Cumulative distribution frequency (CDF) of rainfall fraction contributed by storms categorized by different proxies: (a) Horizontal area; (b) Maximum height of 20 dBZ radar echo; (c) Maximum height of 40 dBZ; (d) Lightning flash count.

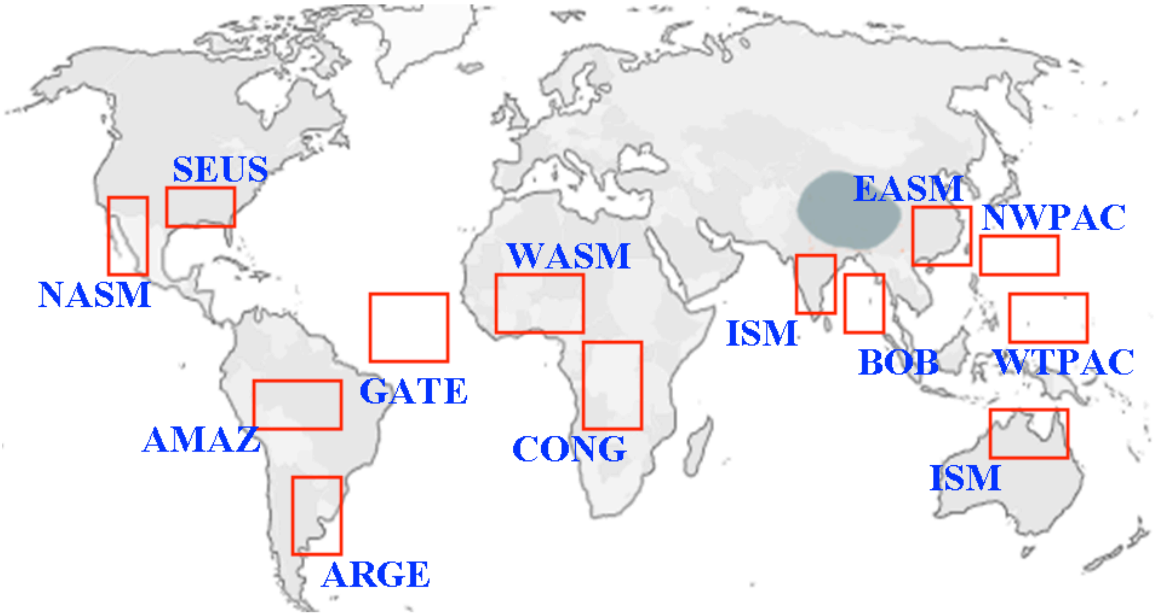

Figure 4.24. Geographic locations of selected regions for the study of monsoon, continental, and oceanic regimes.

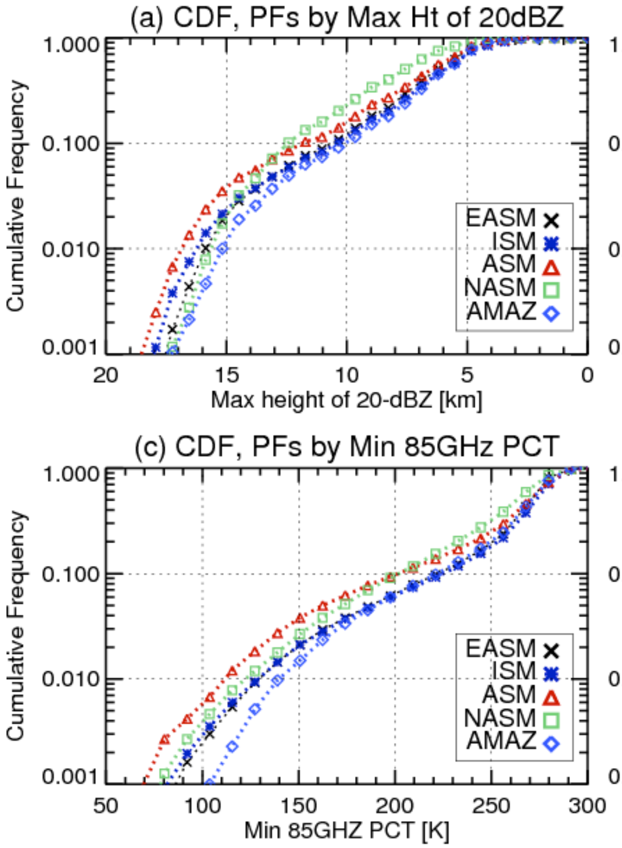

Figure 4.25. Cumulative distribution frequency (CDF) of PF population in selected monsoon regions categorized by (a) Maximum height of 20 dBZ, (b) Maximum height of 40 dBZ, (c) Minimum PCT of microwave at 85GHz, (d) Lightning flash count.

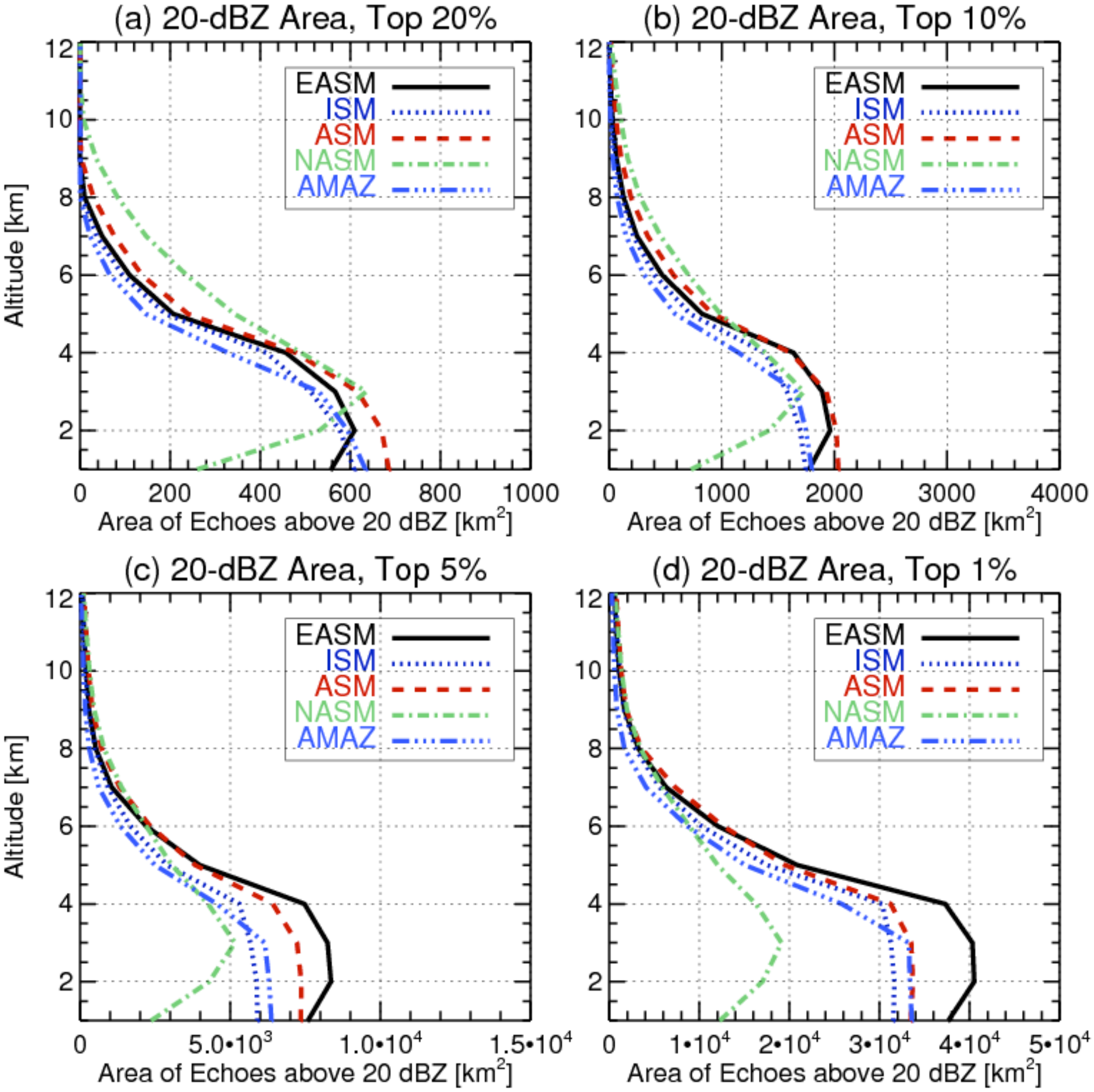

Figure 4.26. Comparisons of vertical profiles of area of radar echoes above 20 dBZ as a function of altitude in PFs for different monsoon regimes: (a) Top 20%, (b) Top 10%, (c) Top 5%, (d) Top 1%.

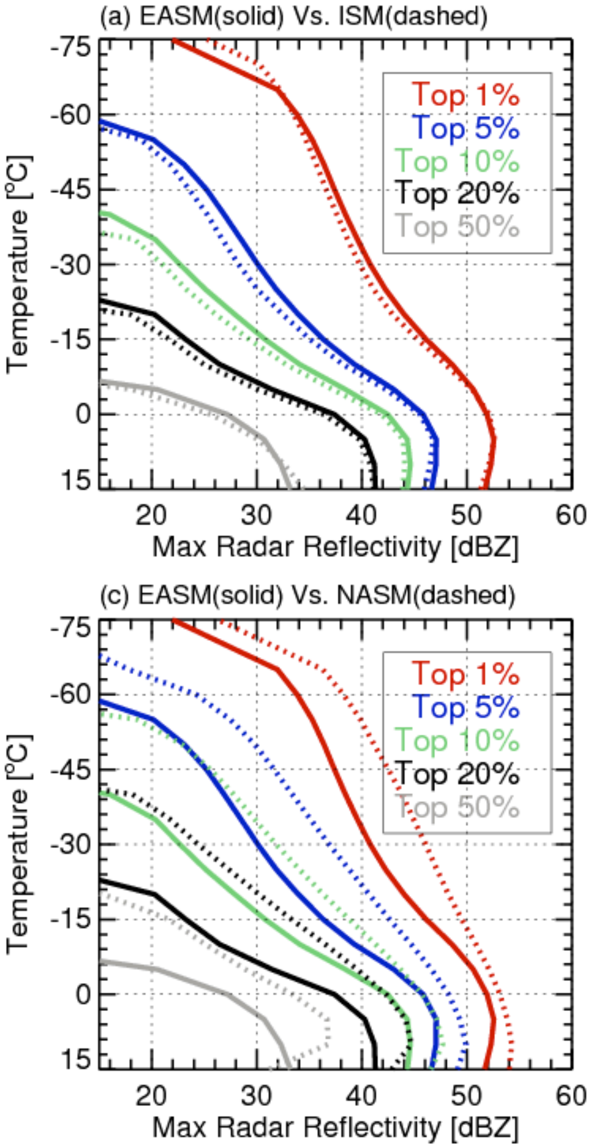

Figure 4.27. Comparisons of vertical profiles of maximum radar reflectivity as a function of temperature of PFs in different monsoon regions: (a) EASM vs. ISM, (b) EASM vs. ASM, (c) EASM vs. NASM, (d) EASM vs. AMAZ.

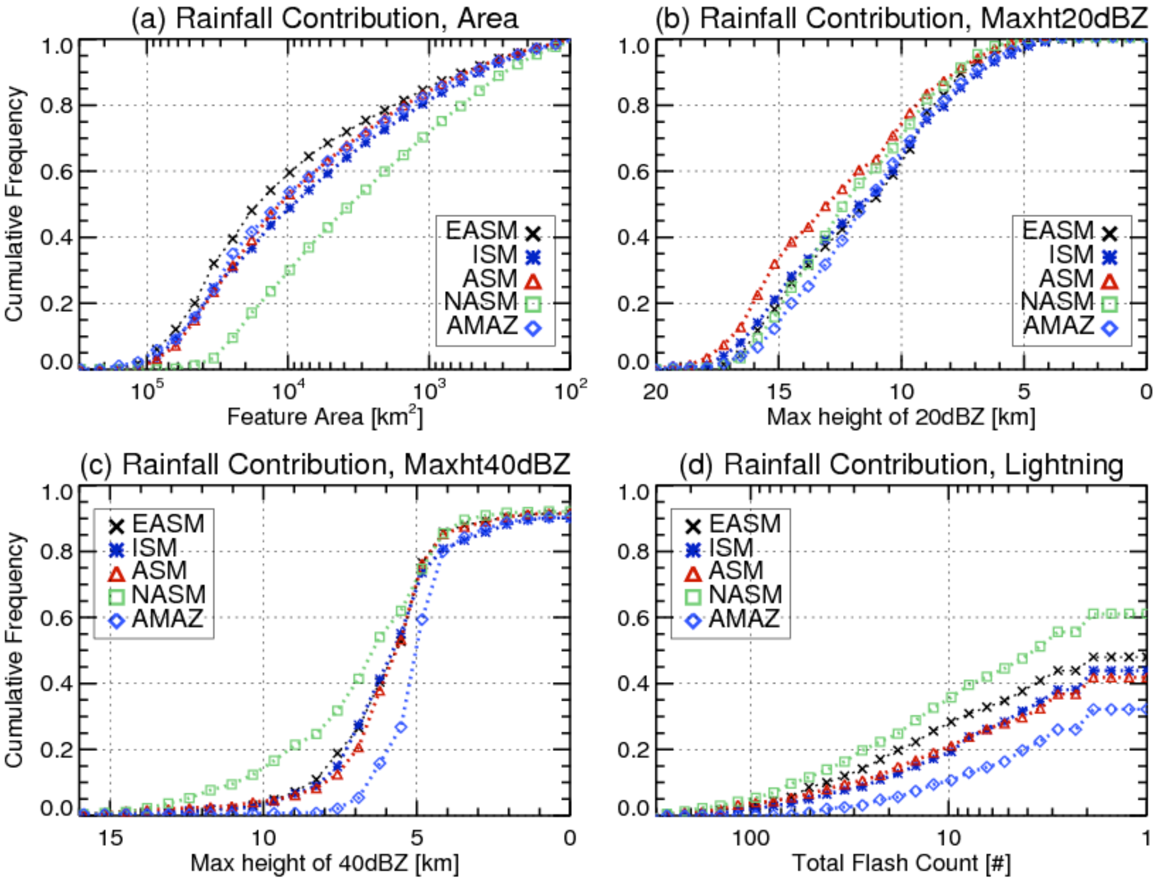

Figure 4.28. Cumulative distribution frequency (CDF) of rainfall fraction contributed by storms in different monsoon regions categorized by different proxies: (a) Horizontal area; (b) Maximum height of 20 dBZ radar echo; (c) Maximum height of 40 dBZ; (d) Lightning flash count.

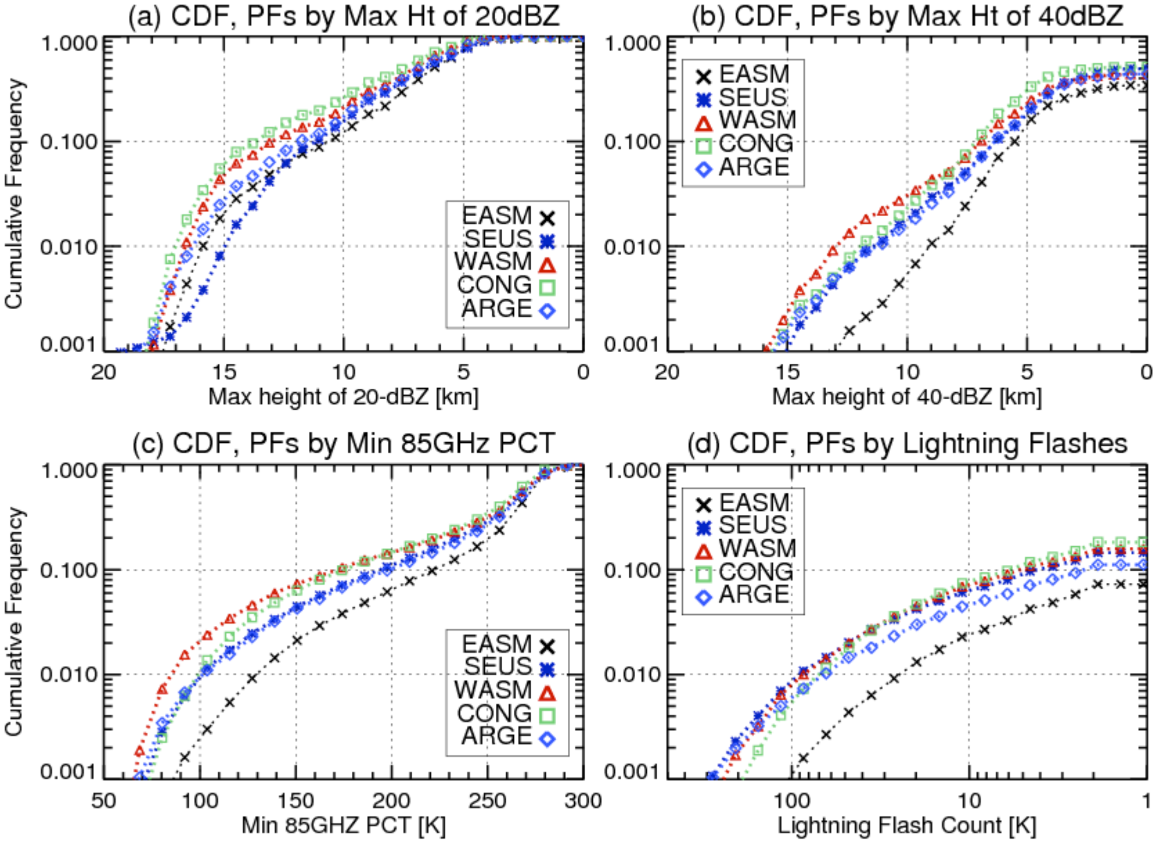

Figure 4.29. Same as Fig. 4.25, but for EASM and some continental regimes.

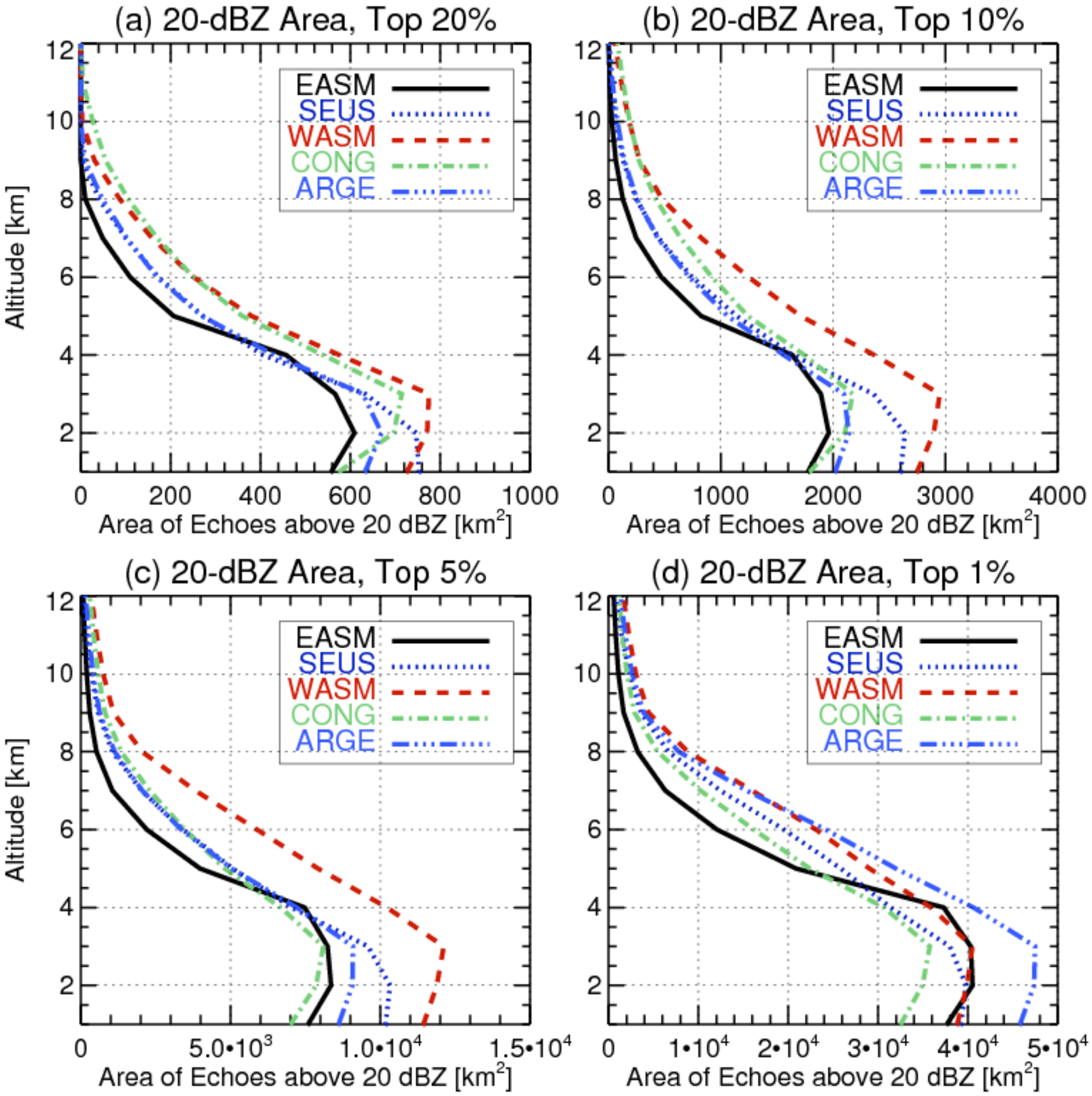

Figure 4.30. Same as Fig. 4.26, but for EASM and some continental regimes.

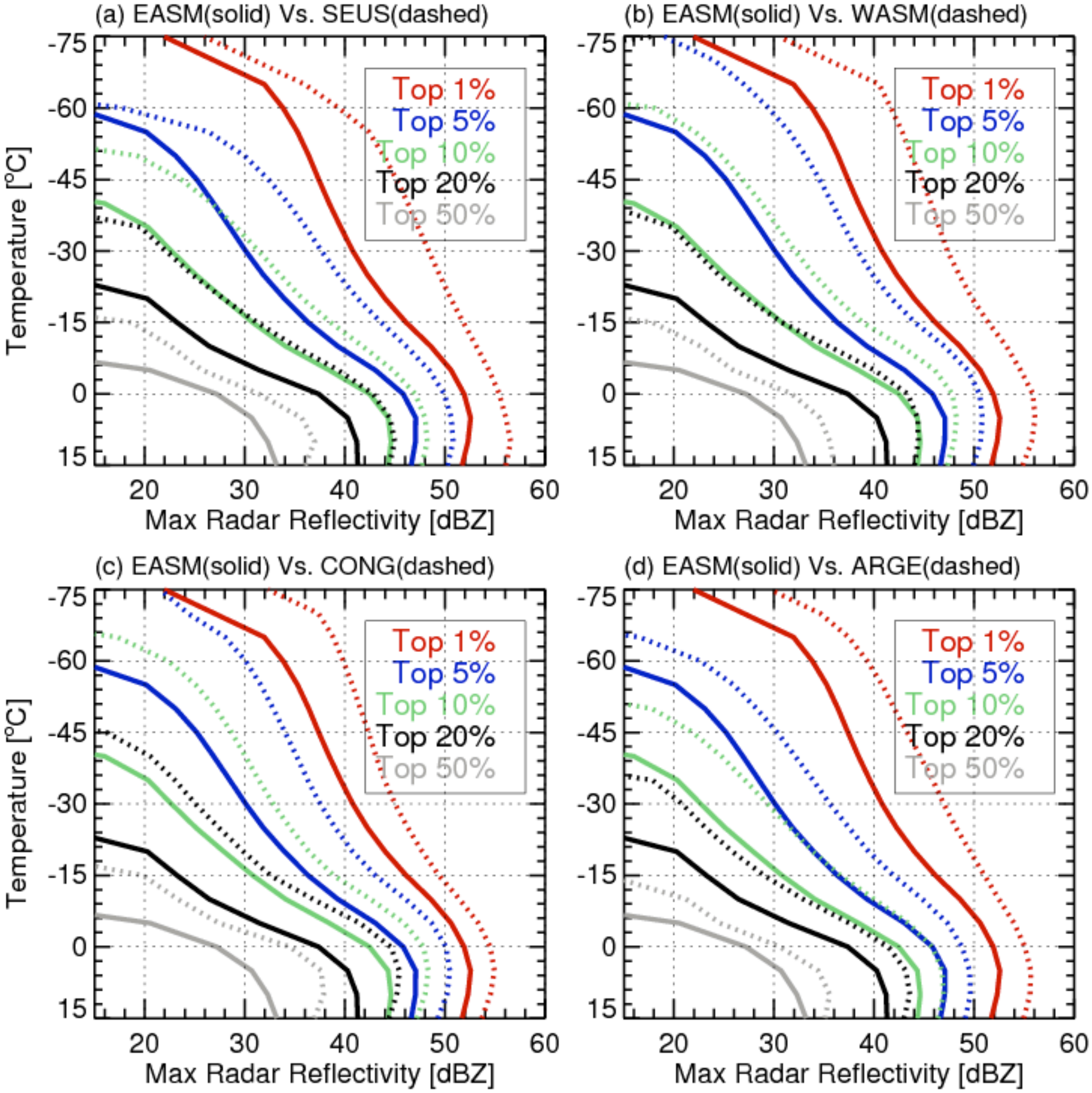

Figure 4.31. Same as Fig. 4.27, but for EASM and some continental regimes.

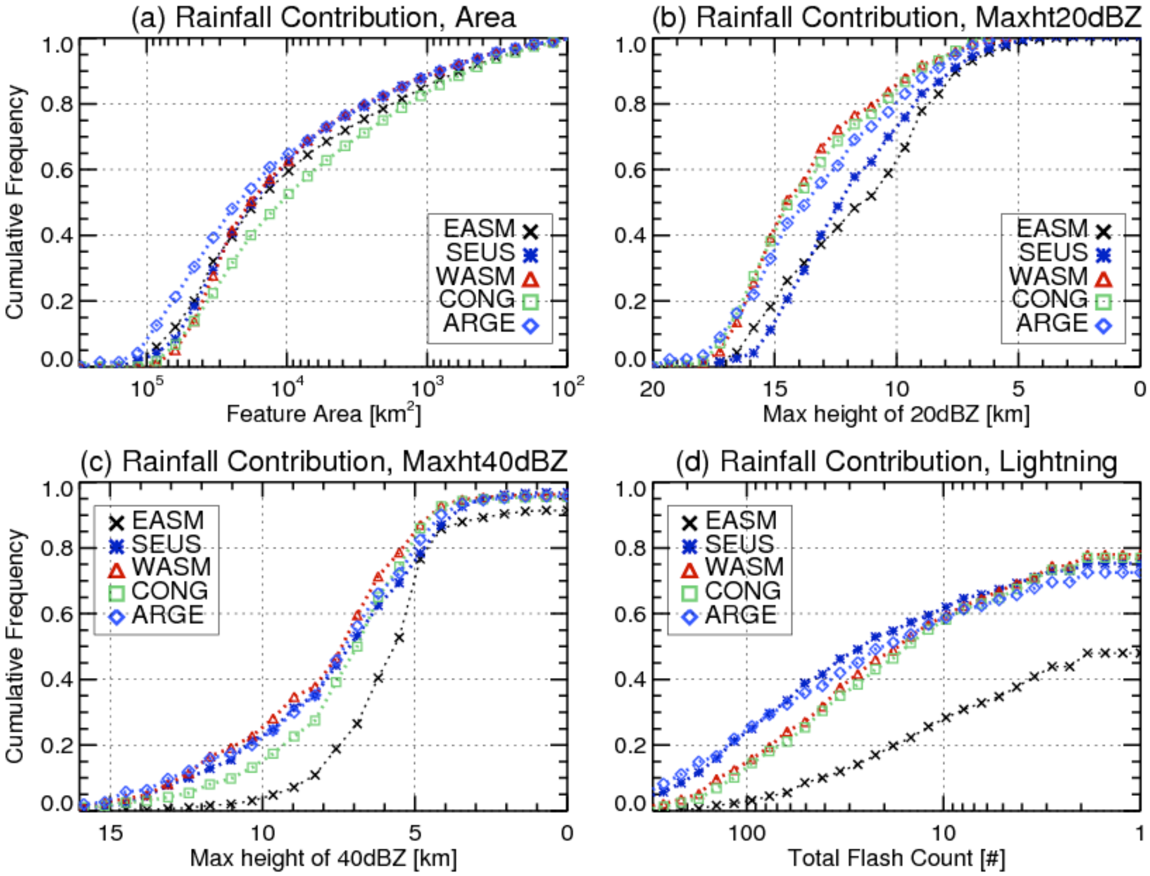

Figure 4.32. Same as Fig. 4.28, but for EASM and some continental regimes.

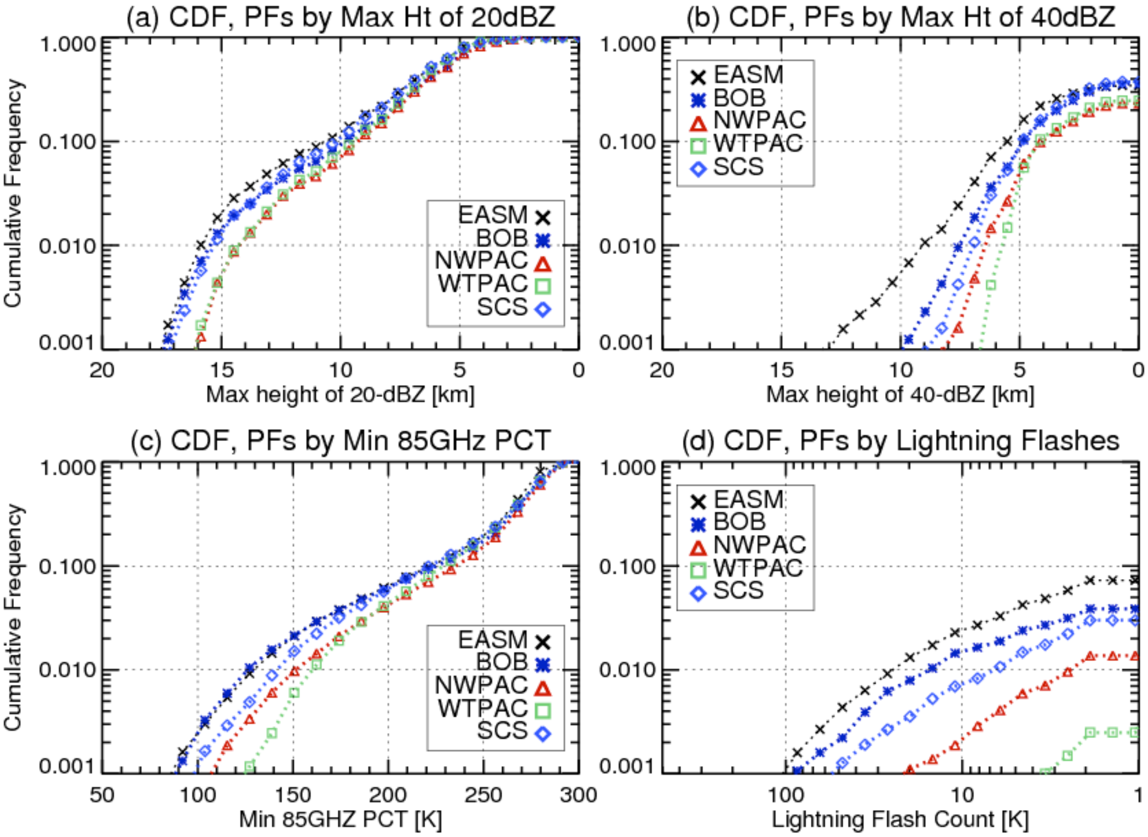

Figure 4.33. Same as Fig. 4.25, but for EASM and some oceanic regimes.

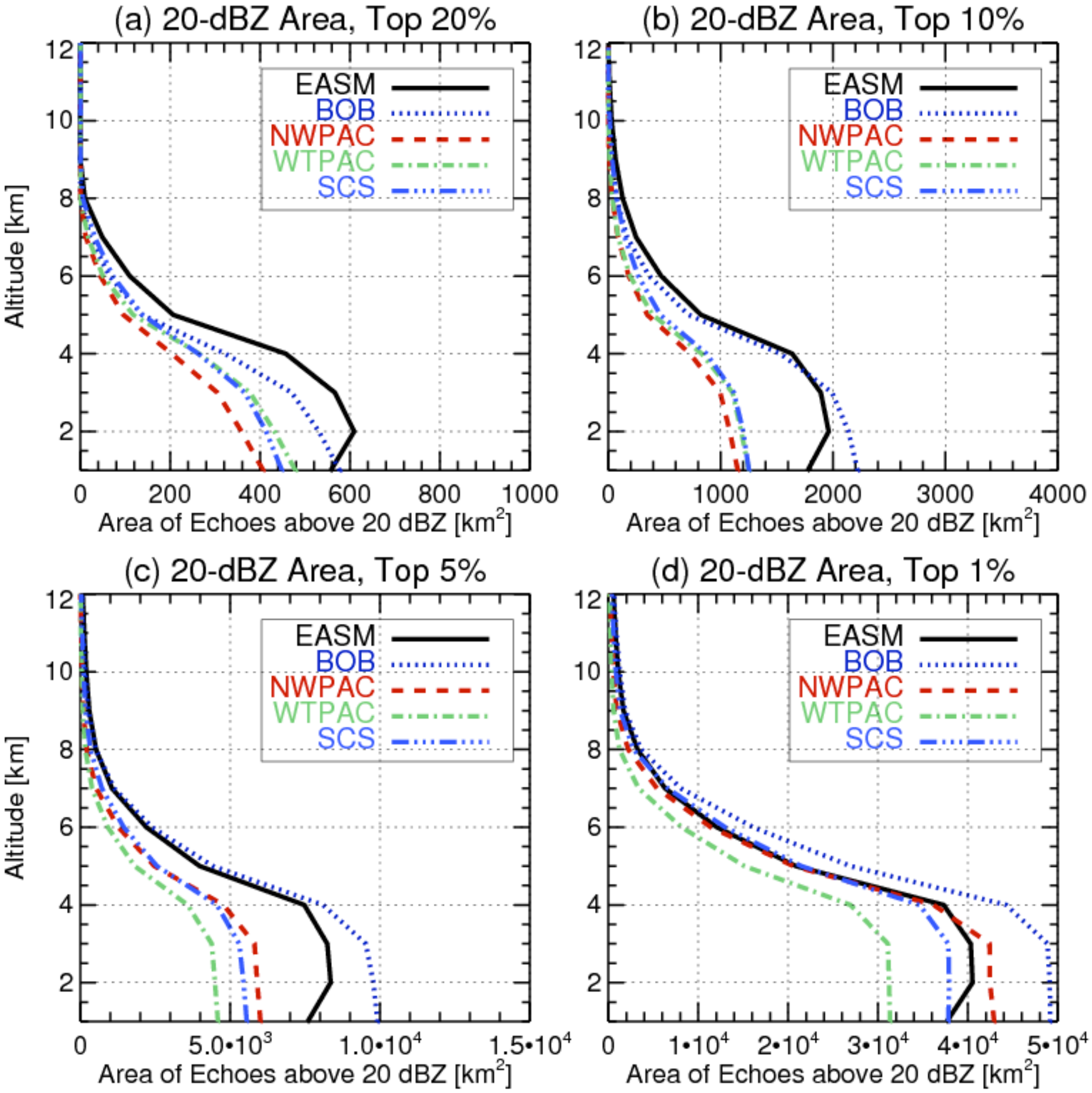

Figure 4.34. Same as Fig. 4.26, but for EASM and some oceanic regimes.

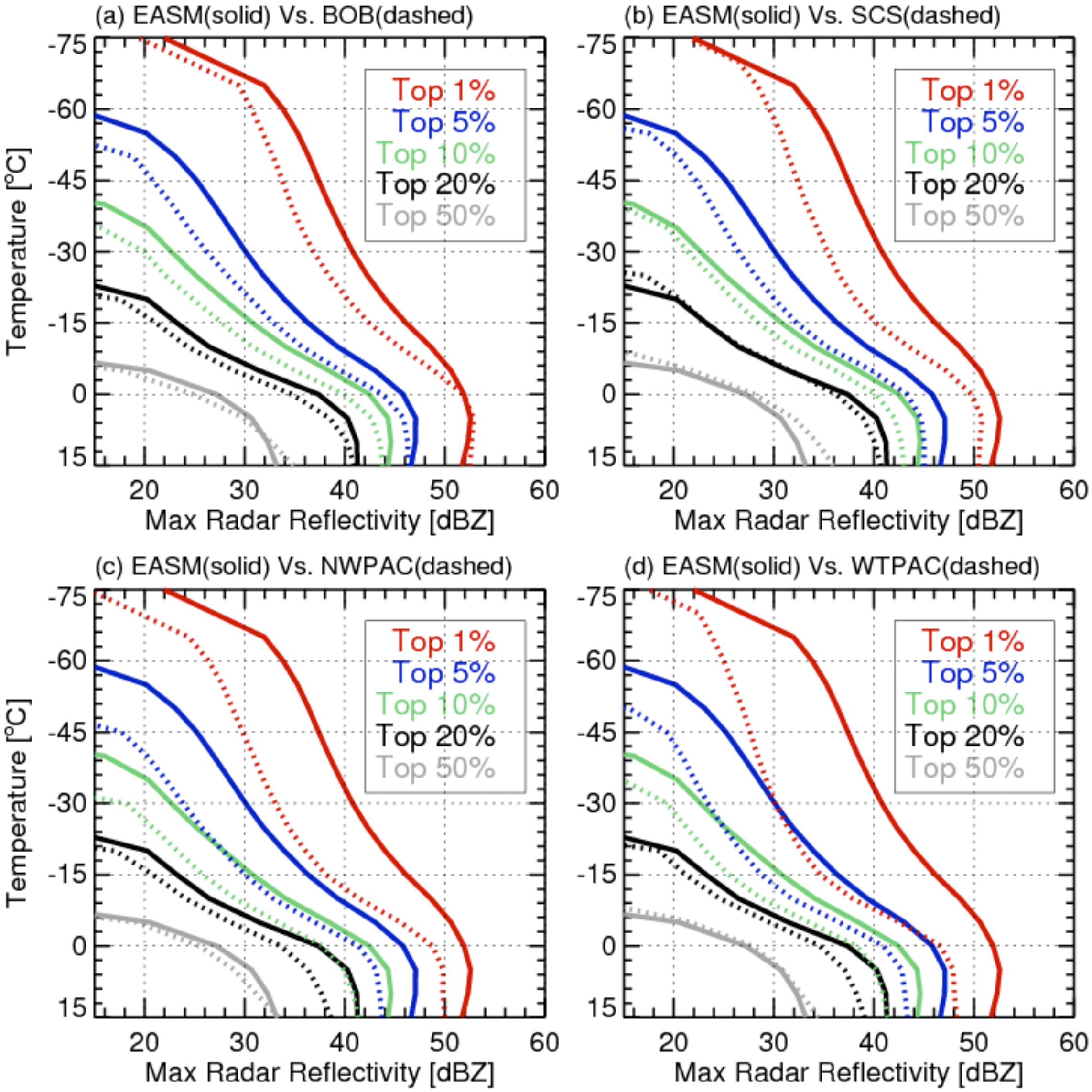

Figure 4.35. Same as Fig. 4.27, but for EASM and some oceanic regimes.

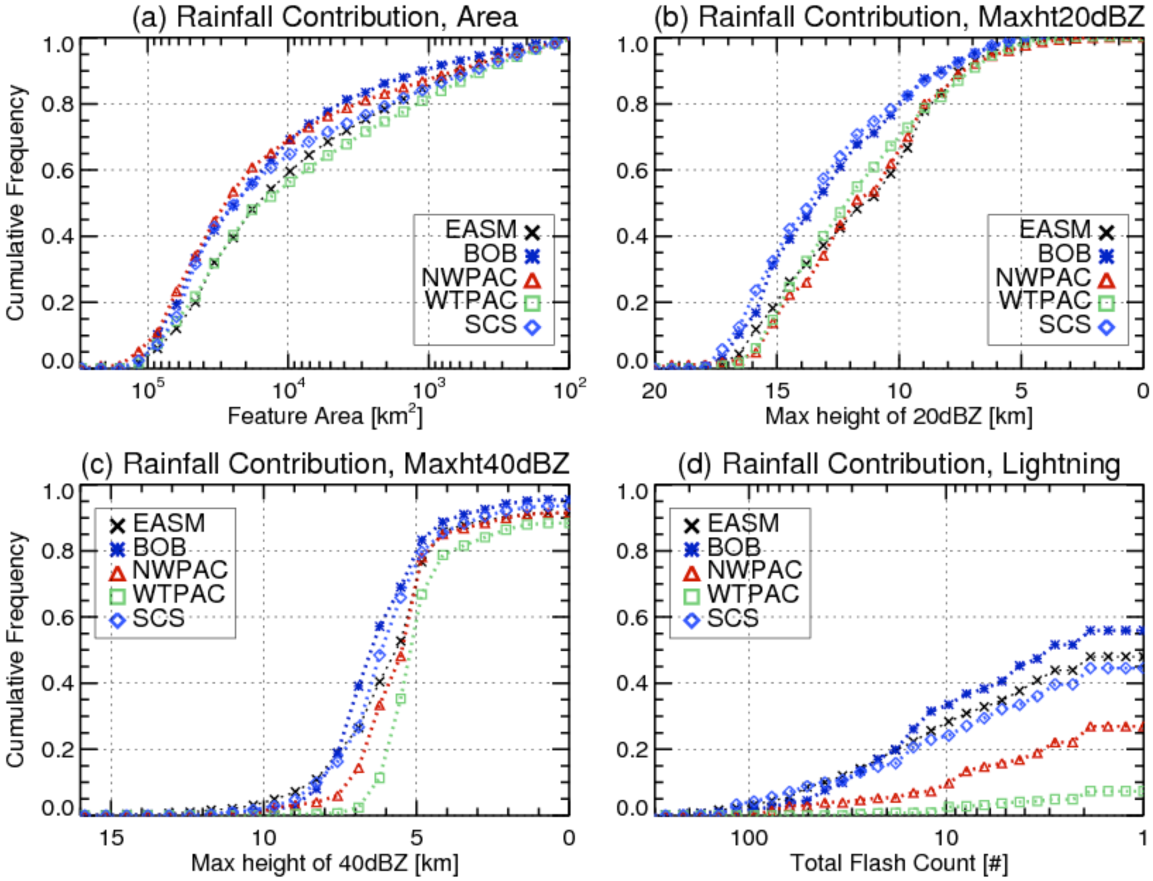

Figure 4.36. Same as Fig. 4.28, but for EASM and some oceanic regimes.

CHAPTER 5

DIURNAL CYCLE

5.1 Background and Introduction

The diurnal cycle of precipitation and convection is one of the most fundamental characteristics of a regional weather regime. It provides an important test for validation of model physics in both weather and climate models (Dai et al. 1999; Lin et al. 2000; Trenberth et al. 2003; Dai and Trenberth 2004). Due to the complex terrain and evident seasonal change of weather regimes (Tao and Chen 1987; Chen 2004; Ding and Chan 2005; Xu et al. 2009), East Asia has been used frequently for investigating diurnal variations of rainfall and convective activities and their underlying physics (summary in e.g., Domros and Peng 1988; Zhao et al. 2005).

Over East Asia, in addition to the widespread afternoon rainfall peak, nocturnal rainfall peaks are often found in the valleys, foothills of high terrain, and over lakes and coastlines due to the low-level convergence by mountain/valley breezes and land/sea breezes (Ohsawa et al. 2001; Fujinami et al. 2005; Hirose and Nakamura 2005; Chen et al. 2005; Li et al. 2008). In addition, eastward phase propagation of precipitation and cloudiness is found downstream of the eastern TP (Asai et al. 1998; Wang et al. 2004, 2005; Yu et al. 2007a; Zhou et al. 2008; Chen et al. 2009). This diurnal phase propagation is similar to that observed leeward of the Rocky Mountains (Wallace 1975; Carbone et al. 2002; Carbone and Tuttle 2008). It is further found that phase propagation of diurnal cycles weakens along with the progress of East Asian Monsoon and almost ceases in the midsummer (Asai et al. 1998; Wang et al. 2005; Chen et al. 2009). Wave-like propagation of afternoon convection, mountain-plain circulation, and nocturnal low-level jet are thought to be possible mechanisms responsible for the propagation and nocturnal rainfall (He and Zhang 2010; Huang et al. 2010).

Most of the above-mentioned papers are focused on diurnal variations of precipitation and cloudiness by using just rain gauge or passive remote sensing observations (e.g., Asai et al. 1998; Wang et al. 2005; Yu et al. 2007a; Chen et al. 2009). Three-dimensional information of storms is never given. It is hard to recognize what kind of storms (vertical structures) mainly contribute to the nocturnal rainfall in those studies. However, diurnal cycles of convection, properties of storms, lightning, and precipitation vertical structures are necessary for better understanding of the underlying physical mechanisms, for evaluating rainfall retrievals, and for physical comparison with model simulations (Nesbitt and Zipser 2003; Hirose and Nakamura 2005; Nesbitt et al. 2008; Liu and Zipser 2008).

The TRMM Precipitation Feature (PF) database combines comprehensive information from the Precipitation Radar, Microwave Imager, and Lightning Sensor together on the storm scale (Nesbitt et al. 2000; Liu et al. 2008a). This database is collocated well enough to investigate the phase difference between diurnal cycles of precipitation, deep convection, shallow convection, MCSs, and lightning (Nesbitt and Zipser 2003; Liu and Zipser 2008). It is now possible to measure how the vertical structure of precipitating systems varies diurnally by this database (Liu and Zipser 2008; Liu et al. 2008b). Furthermore, this feature-based database provides unique insights into the phase propagation of the diurnal cycle from the perspective of precipitating storms.

Starting from that point, this study seeks to answer the following motivating questions: (1) Is there any phase propagation of diurnal variations of precipitating storms downstream from the Eastern TP and how does it vary seasonally? (2) What are the phase differences among diurnal cycles of precipitation, deep convection, and lightning, and how do these change seasonally? (3) How does the precipitation vertical structure vary diurnally? (4) What are the possible mechanisms responsible for the phase propagation and nocturnal rain/convection?

As has been shown in previous chapters, the most evident seasonal change in large-scale circulation and rainfall pattern happens with the onset of Mei-Yu over South China and Taiwan. After the onset of Mei-Yu, deep southwesterlies from the tropics prevail over southern China and rainbands associated with the Mei-Yu front occur frequently. The convection intensity and storm properties of Mei-Yu systems also vary from those of before onset. The monsoon rain belts further progress to Central China and the Yangtze River region but monsoon circulation weakens in the midsummer. This study focuses on the region of the eastern TP and continent downstream in different seasons: before the onset of Mei-Yu, Mei-Yu season in both South China and the Yangtze River, and midsummer. Methods for selecting samples and analyzing diurnal features are described in Chapter 2. Samples of precipitation features are listed in Table 5.1, while parameters are defined in Table 5.2.

5.2 Diurnal Variations of Different Types of Storm

5.2.1 Downstream Phase Propagation

[In this Chapter, phase propagation refers to the apparent total phase speed in the zonal direction, without implying anything about storm propagation with respect to the wind at any level.]

Generally, diurnal cycles of storm population and precipitation are dominated by afternoon maxima over high terrain, but in some seasons and locations exhibit a phase delay, moving eastward into the lowlands, resulting in nocturnal maxima, except in midsummer (Fig. 5.1-5.3). This confirms findings based on GMS retrievals by Asai et al. (1998) and Wang et al. (2005), and is similar to the phase propagation east of the Rocky Mountains during the warm season (Carbone et al. 2002). Another general feature is that the phase propagation is most evident in strip2 in Fig. 5.1b and 5.2b, regions D and E during Premeiyu and Mei-Yu, but disappears in midsummer (Fig. 5.3b).

5.2.2 Phase Differences

The interpretation of the Hovmoller diagrams (Fig. 5.1-5.3) showing phase propagation (or not) in certain locations and seasons can be clarified by also showing the diurnal cycles of precipitation feature number, total rainfall, MCS number, flash counts, and deep convection, all shown in Fig. 5.4-5.6. Samples of each region in different periods are shown in Table 5.1, while definitions of specific parameters are listed in Table. 5.2. There are too many interesting details to describe in this section, so the following discussion is confined to the regimes that seem least ambiguous.

Before discussing the phase propagation (or its absence) in detail, we examine the relatively simple situation on the Tibetan Plateau (regions A and D). In all 3 seasons, these two regions have strong afternoon maxima of PF number, lightning flash counts, and deep convection, followed some hours later by maxima of MCS number and total rain (Figs 5.4ad, 5.5ad, 5.6ad). This common sequence of events is strong evidence of the well-known local control of convection over the TP rather than large scale dynamics (Uyeda et al. 2001; Qie et al. 2003). The time lag is reasonable for organization of local convection into larger mesoscale systems, from which both convective and stratiform rain may fall for several hours.

The Sichuan Basin has marked phase propagation during Premeiyu and Mei-Yu (Figs. 5.4e, 5.5e), all but disappearing in midsummer (Fig. 5.6e). However, the specific sequence of peaking of each parameter is difficult to interpret in detail. The only clear result is that during Premeiyu and Mei-Yu, consistent with the notion of phase propagation of mesoscale phenomena eastward from the TP, all measures have nocturnal maxima, but not as sharp as those seen during the afternoon on the TP. The contrast in midsummer is striking (Fig. 5.6e). While there is no evident phase propagation in the total number of PFs (Fig. 5.3e), which actually have a weak afternoon maximum that suggests some locally generated convection, there are nocturnal maxima of deep convection, lightning and early morning maxima of MCSs and total rain, suggesting that both deep convection and mesoscale systems have a mechanism favoring nocturnal generation in the Sichuan Basin.

5.2.3 Diurnal Cycles of Different Vertical Structures

A great advantage of the TRMM Precipitation Radar data, in spite of the large attenuation at their 2 cm wavelength, is their ability to reveal vertical profiles of radar reflectivity, especially in the upper troposphere. If the attenuation correction (Iguchi et al. 2000) is applied through a large depth of strong echo, their accuracy does suffer, but the height reached by the 20 dBZ echo is not affected. Here, we construct relative frequency of radar echo area >= 20 dBZ at each altitude over selected regions and seasons (Figs 5.7 and 5.8).

Over the Sichuan Basin (box E), consistent with previous findings, extremely deep convection with 20 dBZ to 14 km exists from 00-06 LT during Premeiyu (Fig. 5.8a). But during Mei-Yu and midsummer, the data reveal a very different diurnal cycle of vertical structure. The first part of the early morning maxima still extends up to 15 km but apparently evolves from an earlier (18-21 LT) peak. The second part of the early morning peak (03-06 LT) only goes up to 10 km during Mei-Yu and to 8 km during midsummer, perhaps indicating a predominance of decaying MCSs and stratiform rain, consistent with Fig. 5.6e.

Box G demonstrates a completely different situation. In all 3 seasons, there is a prominent late afternoon and evening peak of extremely deep radar echo, consistent with Figs. 5.4g, 5.5g, and 5.6g, and their lightning peaks, while much lower echo tops occur during early morning.

The diurnal cycles of radar echo structure downstream of the above regions (box F and H) are different from E and G, but do not present any clear phase propagation from upstream. Multiple maxima are observed except during midsummer, when the afternoon peak of very deep echo dominates. In all seasons, region F has an early morning peak with shallow echo tops, which, together with the morning rainfall maxima in Figs. 5.4f, 5.5f, and 5.6f, implies a role for decaying MCSs with stratiform rain. Region H has a complex structure in the Premeiyu, evolving toward a simple domination of an afternoon maximum in midsummer, also shown in Figs. 5.4h, 5.5h, and 5.6h.

5.3 Nocturnal versus Afternoon Peaks

5.3.1 Spatial Distribution of Rainfall

As mentioned above, MCS population and total PR volumetric rain have nocturnal peaks over the foothills of the TP and over central eastern China in certain seasons. Spatial distribution of nocturnal rainfall based on TRMM 3B42 rainfall data (Fig. 5.9) is quite consistent with the above findings and with previous studies (Yu et al. 2008; Li et al. 2008). During Premeiyu, there is a band-shaped nocturnal maximum extending from the Sichuan Basin to the coast. In contrast, afternoon rainfall maxima exist along and within 500 km of the coast of south and central China, with a prominent minimum in the Sichuan Basin. The east-west nocturnal rainfall center may be related to the propagation of precipitation systems downstream of the eastern TP as demonstrated previously.

The band-shaped nocturnal maximum downstream of the eastern TP is less evident during Mei-Yu and disappears in midsummer. Nocturnal rainfall maxima still appear over the south and southeast foothills of the TP, but closer to the foothills. The spatial pattern of afternoon rainfall is quite similar in Mei-Yu and midsummer, except that significant rainfall extends northward and spreads through all of eastern China, while the afternoon minimum persists in the Sichuan Basin.

5.3.2 Distribution of PFs and Lightning Features

Spatial distributions of the occurrence of precipitating features in 2330 – 0530 vs. 1130 – 1730 LT during different seasons are presented in Fig. 5.10. Fig. 5.11 shows the distribution of PFs by numbers of lightning flashes during selected periods in different seasons but with the same total PF population. Over the TP, afternoon storms dominate in every season, similar to the classic diurnal characteristics over high terrain (Fig. 5.10).

In the foothills of the southeastern TP and eastward for 1000 km, higher percentages of nocturnal PFs occur especially during the Premeiyu. Many of these nocturnal precipitation features have lightning of moderate to high flash rate, indicating either intense convection, or large mesoscale convective systems, or both. But during Mei-Yu, this nocturnal peak is less obvious. Lightning downstream of the TP is even less frequent in the afternoon during Mei-Yu than nocturnal lightning during Premeiyu. This seasonal difference in lightning activity has been described in Xu et al. (2010) and is consistent with their finding of higher radar reflectivity from the TRMM PR in the mixed-phase region.

5.4 Discussion about Phase Propagation and Nocturnal Peak

Previous sections show that the nocturnal and afternoon peaks of rainfall and other parameters show both different seasonal and geographic distribution. Here, we ask how the seasonal changes in zonal wind profile and the diurnal cycle in the low-level flow field may help explain the more striking features of the rainfall cycle, most notably, the dominance of nocturnal rainfall in the Sichuan Basin.

5.4.1 Phase Propagation and Zonal Wind Profile

The most obvious phase propagation has been shown to be in strip2, the latitude belt from 28 – 32° N extending from the high TP through the Sichuan Basin and eastward. Figure 5.12 shows the mean zonal wind profile for the region of strongest phase propagation for each season. Both Premeiyu and Mei-Yu have substantial zonal wind components above the 700 hPa level, as well as strong wind shear, especially in Premeiyu. In midsummer, the mean zonal wind in this belt essentially disappears.

Carbone et al. (2002) and others have demonstrated a recurrent pattern of phase propagation of rainfall maxima in the central United States downstream of the Rocky Mountains, related to the maintenance of deep convection and mesoscale systems, initially phase locked to afternoon convection over the Rockies, resulting in nocturnal maxima well downstream, moving in the general direction of “steering level winds” near 700 hPa, but typically about 8 m s^{-1} faster. It is well beyond the scope of this paper to distinguish between the many possible reasons for a specific speed with respect to the wind at any particular level. But we do note that the wind profile in and east of the Sichuan Basin (Fig. 5.12) is fairly close to that of Carbone et al. (2002). Further, the observed phase propagation in the Sichuan Basin is about 15 m s^{-1} and 12 m s^{-1} in Mei-Yu (from Fig. 5.1e, 5.2e) compared with the 14 m s^{-1} of Carbone et al. It is an open question whether our results should be interpreted as having a phase speed 10-12 m s^{-1} faster than our 700 hPa wind, or whether our “steering level winds” should be taken closer to 600 hPa (the TP is higher than the Rocky Mountains), in which case our results also imply a phase speed about 8 m s^{-1} faster.

5.4.2 Nocturnal Peak and Low-level Winds

Despite the rather coarse 1.5° resolution of the Interim ERA reanalysis data used in this paper, the changes between the 18 UTC (01 LT) and 06 UTC (13 LT) low-level wind field are sufficiently large to help explain the diurnal cycle of observed rainfall and precipitation systems. Figure 5.13 shows the west-east vertical cross-section of zonal winds through the center of the Sichuan Basin for each season. Figure 5.14 shows the wind fields for 01 and 13 LT at 850 hPa for a region that includes the Sichuan Basin, while Figure 5.15 shows the anomaly wind fields from the seasonal mean.

Above 700 hPa, there is little change in the tropospheric zonal wind profile between 01 and 13 LT, but there is a large change in the low-level winds. Specifically, the low-level easterly flow near 850 hPa converges in the center of the Sichuan Basin at 01 LT in all seasons, near 105 E, but at 13 LT in all seasons, that convergence is along the slope of the Tibetan Plateau near 103 E. This convergence of about 1 m s^{-1} may seem small, but it is consistent with rising motion on the slopes during the afternoon, and rising motion in the center of the basin during the night. Using the slightly better resolution of 1.0° of the NOAA Global Forecast System (GFS), He and Zhang (2010) demonstrated a very similar magnitude of diurnal wind change, consistent with a similar phase propagation and diurnal cycle of rainfall along the terrain slope in northern China.

Several authors (including Carbone et al. 2002 and He and Zhang 2010) have pointed to the existence of a nocturnal low-level inflow of moist air that may assist the formation and maintenance of nocturnal precipitation in many regions of the world. The anomaly wind field in this case (Fig. 5.15) supports this interpretation in the Sichuan Basin as well. In all 3 seasons, the 850 flow changes from southerly to northerly with a vector change of about 3 m s^{-1} between 01 and 13 LT. In addition, the change from convergence to divergence between 01 and 13 LT is obvious, and of at least as large a magnitude as shown by He and Zhang (2010) for their study region in northern China (their Fig. 5). While the absolute wind speeds hardly qualify for the label "low-level jet" in the seasonal mean, the low-level flow change is consistent with a more favorable flow of potentially unstable air into the Sichuan Basin at night.

5.5 Summary and Conclusions

The principal findings of this study include the following:

(1) There is a phase propagation of diurnal cycles of precipitating storms, total rainfall, convection, and lightning from the foothills of the eastern TP downstream, most evident over the Sichuan Basin during Premeiyu and Mei-Yu seasons, absent during midsummer, and consistent with lack of zonal winds and zonal shear during midsummer;

(2) Before midsummer, the eastern TP foothills are dominated by nocturnal rainfall, but the early morning peak of precipitation is only in phase with deep convection, MCSs, and lightning during Premeiyu;

(3) Most of the nocturnal precipitation is in phase with MCSs and possibly contributed by long-lived MCSs evolving from late afternoon or early night convection, but these early morning MCSs show larger percentages of deep convection in Premeiyu;

(4) In midsummer, most of East Asia is dominated by afternoon precipitation and convection, with the Sichuan basin and the northern part of eastern China as the exception where early morning rainfall prevails, in spite of most deep convection and lightning occurring during the afternoon;

(5) In all the seasons, there is a strong diurnal cycle of low-level convergence and southerly flow into the Sichuan Basin at night, consistent with the nocturnal maximum of rainfall, while divergence during the day is consistent with a marked rainfall minimum.

Table 5.1. Samples of precipitation features in three latitude strips: strip1 (32^{o}-36^{o} N), strip2 (28^{o}-32^{o} N), strip3 (23^{o}-28^{o} N), specifically, 8 boxes (Fig. 2.6).

Region	Strip1: (32-36 N)			Strip2: (28-32 N)			Strip3:(23-28 N)	
Season	A	B	C	D	E	F	G	H
Premonsoon	4808	4747	3781	6694	4507	41559	3256	4576
Mei-Yu	11761	6724	4035	9797	5266	4048	5352	5526
Midsummer	17127	10509	9074	15862	7160	5404	6949	5390

Table 5.2. Definitions of parameters selected for the study of diurnal variations.

Parameter Name	Definition
PF Num	Population of precipitation features defined by grouping PR pixels (Nesbitt et al. 2000; Liu et al. 2008).
MCS Num	Population of MCS defined by PFs with area > 2000 km^2 having at least 1 convective pixel (Houze 1993).
Total rain	Volumetric near surface rainfall retrieved from PR (Iguchi et al. 2000).
Deep Convec	Area of deep convections with PR 20-dBZ at 12 km (similar to Liu and Zipser 2008).
Flash Counts	Total flash counts within all the selected PFs detected by LIS (Cecil et al. 2005).

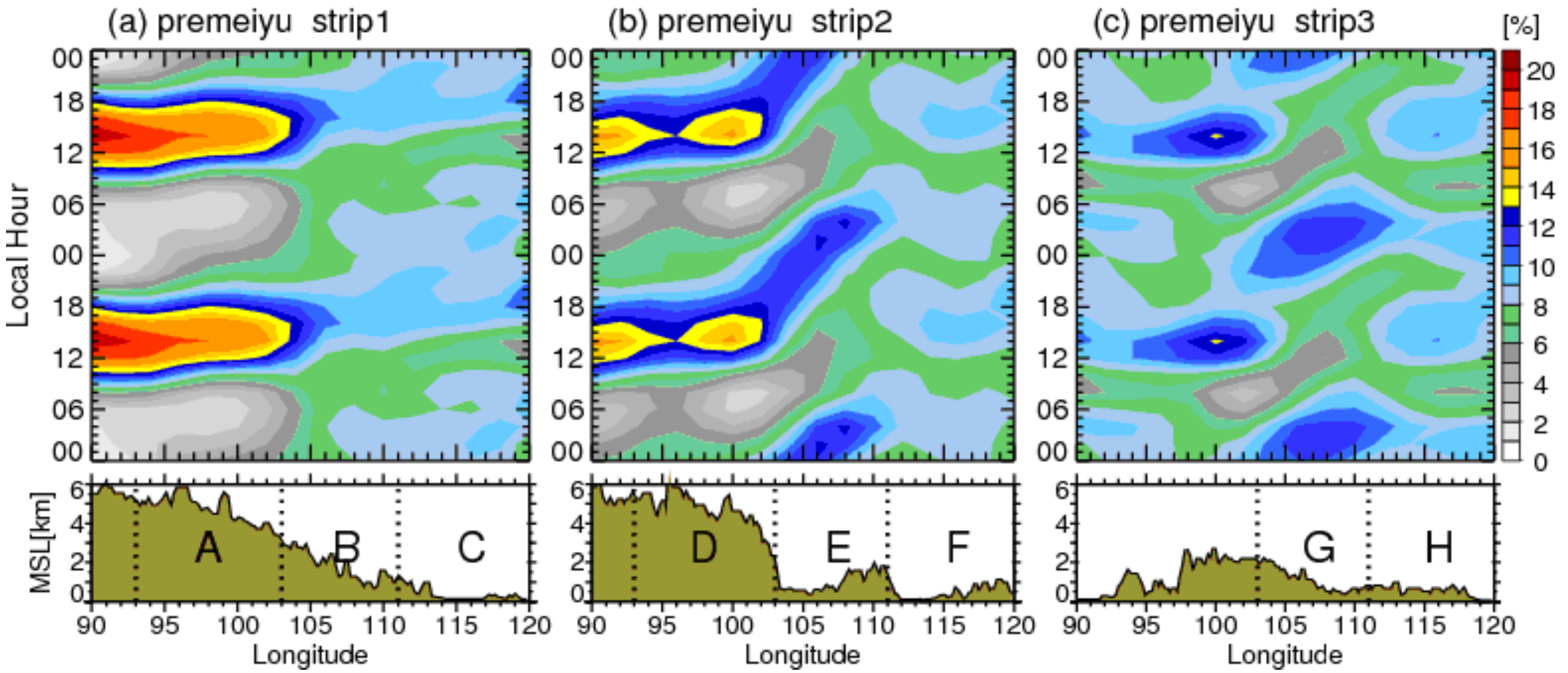

Figure 5.1. Hovmöller diagram of population of precipitation features during premeiyu over different strips: (a) strip1, (b) strip2, and (c) strip3. Bottom panel shows the elevation along the longitude of each strip.

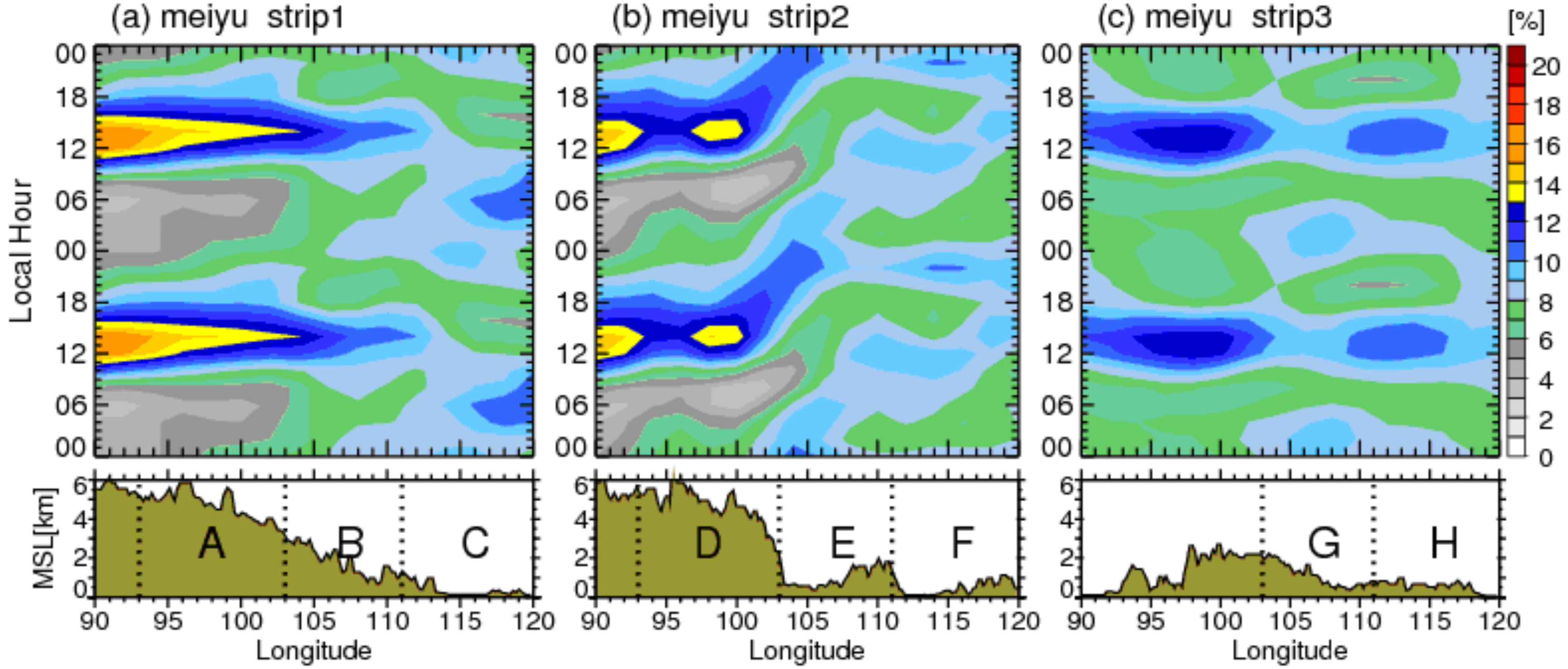

Figure 5.2. Same as in Fig. 5.1, but for Mei-Yu season.

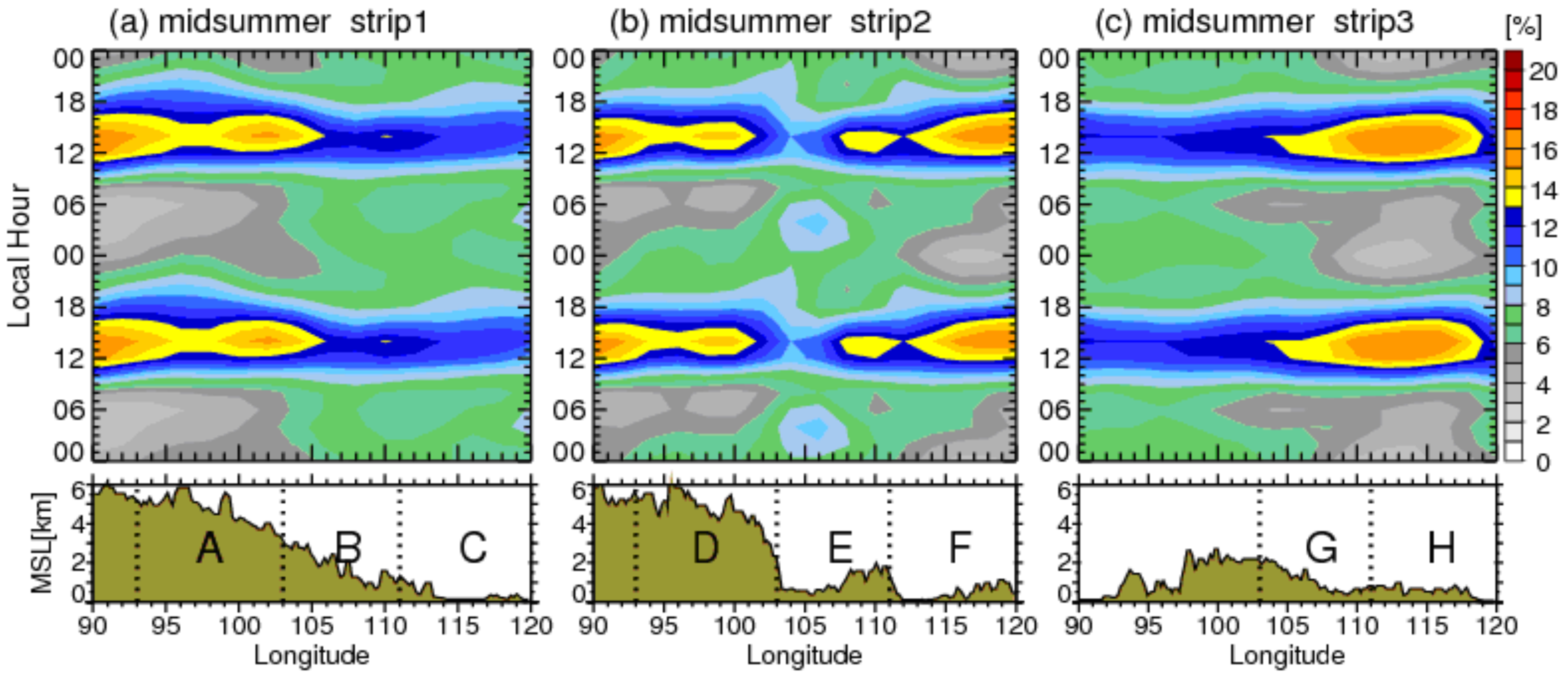

Figure 5.3. Same as in Fig. 5.1, but for midsummer season.

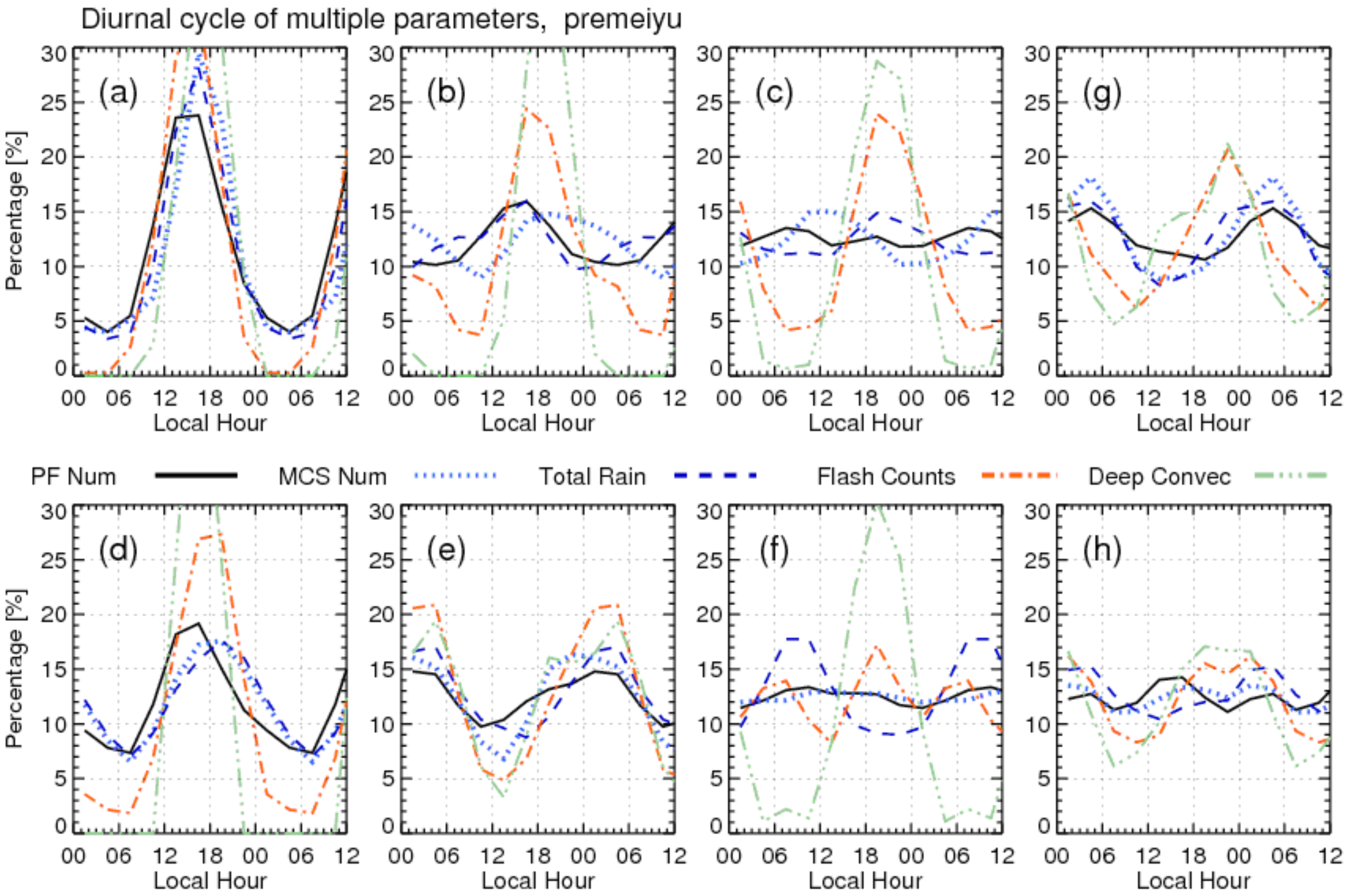

Figure 5.4. Diurnal variations of multiple parameters in premeiyu over different regions: (a)-(h) represents region A to H shown in Fig. 2.6 (marked by capital characters), separately.

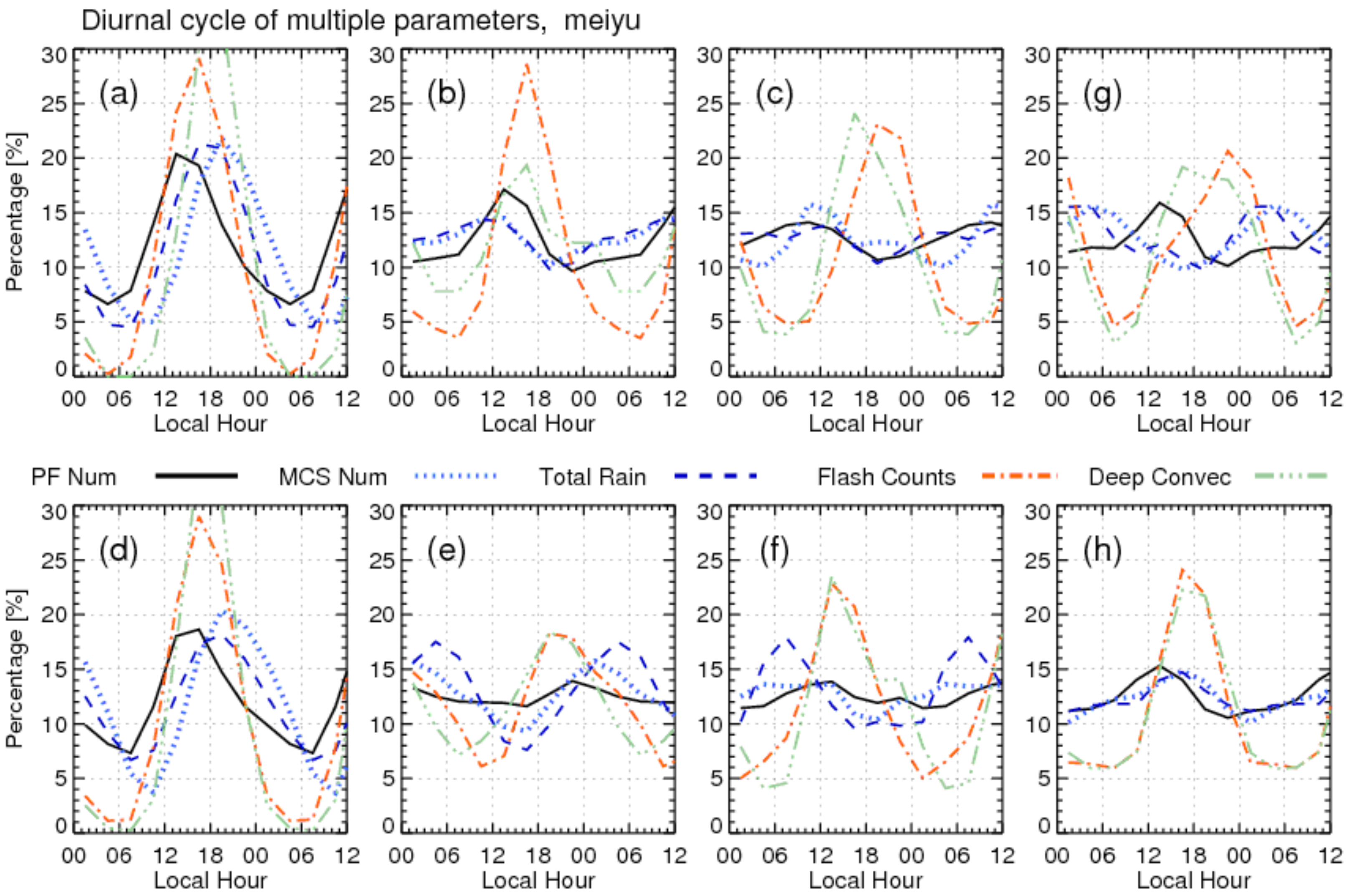

Figure 5.5. Same as Fig. 5.4, but for the meiyu season.

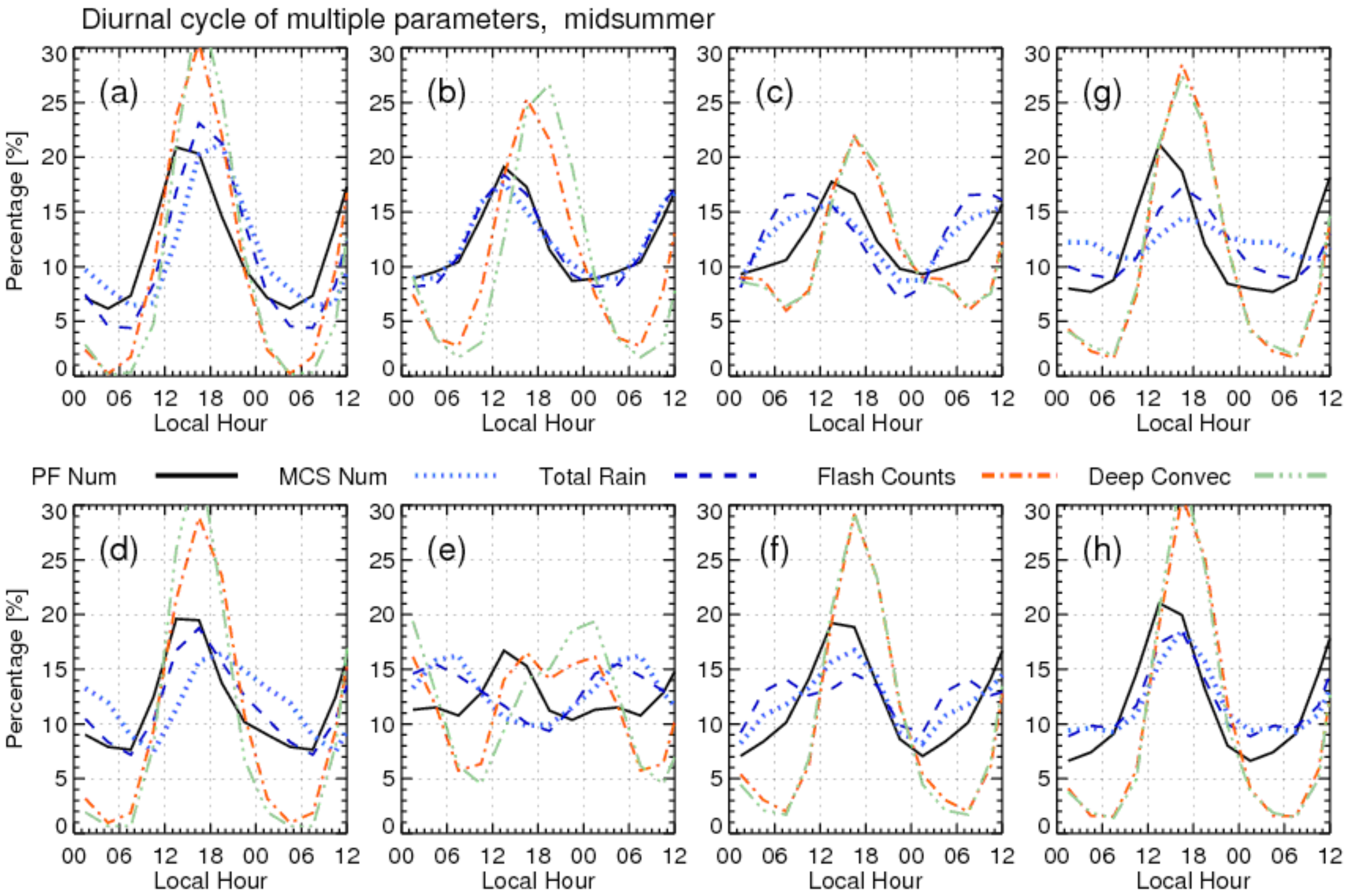

Figure 5.6. Same for Fig. 5.4, but for midsummer season.

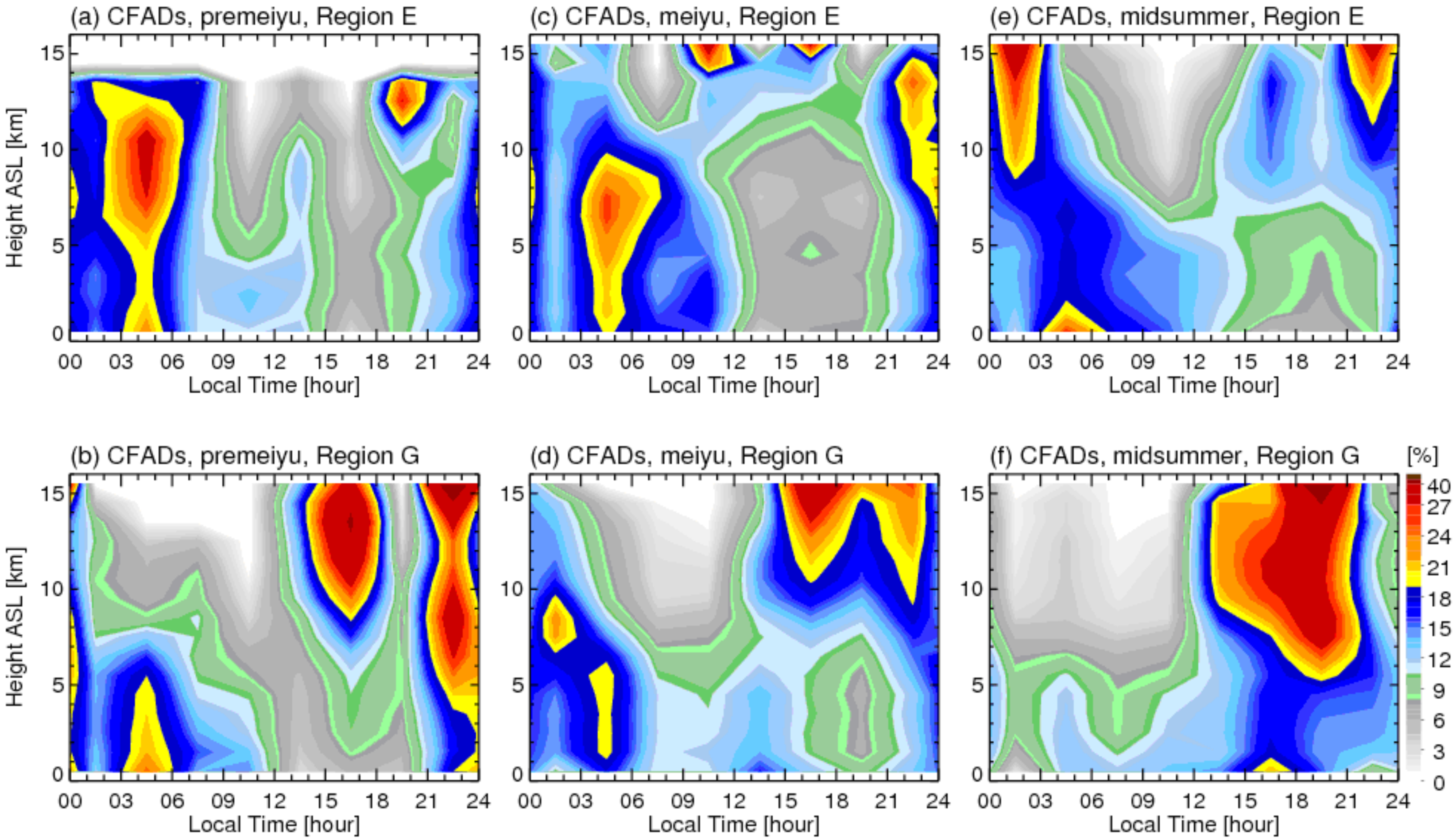

Figure 5.7. Contoured frequency by altitude diagrams (CFADs) of area with PR reflectivity greater than or equal to 20 dBZ with altitude vs. time over (a)-(c) region E, (d)-(f) region G, during premeiyu (left column), meiyu (central column), and midsummer (right column).

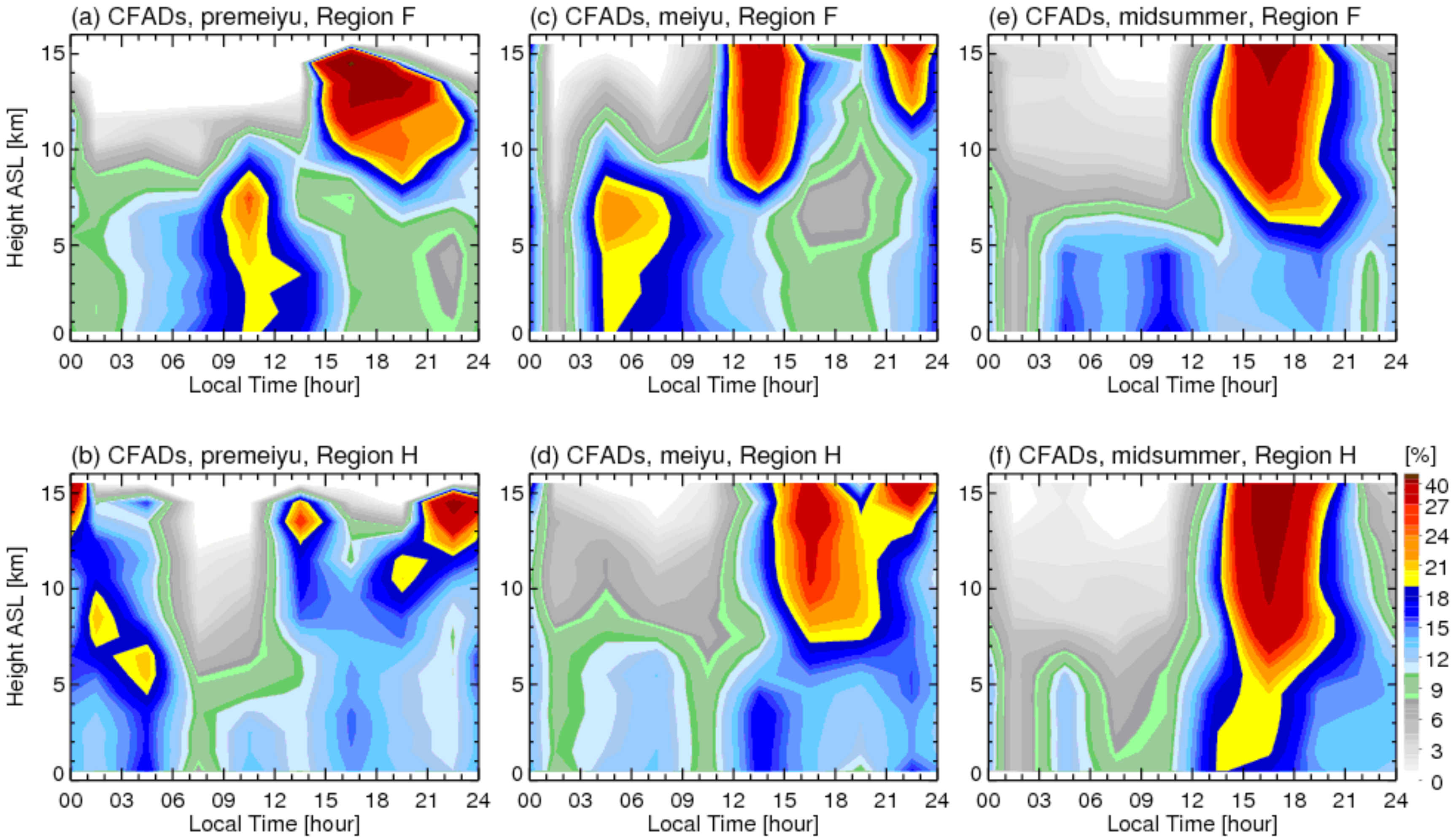

Figure 5.8. Same as in Fig. 5.7, but for region F (a)-(c), and region H (d)-(e).

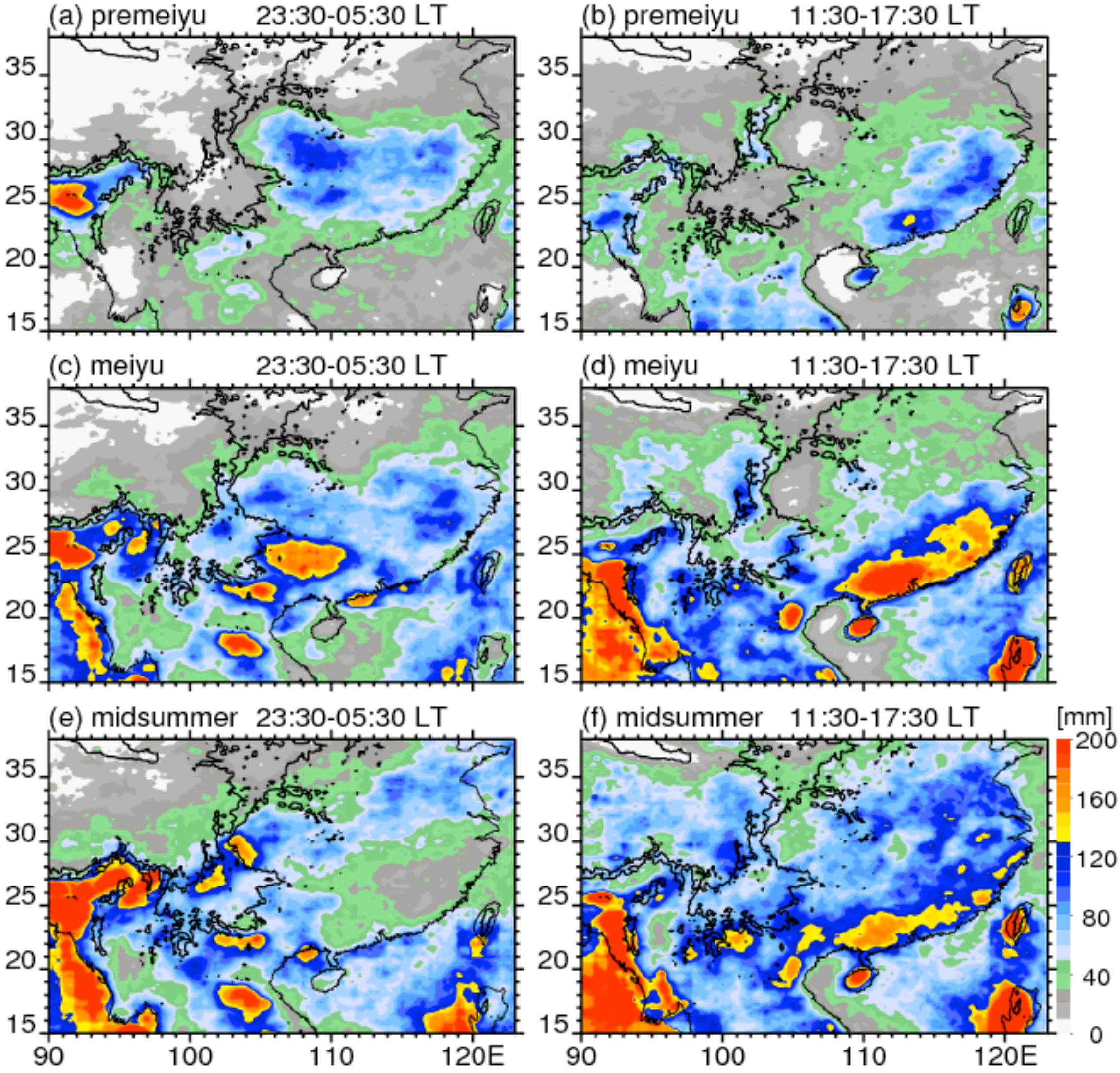

Figure 5.9. 3B42-based seasonal total rainfall in mm occurring in midnight/early morning (23:30-05:30 LT; left column) and afternoon (11:30-17:30 LT; right column) during (a)-(b) premeiyu, (c)-(d) meiyu, and (e)-(f) midsummer.

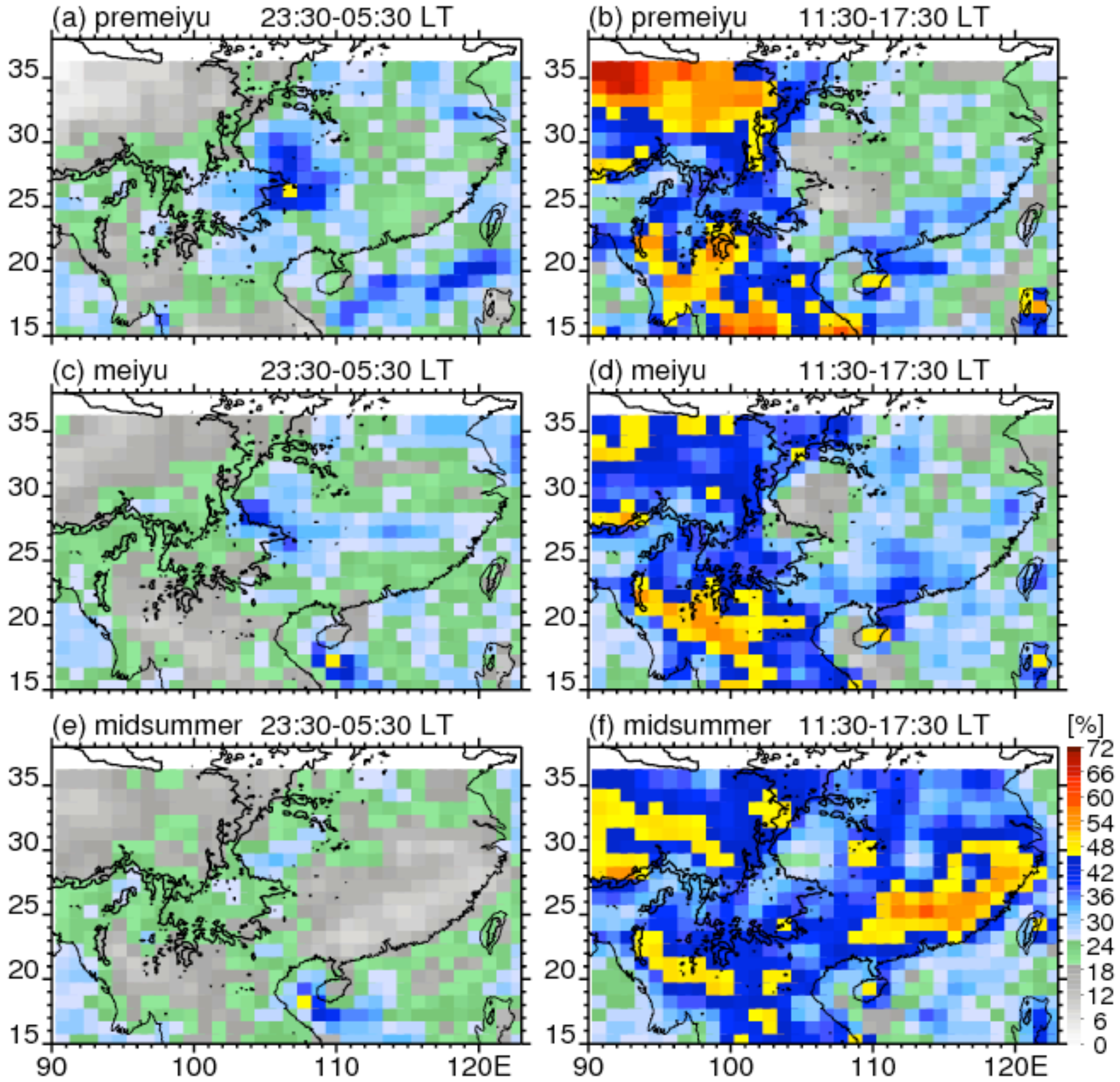

Figure 5.10. Percentage of precipitation features to the total PFs occurring in a 1^o by 1^o box during midnight/early morning (23:30-05:30 LT; left column) and afternoon (11:30-17:30 LT; right column) during (a)-(b) premeiyu, (c)-(d) meiyu, and (e)-(f) midsummer.

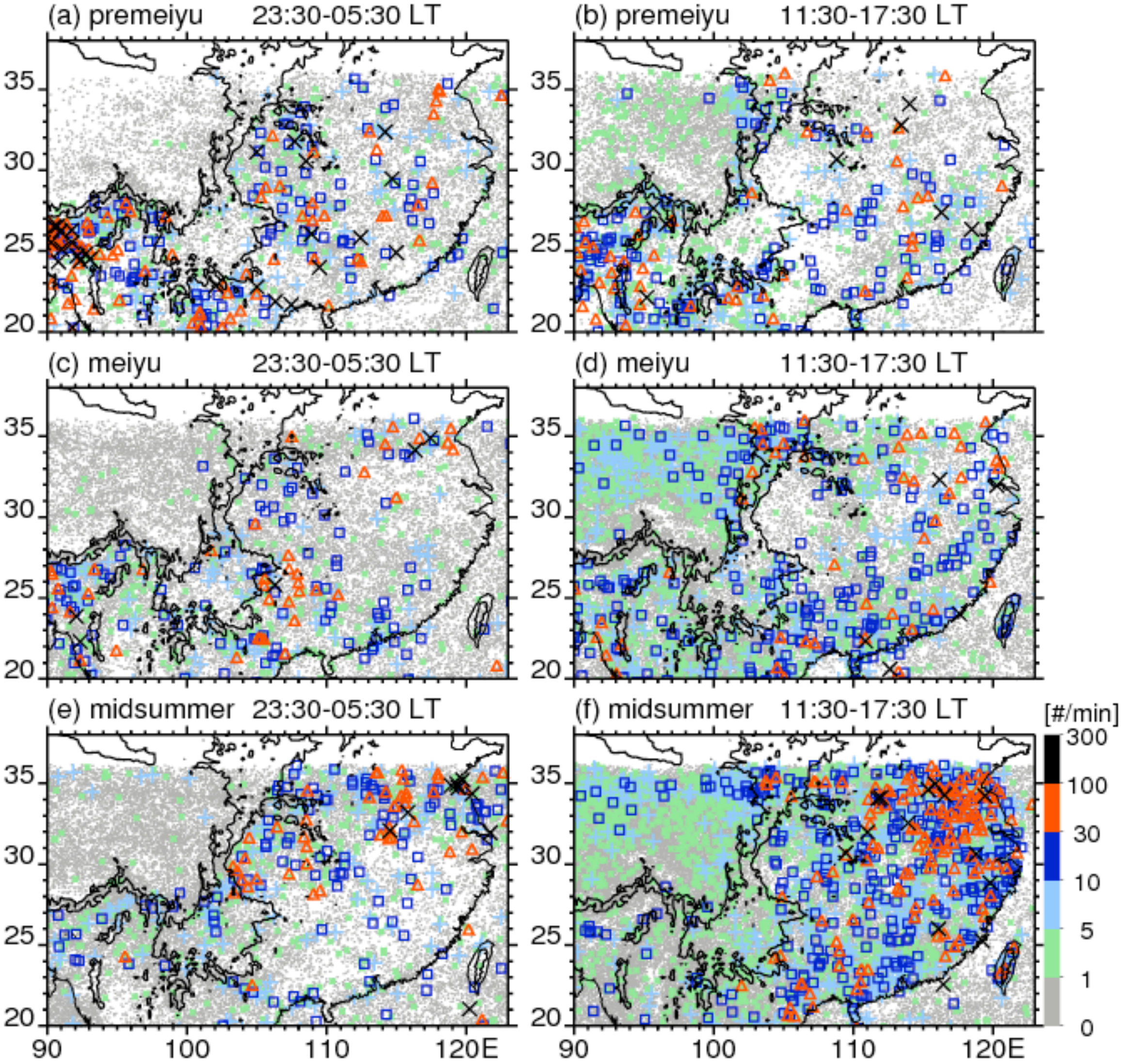

Figure 5.11. Distribution of precipitation features categorized by lightning flash rate occurring in midnight/early morning (23:30-05:30 LT; left column) and afternoon (11:30-17:30 LT; right column) in (a)-(b) premeiyu, (c)-(d) meiyu, and (e)-(f) midsummer. Values of markers in different colors are consistent with the color bar.

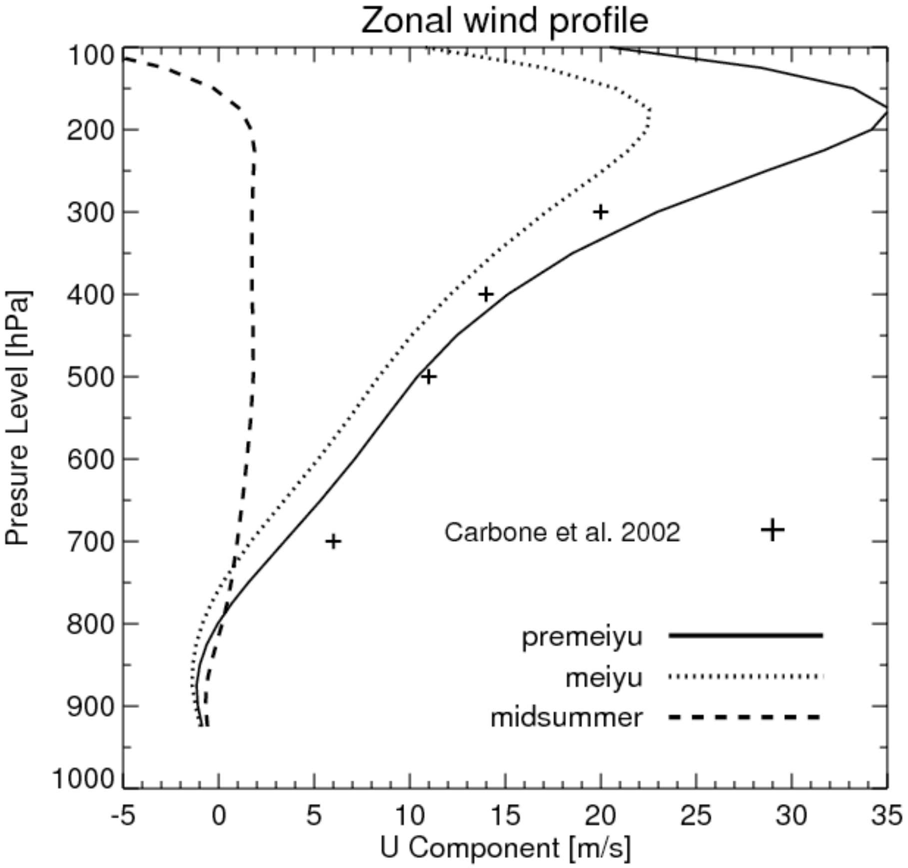

Figure 5.12. Vertical profile of mean zonal wind fields over region (28-32 N; 105-115E) during Premeiyu, Mei-Yu, and midsummer in 1998-2008. The (+) marker indicates the data points from Carbone et al. 2002 over the United States.

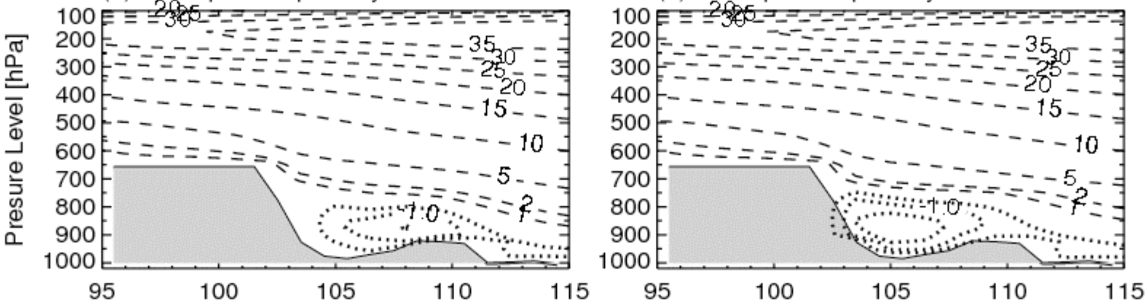

(a) U component, premeiyu, 01 LT

(b) U component, premeiyu, 13 LT

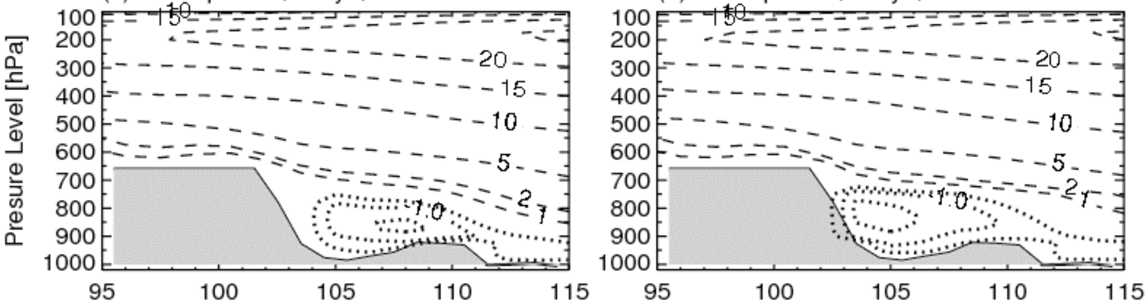

(c) U component, meiyu, 01 LT

(d) U component, meiyu, 13 LT

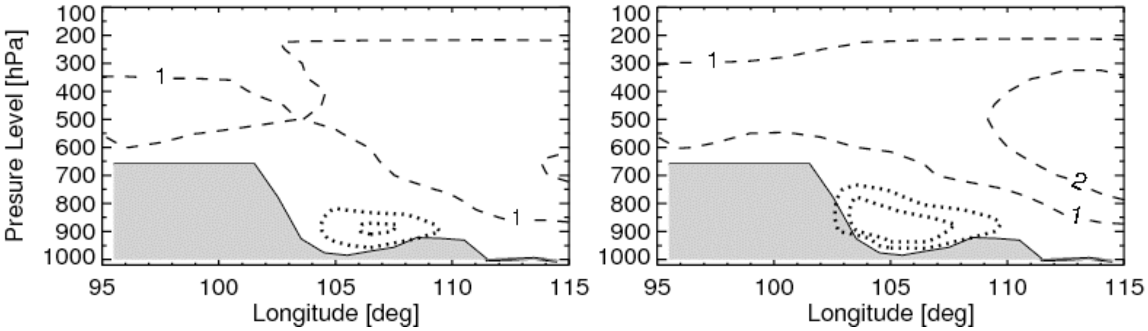

(e) U component, midsummer, 01 LT

(f) U component, midsummer, 13 LT

Figure 5.13. Cross-section of mean zonal wind speed in m s^{-1} (dashed is positive, dotted is negative with interval of -0.5 m s^{-1}) along the latitude of 29-30N, during Premeiyu, Mei-Yu, and midsummer in 1998-2008. The left panel shows data for 01 LT and right panel shows data for 13 LT.

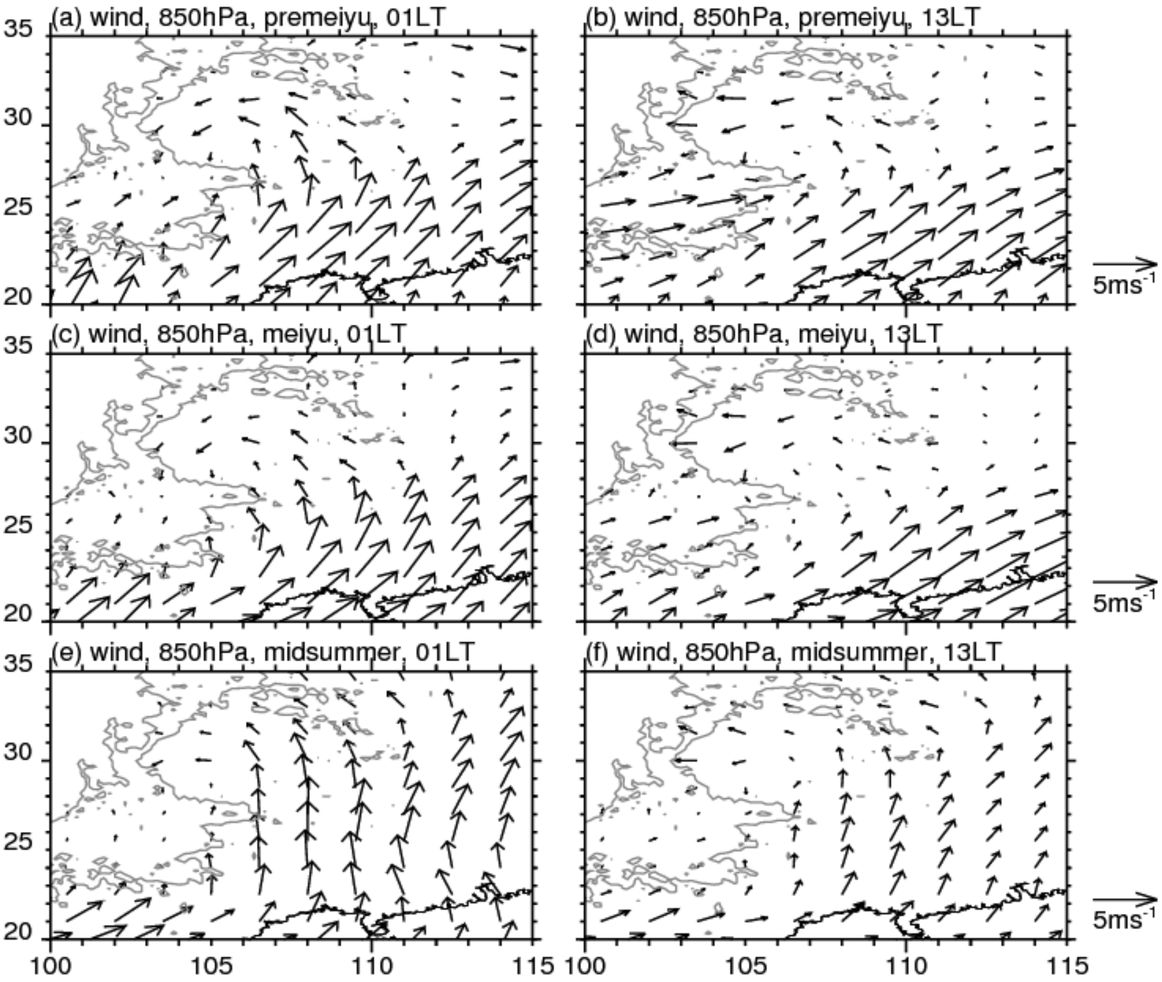

Figure 5.14. Horizontal wind field at 850 hPa during Premeiyu, Mei-Yu, and midsummer in 1998-2008. The left panel shows the wind field in the 01 LT and right panel shows winds at 13 LT. Wind speed is indicated by the arrow on the right side of the figure.

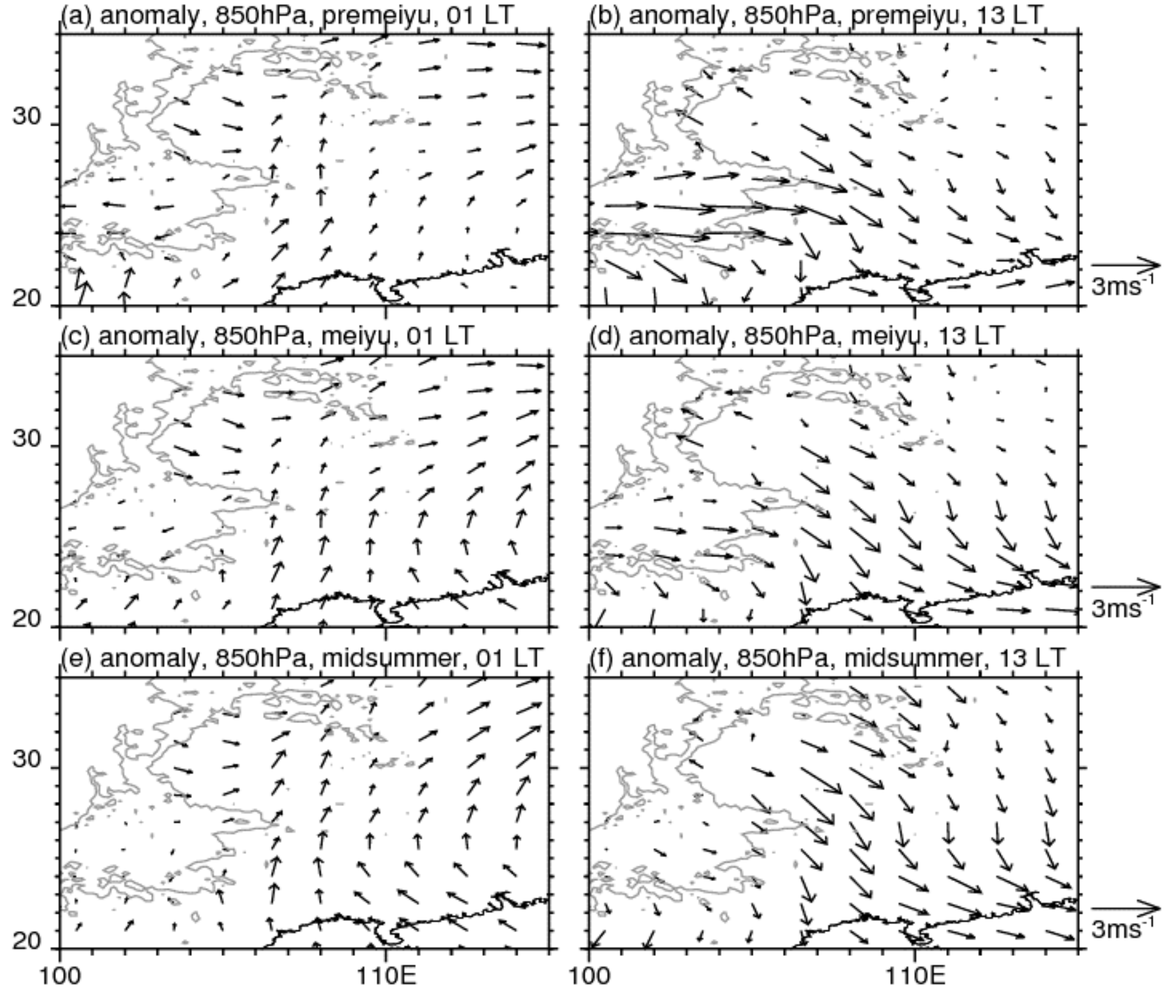

Figure 5.15. Anomaly wind fields at 850 hPa during Premeiyu, Mei-Yu, and midsummer in 1998-2008. The left panel shows the anomaly in the 01 LT and right panel shows the anomaly at 13 LT. Wind speed is indicated by the arrow on the right side of the figure.

CHAPTER 6

HEAVY RAINFALL OBSERVED OVER SOUTHWEST TAIWAN

6.1 Background and Introduction

Based on TRMM-observed results shown in previous chapters, it is very clear that precipitation systems of EASM are intermediate in proxies of convective intensity between the stronger convection over nonmonsoonal continents, and the weaker convection over oceans, while convective properties of active Mei-Yu storms over South China and Taiwan are slightly closer to those of tropical ocean convection. Similar differences on convective structures among continental, monsoon, and oceanic systems in the tropics, or among different meteorological forcing within the same weather regime, were pointed out by many others (Williams et al. 1992; Zipser and Lutz 1994; Petersen and Rutledge 1998; Nesbitt et al. 2000; Toracinta and Zipser 2000; Petersen et al. 2001; Cifelli et al. 2002). Tropical convection was typically separated into two classic regimes: continental and maritime (Zipser and Lutz 1994; Rosenfeld and Lensky 1998; Petersen and Rutledge 2001; Phillips et al. 2007; Ulbrich and Atlas 2007). Intense convection, riming, and melting of graupel are thought to contribute more to precipitation in continental than in maritime regimes.

Since TRMM measurements are based on snapshots and relatively coarser horizontal resolution, we want to know more details of storm evolution, corresponding environments, and specific microphysical processes in the Mei-Yu regime. TiMREX deployed many facilities to observe the multiscale 3-D storm structures and storm environments. TiMREX observed the entire 2008 Mei-Yu season in southwest Taiwan where heavy Mei-Yu rainfall was quite frequent during May and June. During TiMREX, observations targeted upstream conditions and storm evolutions of heavy Mei-Yu precipitation systems, convective and microphysical processes of rainy storms, and orgraphic effects on storm initiation or enhancement.

This chapter first examines convective properties and vertical structures (based on ground-radar precipitation features), storm environments, and microphysics of several heavy rainfall events related to Mei-Yu rain bands in 2008. In addition, storm properties of two different regimes are compared: “intense convection” and “rainy but less convective.” Finally, a detailed case study of a long-duration heavy rainfall event is presented. TiMREX data and analysis methods have been described in Chapter 2.

6.2 Heavy Rainfall Events during TiMREX

This section first describes the rainfall characteristics of the 2008 Mei-Yu season, especially over southwest Taiwan, and determines how unusual it is compared to Mei-Yu climatology. Four major heavy rainfall events (daily rainfall > 100 mm) are selected and analyzed in terms of rainfall characteristics, synoptic conditions, and storm environments.

6.2.1 Rainfall Characteristics of 2008 Mei-Yu

Compared to the 10-yr climatology, the 2008 Mei-Yu had a less well-defined rain belt from southern China to the south of Japan, with a rainfall minimum over oceans close to the southeast China coast and north Taiwan (Fig. 6.1). The rainfall maxima of the seasonal rain belt over the Pearl River Delta of southern China and adjacent ocean are much higher than climatology. For example, the 2008 Mei-Yu has a maximum rainfall of ~1000 mm, while the 10-yr averaged Mei-Yu is ~600 mm. The Mei-Yu rainfall on Taiwan Island in 2008 is quite close to the climatology of about 500 mm. During the 2008 Mei-Yu season, many flooding events were reported in southern China associated with higher frequency of active Mei-Yu fronts than most years. About four major periods with quasi-stationary Mei-Yu fronts were recorded in South China. However, only two well-defined quasi-stationary Mei-Yu fronts approached or affected Taiwan.

In 2008, the first wet spell of monsoon rainfall approaches southwest Taiwan in late May (Fig. 6.2). Significant rainfall related to Mei-Yu rain bands did not show up in Taiwan until June. Two major periods of Mei-Yu heavy rainfall are observed. Each raining period (June 2-5 and June 14-16) lasts for a few days with repeated heavy precipitation persisting from a few hours to more than 10 hours (Fig. 6.3). Based on the

TRMM 3B42 rainfall retrievals (Fig. 6.4a), rainfall maxima during TiMREX are located over the upstream ocean and coastal plain of southwest Taiwan. This is distinct from the rainfall climatology over Taiwan (Chen et al. 1999; Chen et al. 2007). The heaviest rain over the coast rather than the foothills or mountain slope is also confirmed by rain gauge observations (Fig. 6.4b). However, there is a large discrepancy between the satellite-retrieved rainfall (3B42) and surface observed rainfall, with the 3B42 estimates about 40% less than the rainfall recorded by rain gauges. For example, over the coastal plain of southwest Taiwan, the rain gauges recorded rainfall is about 1000 mm, while only about 600 mm is estimated by 3B42.

6.2.2 Selected Heavy Rainfall Events

During the two well-defined quasi-stationary Mei-Yu fronts affecting Taiwan, there are about 6 days with well-defined rain bands and heavy rainfall over southwest Taiwan (Fig. 6.5, and 6.6). Four heavy rainfall events are selected for study; June 2, 5, 14, and 16. Rainfall maxima over the island vary from time to time among these events (Fig. 6.7). For example, heavy rain fell over a valley in southwest Taiwan on June 2, over the whole southern island on June 5, over the both the plain and foothills on June 14, and over the coastal area and upstream ocean on June 16. The location of heavy rainfall within Mei-Yu rain bands over and near Taiwan is affected by upstream conditions, low-level flows, instability of the atmosphere, and orography (Chu and Lin 2000; Chen and Lin 2005a, b; Chen et al. 2005). Climatologically, the highest frequency of heavy rainfall during Mei-Yu occurs over the foothills and slope of mountains over southwest Taiwan, mainly associated with the lifting and blocking effects of the high terrain on the southwesterly monsoon flow (Chen et al. 1999; Chen et al. 2007). In contrast, during days without the influences of Mei-Yu fronts, the rainfall maxima tend to be along the windward slope of the central mountains of southern Taiwan (not shown).

6.2.3 Large Scale Conditions and Storm Environments

As previously mentioned, all the selected heavy rainfall events are related to the approach of quasi-stationary Mei-Yu fronts or rain bands. During these heavy rainfall events, very strong low-level wind shear lines (850 hPa) stay over southeast China coast or the Taiwan Strait, with southwesterlies to the south and northeasterlies to the north (reanalysis in Fig. 6.8 and 6.9). Southwesterly flows originate from the tropical Bay of Bengal and South China Sea. Most of the time, flows upstream of southwest Taiwan satisfy the criteria of low-level jet (LLJ; > 12.5 ms^{-1} at 850 hPa; Bonner 1968; Chen et al. 1988). At the early stage of the Mei-Yu rain bands, the low-level wind shear line is associated with an upper-level trough over eastern China (Fig. 6.8b and 6.9b). After the upper-level trough moves offshore, the wind shear line or Mei-Yu front stays quasi-stationary. LLJs are stronger in mid-June than early June, though upper-level troughs become weaker after mid-June. Similar seasonal changes of the synoptic conditions in mid-June for heavy rain events have also been pointed out by Chen (1993) and Chen and Li (1995).

LLJs over the ocean upstream of southwest Taiwan are also observed by soundings (station 99810). They are between 950-750 hPa with the wind speed exceeding 15 m s^{-1} (Fig. 6.10). The depth of LLJs is quite event-dependent. For example, the LLJ on June 14 is between 950-750 hPa, while the one on June 16 is confined to 950-850 hPa. All the LLJs are southwesterly, but slightly vary among different events. LLJs are only observed over the upstream ocean of southwest Taiwan, while low-level flows decrease from more than 15 m s^{-1} over ocean (station 99810) to less than 10 m s^{-1} approaching the island (Fig. 6.11; station 46750). The wind directions of low-level flows over the island (station 46750) also vary from southeasterly to southwesterly. As mentioned by Chen et al. (2005), the heavy rainfall over Taiwan is highly correlated to the upstream LLJ. The low-level circulation or flows are significantly decelerated or deviated by the steep terrain over the island (Li and Chen 1998; Yeh and Chen 2002; Chen et al. 2005).

Figure 6.12 shows the sounding profiles over the upstream ocean at 00Z or 06Z for selected heavy rainfall days. Accompanied with the LLJ, the upstream low-level (e.g., 925 hPa) atmosphere during these rainy events is warm (27-28 °C) and moist (20 g kg^{-1}). No cold or dry air intrusion is observed above the low-level warm and moist jets. The whole upstream troposphere is unstable with CAPE values of 1500-2000 J kg^{-1}, and very low lifting condensation level (~960 hPa). These unstable environments of upstream ocean are also indicated by the theta-e profiles, as shown in Fig. 6.13a. Therefore, the upstream conditions are quite ready for convection if slight lifting is provided. Compared with upstream, the environments over the island are less unstable or near moist neutral (especially for extreme events on June 5 and 16), except for the case of June 14 (Fig. 6.13). The theta-e profile over the storm site in June 14 (06 Z) shows high values at the lowest level but then decrease very fast with height above indicating a potentially unstable environment. These results indicate that the upstream ocean may be more important for the most robust convection. Convection developing over the upstream ocean may move to the island and help maintain the heavy precipitating systems over land. On the other hand, the air-sea flux and LLJ over the upstream ocean could help to maintain or restore the warm and moist environment upstream if it has been stabilized by development and spreading of cold pools associated with heavy rain

6.3 Storm Morphologies of Heavy Precipitation Systems

Analysis of the storm morphologies and convective properties of selected heavy rainfall events is based on the radar precipitation features (RPFs) derived from the RCCG radar (120.07 E; 23.15 N) measurements at the southwest Taiwan coast (Fig. 2.3). Definition of the PRFs has been described in Chapter 2. Samples of RPFs in different events are listed in Table 6.1 and 6.2.

6.3.1 Occurrence Frequency of Different Storm Types

Figure 6.14 shows the occurrence frequency of precipitation features categorized by specific storm properties in different heavy rainfall events. During these rainy events, radar detected features (>18 dBZ) have an average size of about 200-300 km^2 with about 10% of them exceeding 1000 km^2, and 2-5% of the features exceeding 10000 km (Fig. 6.14a). More than 10% of the storm snapshots have echo top (20 dBZ) extending above 10 km (Fig. 6.14b). There is a significant difference between June 14 and the other rainy events on the occurrence frequency of storms reaching or overshooting the tropopause, i.e., 15 km. Besides the occurrence of extremely deep convection, this large difference also appears on the occurrence frequency of intense convection (40-dBZ above freezing level) or frequent lightning (Fig. 6.14c-d). About 10% of the features have their convective cores (40 dBZ) above 8-km on June 14, but only 1-2% of the features have this intense convection on June 2, 5, and 16. Similarly, June 14 also has much higher frequency of lightning activity within the precipitation features. 7-8% of the precipitation features on June 14 experience lightning of at least 1 flash per minute, but the other rainy events in the comparison only have 1-2% lighting occurrence or less. Based on the above discussion, storm properties could be quite varied within the Mei-Yu heavy rainfall systems. The prefrontal “squall line” system (June 14) has storm properties more like their continental counterparts, while the other heavy precipitation systems are more like oceanic systems in their convective properties. This is consistent with the soundings for the June 14 heavy rain event having a “more continental” (unstable environment) theta-e profile (Fig. 6.13).

6.3.2 Rainfall Contribution by Storm Types

This subsection presents and discusses the fraction of rainfall contributed by specific storm types in those Mei-Yu heavy rainfall events (Fig. 6.15). Because of the large size nature of these systems, about 80-90% of the rainfall is contributed by features with area > 1000 km^2, or by features larger than 100 km in equivalent diameter for the heavy rainfall events of June 14 and 16 (Fig. 6.15a). 90% of the rainfall is from systems with high cloud tops, e.g., max height of 20 dBZ > 10 km (Fig. 6.15b). The case with intense convection (June 14) even has about 60% of the rain contributed by systems extending above 15 km, while the other cases in the comparison have only 20% of rainfall from such deep convection. Similarly, the fraction of rainfall contribution by intense convection or lightning-producing systems also falls into two distinct groups: June 14 and the other rain events (Fig. 6.15c-d). Though all events have more than 80% of the rainfall involving large ice particles (e.g., max height of 40 dBZ > 6 km), June 14 (60%) has much more rainfall contributed by the systems with larger depth of large-size ice particles (e.g., max heigh of 40 dBZ > 8 km) than other events (10%). This is also consistent with the fraction of rainfall contributed by features with frequent lightning. For example, about 60% of the rainfall comes from systems with lightning of at least 10 flashes per minute on June 14. In contrast, less than 10% of the rainfall is produced in features with such frequent lightning on the other days with very heavy rainfall.

6.3.3 Precipitation Vertical Structures

Figure 6.16 shows vertical profiles of maximum radar reflectivity of RPFs in the percentile of 1, 5, 10, 20, and 50 in the comparison of heavy precipitation events, two at a time. Again, vertical profiles can be separated into two different groups. Vertical profiles of RPFs in the first group including June 2, 5, and 16 fit very well with each other. Vertical profiles of RPFs on June 14 events fall into a very different regime. The major difference between profiles of these two groups is in the mixed-phase region and below the freezing level. The regime represented by June 14 (solid lines in Fig. 6.16c) has much higher radar reflectivities in the mixed-phase region than the other regime (dashed lines in Fig. 6.16c), indicating the existence of more large ice particles (e.g., hail or graupel) and precipitation-size supercooled liquid drops in the June 14 regime. The existence of hail or graupel in the mixed-phase region requires significant updraft (> 5 m s^{-1}; Lemone and Zipser 1980; Zipser and Lemone 1980; Zipser and Lutz 1994) for sufficient supercooled liquid cloud water to support rapid riming.

Another major difference is found between profiles of radar reflectivity below the melting level. The reflectivity increases downward below the freezing level in the relatively weak convection regime (June 2, 5, and 16), while profiles on June 14 have near-constant reflectivity with height below the melting level. The above-featured differences are also observed by the SPOL radar about 70 km to the south of the RCCG radar from perspectives of both pixels and precipitation features (Fig. 6.17). The increase of reflectivity below the freezing level (near 5 km) is about 4-dBZ in precipitation systems of June 16. We speculate that difference in the shape of the radar profiles may result from differences in updraft intensity between these two groups. In the weaker updraft convective cores, there is more time for growth of raindrops by collision-coalescence in the warm part of the cloud, and if the updrafts are too weak to loft these raindrops, they are likely to fall through the cloud, continuing to grow until they reach cloud base (seen as a radar reflectivity increase downward). However, in much stronger updrafts, supercooled water, lofting of frozen raindrops, and rapid graupel growth is more likely within the mixed-phase region. Graupel falling out of the convective cores become large raindrops, but may collect less cloud water as they descend toward the surface if they do not fall through updrafts with large cloud water content. These discussions on the regime differences of vertical radar profiles are merely speculations. More vertical profiles and comparisons between the intense convection regime and rainy but less convective regime are shown in Section 6.4.

6.3.4 Ensemble Microphysical Properties

Fig. 6.18 shows vertical profiles of frequency of different hydrometeors within the convective regions retrieved from polarimetric observations of the SPOL radar (Fig. 2.3) during heavy precipitation events. These ensemble microphysics retrievals are based on the NCAR fuzzy logic algorithm (Vivikanandan et al. 1999). This algorithm separates hydrometeors into 17 categories, and its specific description has been given in Chapter 2. It should be mentioned that the frequency of hydrometeors is not based on RPFs but on the statistics of convective regions (> 40 dBZ). Apparently, there is much higher frequency of hail or graupel, including wet and dry status, above the altitude of 6 km on June 14 than on June 16 (Fig. 6.18a). There are no large ice particles indicated above the 8-km level on June 16, consistent with results shown in previous sections. This significant regime difference between June 14 and June 16 on the occurrence frequency of large ice particles, is consistent with the difference of vertical radar profiles above the freezing level between two groups.

Though June 14 has less fraction of dry or wet snow (Fig. 6.18b-c), it also has higher fraction of ice particles on the other end (small ice particles; Fig. 6.18d). It is reasonable to assume that the stronger the midlevel updraft in the convective core, the larger the mass of ice particles that can be lifted to higher levels. Small ice particles involved in the charging process in the mixed-phase region may be eventually advected rearward into the anvil and growing in an ice-saturated environment (Rutledge and MacGorman 1988; Schuur and Rutledge 2000).

6.4 Comparisons between "Intensely Convective" and "Rainy but Less Convective" Regimes

The previous section shows that there are significant differences on storm morphologies and convective properties among heavy rainfall events even with similar large-scale forcing. There are two distinct convective regimes found for Mei-Yu storms: "intensely convective" and "rainy but less convective." This section selects a few events representing these two regimes and further examines their storm properties and convective structures.

6.4.1 Selection of Intense and Weak Regimes

Intense convection in this section is defined as max height of 40 dBZ of an RPF reaching above 8 km. Intensely convective events are defined as rainfall events having at least 10% of RPFs with intense convection. Rainy but less convective events are selected from heavy precipitation events (maximum daily rainfall > 100mm) having less than 5% of RPFs with intense convection. We select 3 events for each category. The intensely convective regime includes May 26, June 13, and June 14, while June 4, 5, and 16 are selected for the rainy but less convective regime. Population of RPFs and RPFs with intense convection of events in each regime is listed in Table 6.2.

6.4.2 Storm Environments and Thermodynamics

An examination of the sounding profiles in the storm location found that the intense convection regime has a very unstable environment, while the rainy but less convective regime owns a moist but near-neutral environment (see June 14 and 16 in Fig. 6.19). The Convective Available Potential Energy (CAPE) in the intense convection regime is around 2000 J kg^{-1}, but less than 500 J kg^{-1} for the rainy but less convective regime. There is a somewhat drier and colder air layer covering the lowest warm and moist air mass. Similar environment difference can be summarized by the vertical theta-e profiles (Fig. 6.20). Theta-e profiles for the intense convection regime show warmer and moister air in the lowest levels ($\theta_e \sim 345$ K) decreasing upward (Fig. 6.20a), a theta-e profile often conducive to strong downdrafts and the production of cold pools in low levels. In contrast, the rainy but less convective group has theta-e profiles with lower values in the boundary layer (~340 K), but more nearly constant with height (Fig. 6.20b).

6.4.3 Storm Properties and Convective Structures

Fig 6.21 shows the occurrence frequency of precipitation features with different storm properties of RPFs for specific days of each regime. Difference on the frequency of storm size and echo top between these two regimes is not great (Fig. 6.21a-b). The occurrence frequency of RPFs with convective proxies such as max height > 8 km or lightning flash rate > 10 min^{-1} in the intense convection regime is about 1 order of magnitude higher than those in the rainy but weakly convective regime (Fig. 6.21c-d). Therefore, the regime separation in convection intensity is very clear.

The vertical profiles of maximum radar reflectivity of RPFs in the intense regime (Fig. 6.22) all present a very different shape from those of the rainy but less convective regime (Fig. 6.16) in the mixed-phase region and below the freezing level. The intense regime has profiles that decrease slowly with altitude, but are nearly constant below the freezing level (Fig. 22a-c). All the heavy precipitating systems in the weak convection regime show significant increase of reflectivity downward on the radar profiles below the freezing level (Fig. 6.16a, 6.16b, and 6.16d). Interpretations on the difference between these two regimes have been discussed in Section 6.3.3.

6.5 Storm Evolution and Possible Triggering-maintenance Mechanisms of an Extreme Rainfall Event

Previous sections have examined the general large-scale conditions, storm environments, and convective properties of several Mei-Yu rain band related heavy rainfall events observed by TiMREX in 2008. This section selects one extreme rainfall event (June 16) and analyzes its storm environments, storm evolution, convective processes, and possible mechanisms of triggering and maintenance.

6.5.1 Review of Extreme Rainfall Mechanisms

Since total precipitation at any point is directly proportional to the rate and duration of rainfall (Doswell et al. 1996), quasi-stationary or slowly moving MCSs are favorable for producing extreme rainfall over a region. MCSs, especially slowly moving or quasi-stationary MCSs, are major causes of extreme rainfall in the warm season, e.g., in the United States (Maddox et al. 1979; Houze et al. 1990; Moore et al. 2003; Schumacher and Johnson 2005, 2006). All these authors agree with the importance of a LLJ to those quasi-stationary heavily precipitating MCSs through persistent advection of warm moist air into the system. Another major component is the continuous deep convection moving over the same region (Chappell 1986; Doswell et al. 1996; Davis 2001) triggered by surface fronts, outflow boundaries, mesoscale convective vortices

(MCVs), or orographic lifting (Raymond and Jiang 1990; Pontrelli et al. 1999; Sanders 2000; Schumacher and Johnson 2008, 2009). “Training line” and “Back-building” processes are two major patterns (Schumacher and Johnson 2005, 2006). The training line process occurs when a series of convective cells move in a line parallel to the storm direction of motion, but propagate very little in the perpendicular direction. On the other hand, the back-building process is related to situations when convective cells repeatedly develop upstream of previous deep convection and pass over the same region.

During the Mei-Yu season, heavy rainfall and rainfall maxima are often produced by MCSs embedded in the Mei-Yu frontal cloud band (Kuo and Chen 1990; Zhang 1990; Chen and Li 1995; Ninomiya 2000). Some of the rainy MCSs are associated with low-level vortices (Kuo et al. 1986; Chang et al. 1998; Tao and Ding 1998). Complex terrain can also help to enhance or elongate heavy precipitaiton through the interaction between the persistent monsoon flow and orography-generated local circulation (Li et al., 1997; Yeh and Chen 1998; Li and Chen 1998; Chen et al. 2005). Mechanisms for orography-enhanced heavy precipitation can be summarized as follow: 1) lifting effect by the terrain, through forced ascent as the air moves over the slope, or more indirectly, as the airflow is blocked by the mountain, or when mountains act as a high-level heat source (Chen et al. 1991; Akaeda et al. 1995; Chen and Feng 2001); 2) convergence between the prevailing monsoon flow and offshore flow during the night time (Chen and Li 1995; Yeh and Chen 2002; Chen 2005); 3) convergence between monsoon southwesterly and low-level barrier jet deviated by the terrain or between postfrontal northwesterly flow and the barrier jet (Chen and Li 1995; Li et al. 1997; Yeh and Chen 2002); 4) stagnation of MCSs or squall lines blocked by the high terrain, leading to extreme accumulation of precipitation (Reeves and Lin 2006).

In this study, we will examine both orographic effects and quasi-stationary MCS ideas, through detailed analysis of storm evolution, upstream and storm environments, and convection processes.

6.5.2 Weather Conditions and Storm Environments

During the period of June 14-16, a quasi-stationary Mei-Yu wind shear line approached and stayed over the southeast China coast or the Taiwan Strait (Fig. 6.9). Associated with the Mei-Yu front, robust convection and heavy precipitation systems developed over and southwest of Taiwan on June 14. These rainy convective systems passed southwest Taiwan by June 15, but new convective mesoscale systems developed on the evening of June 15 and evolved further on June 16 (Fig. 6.6). Though rainy systems on June 14 and 16 both have a long duration, their storm type and evolution is quite different. Storms on June 14 evolve more like squall lines and propagate from northwest to southeast, while raining systems on June 16 remain nearly stationary. This section examines the rainfall distribution, synoptic conditions, upstream conditions, and storm environments for the extreme rainfall event.

6.5.2.1 Rainfall Distributions

The quasi-stationary raining system of June 16 drops the heaviest rain over the upstream ocean and the coastal cities of southwest Taiwan (Fig. 6.23). Rainfall maxima over the southwest coast exceed 300 mm and decrease toward the mountain ranges, with only about 100 mm produced over the slope or mountain regions. Very little precipitation crosses the mountain, with less than 50 mm rain on the eastern side of the mountain ridge. We can show that this rainfall distribution pattern is explained by the movement of precipitating clouds that continuously develop over the upstream ocean to the coast of the island, instead of developing or enhancing over the island. This long-duration precipitation system is quite stationary and heavy rainfall is limited to the southwest part of the island (heavy rain region less than 100 km in diameter).

Figure 6.24 shows the rainfall distribution accumulated every 4 hours. It further reveals that during the 16-hour period of precipitation, the heaviest rain is always confined to the coast of southwest Taiwan with very slight changes of location. The heavy rain approaches the coast at about 20 UTC on June 15 or 04 LT on June 16 (Fig. 6.24a) after the Mei-Yu front-related rain band moves to the south of the island in the local afternoon of June 15. The heaviest rain peaks during 00-04 UTC (08-12 LT) on June 16, dropping about 60-80 mm of rain on the coastal plain during this 4-hour time period (Fig. 6.24b). During this period, heavy precipitation (about 10 mm hr^{-1}) reaches the foothills of the south-north-oriented mountain range. After 04 UTC (12 LT) on June 16, heaviest precipitation moves slightly to the north, but still on the southwest coast of the island (Fig. 6.24c-d). Precipitation almost ceased after 12 UTC (20 LT) on the June 16.

6.5.2.2 Synoptic Overview

The development of the Mei-Yu shear-line or related trough/depression producing this heavy rainfall event on June 16 can be traced back to June 12 when a southwest vortex and Plateau leeside trough (Ding and Chan 2005) develop. By June 13, the low-level vortex (925-700 hPa) becomes very well-defined over southwest China at the foothills of the Yun-Gui Plateau and propagates toward the northeast (Fig. 6.25). This southwest vortex is accompanied by a short-wave trough at the midtroposhere, e.g., 500 hPa (Fig. 6.26). As the midlevel trough moves northeastward (Fig. 6.26a-b), it decays and becomes unrecognizable on June 15 (Fig. 6.26c). However, it is caught up by a midlatitude trough and they merge on June 16 over eastern central China (Fig. 6.26d). At low levels, the low pressure system propagates northeastward from southwest China to eastern central China and moves offshore on June 16 (Fig. 6.25). Also on June 16, another low pressure system develops in the lower troposphere (Fig. 6.25d) over southwestern China. But this low pressure system is not as strong as the one on June 13, and the cyclonic winds around this system are much weaker. Since this low pressure system is on a relatively small scale (200 km diameter) and still far from Taiwan (500 km), the influence of this system on the heavy precipitation system over South China Sea and Southwest Taiwan is uncertain.

6.5.2.3 Upstream Low-Level Jets

Before the development of the quasi-stationary heavy precipitation system over southwest Taiwan and upstream ocean, low-level southwest flows start to restore warm and unstable conditions within the “cold pool” that formed from previous precipitation on June 14-15. By 00 UTC on June 16, the upstream flows off southwest Taiwan coast reach the intensity of low-level-jet (LLJ; e.g., 850 hPa wind > 12.5 m s^{-1}) as shown in Fig. 6.27. The LLJ is only limited to the upstream ocean away from southwest Taiwan, while low-level winds over the coast of southeast China and southern Taiwan are much weaker. LLJ is strong only up to 850-800 hPa and disappears at 700 hPa. The LLJ is also recorded in the radar radial velocity from the southwest direction (Fig. 6.28). The LLJ extends from the upstream ocean to within about 50-60 km from the southwest Taiwan coast. There is strong convergence between the upstream LLJ and weak winds within 40-50 km of the island.

Vertical profiles of wind speed and wind direction from soundings over the upstream ocean and southwest coast are shown in Fig. 6.29. Again, they confirm the above discussions and conclusions. During the heavy precipitation period of 00-06 Z on June 16, the southwesterly LLJ blows more than 15 m s^{-1} between 950-900 hPa (Fig. 6.29a-b). But over the coast, winds have average speed around 5 m s^{-1} (Fig. 6.29c). The wind direction is southeasterly in the lowest hundred meters and turns anticyclonically with elevation (Fig. 6.29d). By comparing winds upstream and near the coast, it can be concluded that significant convergence exists between the upstream ocean and the southwest coast of Taiwan. Not coincidentally, this region happens to be the exact region where convection and heavy precipitation continuously develops for about 15 hours on this day.

6.5.2.4 Upstream Conditions and Storm Environments

Figure 6.30 and 6.31 show soundings at the first few hours of the precipitation system over the upstream and coastal site, separately. There is a clear difference between upstream conditions and storm environment over the coast. After the storm system of June 14 passes Taiwan, the low-level environment over southwest Taiwan becomes relatively colder and stable. However, the upstream atmosphere becomes more unstable with large CAPE (> 2000 J kg^{-1}) by 1800Z on June 15. It is likely that previous precipitation formed a shallow and widespread cold pool covering the island and adjacent ocean, but air-sea fluxes restored the upstream environment faster than the atmosphere over the island. The unstable air mass and LLJ over the upstream ocean combined to initiate new convection and provide a continuing moisture source for the long-lived raining system. Though the neutral moist air over southwest Taiwan can be easy to lift and form precipitation, it can not support strong convection. Continuous precipitation further cools and stabilizes the atmosphere over the island. In this case, convection triggered upstream and fed by warm and moist air from upstream is important to this long-duration mesoscale rainy storm.

6.5.2.5 Weak Precipitation Cold Pool

The precipitation on June 14 probably created and left behind a cold pool. Based on the comparison of near surface temperature in Fig. 6.30 and Fig. 6.31, there is about 3 ^{o}C difference between the upstream ocean and the island in the local morning of June 16 (18Z June15 and 00Z June 16). In addition, there is about 4-5 K difference of potential temperature between the upstream ocean and the island at that time (Fig. 6.32). The potential temperature near the surface drops more than 5 K after the heavy precipitation over southwest Taiwan on June 14 (Fig. 6.32b). This lower temperature layer is 500-600 m deep and lasts from the middle of June 14 to June 16. Thus, a precipitation formed cold pool, though weak, exists over the southwest part of the island and is maintained by continuous precipitation.

In spite of having a weak temperature boundary between the upstream warm and moist LLJ, and the relatively cool and calm air mass, in this case there was significant convergence between these air masses. The upstream LLJ could be lifted over the shallow cold pool extending from the island, as shown by the example in Fig. 6.28. However, over time, the LLJ may also help to shrink the cold pool.

6.5.3 Evolution of Heavily Raining Systems

This section examines the evolution of the heavy precipitation system in terms of large-scale view from satellite, mesoscale evolution from radar images, and finer scale evolution of convection and precipitation upstream and near the coast of southwest

Taiwan, and statistics of convective cells.

6.5.3.1 Snapshots of Satellite and Radar Measurements

As has been mentioned above, vigorous convection and precipitation developed along the rain band of Mei-Yu front over the coast of southeast China and the Taiwan Strait starting from June 14. In the day time of June 15, convection propagates quite far south of Taiwan Island, with only scattered precipitation over the island. However, deep convection, indicated by the very cold IR brightness temperature (BT), starts to develop over the adjacent upstream ocean and coast of southwest Taiwan by 20Z of June 15 (Fig. 6.33). Two hours later, convection extends a very well-defined Mesoscale Covnective System (MCS) with low BT covering the all of southwest Taiwan and the adjacent ocean area. This IR-viewed MCS persists more than 12 hours over exactly the same region, although decreasing slightly in area with time. The coldest region of the IR images is located slightly away from southwest Taiwan, indicating the development of deep convection upstream offshore (Fig. 6.33d-f).

Snapshots of radar images shown in Fig. 6.34 reveal more details about the convective cores related to the large precipitation region. In summary, convective cells or lines (e.g., echoes > 40 dBZ) keep developing over the upstream ocean and move very slowly to the southwest coast, but decay after reaching the island. The large heavy precipitation shield appears stationary, supported by the continuous development of new convection. Before 06Z, convective lines stay quasi-stationary over the upstream ocean with heavy precipitation reaching southwest Taiwan. Smaller regions of new convection continue to develop over the southwest of the island and merge into these convective lines.

6.5.3.2 Statistics of Precipitation and Convection

The above summaries of the storm evolution are also confirmed by the occurrence frequency of both significant radar echoes and defined convective pixels during the period of heavy precipitation (Fig. 6.35). About 90% of the time during June 15 22Z- 16 12Z, southwest Taiwan and the upstream ocean 100 km away experience precipitation with radar reflectivity > 30 dBZ (Fig. 6.35a). The maximum area of 30-dBZ occurrence appears oval-shaped from 119.0 E to 120.5 E. The distribution of occurrence of convective radar echoes is very different from that of 30-dBZ occurrence (Fig. 6.35b). A west-east-oriented band-shape maximum of convection frequency (35%) locates over the upstream ocean with about 40 km away from the coast. Another convection occurrence maximum center (25%) is located just on the edge of the southwest coast. However, very low frequency (< 10%) of convection is observed over the heavy precipitation region of the plain of southwest Taiwan. In other words, the large amount of precipitation over southwest Taiwan is not mainly contributed by convective rain, but by heavy stratiform precipitation evolving from the upstream convection. Therefore, continuous development and upscale growth of convection upstream is the main cause of the heavy precipitation over the island on June 16.

6.5.3.3 Evolution of Convective Cells

Figure 6.36 shows the distribution of defined convective cells of different size every 3 hours. During the first 6 hours, a lot of convective lines (medium to large size with diameter > 10 or 20 km) are concentrated over the west-east band-shape region 40-50 km from the southwest coast (Fig 6.36a-b). Some convective cells, either large or small, propagate downstream to the coast, but very few survive. Before 09Z, only a few small cells appear over the low land of southwest Taiwan (Fig. 6.36a-c). At the same time, many small convective cells (e.g., with diameter < 10 km) develop over the southwest edge of the heavy precipitation region. These small convective cells deepen while propagating downstream and finally merge with those large convective lines (not shown). In summary, convective cells keep developing upstream during the heavy precipitation period within the thermodynamically unstable environment and support those major convective cores by merging with them. Conditions are closer to moist neutral over the island, so the deep convection does not persist there, but evolves into continuous stratiform precipitation.

6.5.3.4 Mesoscale Flow Structures Based on Dual-Doppler Wind Analysis

Figure 6.37 shows dual-Doppler derived horizontal wind field and vertical motion at different levels at 0016Z June 16. The southwesterly LLJ is clearly defined up to the 2 km level upstream, southwest of the convective line (40 dBZ), converging with weaker southwesterly winds downstream (Fig. 6.37a). To the north of the major convective core, westerly winds are observed. Evidently, the major convection region is in this convergence zone between the strong upstream southwesterly flows, weaker downstream southwesterlies, and westerlies to the north. Above the southwest LLJ, the flow trends to weaker westerlies with altitude (Fig. 6.37b-d). This is quite consistent with that observed by the ship soundings over the upstream ocean (Fig. 6.29). The derived upward motion is located very close to the deep convection and convergence zone and peaks in the midtroposphere (6-8 km). However, the vertical motion related to the convective cores is possibly overestimated, especially above midtroposphere (with average above 10 m s^{-1}). Therefore, the vertical cross section of the mesoscale flows is not shown.

6.5.4 Hypothesis of Triggering-maintenance and Supporting Evidence

6.5.4.1 Hypothesis of Triggering-maintenance

Based on above-mentioned results and discussions, it can be summarized that the long-duration heavy precipitating system is maintained by convection developing continuously over the upstream ocean, with convective cells growing as they move toward the island. This process is similar to "echo-training" or "back building" process (Chappell 1986; Doswell et al. 1996; Davis 2001; Schumacher and Johnson 2005). The back-building system features new convection developing from the rear of the storm and propagating over the same region before the older convection completely disappears. This process requires some triggering factors to initiate the developing convection from the backside continuously. Triggering conditions include such as surface fronts, convectively generated outflow boundaries, cold pool boundaries, orographic lifting, or interaction between mesoscale convective vortex (MCVs) and a LLJ (Schumacher and Johnson 2005).

Of all the conditions listed above, surface fronts and MCVs evidently do not exist in the case being studied. Our working hypothesis is that previous precipitation before the development of the long-duration system formed a cold pool over the island and adjacent ocean, and the boundary between the cold pool and upstream moist air triggers new convection. This cold pool may be weak and shallow, but acts as if to extend the island and mountains 40-50 km into the upstream ocean. The cold pool could also be enhanced by the precipitation cooling. As a result, the upstream LLJ starts being lifted well offshore rather than at the foothills of the mountain range over the island. After the cold pool weakens and becomes mixed with the upstream air mass, the new convection stops developing, and the precipitation system slowly dies. A schematic diagram of the hypothesis is shown in Fig. 6.38.

6.5.4.2 Summary of Supporting Evidence

Key components supporting the triggering and maintenance of the long-duration back-building system are shown in Fig. 6.38. They include (1) LLJ over the upstream ocean, (2) warm and moist unstable air over the upstream ocean, (3) cold pool (stable air) over the island and adjacent ocean, (4) convergent boundary between the upstream LLJ and calmer winds over the coast, and (5) convection developing near continuously near this boundary for many hours.

Figures 6.27 through 6.29 clearly show LLJs over upstream ocean and properties of LLJs including depth, area, intensity, and time series. In addition, all the soundings made between June 15 1800Z and June 16 1200Z over the upstream ocean indicate the warm and moist unstable nature of the upstream air mass (Fig. 6.30). On the other hand, the cold pool (or stable air) over the island and adjacent ocean is revealed through the difference between near surface temperature or potential temperature over the upstream ocean and the coast (Figs. 6.30, 6.31, 6.32), or the wind boundaries between the low level jet and light wind within the cold pool (Fig. 6.28). Furthermore, the radial velocity of several RHI scans toward the southwest from SPOL clearly shows an evident boundary between the LLJ and downstream lower troposphere (Fig. 6.28). The boundaries and convergence between the LLJ and relative calm flow downstream is also indicated by the wind analysis from soundings (Fig. 6.27) and dual-Doppler retrievals (Fig. 6.37). All these environmental components are acting together to continuously trigger and organize convection from the backside of the long-lived multiple MCSs (Fig. 6.33-6.36).

6.6 Summary and Conclusions

This study first examines the rainfall characteristics, synoptic condition, and storm environments of several heavy precipitation systems occurred during TiMREX.

Storm morphologies and convective properties are further analyzed and compared by separating the events into two different convective regimes. In addition, a long-duration extreme rainfall system is investigated in terms of storm evolution, convective processes, upstream, and storm environments. A hypothesis for the triggering and maintenance of the long-duration heavy precipitation process is developed and examined. Major conclusions are summarized as follows:

(1) Rainfall maxima during TiMREX in 2008 are located over the upstream ocean and flat terrain of southwest Taiwan, somewhat different from the long-term rainfall climatology over Taiwan during Mei-Yu;

(2) Most of the heavy rainfall is associated with Mei-Yu rain bands, while they are observed to be more influenced by upstream low-level jets, unstable upstream conditions, moist neutral storm environment, but less by upper level conditions;

(3) Though intense convection and vigorous lightning activities are observed before the onset of Mei-Yu and two cases within the rainy Mei-Yu system, most of the Mei-Yu heavy precipitation systems have only weak to moderate convection and very low lightning occurrence;

(4) Within storms during the intense convection regime, vertical profiles of radar reflectivity have much higher values in the mixed-phase region, indicating the strong updraft and vigorous processes of rain drop frozen and riming of graupel with supercooled liquid drops;

(5) Verticals profiles of radar reflectivity for rainy but less convective storms

increase downward below the freezing level but decrease very fast upward, and are speculated to be associated with weaker updraft and significant warm-rain collision and coalescence processes when rain drops falling through the cloud drops within the updraft;

(6) Associated with the northeastward propagation of a southwest vortex and upper-level short wave trough, a quasi-stationary Mei-Yu rain band developed over Taiwan Strait, South China Sea, and western Taiwan during June 14-16;

(7) Mei-Yu front related "squall lines" passed South Taiwan on June 14 and convection over southwest Taiwan stops on June 15, but new convection redevelops southwest offshore by 18Z of June 15 and forms heavily raining MCSs over southwest Taiwan and adjacent ocean for about 18 hours;

(8) Inside the large MCSs, new convection keeps developing upstream offshore but decays or dies after moving into the island, dropping the heaviest rain over upstream ocean and coastal regions;

(9) A hypothesis of "cold pool extending orographic effect" has been developed and examined: Old "cold pool" from previous persistent precipitation forms partial barrier to low-level moist SW airflow, but LLJ and sea-air flux partially restores the warm, moist air upstream of Taiwan and destabilizes the lower atmosphere upstream, convection is then triggered upstream of the cold pool boundary, evolving into heavy stratiform rain that is responsible for most of the rain over the island.

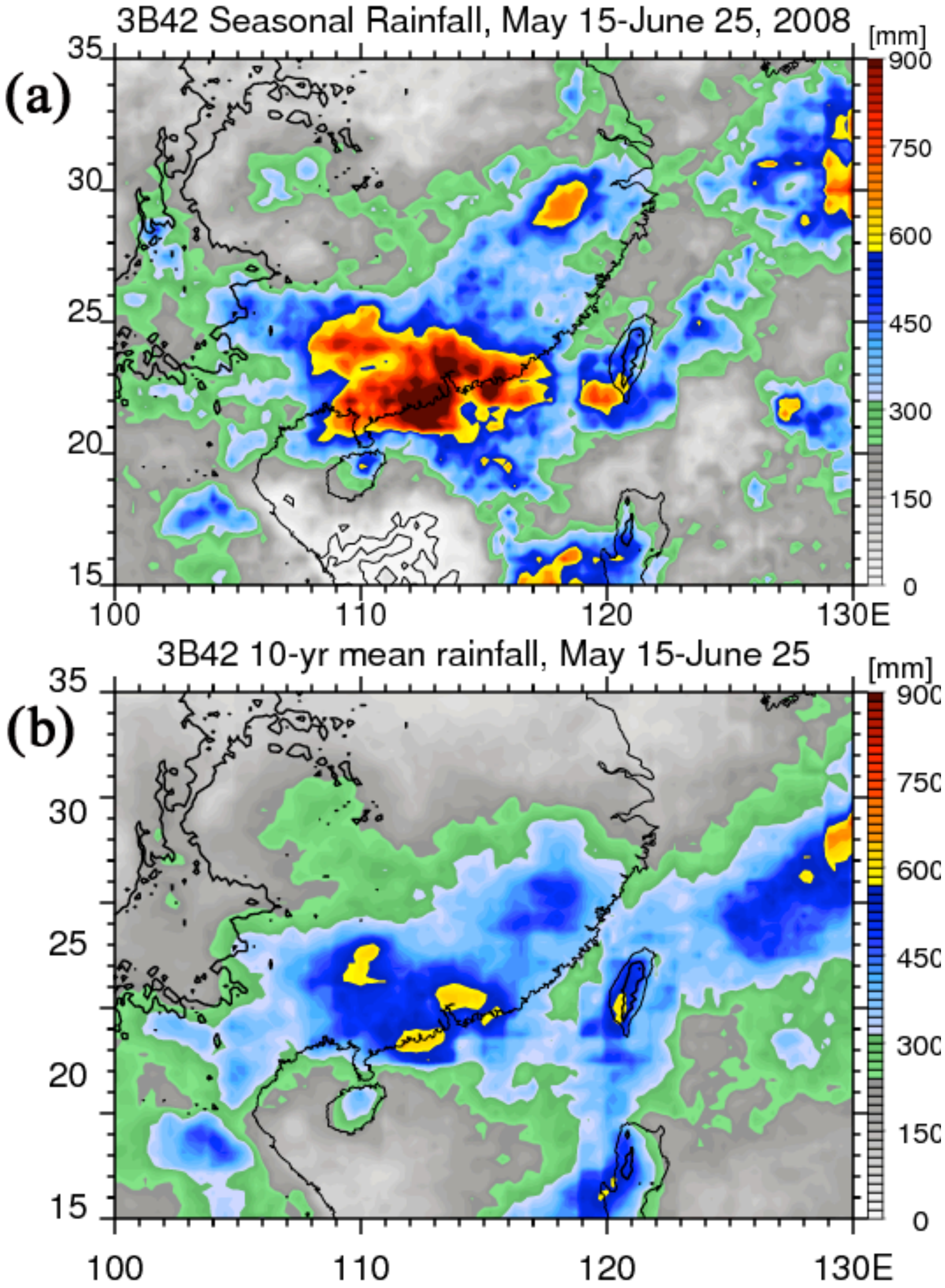

Figure 6.1. Accumulated rainfall (in mm) over East Asia during May 15-June 25 of (a) 2008, and (b) 10-yr mean during 1998-2007, based on TRMM 3B42 rainfall product.

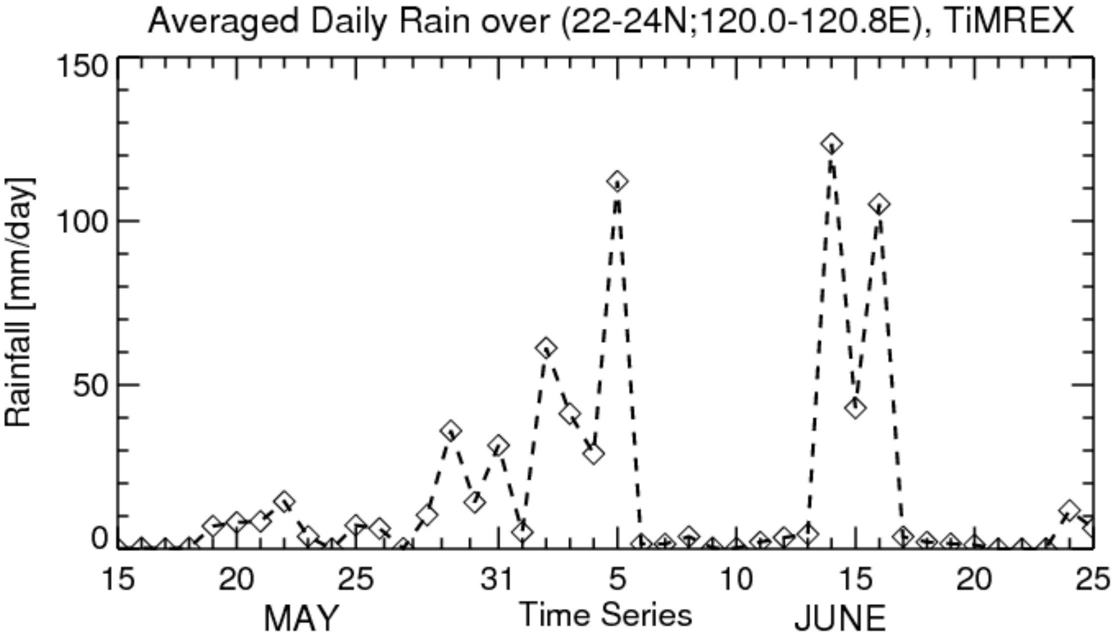

Figure 6.2. Time series of averaged daily rainfall (mm/day) over the region of southwest Taiwan (22-24 N; 120-120.8 E) during TiMREX, based on measurements of rain gauges over the island.

(a) Averaged Hourly Rain, (22-24N;120.0-12.8E), June 1-6

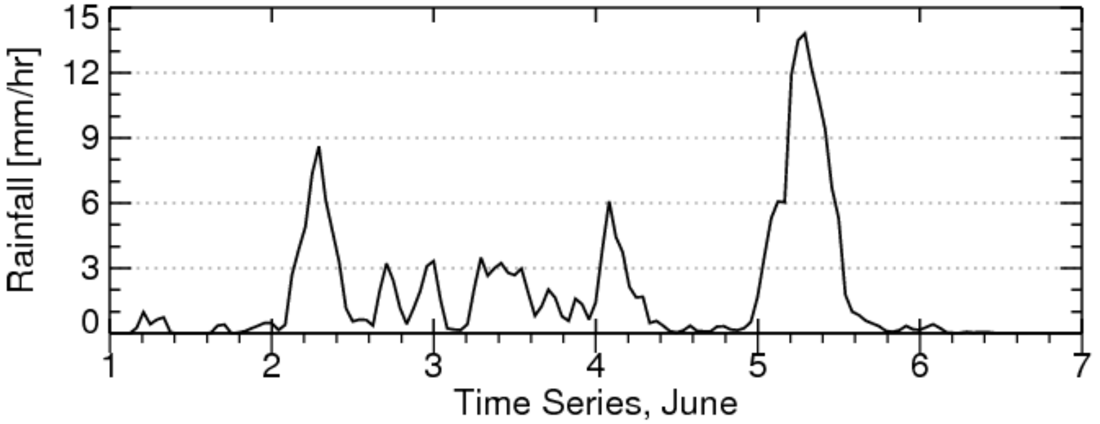

(b) Averaged Hourly Rain, (22-24N;120.0-12.8E), June 12-17

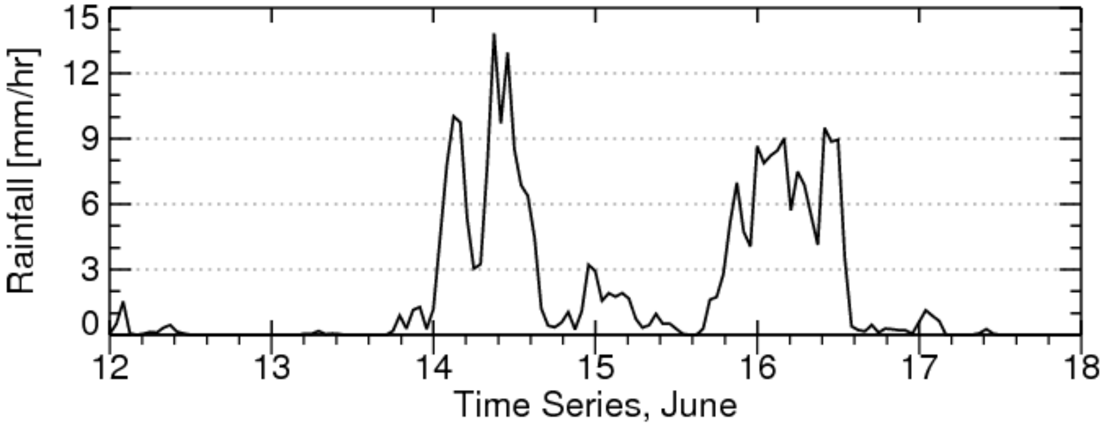

Figure 6.3. Time series of averaged hourly rainfall (mm/day) based on measurements of rain gauges over the region of (22-24 N; 120-120.8 E) during (a) June 1-6, and (b) June 12-17.

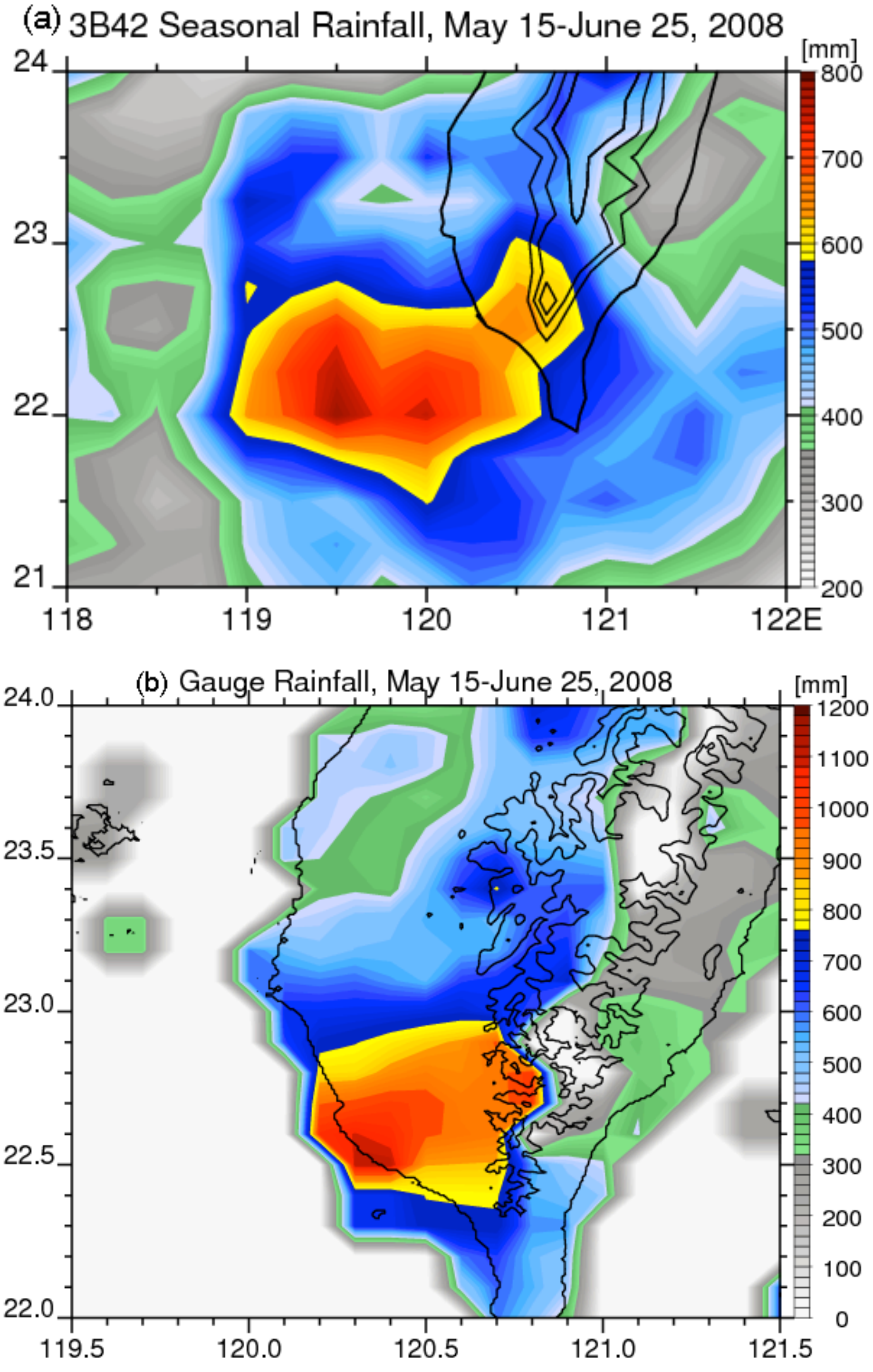

Figure 6.4. The accumulated rainfall (in mm) over southern Taiwan during May 15-June 25 in 2008, based on (a) TRMM 3B42 rainfall analysis, and (b) rain gauges. Note that color scales are different for (a) and (b).

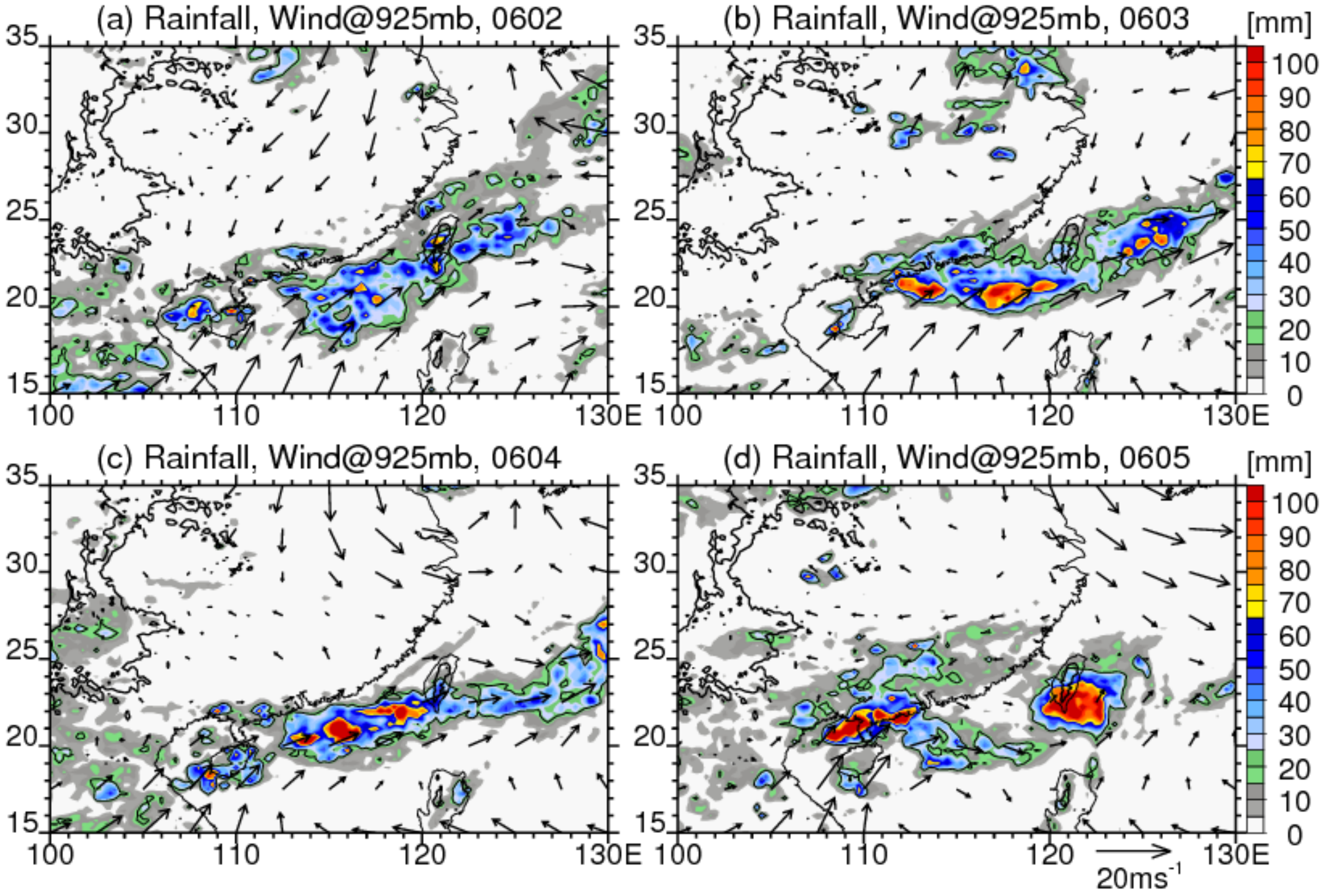

Figure 6.5. Wind field at 925 hPa based on the NCEP reanalysis data coupled with daily rainfall derived from the TRMM 3B42, from June 2 to 5: (a)-(d). The scale of the wind arrow is marked on (d), while the rainfall is revealed by the color bar.

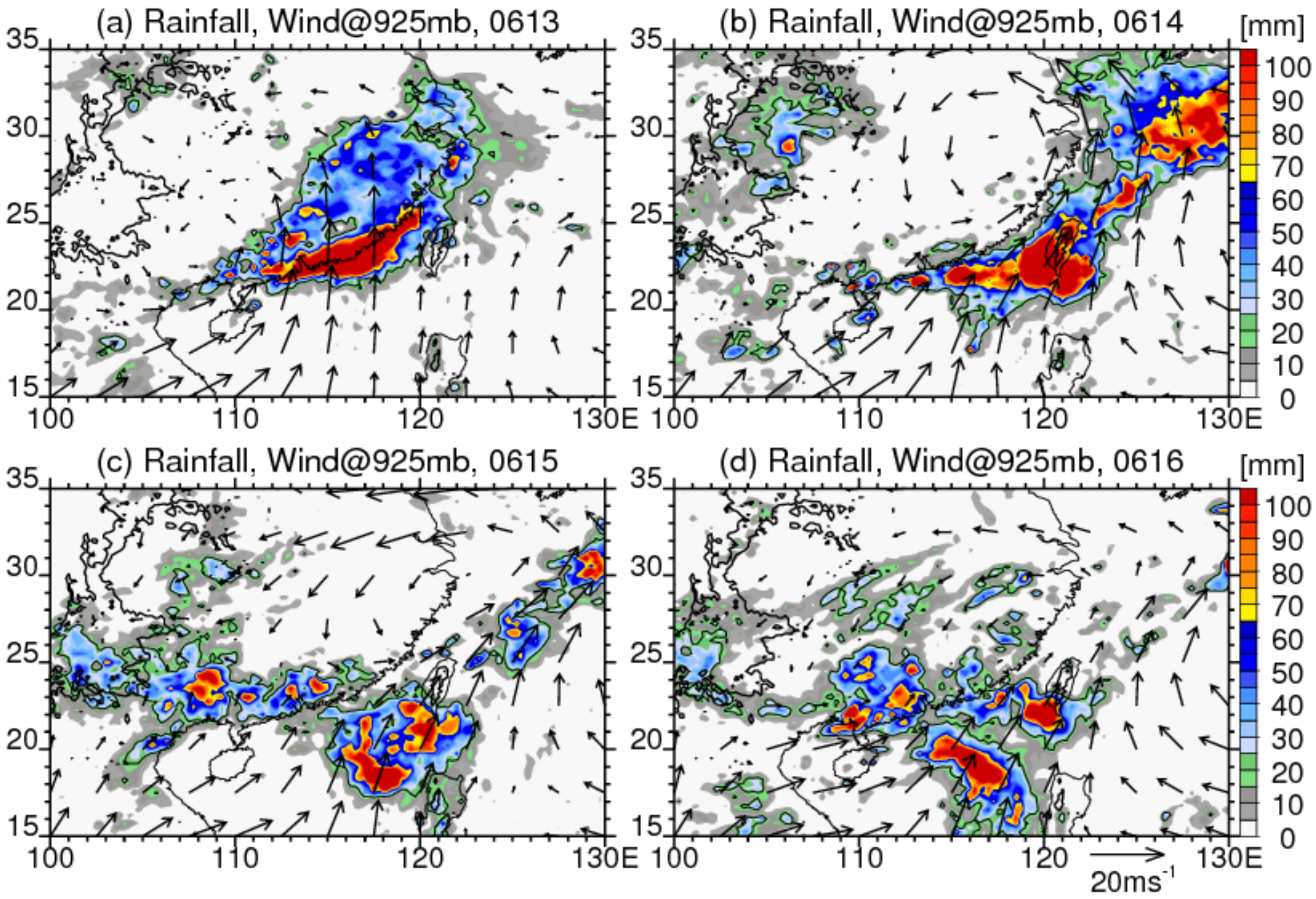

Figure 6.6. Same as Fig. 6.5, but for days of June 13-16.

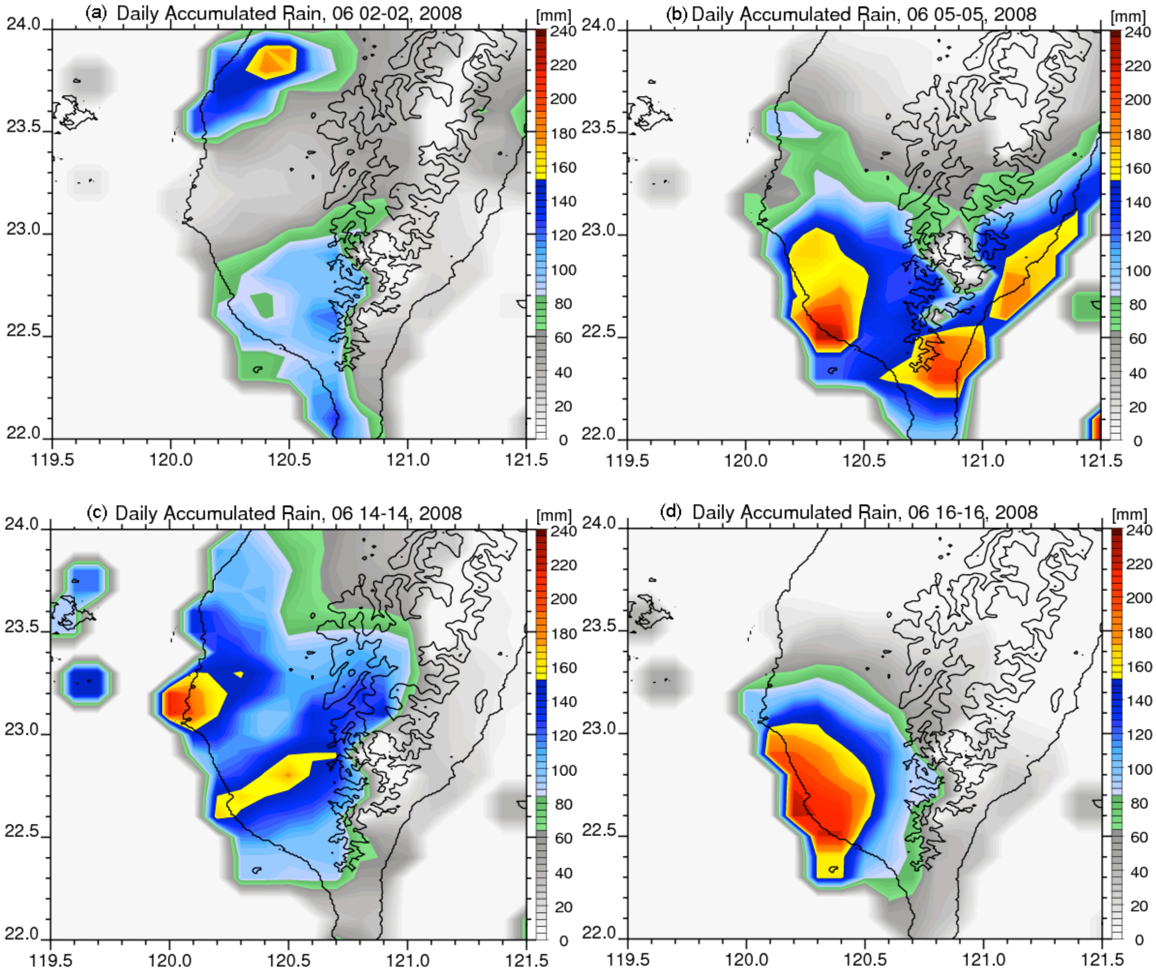

Figure 6.7. The daily accumulated rainfall (in mm) measured by rain gauges over southern Taiwan on (a) June 2, (b) June 5, (c) June 14, and (d) June 16, 2008.

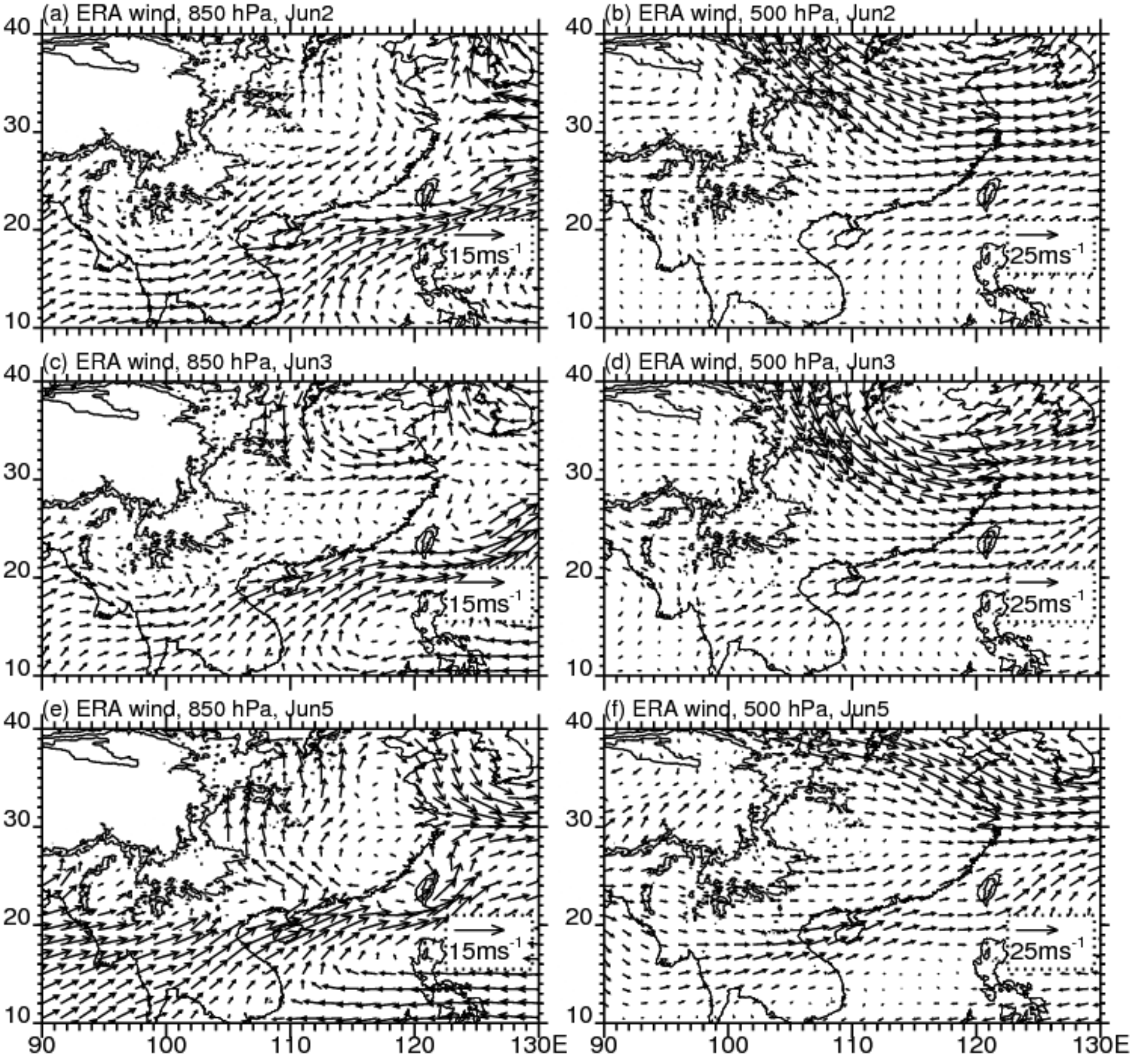

Figure 6.8. Daily mean wind field from June 2-5 based on ERA-Interim reanalysis at (a) 850 hPa, and (b) 500 hPa. The scale of the wind arrow is located at the bottom right corner of each panel.

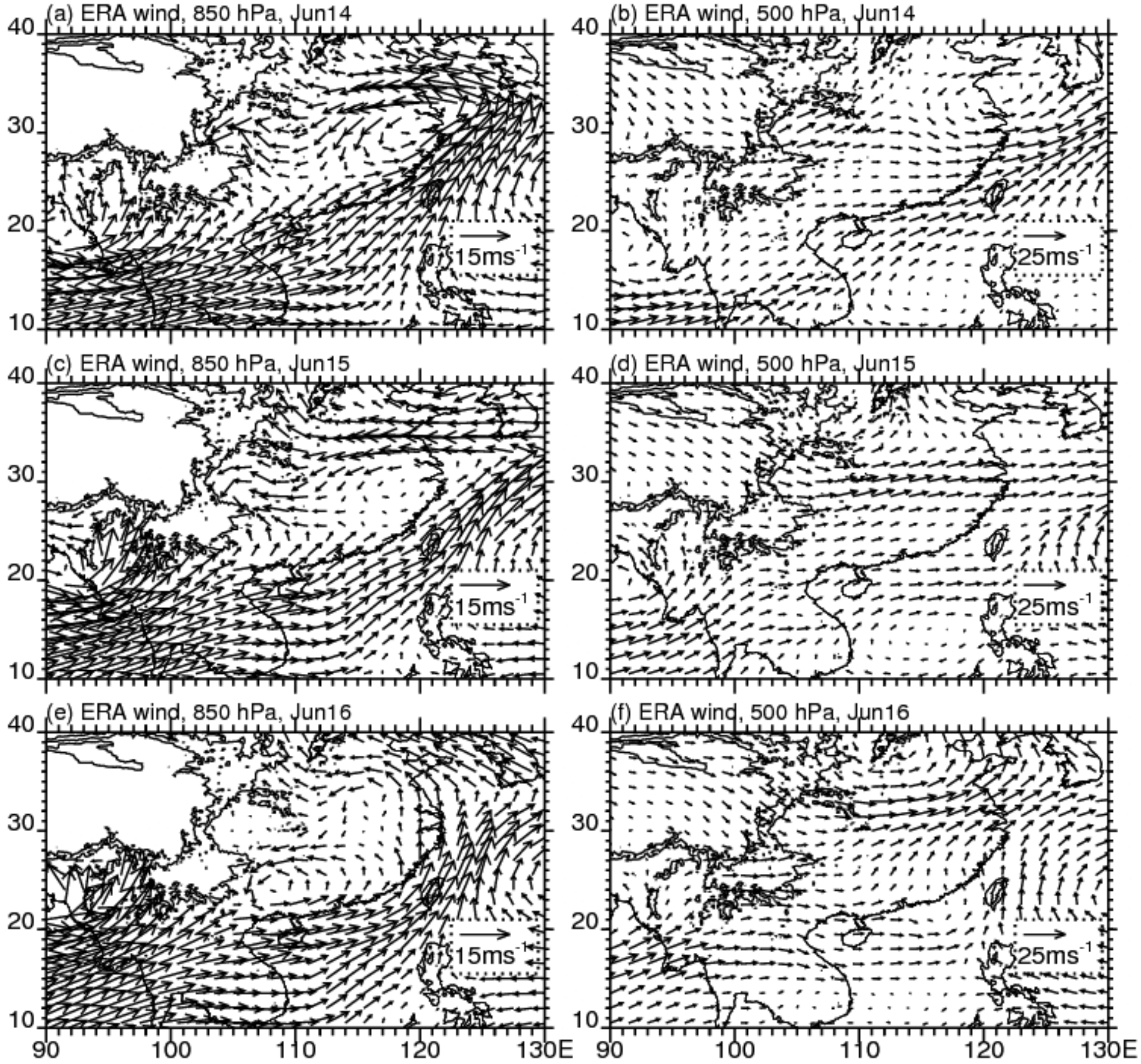

Figure 6.9. Same as Fig. 6.8, but for June 14-16.

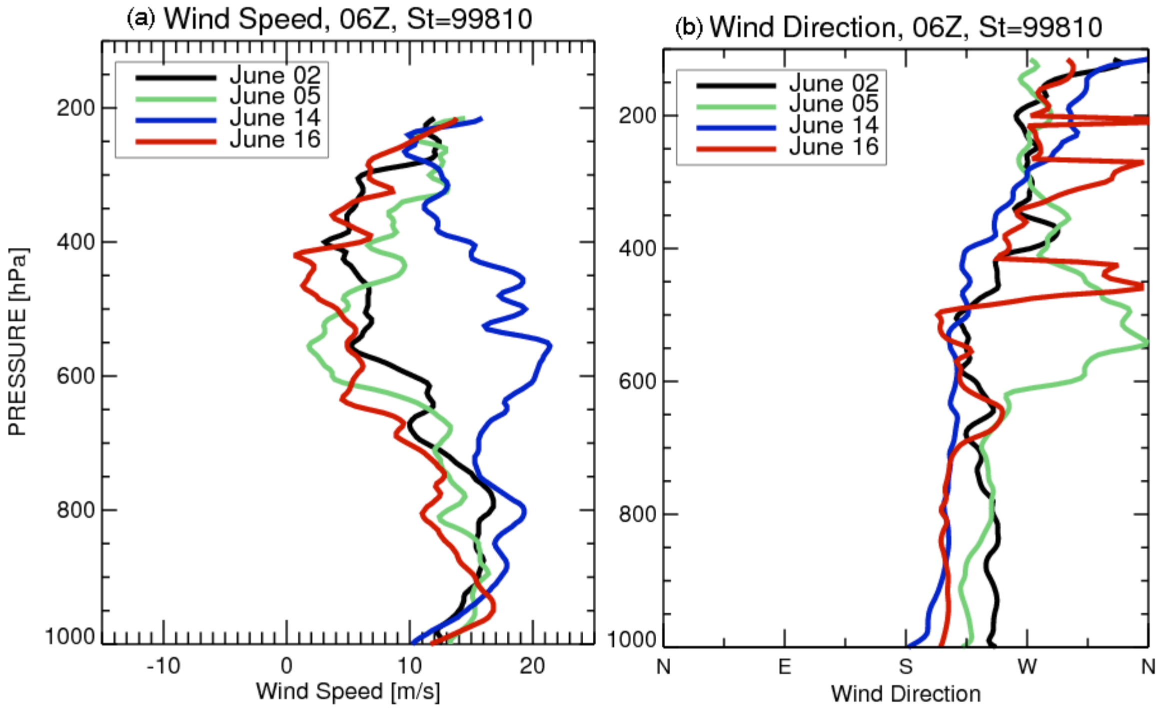

Figure 6.10. (a) Wind speed profiles, and (b) wind direction profiles from ship soundings over the upstream ocean (station 99810) at 06Z on different heavy rainfall days.

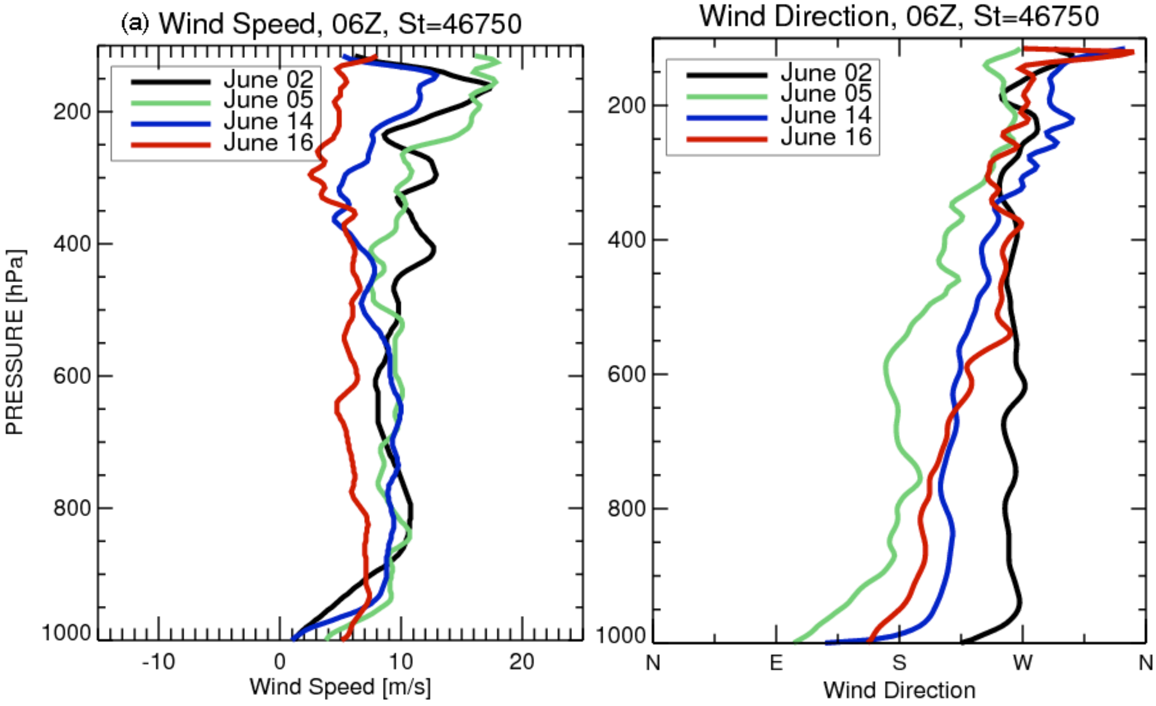

Figure 6.11. Same as Fig. 6.10, but for soundings over the coast of southwest Taiwan (station 46750).

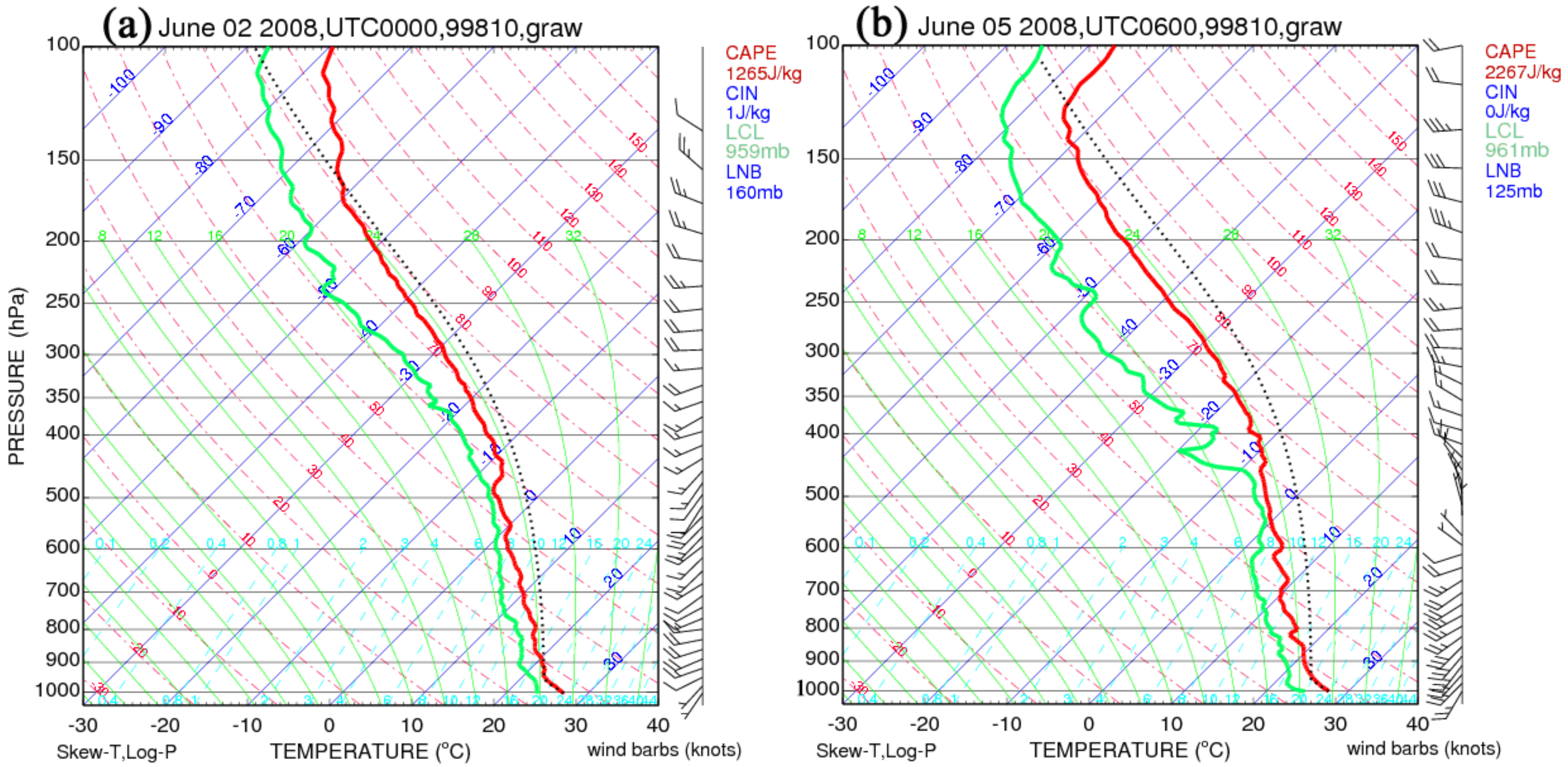

Figure 6.12. Sounding profiles over the upstream ocean (station 99810) at 00Z or 06Z on different heavy rainfall days: (a) June 02, (b) June 05, (c) June 14, and (d) June 16.

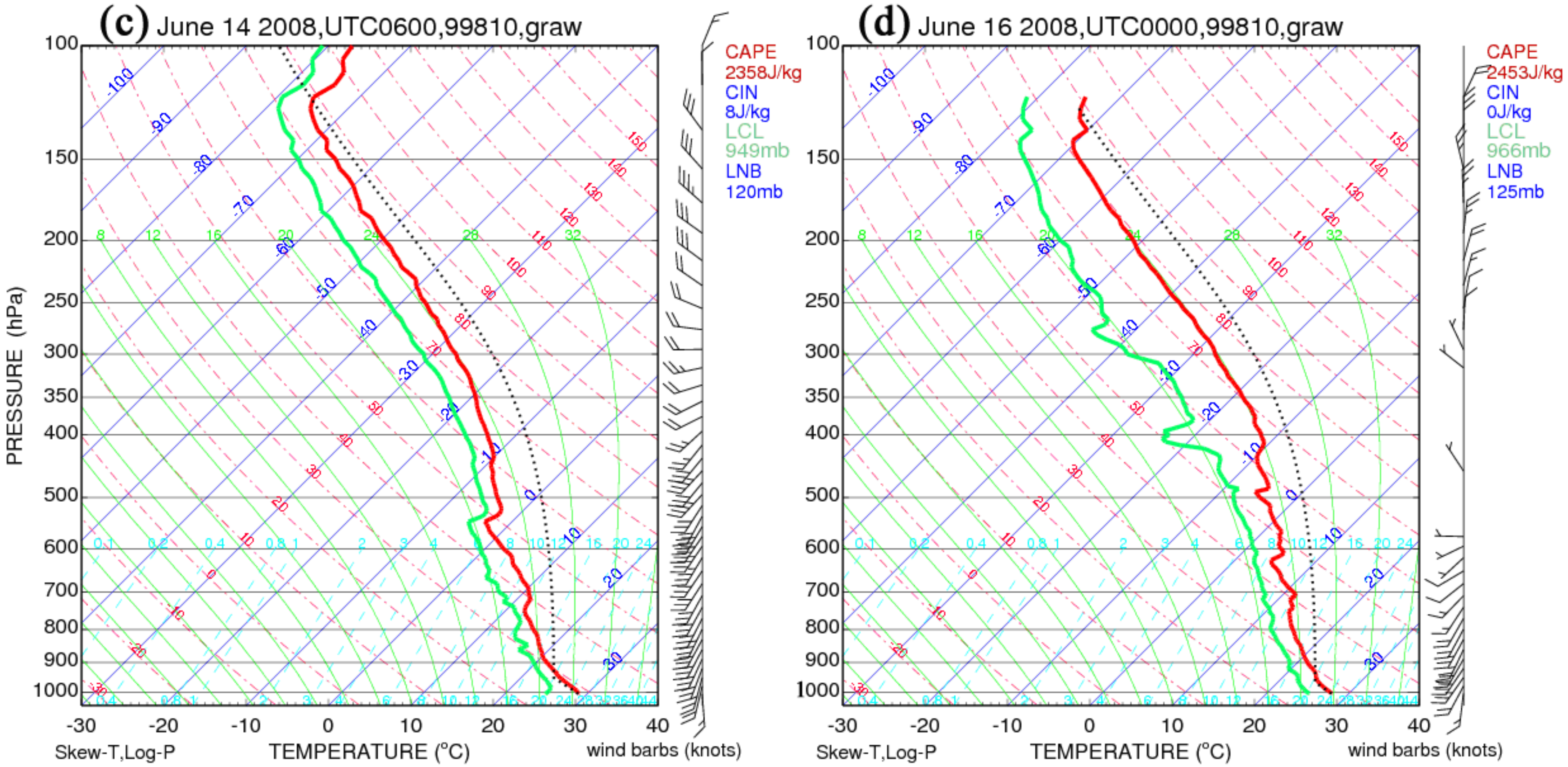

Figure 6.12. continued.

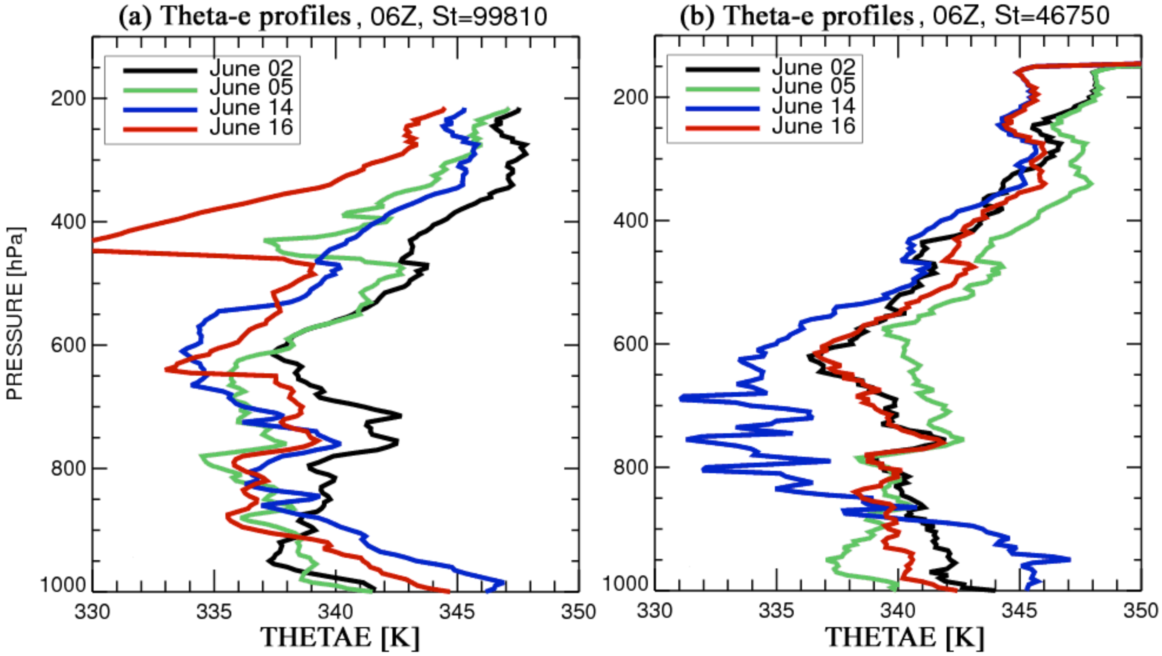

Figure 6.13. Vertical profiles of theta-e derived from the soundings over (a) the upstream ocean (station 99810) and (b) southwest Taiwan coast (station 46750) for different events.

Table 6.1. Population of radar precipitation systems (RPFs) based on RCCG radar during different selected heavy rainfall events.

	June 2	June 5	June 14	June 16
RPFs	3955	2339	2829	2901

Table 6.2. Population of radar precipitation systems (RPFs) based on RCCG radar during “intensely convective” and “rainy but less convective” events. Number of intense convective RPFs (max height of 40 dBZ > 8 km) is also shown.

Weakly convective	June 4	June 5	June 16
Total RPFs	1909	2339	2901
Intense RPFs	39	75	52
Intensely convective	May 26	June 13	June 14
Total RPFs	270	3008	2829
Intense RPFs	46	329	306

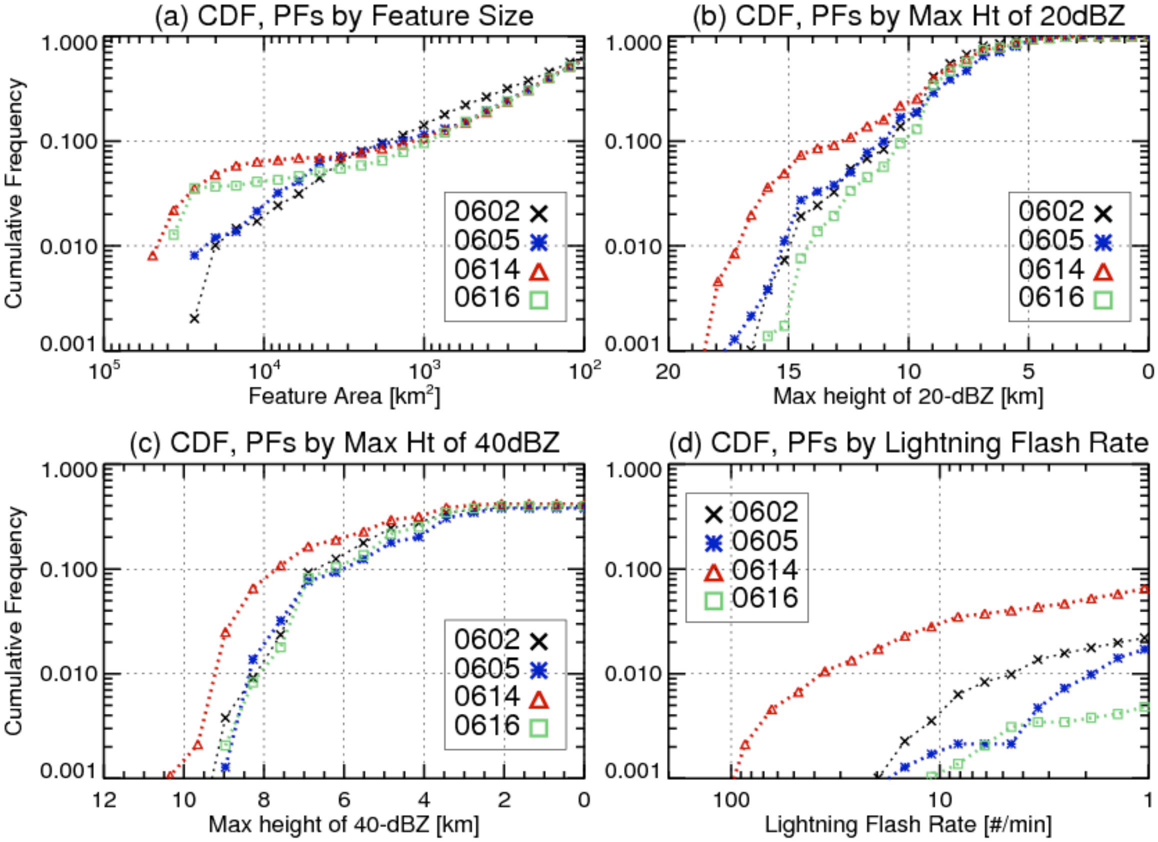

Figure 6.14. Cumulative Distribution Function (CDF) of the population of precipitation features of different heavy rainfall events categorized by (a) Feature size, (b) Maximum height of 20-dBZ, (c) Maximum height of 40-dBZ, (d) Cloud-to-ground lightning flash rate.

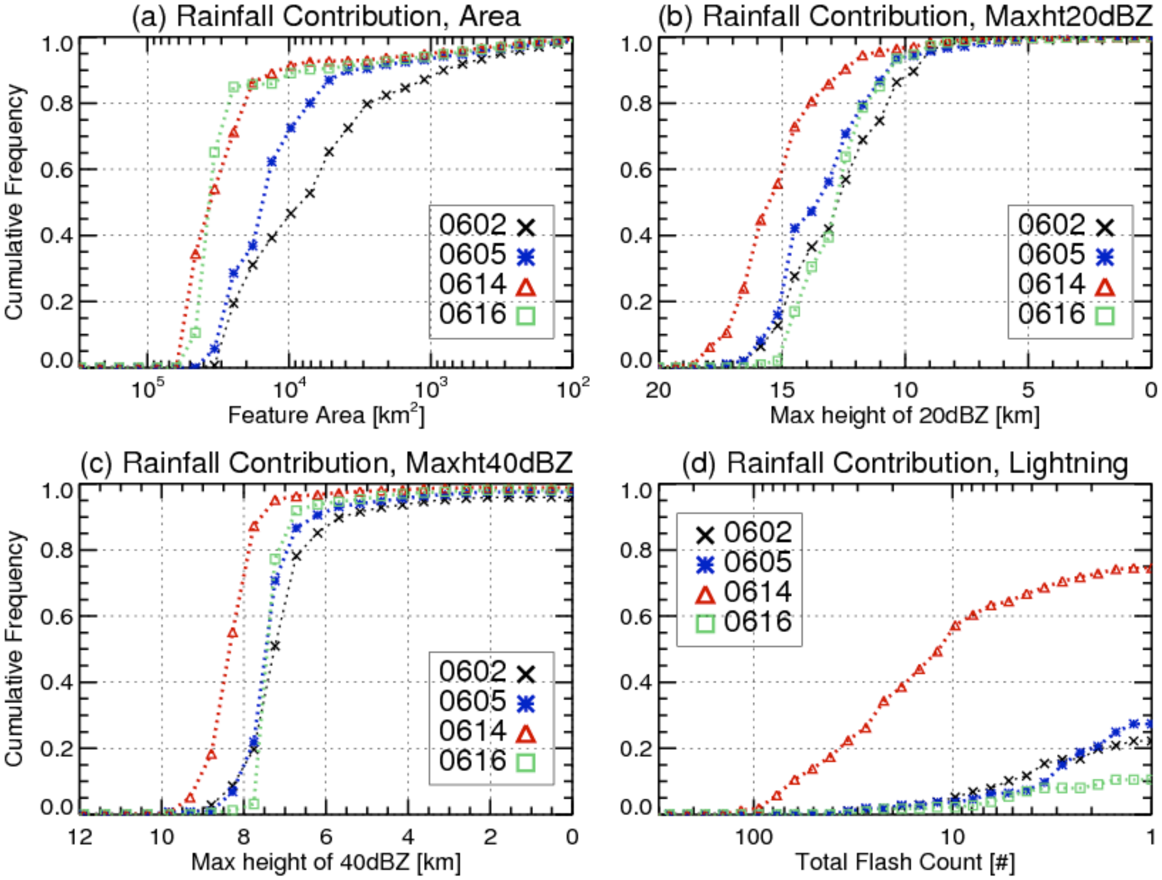

Figure 6.15. Cumulative Distribution Function (CDF) of the rainfall contribution by precipitation features with different properties (a) Feature size, (b) Maximum height of 20-dBZ, (c) Maximum height of 40-dBZ, (d) Cloud-to-ground lightning flash rate.

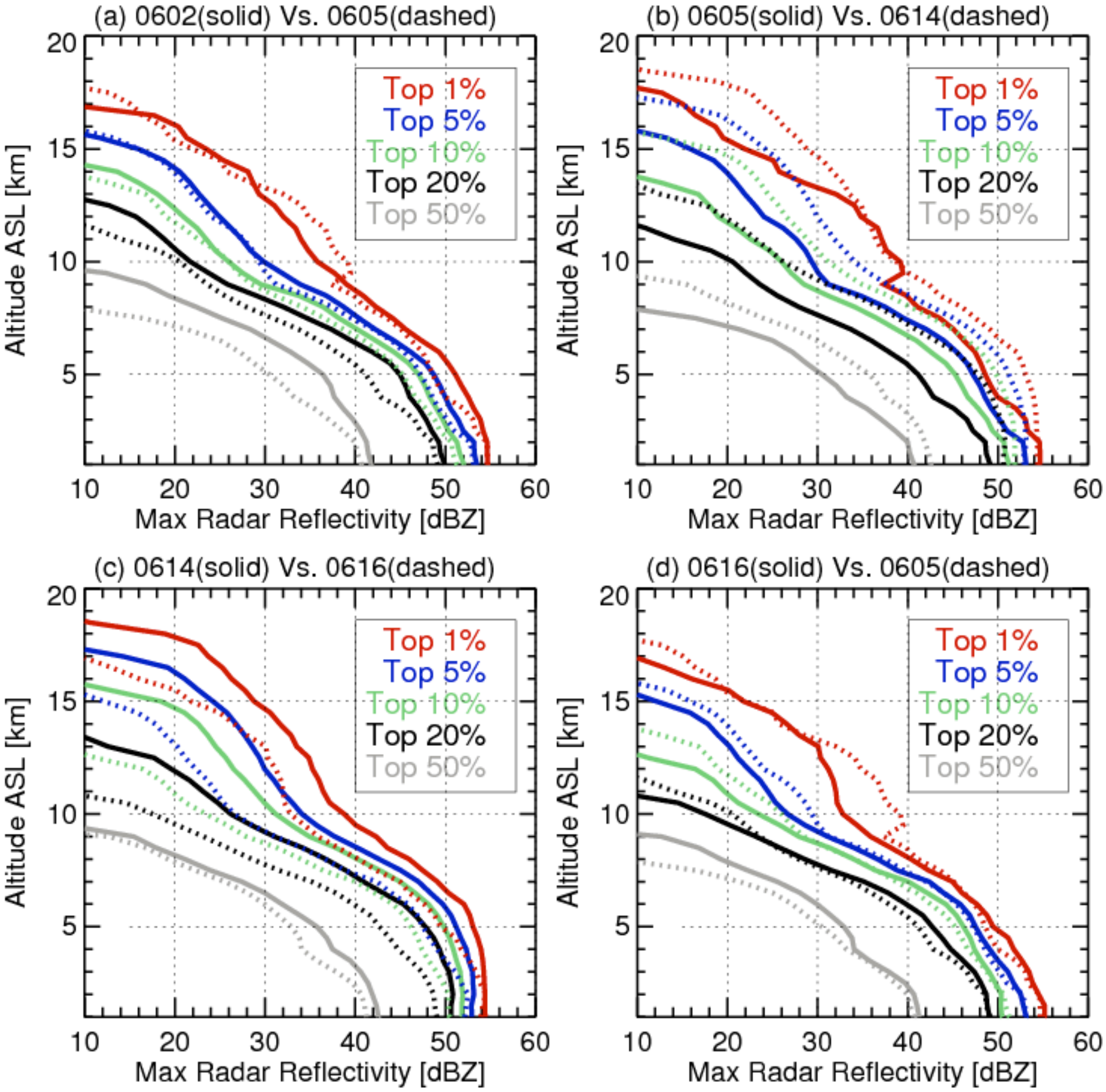

Figure 6.16. Vertical profiles of maximum radar reflectivity of RPFs in the percentile of 1, 5, 10, 20, and 50, for the comparison between two specific heavy precipitation events: (a) June 2 (solid) vs. June 5 (dashed); (b) June 5 (solid) vs. June 14 (dashed); (c) June 14 (solid) vs. June 16 (dashed); (d) June 16 (solid) vs. June 5 (dashed).

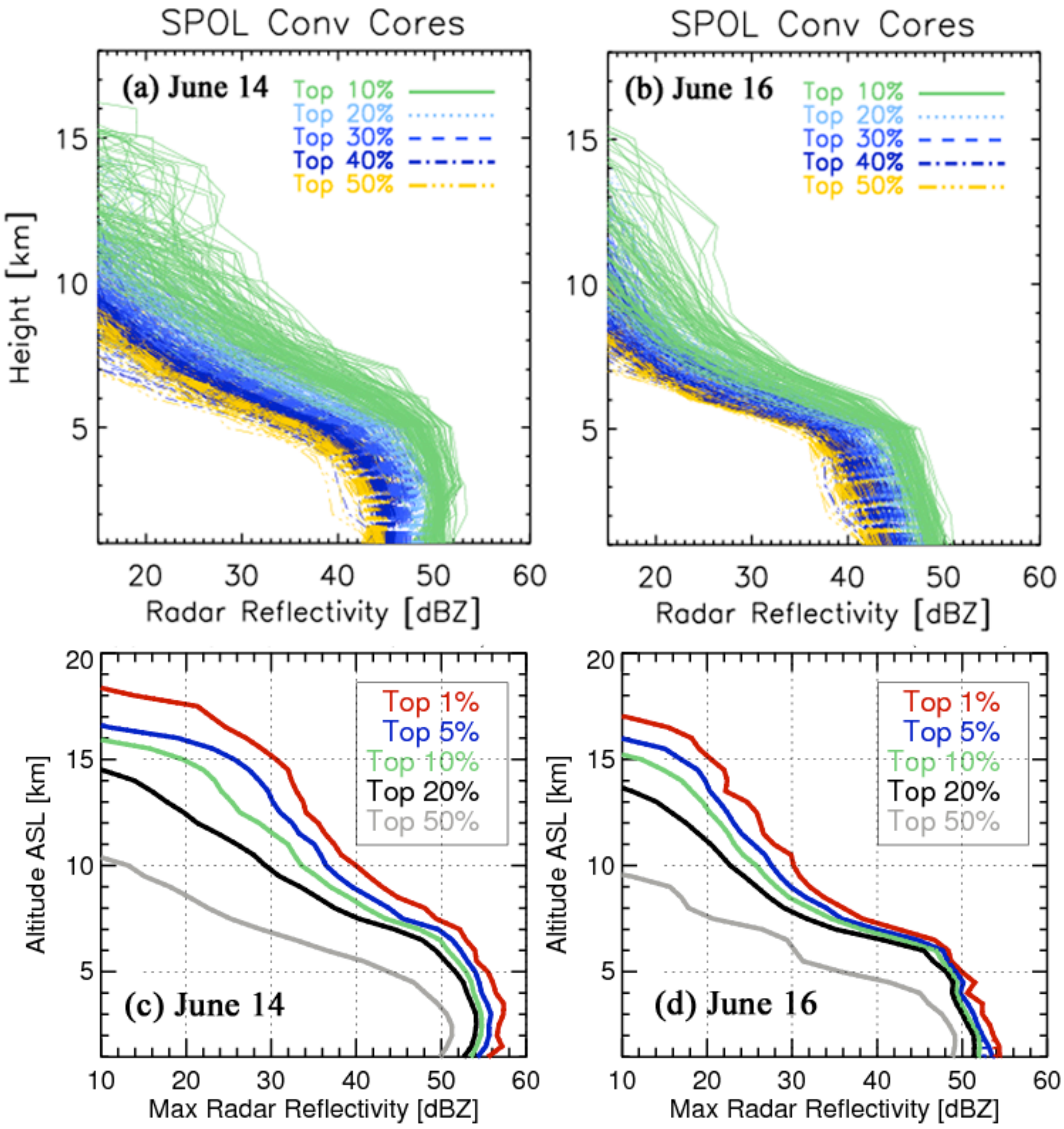

Figure 6.17. SPOL-based vertical profiles of (a)-(b) radar reflectivity in convective cores (>40 dBZ); (c)-(d) maximum radar reflectivity of precipitation features.

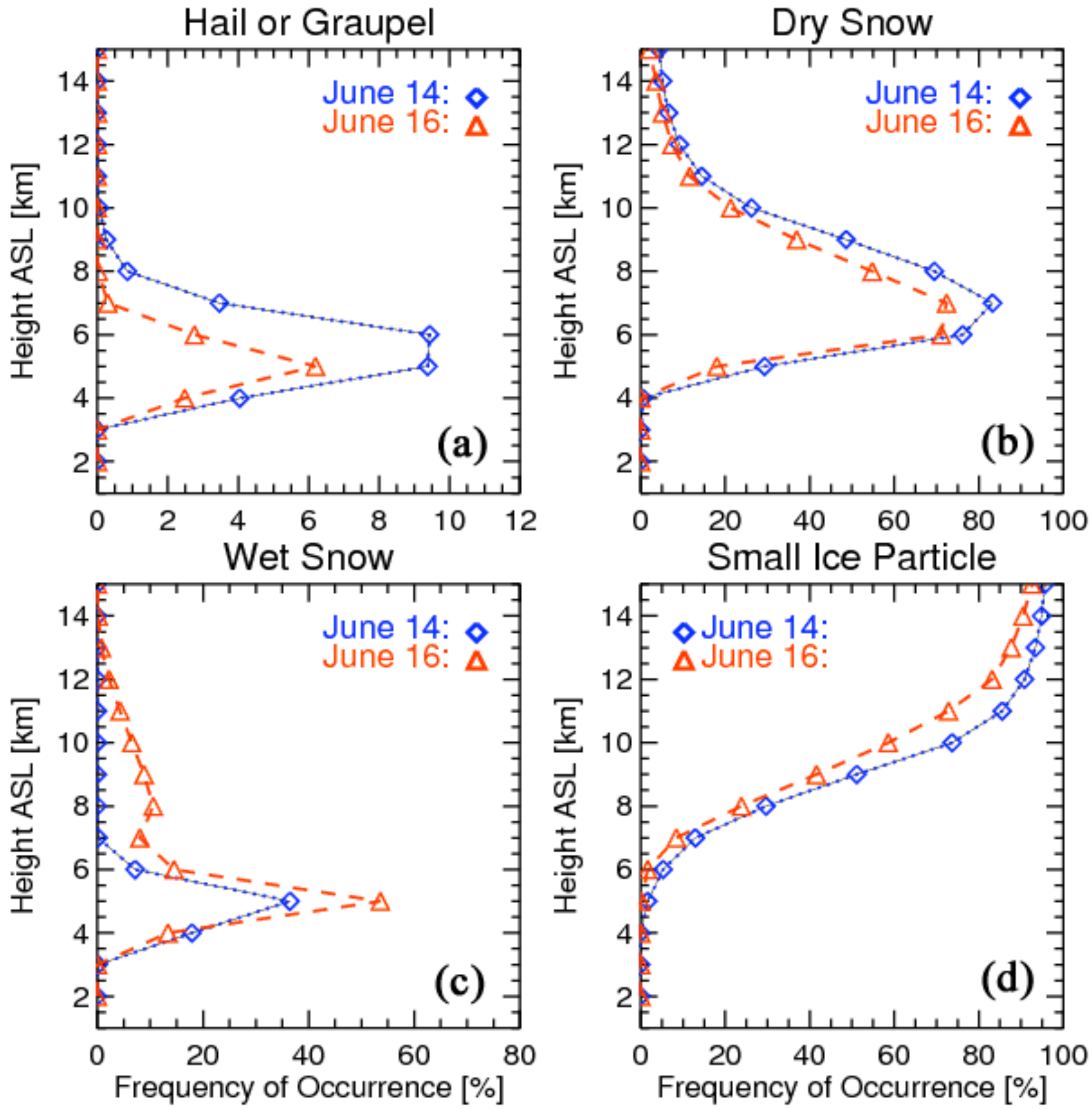

Figure 6.18. Vertical profiles of frequency of different hydrometeors within the convective regions retrieved from SPOL polarimetric observations during heavy precipitation events: (a) Hail or graupel; (b) Dry snow; (c) Wet snow; (d) Small ice particle.

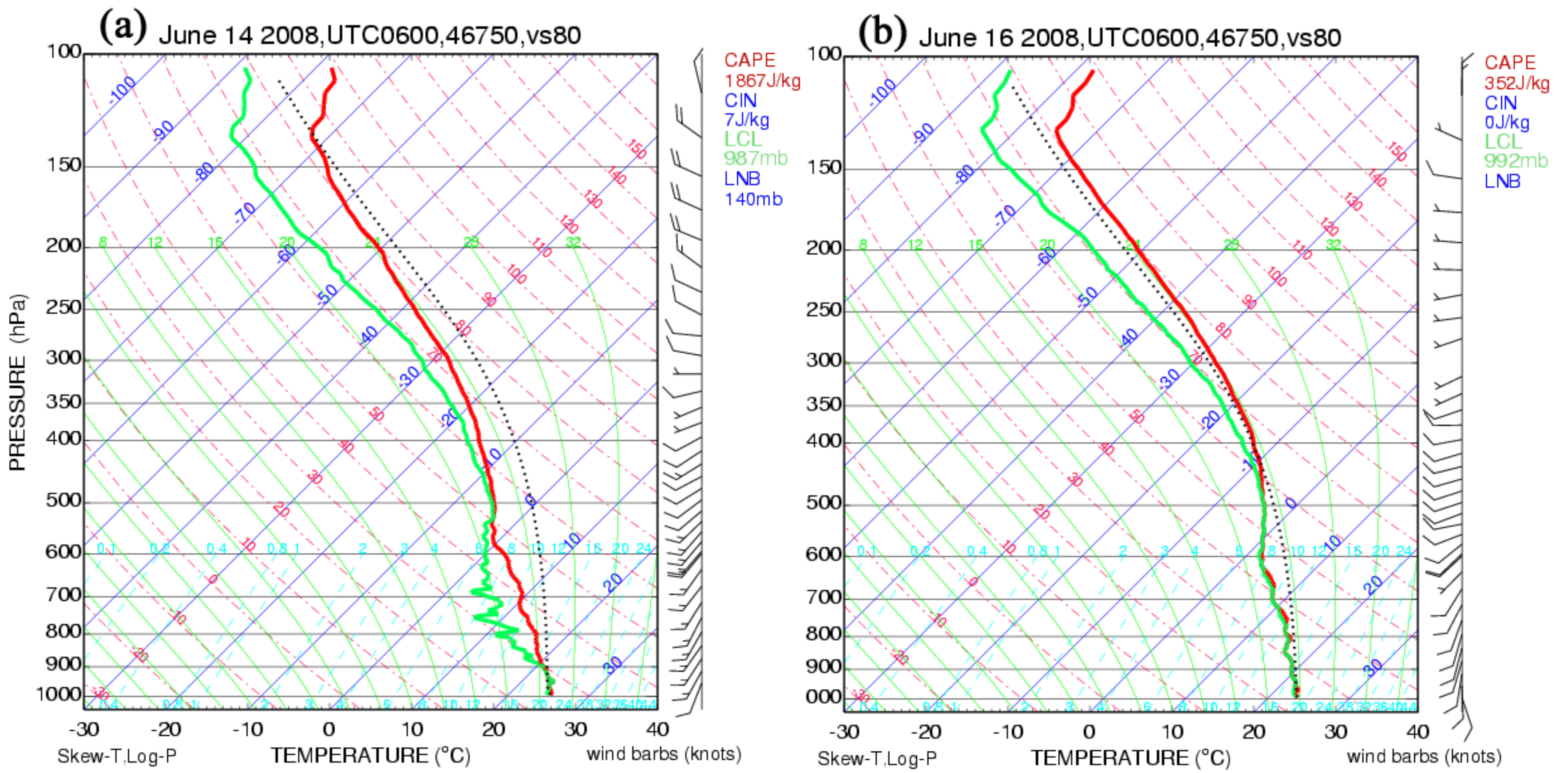

Figure 6.19. Sounding profiles over the southwest Taiwan coast (station 46750) at 06Z on: (a) June 14, (b) June 16.

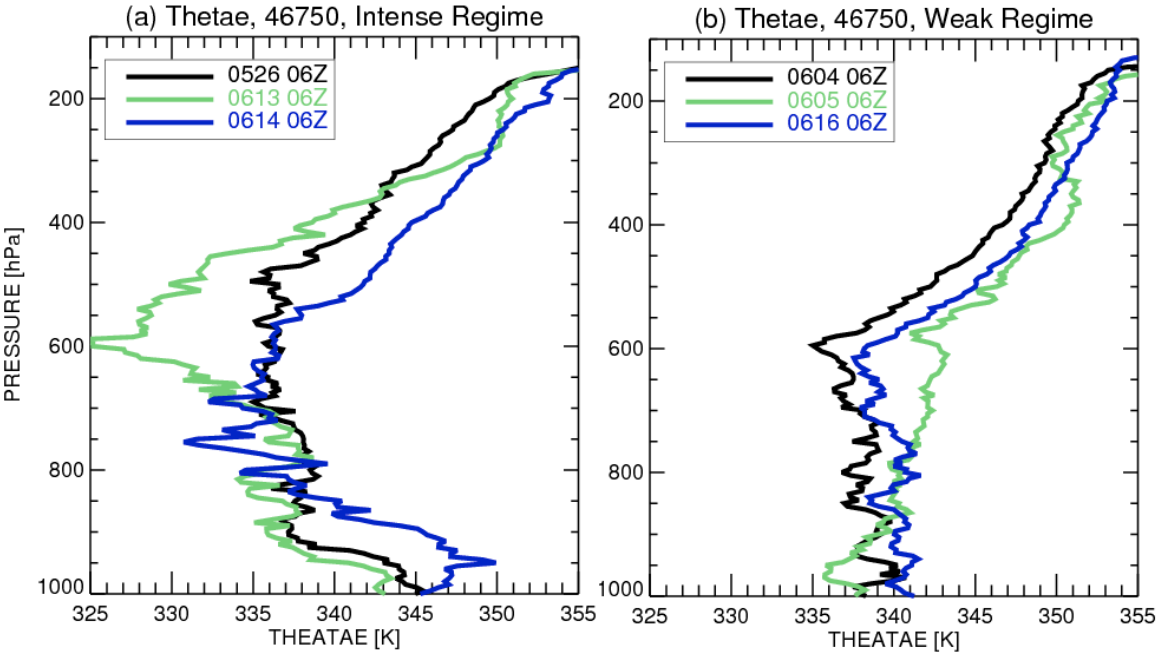

Figure 6.20. Vertical profiles of theta-e derived from the soundings over the southwest Taiwan coast (station 46750) at 06Z during days of (a) intense convection regime, and (b) rainy but less convectively intense regime.

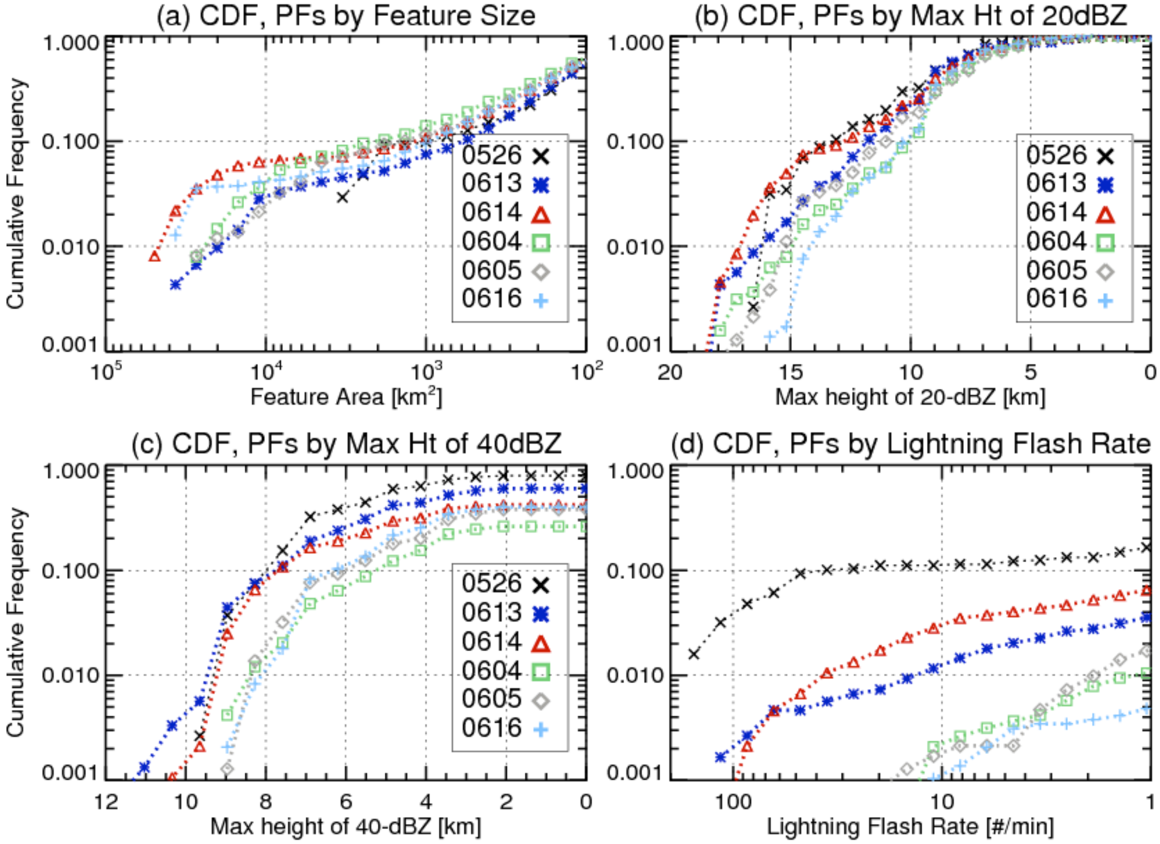

Figure 6.21. Cumulative Distribution Function (CDF) of the population of precipitation features of different systems categorized by (a) Feature size, (b) Maximum height of 20-dBZ, (c) Maximum height of 40-dBZ, (d) Cloud-to-ground lightning flash rate; during days with intense convection (May 26, June 13, 14), and days with heavy precipitation but moderate convection (June 4, 5, and 16).

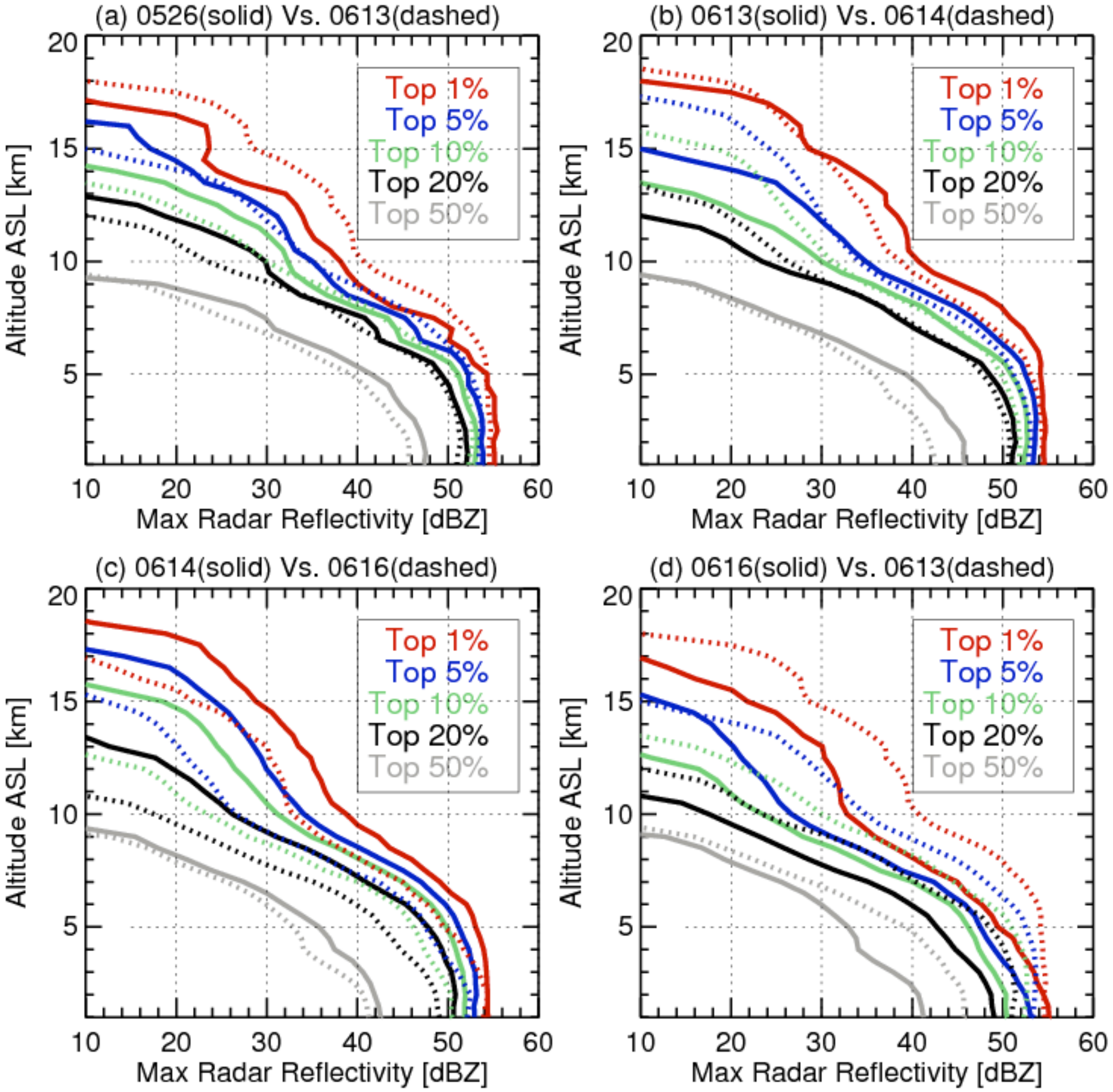

Figure 6.22. Same as Fig. 6.16, but for comparisons between different days: (a) May 26 (solid) vs. June 13 (dashed); (b) June 13 (solid) vs. June 14 (dashed); (c) June 14 (solid) vs. June 16 (dashed); (d) June 16 (solid) vs. June 13 (dashed).

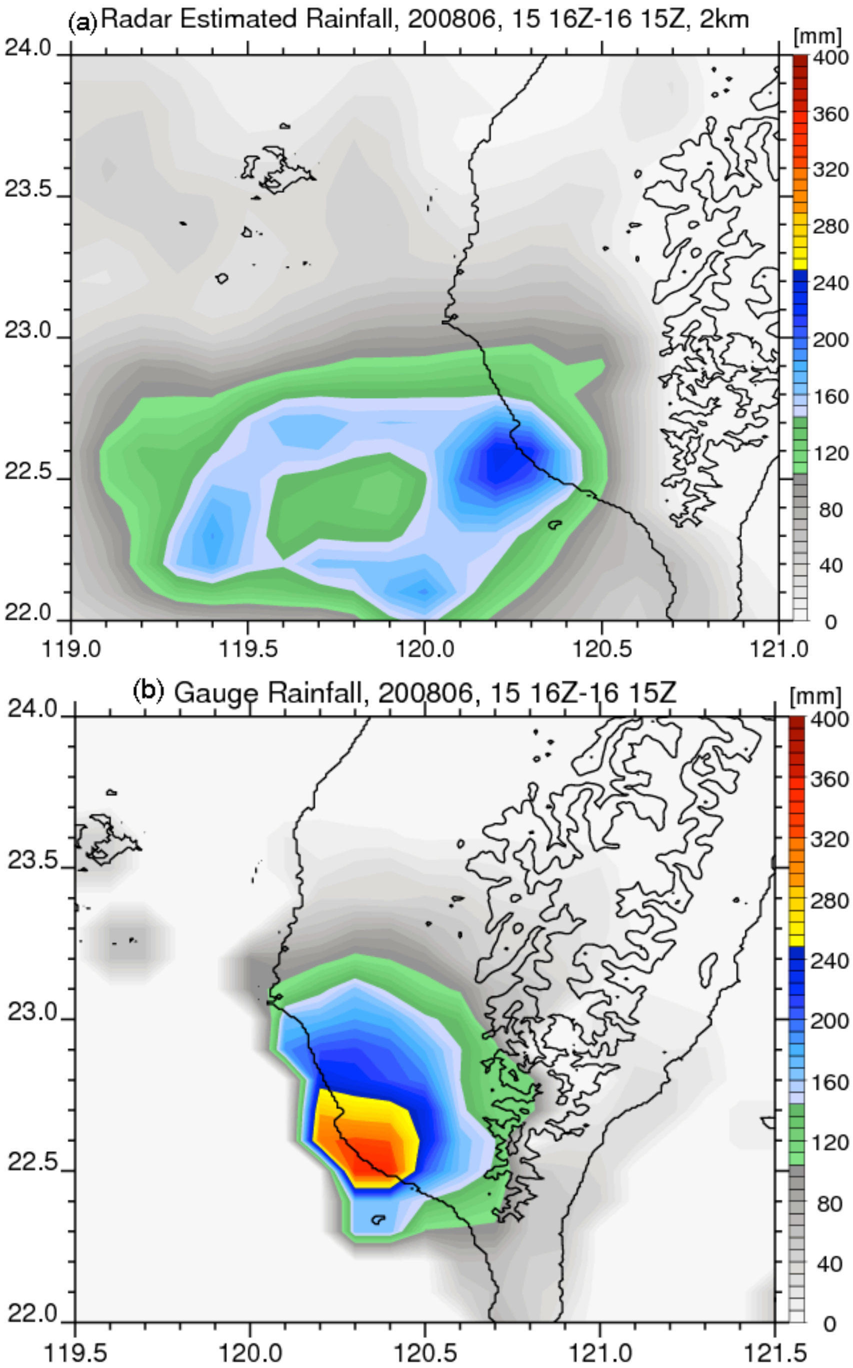

Figure 6.23. Event-based rainfall derived from the S-POL radar and rain gauges from June 15 16Z to June 16 15Z. Terrains are contoured at 1000 and 2000 m.

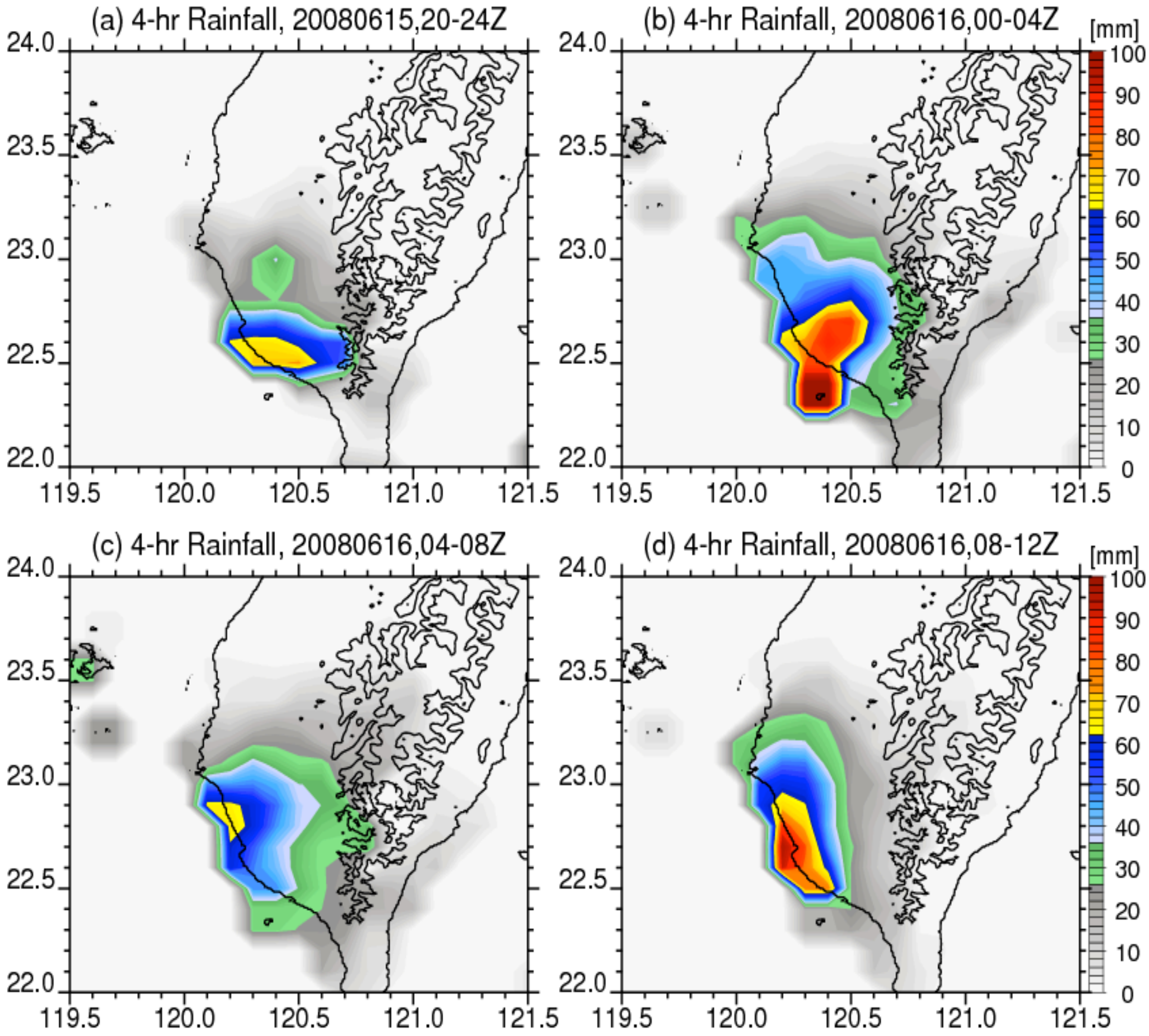

Figure 6.24. Distribution of 4-hourly rainfall based on rain gauges during (a) June 15, 20-24Z; (b) June 16, 00-04Z; (c) June 16, 04-08Z; (d) June 16, 08-12Z.

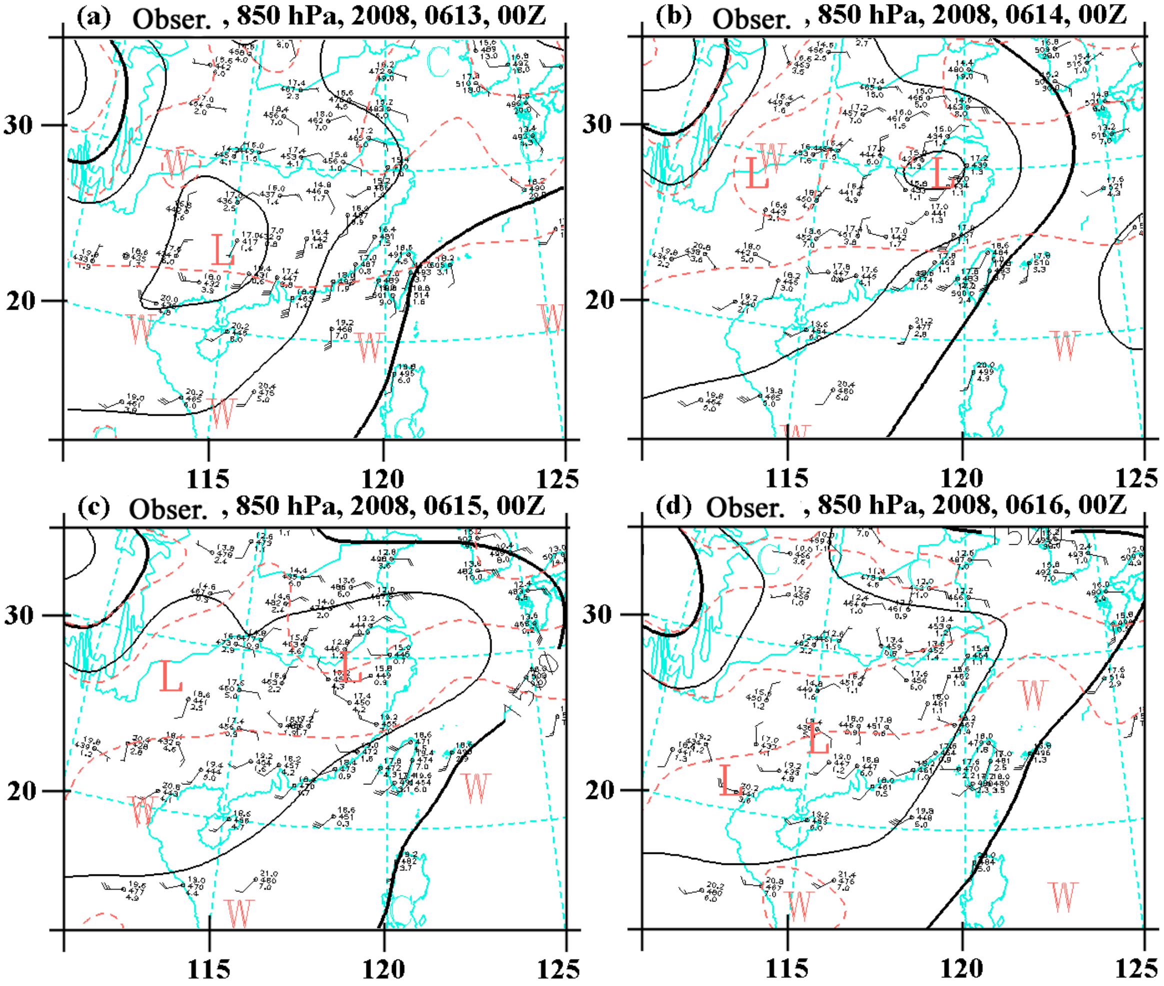

Figure 6.25. 850 hPa upper air observations over East Asia at 00Z on (a) June 13, (b) June 14, (c) June 15, and (d) June 16, 2008.

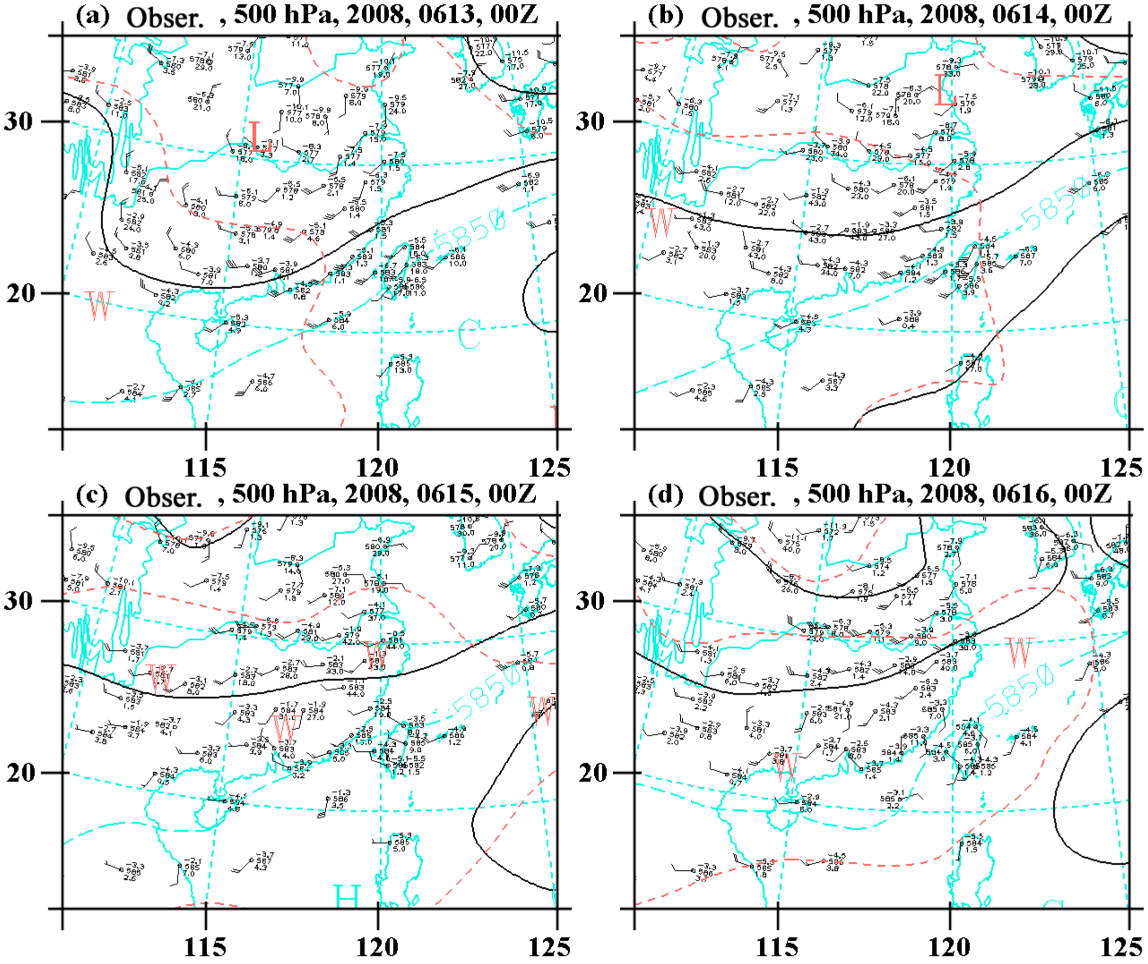

Figure 6.26. Same as Fig. 6.25, but for observations at 500 hPa.

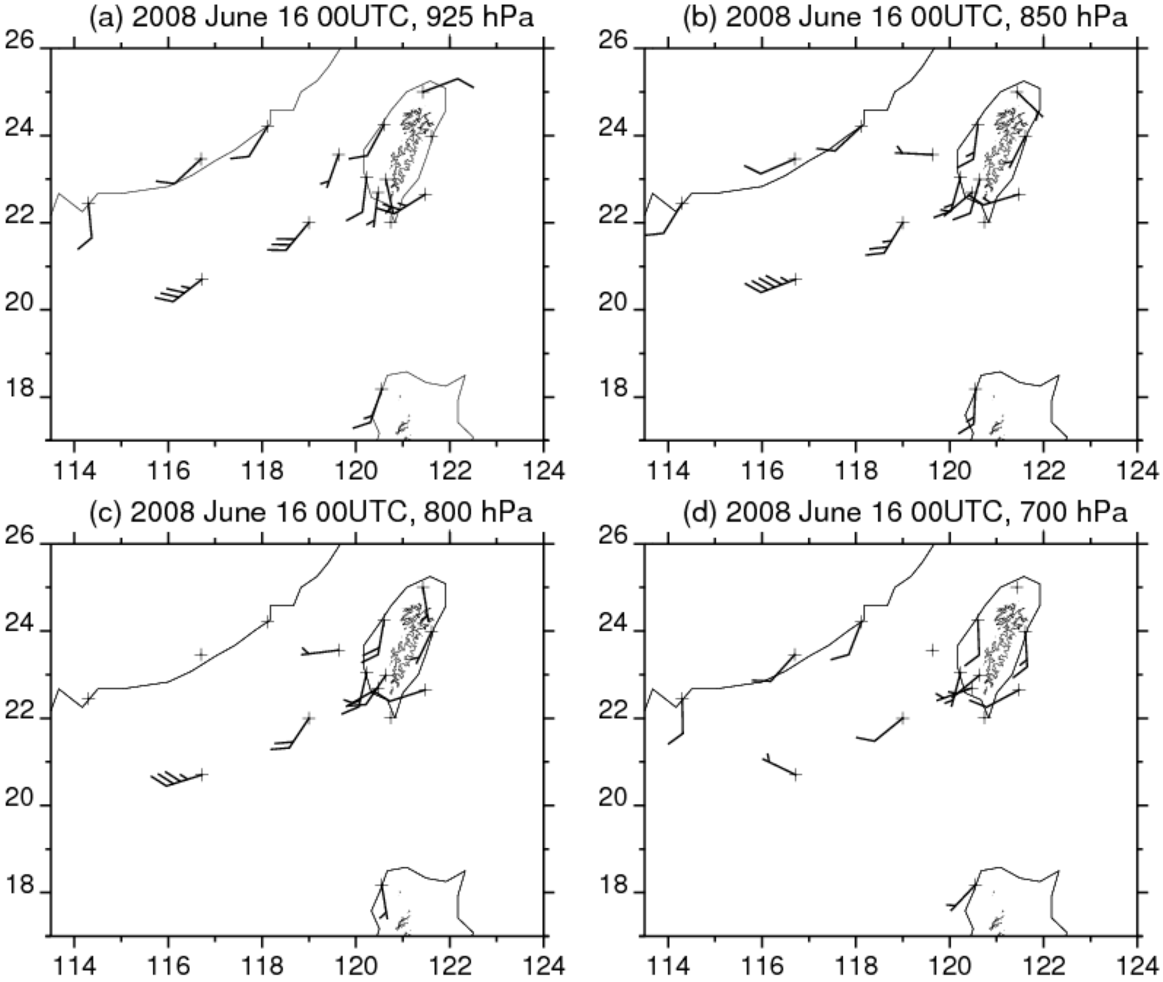

Figure 6.27. Observations of wind field from soundings over Taiwan and adjacent area at 00Z on June 16, 2008. Wind field is shown at different levels: (a) 925 hPa, (b) 850 hPa, (c) 800 hPa, (d) 700 hPa.

(a) RHI, 222 degrees, SPOL, 0616 0159Z

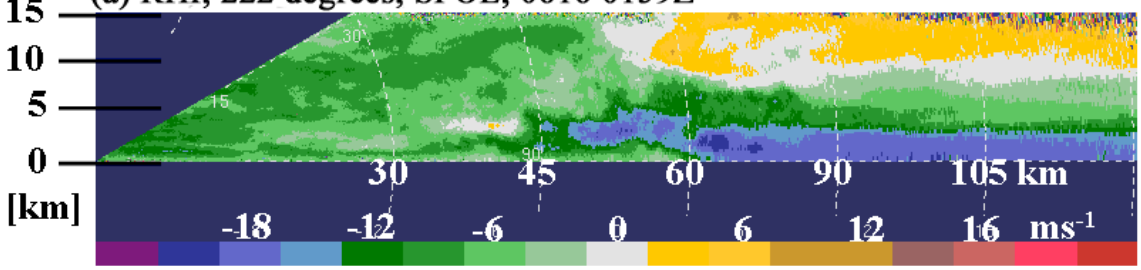

(b) RHI, 224 degrees, SPOL, 0616 0159Z

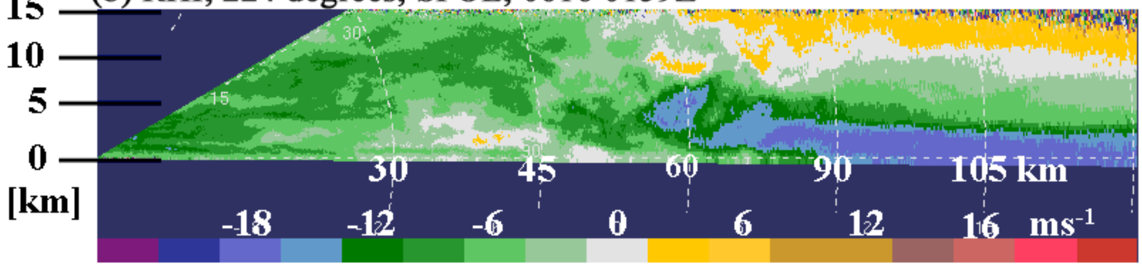

(c) RHI, 228 degrees, SPOL, 0616 0200Z

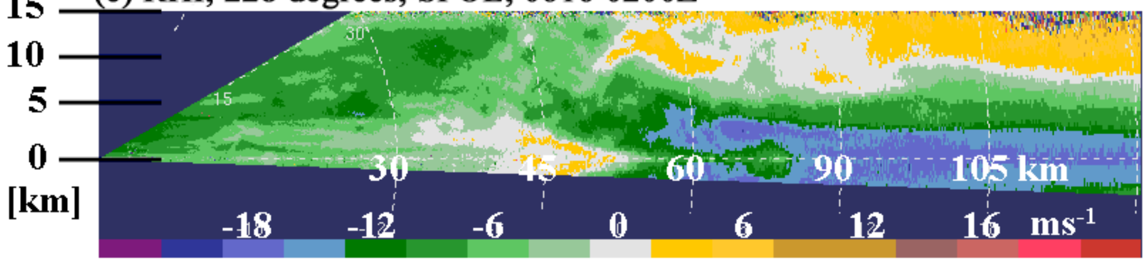

Figure 6.28. Radial velocity derived from SPOL radar RHI scans at different directions near June 16 0200Z: (a) 222 degrees, (b) 226 degrees, and (c) 228 degrees.

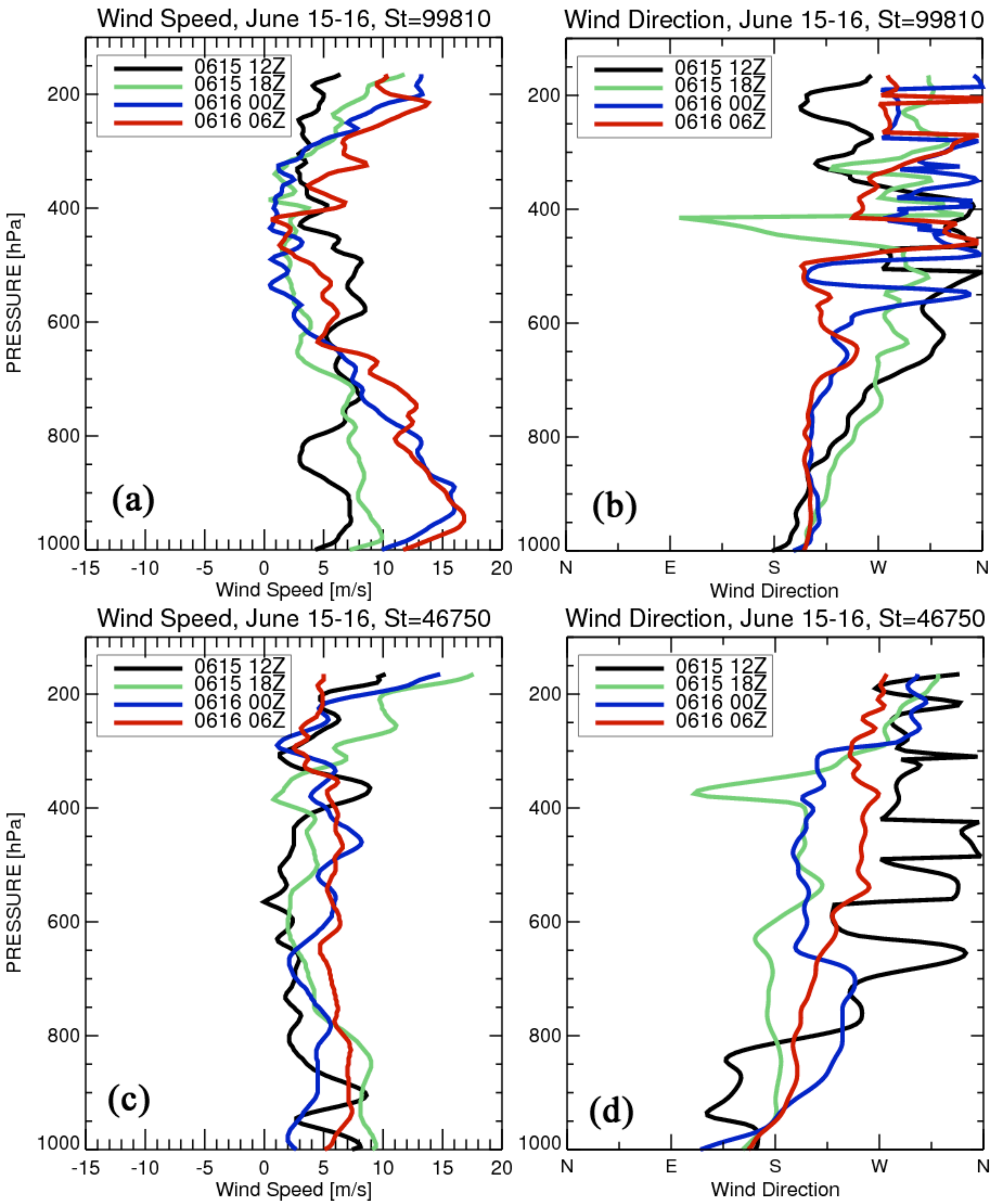

Figure 6.29. Vertical profiles of wind speed and wind direction for soundings over (a)-(b) upstream ocean, and (c)-(d) southwest coast, during different times as shown in the legend of each subfigure.

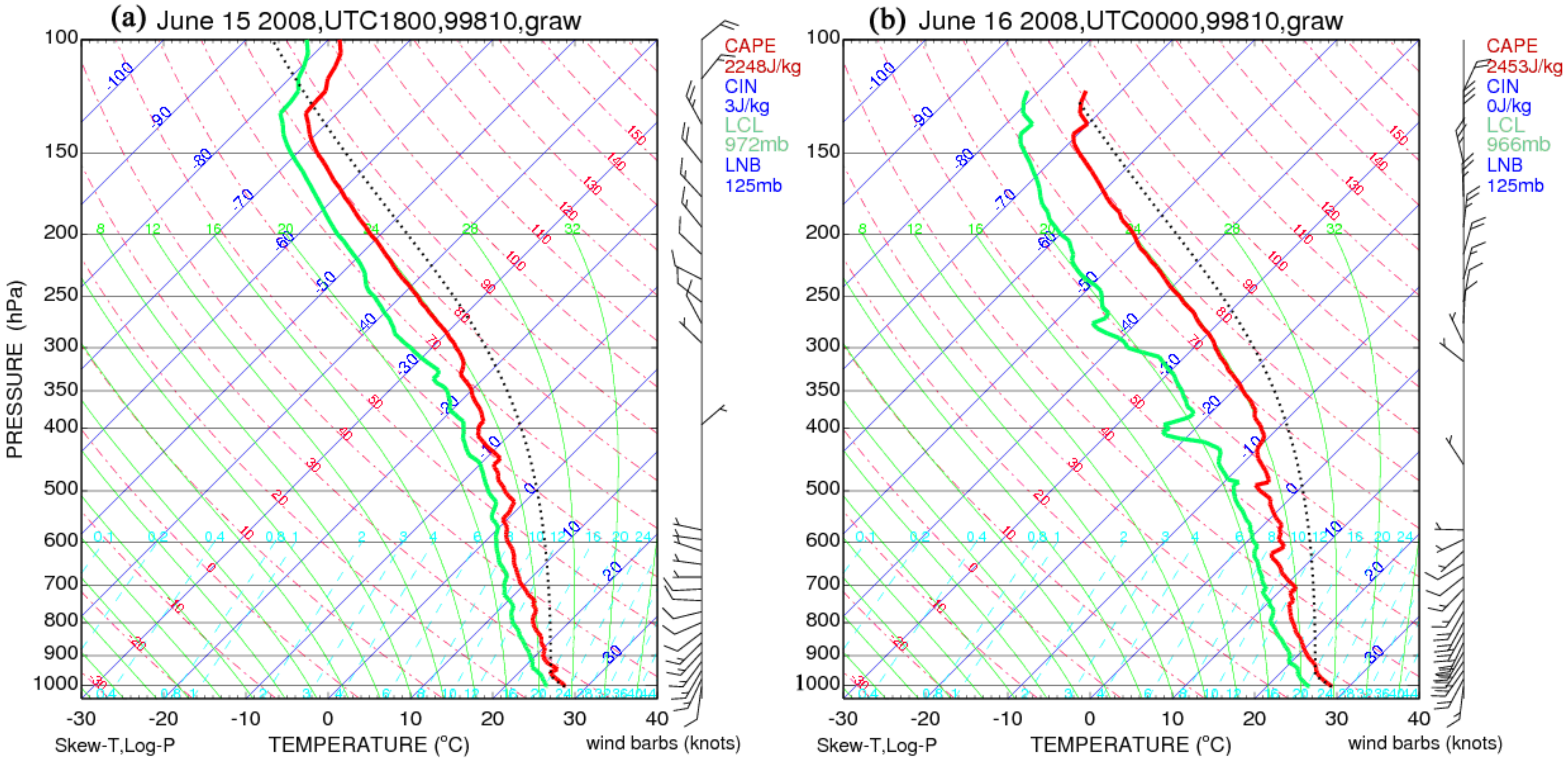

(a) June 15 2008,UTC1800,99810,graw

(b) June 16 2008,UTC0000,99810,graw

Figure 6.30. Sounding profiles over the upstream ocean of southwest Taiwan (station 99810) at (a) 06Z, June 15; and (b) 00Z, June 16.

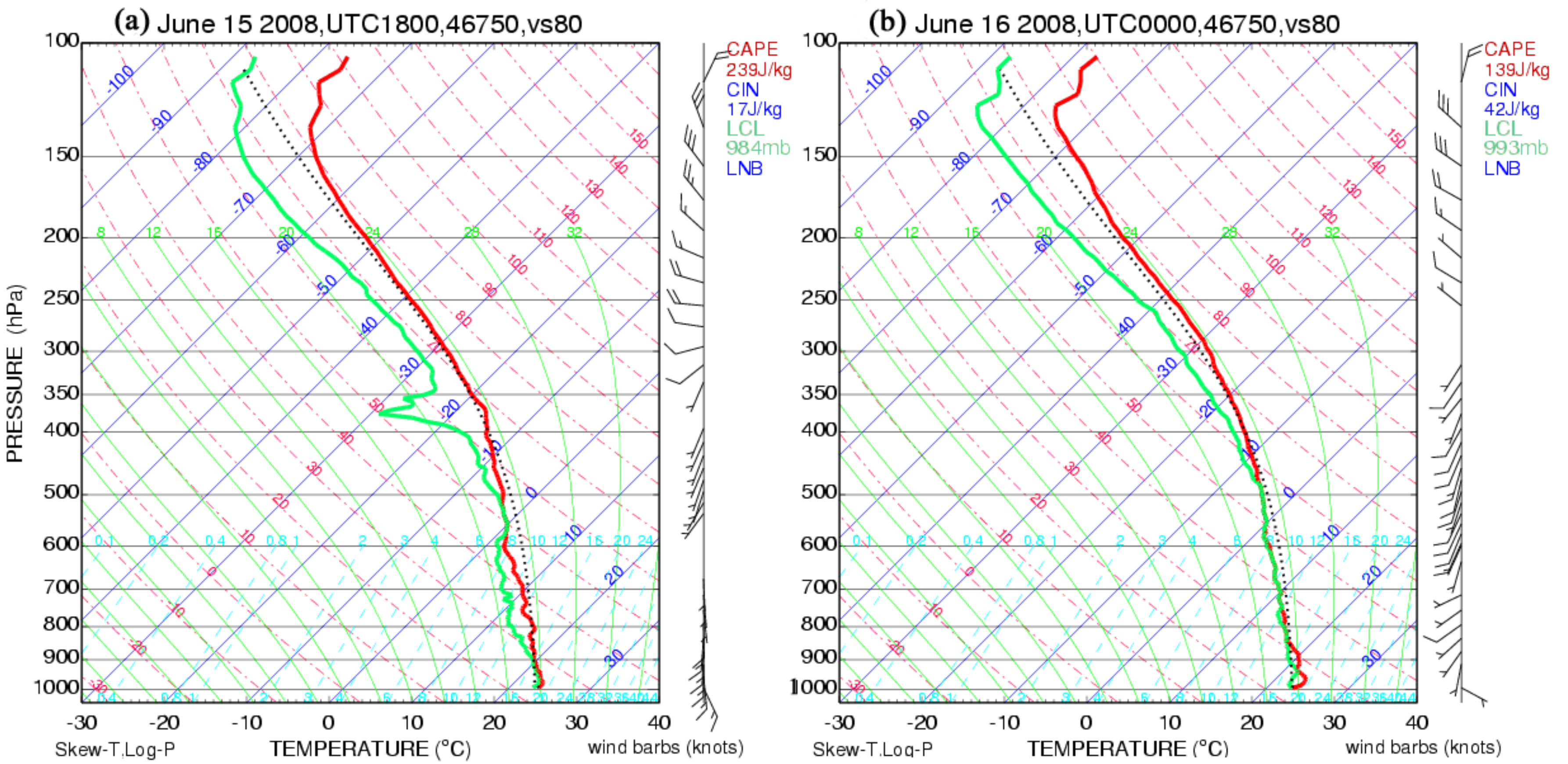

Figure 6.31. Same as Fig. 6.30, but for sounding site at the southwest Taiwan coast (station 46750).

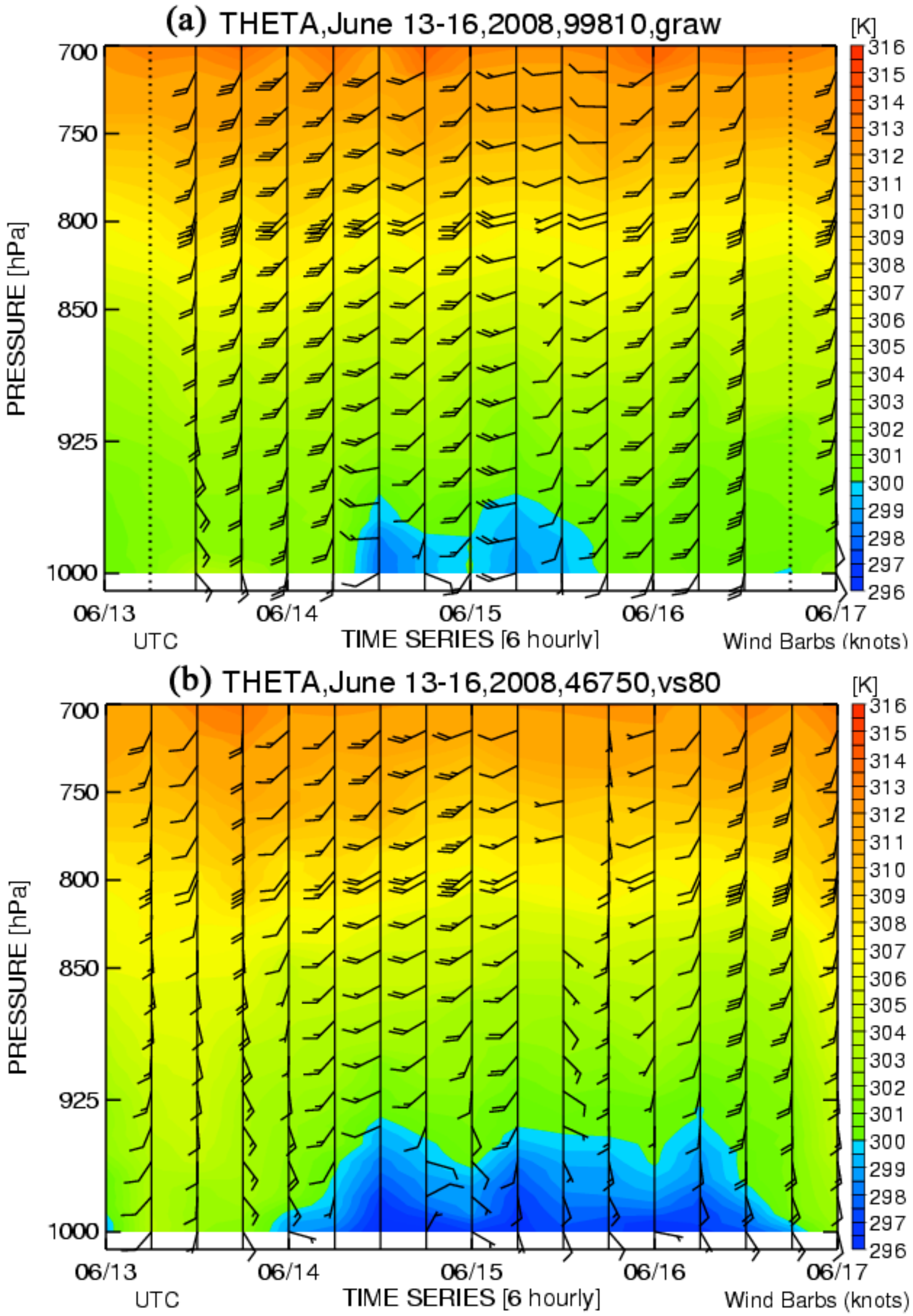

Figure 6.32. Time-height cross section of potential temperature (K) over (a) upstream ocean, and (b) coast sounding site.

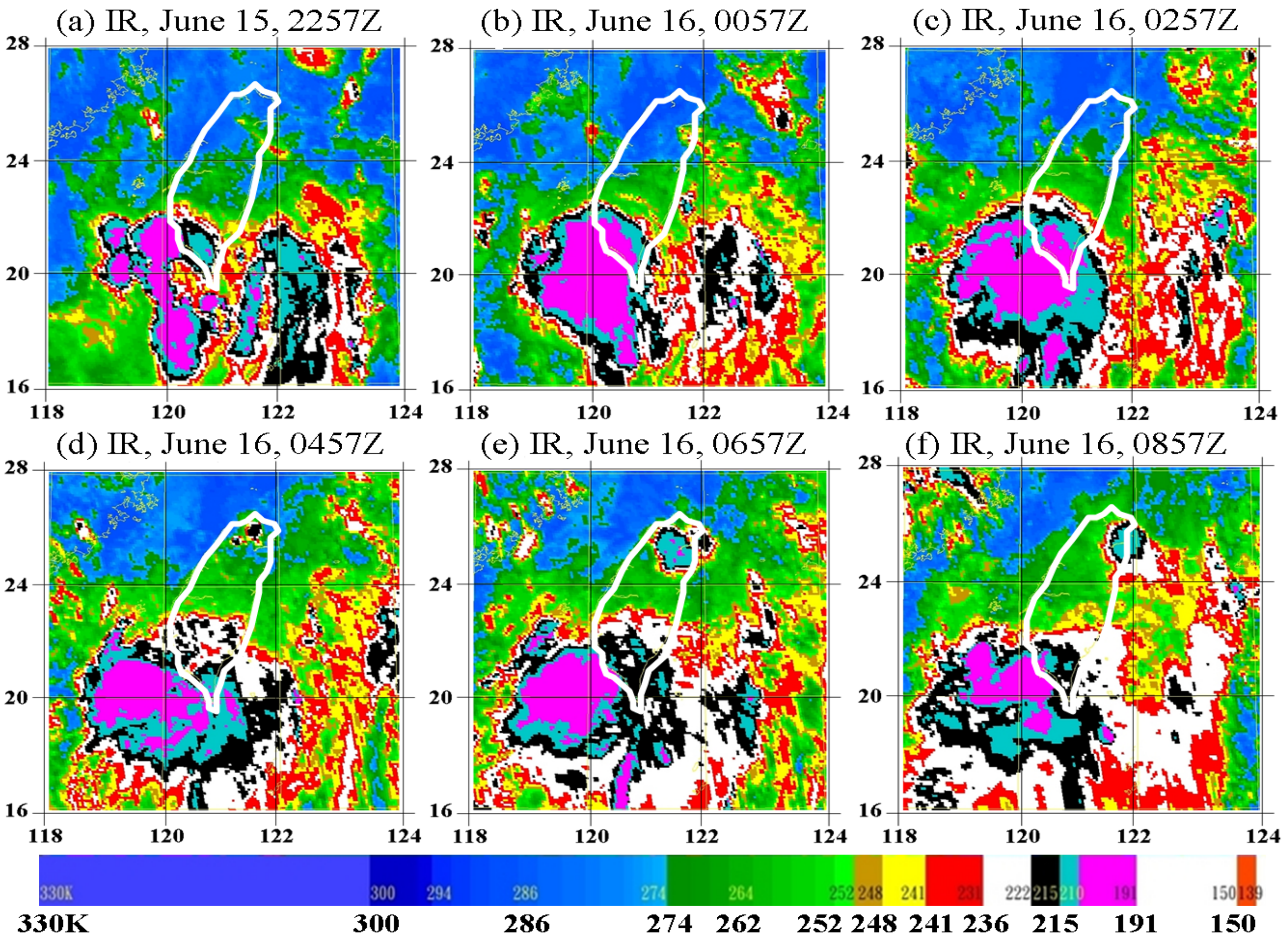

Figure 6.33. Brightness temperature (K) from IR channel of MASAT over and around Taiwan at (a) June 15 2257 UTC and thereafter every 2 hours (b)-(f).

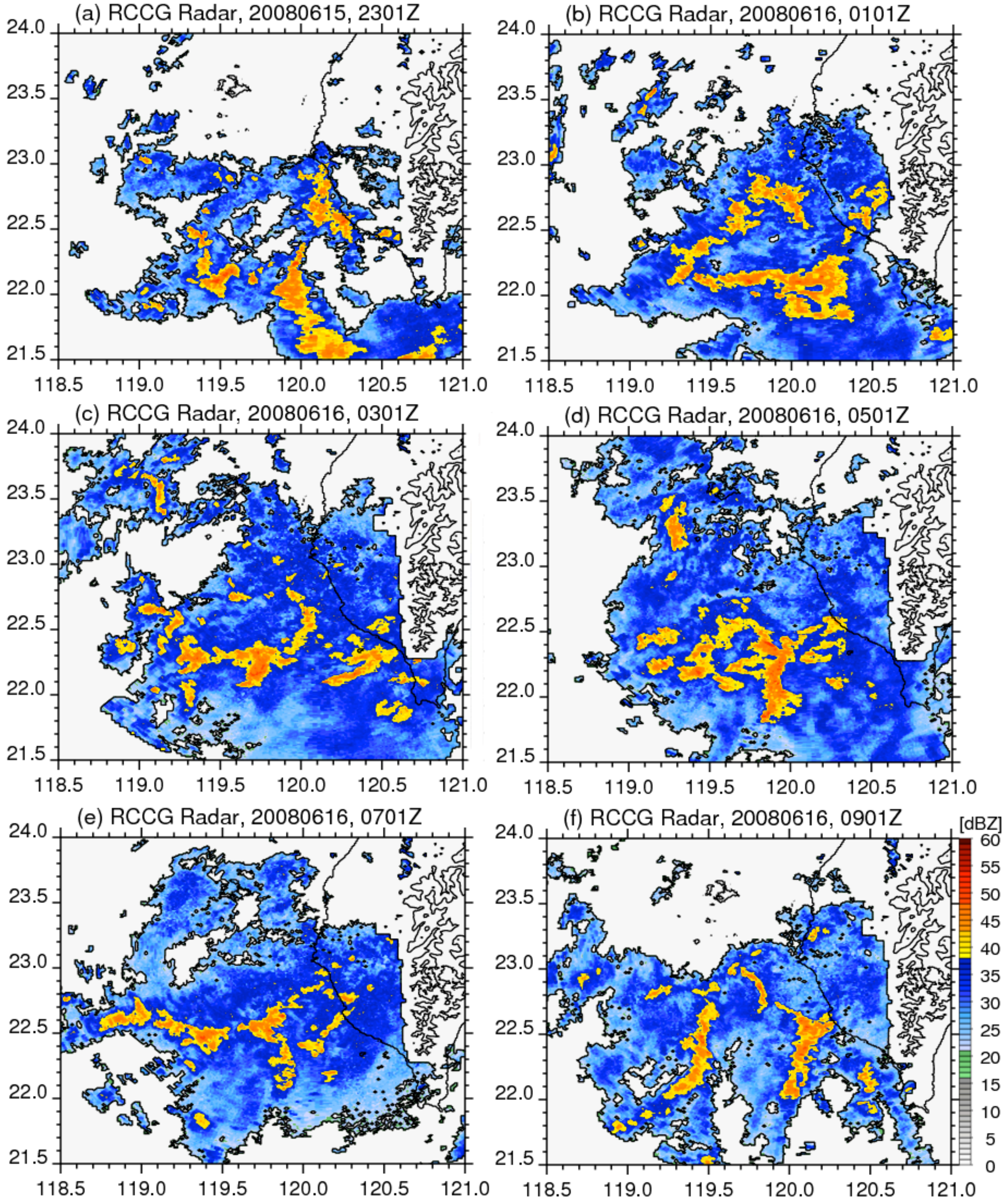

Figure 6.34. Radar images with reflectivity > 20 dBZ from RCCG over southwest Taiwan at (a) June 15 2301UTC and thereafter every 2 hours (b)-(f).

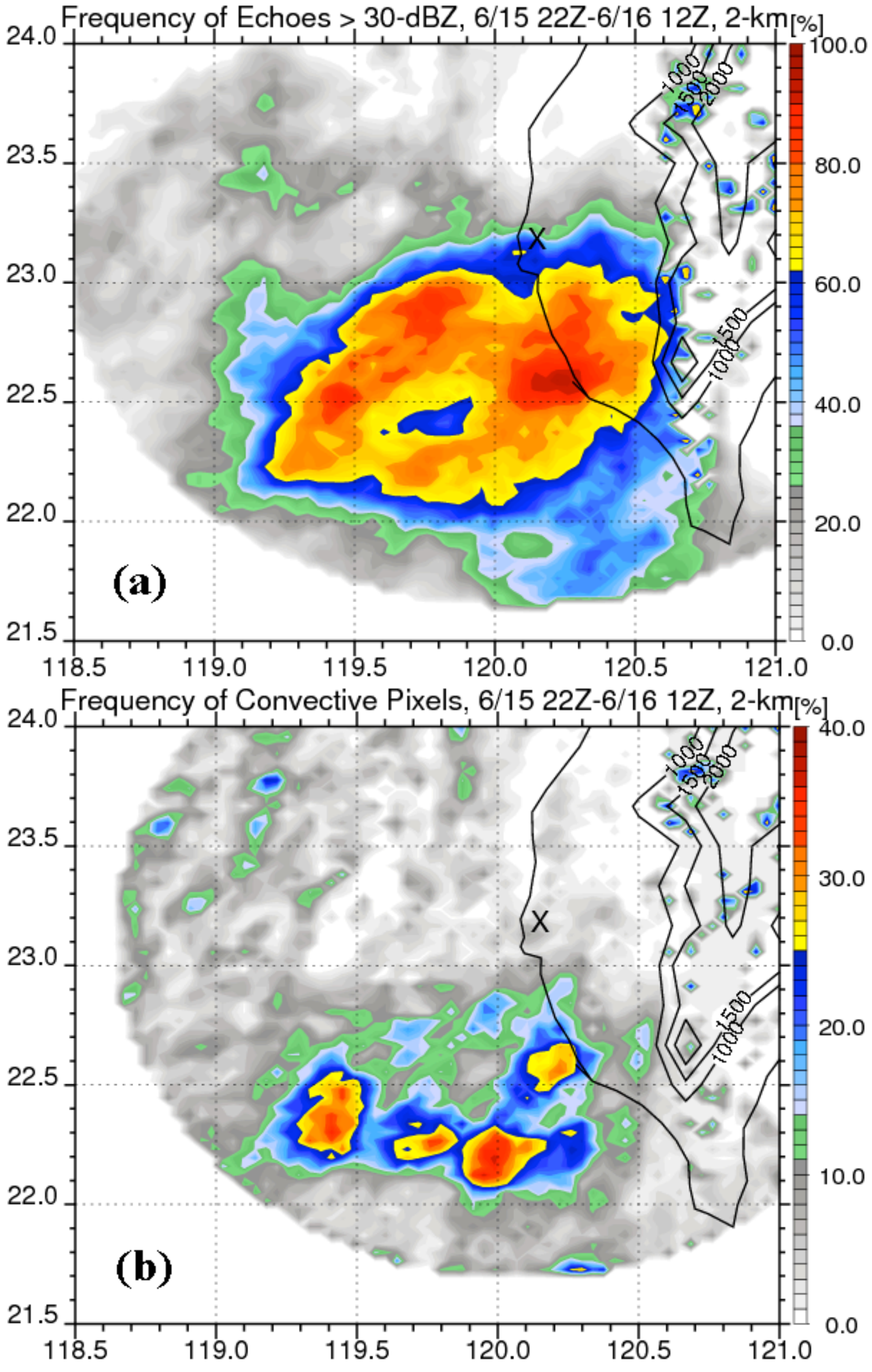

Figure 6.35. Occurrence frequency (in %) of (a) radar echoes > 30 dBZ, and (b) defined radar convective pixels, during period of June 15 22Z-16 12Z.

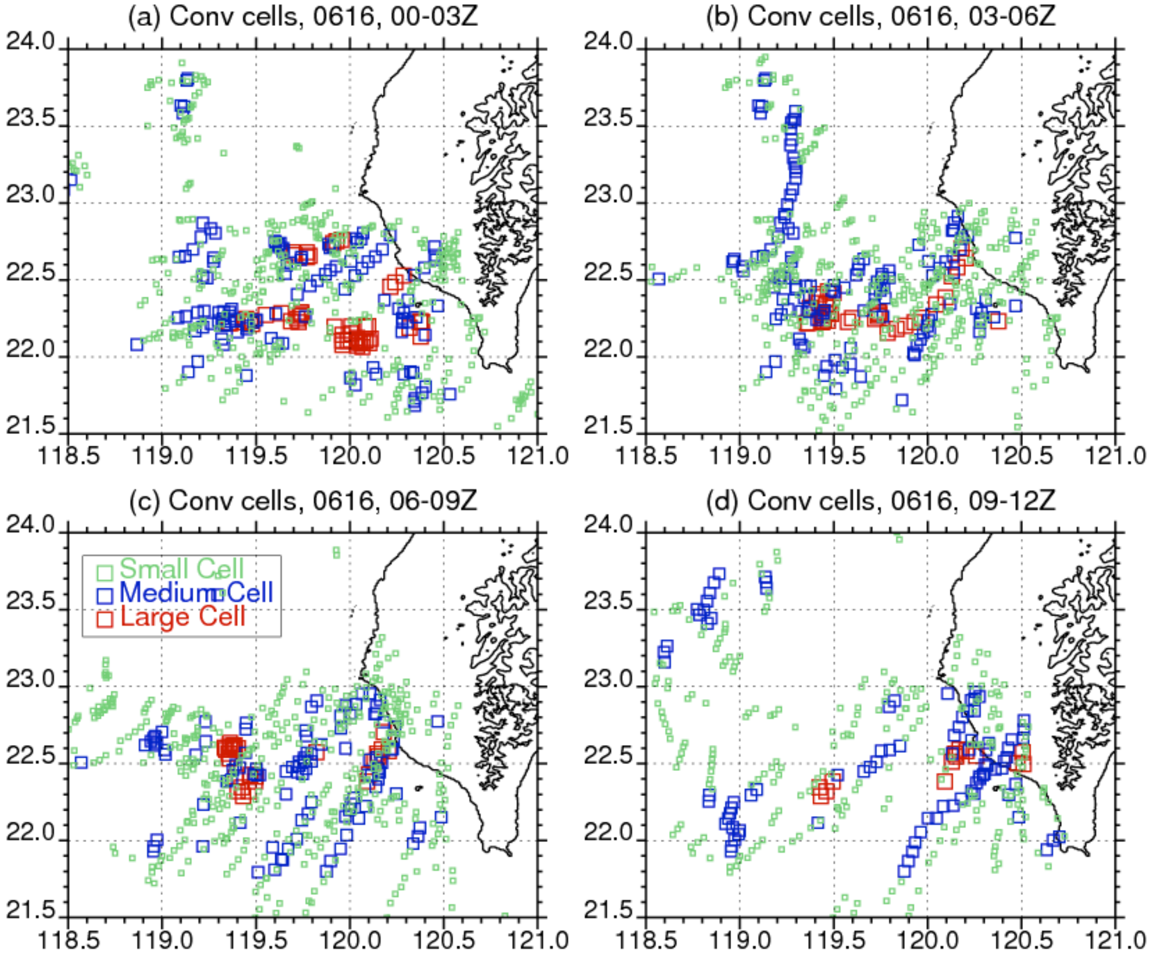

Figure 6.36. Distribution of defined convective cells of different size in every 3 hours on June 16: (a) 00-03Z; (b) 03-06Z; (c) 06-09Z; (d) 09-12Z. Meanings of different markers are indicated in the legend of (c).

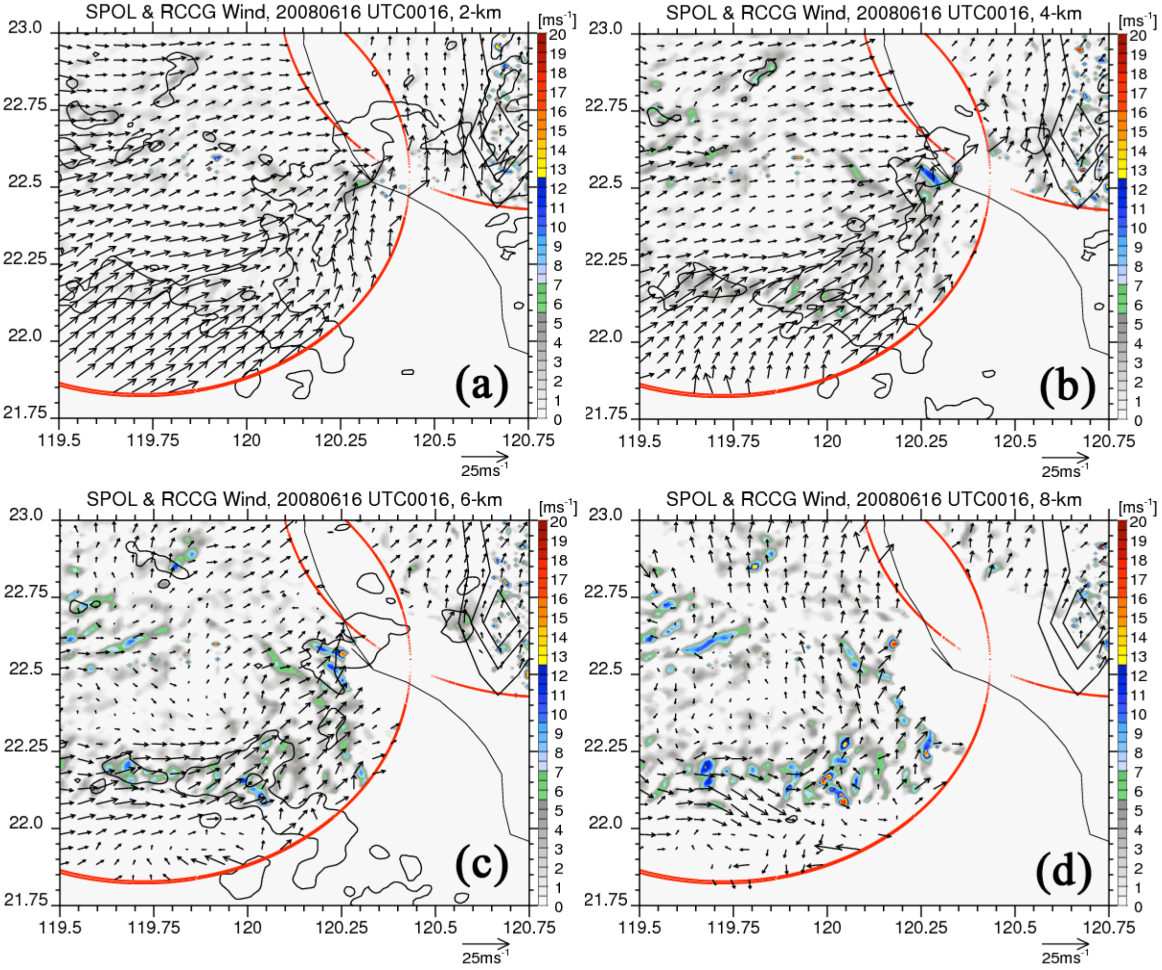

Figure 6.37. Horizontal dual-Doppler wind analysis at (a) 2-km, (b) 4-km, (c) 6-km, and (d) 8-km. The scale of the wind arrow is located at the bottom. The shaded color indicates vertical motion, while the black contours represent regions with radar reflectivity > 40 dBZ.

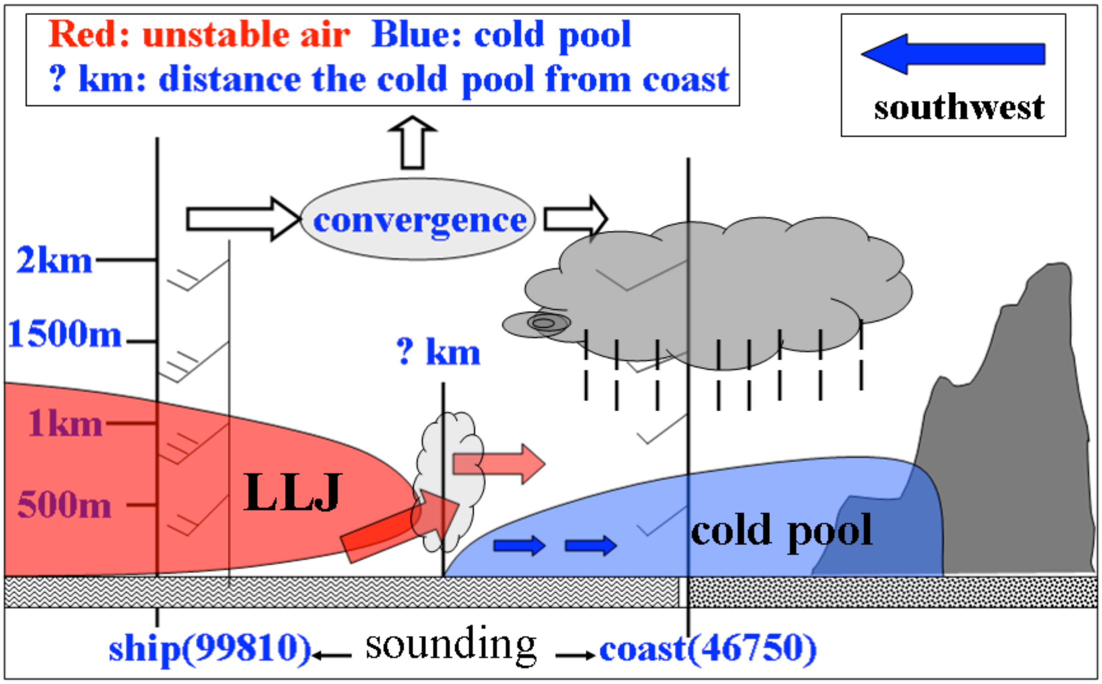

Figure 6.38. Schematic diagram of the hypothesis of triggering and maintenance for the long-duration heavy precipitation system.

CHAPTER 7

DISCUSSION AND SUMMARY

7.1 Discussion

7.11 Convection Type of Monsoon Precipitation

One of the most important questions this study aims to answer is what kinds of storms, categorized by convective properties, mainly contribute to the monsoon rainfall? Therefore, identifying particular convective regimes within the monsoon context becomes the major motivation of this study. As has been mentioned, tropical convection was typically separated into two classic regimes: continental and maritime (Zipser and Lutz 1994; Rosenfeld and Lensky 1998; Petersen and Rutledge 2001; Phillips et al. 2007; Ulbrich and Atlas 2007). Ice-based processes associated with vigorous convection are thought to be more important in the precipitation in the continental regime than in the maritime regime. Maritime rainfall likely has a more significant contribution from low-level warm-rain collision and coalescence processes, though ice-based processes are still important. Results in this study show that the convection properties in the East Asian monsoon are intermediate between these two classic convective regimes.

Before the onset of the monsoon, or in break periods, convection and embedded microphysics more closely resembles the continental regime. More than half of the rainfall is contributed by storms with intense convection. The major microphysical processes involved in these precipitation systems include graupel production in the mixed-phase region melting into large raindrops after descending below the freezing level. In contrast, storm morphologies of precipitation in the active monsoon phase, especially in Mei-Yu rain bands, more closely resemble the maritime regime. Convective vertical structures similar to those of maritime regime are observed: rapid decreasing in radar reflectivity with altitude above the freezing level but reflectivity increasing downward below the freezing level toward the surface.

The EASM is very similar to the Indian Summer Monsoon and Australia Summer Monsoon in convective properties, as it is affected by tropical, subtropical, and midlatitude systems. However, the EASM is much weaker than the North American Monsoon (NAM) in convection intensity, but stronger than the Amazon Monsoon. Compared to the EASM, NAM is in a drier environment with less seasonal rainfall amount, while the Amazon Monsoon is in a wetter and warmer environment with larger rainfall amount.

EASM convection type on average is intermediate between the continental regime, and convection over the open ocean. Yet, even in the active monsoon phase or heavy monsoon precipitation events, both strong convection with graupel extending to high altitudes with lightning activity and weak convective systems are observed. These convective systems close to the continental or oceanic types are less frequent but can be distinctly separated from those of typical monsoon convection on perspectives of rainfall contribution by convection types, convective vertical structures, convection intensity, and lightning activities. The weather regime with more intense convection has higher CAPE and a theta-e profile more like continental convection, for example.

7.1.2 Relationships among Convective Rainfall, Convective Properties, and Lightning Activities

Accurate rainfall estimation is very important for many scientific and practical applications such as the now-casting of heavy precipitation and flash flooding. Implications from relationships, if quantified and validated, between rainfall and convective properties of storm or rainfall and lightning activities, could be very useful. Many studies have reported close links between convective rainfall and lightning, both for individual (or ensemble) storms (Soula and Chauzy, 2001; Seity et al., 2001) and for long temporal and large spatial domains (e.g., Sheridan et al., 1997; Petersen and Rutledge, 1998; Soriano et al., 2001). The rainrate-lightning relationship has further been employed to improve the estimation of convective rainfall, especially for rainfall retrievals based on passive microwave or IR (Sheridan et al. 1997; Cheze and Sauvageot, 1997; Tapia et al., 1998; Grecu et al., 2000; Soriano and Pablo, 2003).

However, there is no clear relationship between rainfall and lightning in the Mei-Yu precipitation systems (Xu et al. 2010). Xu et al. 2010 is an extended study from this dissertation using the TRMM PF database, although not included here. As discussed above, during the active monsoon phase, the low-level warm rain collision- coalescence process may be relatively more important in precipitation processes than ice-based processes. But lightning activity is closely related to the ice flux or existence of large ice particles and supercooled liquid drops. Based on these facts, it is not surprising that monsoon precipitation is not well correlated with lightning activity for the more oceanic-type systems. For example, this may help explain why the rainy but less convective system of June 16 (Chapter 6) has its rainfall underestimated by the 3B42 algorithm.

Xu et al. (2010) further examine the relationship between lighting activity and a set of convective proxies. Results indicate that oceanic systems show slightly lower probabilities of lightning even with the same thresholds of maximum radar reflectivity than storms over land. For lightning systems over land, the total area of radar echo above 35-dBZ has the best relationship with lightning flash rate at temperatures between -5 and -15 ^{o}C of all the parameters. The area of lower radar reflectivity at colder temperature, e.g., area of 20-dBZ at -40 ^{o}C, is also highly correlated with lightning frequency. However, the highest correlation between area of specific radar reflectivity and lightning frequency is found at lower temperatures when the oceanic lightning systems are examined.

7.1.3 TRMM Climatology versus TiMREX Statistics

Because of the sampling difference, statistics such as occurrence frequency of storm types deriving from TiMREX observations can not be directly compared to those based on TRMM measurements. However, the storm properties or occurrence frequencies of precipitation systems that occur during TiMREX (results in Chapter 6) can be used to evaluate how unusual these storms are relative to the entire TRMM database in this region (results in Chapter 4).

Figure 6.14a shows the frequencies of PFs of different sizes during TiMREX 2008, while those of TRMM PFs in Mei-Yu season over different regions of East Asia during 1998-2007 are shown in Fig. 4.20a. During TiMREX, the size of the top 10% storms is about 1000 km^2, and about 3-5% of large systems cover an area of more than 10000 km^2. If these storms are placed in the TRMM climatology of Mei-Yu, they are also in the top percentage of 10% and 3%, respectively. More interestingly, if specific percentiles of TiMREX rainy systems categorized by echo top (20-dBZ) height or max height of 40 dBZ (Fig. 6.14b-c), e.g., top 10% or 5%, are placed in the TRMM-base Mei-Yu climatology, they are in the similar positions in the whole database of TRMM-detected storms (Fig. 4.22a-b). In other words, storm properties of precipitation systems observed by ground-based radar in the Mei-Yu season of 2008 over southwest Taiwan are similar to those of TRMM-observed Mei-Yu storms in the whole Mei-Yu region, if compared at the same occurrence level.

On the other hand, TRMM-detected vertical convective structures are very close to those derived from the ground-radar measurements of individual events (Fig 7.1). As shown in Chapter 6, vertical reflectivity profiles increasing below the melting level toward the surface are quite common in the heavy precipitation events without intense convection. However, vertical reflectivity profiles of the majority of TRMM PR observations are more like those of continental-like systems on June 14 with values near-constant below the freezing level.

7.2 Summary of Major Results

This study first investigates monsoon rain bands during the Mei-Yu season over South China/Taiwan and the Yangtze River. Mei-Yu rain bands and associated rainfall characteristics are examined in terms of population, location, variability, rainfall frequency, and large-scale flow, with the focus on the South China and Taiwan region. Different weather regimes have been separated based on the monsoon onset and existence of well-defined rain bands. The second goal of the study is to recognize the convection type and properties of monsoon precipitation in different weather regimes. Specifically, convection/precipitation occurrence, storm properties, vertical structures, and rainfall contribution are quantified for different storm types. Comparisons of the above-mentioned quantities are further made among monsoon, continental, and oceanic regimes within the tropics. From the long-term TRMM climatology, heavy Mei-Yu precipitation systems occurring during TiMREX in 2008 are analyzed from perspectives of storm evolution, storm and upstream environment, storm morphologies, convective properties, and microphysical information. Lastly, this study also examines diurnal variations of rainfall, convection and lightning, phase propagation of diurnal cycles, and vertical structures, with possible mechanisms.

Major results from this dissertation are summarized as follows:

(1) The frequency, rainfall contribution, and associated large-scale monsoon flow of Mei-Yu rain bands over South China/Taiwan or the Yangtze River show substantial spatial and interannual variability:

- During the South China/Taiwan Mei-Yu season, about 5-7 well-defined rain bands pass over the South China and Taiwan region every year, with the maximum frequency and rainfall maxima located at Pearl River Delta and foothill of Yun-Gui Plateau, while during breaks, rainfall spreads widely over South China with far less seasonal amount;
- The low-level monsoon southwesterly flows over South China and South China Sea during active periods are much more intense than during break periods, and they turn to be more southerly during break periods;
- About 3-5 rain bands affect the Yangtze River region during the Yangtze River Mei-Yu season, and very few of them move to South China after the monsoon rain belt gets stabilized over the Yangtze River valley;
- The Mei-Yu rain bands and associated rainfall have very evident interannual variability: during the active years, Mei-Yu rain bands are very active and contribute about twice as much rainfall as in dry years when very few rain

bands propagate down to South China Sea or Taiwan;

(2) There is evident intraseasonal variability or regime difference on the storm morphologies, occurrence frequencies, and convective properties of the monsoon precipitation over East Asia:

- Frequency of storms with high cloud tops, strong convection, and evident ice scattering signature is greatest before monsoon onset, then progressively less so in Postmeiyu, break periods, and least frequent during active Mei-Yu;
- Break periods and preseason have larger fractions of intense convection that behave more like the classic continental tropical convection with major ice-based rainfall processes, while active Mei-Yu convection more closely resembles classic tropical maritime convection: more dependent on the "warm-rain" collision and coalescence processes with weak convection but heavy precipitation;
- Monsoon precipitation over the Yangtze River region, though with similar sizes and cloud tops, is distinct from its counterpart in South China in the convection type, with convection having more continental properties;

(3) TRMM climatology of convection type and rainfall convective properties of different precipitation regimes around the world shows significant differences:

- EASM is comparable to other monsoon regimes in storm morphologies and convective properties, with less continental-like convection than the less rainy monsoon regime (North American Summer Monsoon) but less maritime-like convection than the more rainy monsoon regime (Amazon Monsoon);

- Monsoon precipitation is generally intermediate in convective intensity between classic intense continental convection and classic maritime precipitation with weaker convection.

(4) Analysis of the TiMREX observations shows considerable details on the storm environment, convective properties, and microphysics of heavy precipitation systems:

- Though intense convection and vigorous lightning activity are observed before the onset of Mei-Yu and for two cases within the rainy Mei-Yu regime, most of the Mei-Yu heavy precipitation systems have only weak to moderate convection and very low lightning occurrence;
- Two basic convective regimes can be found for heavy rainfall events: “rainy and convectively intense,” and “rainy but less intense”; environment of large CAPE, higher fraction of large-ice particles in the mixed-phase region, and continental-like convective vertical structures are observed in the rainy and intense regime, while more moist neutral environment, LLJ, and maritime convective vertical structures are observed in the rainy but less convective regime;
- Most of the heavy rainfall is associated with Mei-Yu rain bands; they are observed to be more influenced by upstream low-level jets, unstable upstream conditions, moist neutral storm environments, but less by upper level

conditions, which is favorable for long-duration heavy precipitation through supporting continuous development of new convection;

(5) Monsoon precipitation has different phases and structures of diurnal cycle over different regions of East Asia:

- There is a phase propagation of the diurnal cycles of precipitating storms, total rainfall, convection, and lightning from the foothills of the eastern TP downstream, most evident during Premeiyu and Mei-Yu seasons, but absent during midsummer;
- Before midsummer, the eastern TP foothills are dominated by nocturnal rainfall, but the early morning peak of precipitation is only in phase with deep convection, MCSs, and lightning during Premeiyu;
- Most of the nocturnal precipitation is in phase with MCSs and possibly contributed by long-lived MCSs evolving from late afternoon or early night convection, but these early morning MCSs show larger percentages of deep convection in Premeiyu;
- In midsummer, most of East Asia is dominated by afternoon precipitation and convection, with the Sichuan basin and northern part of eastern China as the exception where early morning rainfall prevails, in spite of most deep convection and lightning occurring during the afternoon.

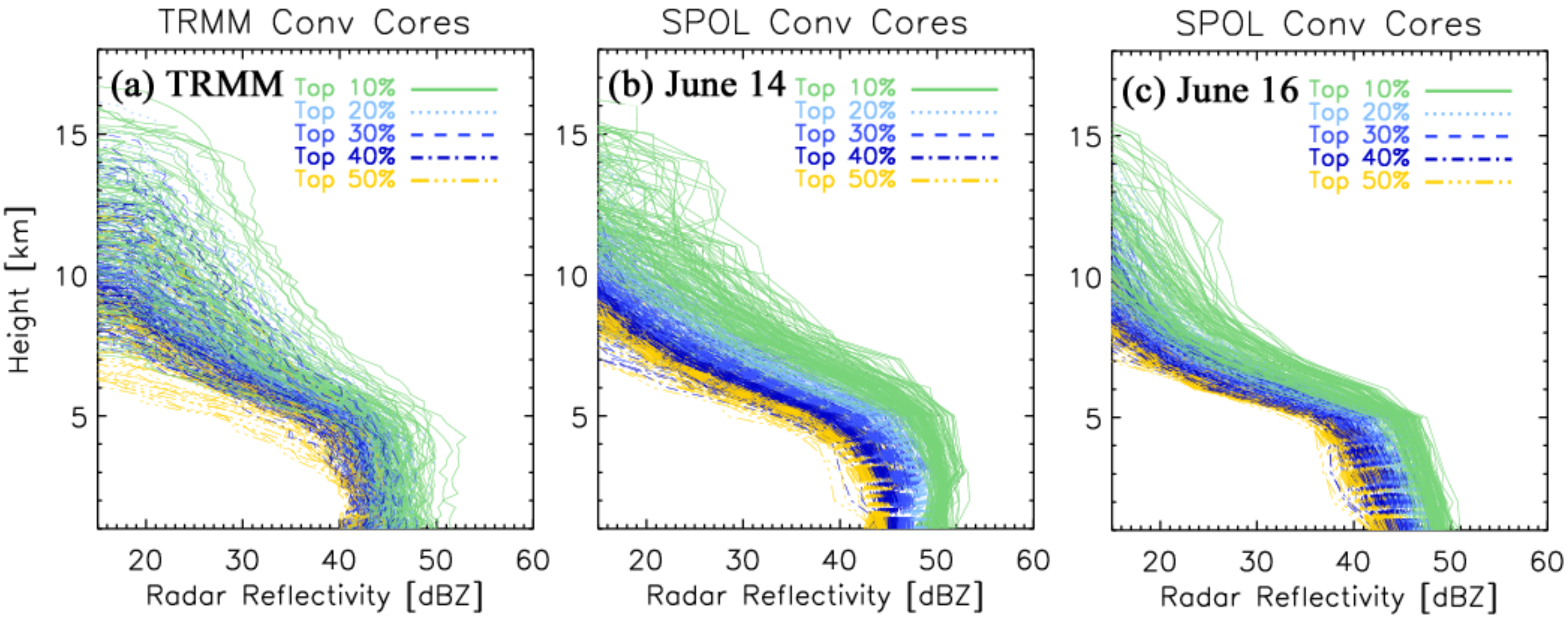

Figure 7.1. Vertical profiles of radar reflectivity in convective cores (> 40 dBZ) in precipitation systems (a) measured by TRMM over southern Taiwan, (b) observed by SPOL on June 14, 2008, and (c) on June 16. Profiles are in 10, 20, 30, 30, 40, and 50 percentile indicating by colors.

BIBLIOGRAPHY

Akaeda, K., J. Reisner, and D. Parsons, 1995: The role of mesoscale and topographically induced circulations initiating a flash flood observed during the TAMEX project. *Mon. Wea. Rev.*, **123,** 1720–1739.

Arakawa, A., W. H. Schubert, 1974: Interaction of a Cumulus Cloud Ensemble with the Large-Scale Environment, Part I. *J. Atmos. Sci.*, **31**, 674–701.

Arakawa, A., 1975: Modelling clouds and cloud processes for use in climate model. *The Physical Basis of Climate and Climate Modelling,* GARP Publication Series, No. **16**, WMO, 183–197.

Arakawa, A., 2004: The Cumulus Parameterization Problem: Past, Present, and Future. *J. Climate*, **17**, 2493–2525.

Asai, T., S. Ke, and Y.-M. Kodama, 1998: Diurnal variability of cloudiness over East Asia and the Western Pacific Ocean as revealed by GMS during the warm season. *J. Meteor. Soc. Japan,,* **76**, 675-684.

Awaka, J., T. Iguchi, H. Kumagai, and K. Okamoto, 1997: Rain type classification algorithm for TRMM precipitation radar. *Proc. 1997 Int. Geoscience and Remote Sensing Symp*., Singapore, IEEE, 1633–1635.

Berrisford P., D. P. Dee, K. Fielding, M. Fuentes, P. Kallberg, S. Kobayashi, S. M. Uppala, 2009: The ERA-Interim Archive. *ERA Report Series No. 1*, ECMWF, Reading, UK.

Boccippio, D. J., W. A. Petersen, and D. J. Cecil, 2005: The tropical convective spectrum. Part I: Archetypal vertical structures. *J. Climate*, **18,** 2744–2769.

Bonner, W. D., 1968: Climatology of the low level jet. *Mon. Wea. Rev.*, **96**, 833–850.

Carbone, R. E., J. D. Tuttle, D. A. Ahijevych, and S. B. Trier, 2002: Inferences of predictability associated with warm season precipitation episodes. *J. Atmos. Sci.,* **59**, 2033-2056.

Carbone, R. E., and J. D. Tuttle, 2008: Rainfall occurrence in the United States in warm season: The diurnal cycle. *J. Climate*, **21**, 4132-4136.

Carey, L. D., and S. A. Rutledge 1998: Electrical and multiparameter radar observations of a severe hailstorm, *J. Geophys. Res.*, **103**, 13,979–14,000, doi:10.1029/97JD02626.

Cecil, D. J., and E. J. Zipser, 1999: Relationships between tropical cyclone intensity and satellite-based indicators of inner core convection: 85-GHz ice-scattering signature and lightning. *Mon. Wea. Rev.*, **127**, 103-123.

Cecil, D. J., S. J. Goodman, and D. J. Boccippio, 2005: Three years of TRMM precipitation features. Part I: Radar, radiometric, and lightning characteristics. *Mon. Wea. Rev.*, **133**, 543-566.

Cecil, D. J., 2011: Relating passive 37-GHz scattering to radar profiles in strong convection. *J. Appl. Meteor. Climatol.*, **50**, 233–240.

Chang, C.-P., and T. Krishnamurti, 1987: *Monsoon Meteorology*. Oxford University Press, USA, 560 pp.

Chang, C.-P., S.-C. Hou, H.-S. Kuo, G.T.-J. Chen, 1998: The development of an intense East Aian summer monsoon disturbance with strong vertical coupling. *Mon. Wea. Rev.*, **126**, 2692-2712.

Chang, C.-P., 2004: *East Asian Monsoon*. World Scientific Publishing Company, Singapore, 564 pp.

Chang, P.-L., P.-F. Lin, Ben J.-D. Jou, J. Zhang, 2009: An application of reflectivity climatology in constructing radar hybrid scans over complex terrain. *J. Atmos. Oceanic Tech.*, **26**, 1315-1327.

Chappell, C. F., 1986: Quasi-stationary convective events. *Mesoscale Meteorology and Forecasting,* P. S. Ray, Ed. Amer. Meteor. Soc., 289–309.

Chen, C.-S., W.-S. Chen, and Z.-S. Deng, 1991: A study of a mountain-generated precipitation system in northern Taiwan during TAMEX IOP 8. *Mon. Wea. Rev.*, **119,** 2574–2606.

Chen, C.-S., W.-C. Chen, Y.-L. Chen, P.-L. Lin, and H.-C. Lai, 2005: Investigation of orographic effects on two heavy rainfall events over southwestern Taiwan during the Mei-yu season. *Atmos. Res.*, **73**, 101-130.

Chen, C.-S., Y.-L. Chen, C.-L. Liu, P.-L. Lin, and W.-C. Chen, 2007: The statistics of heavy rainfall occurrences in Taiwan. *Wea. Forecasting.*, **22**, 981-1002.

Chen, G.T.-J., 1977: A synoptic case study of on mean structures of Mei-Yu in Taiwan. *Atmos. Sci.*, **4**, 38-47.

Chen, G.T.-J., 1983: Observational aspects of the Meiyu phenomena in subtropical China. *J. Meteor. Soc. Japan.*, **61**, 306-312.

Chen, G.T.-J., 1988: On the synoptic climatological characteristics of the East Asian Meiyu front. *Atmos. Sci.*, **16**, 435-446 (in Chinese with English abstract).

Chen, G.-T.-J., and C.-C. Yu, 1988: Study of low-level jet and extremely heavy rainfall over northern Taiwan in the Mei-Yu season. *Mon. Wea. Rev.*, **116**, 884-891.

Chen, G.T.-J., 1994: Large-scale circulations associated with the East Asian summer monsoon and the Mei-Yu over South China and Taiwan. J. Meteor. Soc. Japan, **72**, 959–983.

Chen, G.T.-J., 2004: Research on the phenomena of Meiyu during the past quarter century: An overview. *The East Asian Monsoon*, C.-P. Chang, Ed., World Scientific, 357-403.

Chen, G.T.-J., C.-C. Wang, and D. T.-W. Lin, 2005: Characteristics of low-level jets over northern Taiwan in Mei-Yu season and their relationship to heavy rain events. *Mon. Wea. Rev.*, **133**, 20-43.

Chen, G.T.-J., C.-C. Wang, and L.-F. Lin, 2006: A diagnostic study of a retreating Mei-Yu front and the accompanying low-level jet formation and intensification. *Mon. Wea. Rev.*, **134**, 874-896.

Chen, G. T.-J., C.-C. Wang, and S. W. Chang, 2008: A diagnostic case study of Meiyu frontogenesis and development of wave-like frontal disturbances in the subtropical environment. *Mon. Wea. Rev.*, **136**, 41-61.

Chen, G., W. Sha, and T. Iwasaki, 2009: Diurnal variation of precipitation over southeastern China: Spatial distribution and its seasonality. *J. Geophys. Res.*, **114**, D13101, doi:10.1029/2008JD011103.

Chen, H., R. Yu, J. Li, W. Yuan, and T. Zhou, 2010: Why nocturnal long-duration rainfall presents an eastward-delayed diurnal phase of rainfall down the Yangtze river valley. *J. Climate*, **23**, 905-917.

Chen, S.-H., and Y.-L. Lin, 2005a: Orographic effects on a conditionally unstable flow over an idealized three dimensional mesoscale mountain. *Meteor. Atmos. Phys.*, **88**, Chen, S.-H., and Y.-L. Lin, 2005b: Effects of the basic wind speed and CAPE on flow regimes associated with a conditionally unstable flow over a mesoscale mountain. *J. Atmos. Sci.*, **62**, 331-350.

Chen, S.-J., W. Wang, K. H. Lau, Q. H. Zhang, and Y. S. Chung, 2000: Mesoscale convective systems along the Meiyu front in a numerical model. *Meteor. Atmos. Phys.*, **75**, 149-160.

Chen, T.-C., M.-C. Yan, J.-C. Hsieh, and R. W. Arritt, 1999: Diurnal and seasonal variations of the rainfall measured by the automatic rainfall and meteorological telemetry system in Taiwan. *Bull. Amer. Meteor. Soc.*, **80**, 2299-2312.

Chen, Y.-L., and N. B-F. Hui, 1990: Analysis of a shallow front during the Taiwan area mesoscale experiment. *Mon. Wea. Rev.*, **118,** 2649–2667.

Chen, Y.-L., 1993: Some synoptic-scale aspects of the surface fronts over southern China during TAMEX. *Mon. Wea. Rev.*, **121**, 50-64.

Chen. Y.-L., and J. Li, 1995: Large-scale conditions favorable for the development of heavy rainfall during TAMEX IOP 3. *Mon. Wea. Rev.*, **123**, 2978-3002.

Chen, Y.-L., and J. Feng, 2001: Numerical simulations of airflow and cloud distributions over the windward side of the island of Hawaii. Part I: The effects of trade-wind inversion. *Mon. Wea. Rev.*, **129,** 1117–1134.

Cheze, J. L., and H. Sauvageot, 1997: Area-average rainfall and lightning activity. *J. Geophys. Res.,* **102,** 1707–1715.

Christian, H. J. (1999), Optical detection of lightning from space. *Proc. 11th Int. Conf. on Atmospheric Electricity*, NASA/CP-1999-209261, pp. 715-718, Guntersville, Ala., 10-11 June.

Chu, C.-M., and Y.-L. Lin, 2000: Effects of orography on the generation and propagation of mesoscale convective systems in a two-dimensional conditionally unstable flow. *J. Atmos. Sci.*, **57**, 3817-3837.

Ciesielski, P. E., and Coauthors, 2010: Quality-controlled upper-air sounding dataset for TiMREX/SoWMEX: Development and corrections. *J. Atmos. Oceanic Technol.*, **27**, 1802–1821.

Cifelli, R., and S. A. Rutledge, 1998: Vertical motion, diabatic heating and rainfall characteristics in north Australia convective systems. *Quart. J. Roy. Meteor. Soc.*, **124**, 1133-1162.

Cifelli, R., W. A. Petersen, L. D. Carey, S. A. Rutledge, and M. A. F. da Silva Dias, 2002: Radar observations of the kinematic, microphysical, and precipitation characteristics of two MCSs in TRMM LBA, *J. Geophys. Res.*, **107**, 8077, doi:10.1029/2000JD000264.

Clemens, S., W. Prell, D. Murray, G. Shimmield, G. Weedon, 1991: Forcing mechanisms of the Indian Ocean monsoon. *Nature*, **353**, 720 – 725.

Dai, A., F. Giorgi, and K. E. Trenberth, 1999: Observed and model simulated precipitation diurnal cycle over the contiguous United States. *J. Geophys. Res.*, **104**, 6377-6402.

Dai, A., and K. E. Trenberth, 2004: The diurnal cycle and its depiction in the Community Climate System Model. *J. Climate*, **17**, 930-951.

Dee, D. P., and S. Uppala, 2009: Variational bias correction of satellite radiance data in the ERA-Interim reanalysis. *Q. J. R. Meteorol. Soc.*, **135**, 1830-1841.

Dee, D. P., with 35 co-authors, 2011: The ERA-Interim reanalysis: configuration and performance of the data assimilation system. *Quart. J. R. Meteorol. Soc.*, **137**, 553-597.

Davis, R. S., 2001: Flash flood forecast and detection methods. *Severe Convective Storms, Meteor. Monogr.,* No. 50, Amer. Meteor. Soc., 481–525.

Deierling, W., J. Latham, W. A. Petersen, S. M. Ellis, and H. J. Christian Jr., 2005: On the relationship of thunderstorm ice hydrometeor characteristics and total lightning measurements, *Atmos. Res.*, **76**, 114-126.

DeMott, C. A., and S. A. Rutledge, 1998: The vertical structure of TOGA COARE convection. Part I: Radar echo distributions. *J. Atmos. Sci*., **55**, 2730-2747.

Ding, Y., 1992: Summer monsoon rainfalls in China. *J. Meteor. Soc. Japan.*, **70**, 373-396.

Ding, Y., and J. C.-L. Chan, 2005: The East Asian summer monsoon: An overview. *Meteor. Atmos. Phys.*, **89**, 117-142.

Domros, M. and G. Peng, 1988: *The Climate of China*. Springer Verlag, 360 pp.

Donaldson, R. J., 1961: Radar reflectivity profiles in thunderstorms. *J. Meteor.,* **18**, 292-305.

Doswell III, C. A., H. E. Brooks, and R. A. Maddox, 1996: Flash flood forecasting: An ingredients-based methodology. *Wea. Forecasting*, **11,** 560–581.

Doviak, R. J., and D. S. Zrnic, 1993: *Doppler Radar and Weather Observations.* 2nd ed. Academic Press, 562 pp.

Doviak, R. J., P. S. Ray, R. G. Strauch, L. J. Miller, 1976: Error estimation in wind fields derived from dual-Doppler radar measurement. *J. Appl. Meteor.*, **15**, 868–878.

Dye, J. E., W. P. Winn, J. J. Jones, and D. W. Breed, 1989: The electrification of New Mexico thunderstorms. 1. Relationship between precipitation development and the onset of electrification. *J. Geophys. Res*., **94**, 8643-8656.

Fritsch, J. M, and R. E. Carbone, 2004: Improving quantitative precipitation forecasts in the warm season: A USWRP research and development strategy. *Bull. Amer. Meteor. Soc.,* **85,** 955-965.

Fu*,* Y. and G. Liu, 2003: Precipitation characteristics in mid-latitude East Asia as observed by *TRMM* PR and. TMI, *J. Meteor. Soc. Japan*, **81**, 1353-1369.

Fu, Y., Y. Lin, G. Liu, et al., 2003: Seasonal. characteristics of precipitation in 1998 over East Asia as derived from TRMM PR, *Adv. Atmos. Sci.*, **20**, 511-529.

Fujinami, H., S. Nomura, and T. Yasunari, 2005: Characteristics of diurnal variations in convection and precipitation over the southern Tibetan Plateau during summer. *SOLA,* **1**, 049-052.

Grabowski, W. W., 2004: An improved framework for superparameterization. *J. Atmos. Sci.*, **61**, 1940–1952.

Grecu, M., E. N. Anagnostou, R. F. Adler, 2000: Assessment of the use of lightning information in satellite Infrared rainfall estimation. *J. Hydrometeorology.,* **1**. 211-221.

Iguchi, T., T. Kozu, R. Meneghini, J. Awaka, and K. Okamoto, 2001: Rain-profiling algorithm for the TRMM precipitation radar. *J. Appl. Meteorol.,* **39**, 2038-2052.

Hartman, D. L., H. H. Hendon, and R. A. Houze Jr., 1984: Some implications of the mesoscale circulations in tropical cloud clusters for large scale dynamics and climate. *J. Atmos. Sci*, **41**:113–121.

He, H., J.W. McGinnis, Z. Song, M. Yanai, 1987: Onset of the Asian summer monsoon in 1979 and the effect of the Tibetan Plateau. *Mon. Wea. Rev.*, **115**, 1966-1995.

He, H., and F. Zhang, 2010: Diurnal variations of warm-season precipitation over

Northern China. *Mon. Wea. Rev.*, **138**, 1017-1025.

Hirose, M., and K. Nakamura, 2005: Spatial and diurnal variation of precipitation systems over Asia observed by the TRMM precipitation radar. *J. Geophys. Res.*, **110**, D05106, doi:10.1029/2004JD004815.

Horel, J. D. and J. M. Wallace, 1981: Planetary scale atmospheric phenomena associated with the southern oscillation. *Mon. Wea. Rev*, **109**:813–829.

Houze, R. A., Jr., 1977: Structure and dynamics of a tropical squall–line system. *Mon. Wea. Rev.*, **105**, 1540–1567.

Houze, R. A., and C. P. Cheng, 1977: Radar characteristics of tropical convection observed during GATE - mean properties and trends over summer season. *Mon. Wea. Rev.*, **105,** 964-980.

Houze, R. A., Jr., and A. K. Betts, 1981: Convection in GATE. *Rev. Geophys. Space Phys.,* **19**, 541-576.

Houze, R. A., Jr., 1982: Cloud clusters and large-scale vertical motions in the tropics. *J. Meteor. Soc. Japan*, **60**, 396-410.

Houze, R. A., Jr., 1989: Observed structure of mesoscale convective systems and implications for large-scale heating. *Quart. J. Royal Meteor. Soc.*, **115**, 425-461.

Houze, R. A., Jr., B. F. Smull, and P. Dodge, 1990: Mesoscale organization of springtime rainstorms in Oklahoma. *Mon. Wea. Rev.*, **118,** 613–654.

Houze, R. A., Jr., 1993: *Cloud Dynamics*. Academic. San Diego, Calif, 573 pp.

Houze, R. A., Jr., 2004: Mesoscale convective systems. *Rev. Geophys.*, **42**, RG4003, doi:10.1029/2004RG000150.

Huang, R., and F. Sun, 1992: Impacts of the tropical western Pacific on the East Asian summer monsoon. *J. Meteorol. Soc. Japan.*, **70**, 243-256.

Huang, H.-L., C.-C. Wang, G. T-J Chen, R. E. Carbone, 2010: The role of diurnal solenoidal circulation on propagating rainfall episodes near the Eastern Tibetan Plateau. *Mon. Wea. Rev.*, **138**, 2975-2989.

Huffman, G. J., and Coauthors, 2007: The TRMM Multisatellite Precipitation Analysis (TMPA): Quasi-global, multiyear, combined-sensor precipitation estimates at fine scales. *J. Hydrometeor.*, **8**, 38-55.

Iguchi, T., T. Kozu, R. Meneghini, J. Awaka, and K. Okamoto, 2000: Rain-profiling algorithm for the TRMM precipitation radar. *J. Appl. Meteor*., **39**, 2038-2052.

Johnson, R. H., J. F. Bresch, 1991: Diagnosed characteristics of precipitation systems over Taiwan during the May–June 1987 TAMEX. *Mon. Wea. Rev.*, **119**, 2540–2557.

Johnson, R.H., T.M. Rickenbach, S.A. Rutledge, P.E. Ciesielski, W. H. Schubert, 1999: Trimodal characteristics of tropical convection. *J. Climate*, **12**, 2397–2418.

Johnson, R. H., S. A. Aves, P. E. Ciesielski, and T. D. Keenan, 2005: Organization of oceanic convection during the onset of the 1998 East Asian Summer Monsoon. *Mon. Wea. Rev*., **133**, 131-148.

Jorgensen, D. P., M. A. LeMone, 1989: Vertically velocity characteristics of oceanic convection. *J. Atmos. Sci.*, **45**, 2097–2122.

Jorgensen, D. P., M. A. LeMone, and B. J.-D. Jou, 1991: Precipitation and kinematic structure of an oceanic mesoscale convective system. Part I: Convective line structure. *Mon. Wea. Rev.*, **119**, 2608-2637.

Kang, I.-S., C.-H. Ho, Y.-K. Lim, K.-M. Lau, 1999: Principal modes of climatological seasonal and intraseasonal variations of the Asian Summer Monsoon. *Mon. Wea. Rev.*, **127**, 322–340.

Kawamura, R., 1998: A possible mechanism of the Asian summer monsoon-ENSO coupling. *J. Meteorol. Soc. Japan.*, **76**, 1009-1027.

Kodama, Y.-M., A. Ohta, M. Katsumata, S. Mori, S. Satoh, and H. Ueda, 2005: Seasonal transition of predominant precipitation type and lightning activity over tropical monsoon areas derived from TRMM observations. *Geophys. Res. Lett.*, **32**, L14710, doi:10.1029/2005GL022986.

Krishnamurthy, V., B. N. Goswami, 2000: Indian Monsoon–ENSO relationship on interdecadal timescale. *J. Climate*, **13**, 579–595.

Kummerow, C., W. Barnes, T. Kozu, J. Shiue, and J. Simpson, 1998: The Tropical Rainfall Measuring Mission (TRMM) sensor package. *J. Atmos. Oceanic technol*., **15**, 809-817.

Kuo, Y.-H., L. Cheng, R. A. Anthes, 1986: Mesoscale analysis of Sichuan flood catastrophe, 11-15 July, 1981. *Mon. Wea. Rev.*, **114**, 1984-2003.

Kuo, Y.-H., and G. T.-J. Chen, 1990: The Taiwan Area Mesoscale Experiment

(TAMEX): An overview. *Bull. Amer. Meteor. Soc*., **71**, 488-503.

Lau, K.-M., M.-T. Li, 1984: The monsoon of East Asia and its global associations—A survey. *Bull. Amer. Meteor. Soc.*, **65**, 114–125.

Lau, K.-M. 1992: East Asian Summer Monsoon rainfall variability and climate teleconnection. *J. Meteor. Soc. Japan.*, **70**, 211-242.

Lau, K. M., and Coauthors, 2000: A report of the field operations and early results of the South China Sea Monsoon Experiment (SCSMEX). *Bull. Amer. Meteor. Soc.*, **81**, 1261–1270.

Lee W.-C., B. J. D. Jou, C.-R. Chen, and J.-A. Moore, 2009: Overview of SoWMEX/TiMREX. AMS *34th Conference on Radar Meteorology*, October 2009, Williamsburg, VA.

Li, C., and M. Yanai, 1996: The onset and interannual variability of the Asian Summer Monsoon in relation to land–sea thermal contrast. *J. Climate*, **9**, 358–375.

Li, J., R. Yu, and T. Zhou 2008: Seasonal variations of the diurnal cycle of rainfall in the southern contiguous China. *J. Climate*, **21**, 6036-6043.

Li, J., Y.-L. Chen, and W.-C. Lee, 1997: Analysis of a heavy rainfall event during TAMEX. *Mon. Wea. Rev*. **125**, 1060-1082.

Li, J., and Y.-L. Chen, 1998: Barrier jets during TAMEX. *Mon. Wea. Rev*., **126**, 959-971.

Li, Z., T. Takeda, K. Tsuboki, K. Kato, M. Kawashima, and Y. Fujiyoshi, 2007: Nocturnal evolution of cloud clusters over eastern China during the intensive observation periods of GAME/HUBEX in 1998 and 1999. *J. Meteor. Soc. Japan*, **85**, 25-45.

Lin, X., D. A. Randall, and L. D. Fowler, 2000: Diurnal variability of the hydrologic cycle and radiative fluxes: Comparisons between observations and a GCM. *J. Climate*, **13**, 4159-4179.

Lin Y.-L., S. Chiao, T.-A. Wang, M. L. Kaplan, R. P. Weglarz, 2001: Some common ingredients for heavy orographic rainfall. *Wea. Forcasting.*, **16**, 633-660.

Liou, Y.-C., Y.-J. Chang, 2009: A variational multiple–Doppler radar three-dimensional wind synthesis method and its impacts on thermodynamic retrieval. *Mon. Wea. Rev.*, **137**, 3992–4010.

Liu, C., and E. J. Zipser, 2008: Diurnal cycles of precipitation, clouds, and lightning in the tropics from 9 years of TRMM observations. *Geophys. Res. Lett.,* **35**, L04819, doi:10.1029/2007GL032437.

Liu, C., E. J. Zipser, D. J. Cecil, S. W. Nesbitt, and S. Sherwood, 2008: A cloud and precipitation feature database from nine years of TRMM observations. *J. Appl. Meteor.*, **47**, 2712-2728.

Liu, C., E. J. Zipser*,* G.G. Mace*,* and S. Benson*,* 2008: Implications of the differences between daytime and nighttime CloudSat observations over the tropics. *Geophys. Res. Lett.,* **113**, D00A04, doi:10.1029/2008JD009783.

Luo, H., and M. Yanai, 1983: The large-scale circulation and heat sources over the Tibetan Plateau and surrounding areas during the early summer of 1979. Part I: Precipitation and kinematic analyses. *Mon. Wea. Rev.*, **111**, 922–944.

Luo, H., and M. Yanai, 1984: The large-scale circulation and heat sources over the Tibetan Plateau and surrounding areas during the early summer of 1979. Part II: Heat and moisture budgets. *Mon. Wea. Rev.*, **112**, 966–989.

Luo, Y., R. Zhang, H. Wang, 2009: Comparing occurrences and vertical structures of hydrometeors between eastern China and the Indian Monsoon region using CloudSat/CALIPSO data. *J. Climate*, **22**, 1052–1064.

Maddox, R. A., C. F. Chappell, and L. R. Hoxit, 1979: Synoptic and meso-α scale aspects of flash flood events. *Bull. Amer. Meteor. Soc.*, **60,** 115–123.

Mapes, B. E. and R. A. Houze Jr., . 1995: Diabatic divergence profiles in western Pacific mesoscale convective systems. *J. Atmos. Sci*, **52**:1807–1828.

Mohr, C. G., L. J. Miller, R. L. Vaughan, and H. W. Frank, 1986: The merger of mesoscale datasets into a common Cartesian format for efficient and systematic analyses. *J. Atmos. Oceanic Technol.,* **3,** 143–161.

Mohr, K. I., E. J. Zipser, 1996: Mesoscale convective systems defined by their 85-GHz ice scattering signature: Size and intensity comparison over tropical oceans and continents. *Mon. Wea. Rev*., **124**, 2417-2437.

Moore, J. T., F. H. Glass, C. E. Graves, S. M. Rochette, and M. J. Singer, 2003: The environment of warm-season elevated thunderstorms associated with heavy rainfall over the central United States. *Wea. Forecasting*, **18,** 861–878.

Murakami, T., 1958: The sudden change of upper westerlies near the Tibetan plateau at the beginning of summer season. *J. Meteor. Soc. Japan*, **36**, 239-247.

Murakami, T., and Y. Ding, 1982: Wind and temperature changes over Eurasia during the early summer of 1979. *J. Meteor. Soc. Japan*, **60**, 182-196.

Negri, A. J., T. L. Bell, and L. Xu, 2002: Sampling of the diurnal cycle of precipitation using TRMM. *J. Atmos. Oceanic Technol.*, **19**, 1333-1344.

Nesbitt, S. W., E. J. Zipser, and D. J. Cecil, 2000: A census of precipitation features in the tropics using TRMM: Radar, ice scattering, and lightning observations. *J. Climate.*, **13**, 4087-4106.

Nesbitt, S. W., and E. J. Zipser, 2003: The diurnal cycle of rainfall and convective intensity according to three years of TRMM measurements. *J. Climate,* **16**, 1456-1475.

Nesbitt, S. W., R. Cifelli, S. A. Rutledge, 2006: Storm morphology and characteristics of TRMM precipitation features. *Mon. Wea. Rev.*, **134**, 2702-2721.

Nesbitt, S. W., D. J. Gochis, and T. J. Lang, 2008: The diurnal cycle of clouds and precipitation along the Sierra Madre Occidental observed during NAME-2004: Implications for warm season precipitation estimation in complex terrain. *J. Hydrometeor.,* **9**, 728-743.

Ninomiya, K., T. Akiyama, 1992: Multi-scale features of Baiu, the summer monsoon over Japan and East Asia. *J. Meteor. Soc. Japan*, **70**, 467-495.

Ninomiya, K., 2000: Large and Meso-α-scale characteristics of Meiyu/Baiu front associated with intense rainfalls in 1-10 July 1991. *J. Meteor. Soc. Japan.*, **78**, 141-157.

Ohsawa, T., H. Ueda, T. Hayashi, A. Watanabe, and J. Matsumoto, 2001: Diurnal variations of convective activity and rainfall in tropical Asia. *J. Meteor. Soc. Japan.*, **79**, 333-352.

Olson, W. S., C. D. Kummerow, Y. Hong, and W-K. Tao, 1999: Atmospheric latent heating distributions in the Tropics derived from satellite passive microwave radiometer measurements. *J. Appl. Meteor*, **38**:633–664.

Ooyama, K., 1971: A theory of parameterization of cumulus convection. *J. Meteor. Soc. Japan*, **49**, 744-756.

Oye, D., and M. Case, 1995: REORDER: A program for gridding radar data. Installation and use manual for the UNIX version. NCAR/ATD, 30 pp.

Parker, M. D., and R. H. Johnson, 2000: Organizational modes of midlatitude mesoscale convective systems. *Mon. Wea. Rev.*, **128,** 3413–3436.

Parker, M. D., and R. H. Johnson, 2004: Structures and dynamics of quasi-2D mesoscale convective systems. *J. Atmos. Sci.*, **61,** 545–567.

Petersen, W. A., S. A. Rutledge, and R. E. Orville, 1996: Cloud-to-ground lightning observations from TOGA COARE: Selected results and lightning location algorithms. *Mon. Wea. Rev*., **124**, 602-620.

Petersen, W. A., R. C. Cifelli, S. A. Rutledge, B. S. Ferrier, and B. F. Smull, 1999: Shipborne dual-Doppler operations during TOGA COARE: Integrated observations of storm kinematics and electrification. *Bull. Amer. Meteor. Soc*., **80**,81-96.

Petersen, W. A., and S. A. Rutledge, 2001: Regional variability in tropical convection: Observation from TRMM. *J. Climate*., **14**, 3566-3586.

Petersen, W. A., S.W. Nesbitt, R. J. Blakeslee, R. Cifelli, P. Hein, and S. A. Rutledge, 2002: TRMM observations of intraseasonal variability in convective regimes over the Amazon. *J. Climate*., **15**, 1278-1294.

Phillips, V. T. J., A. Pokrovsky, and A. Khain, 2007: The influence of time-dependent melting on the dynamics and precipitation production in maritime and continental storm clouds. *J. Atmos. Sci.*, **64,** 338–359.

Pontrelli, M. D., G. Bryan, and J. M. Fritsch, 1999: The Madison County, Virginia, flash flood of 27 June 1995. *Wea. Forecasting*, **14,** 384–404.

Qie, X., R. Toumi, and T. Yuan, 2003: Lightning activities on the Titetan Plateau as observed by the lightning imaging sensor. *J. Geophys. Res.*, **108**, 4551, doi:10.1029/2002JD003304.

Ramage, C., 1971: *Monsoon Meteorology*. International Geophysics Series, Academic Press, San Diego, Calif., 296 pp.

Randall, D., M. Khairoutdinov, A. Arakawa, W. Grabowski, 2003: Breaking the Cloud Parameterization Deadlock. *Bull. Amer. Meteor. Soc.*, **84**, 1547–1564.

Raymond, D. J., and H. Jiang, 1990: A theory for long-lived mesoscale convective systems. *J. Atmos. Sci.*, **47,** 3067–3077.

Reeves, H. D., and Y.-L. Lin, 2007: The effects of a mountain on the propagation of a pre-existing convective systems for blocked and unblocked regimes. *J. Atmos.*

Sci., **64**, 2401-2421.

Riehl, H., and J. S. Malkus, 1958: On the heat balance in the equatorial trough zone. *Geophysica*, **6**, 503-538.

Riehl, H., and J. S. Simpson, 1979: The heat balance in the equatorial trough zone, revisited. *Contrib. Atmos. Phys.*, **52**, 287-305.

Rosenfeld, D., and I. M. Lensky, 1998: Satellite-based insights into precipitation formation processes in continental and maritime convective clouds. *Bull. Amer. Meteor. Soc.*, **79,** 2457–2476.

Rotunno, R., R. A. Houze, 2007: Lessons on orographic precipitation from the Mesoscale Alpine Programme. *Quart. J. Roy. Meteo. Soc.*, **133**, 811-830.

Rowe, A. K., S. A. Rutledge, T. J. Lang, P. E. Ciesielski, and S. M. Saleeby, 2008: Elevation-dependent trends in precipitation observed during NAME. *Mon. Wea. Rev.*, **136,** 4962–4979.

Rutledge, S. A., and D. R. MacGorman, 1988: Cloud-to-ground lightning activity in the 10-11 June 1985 mesoscale convective system observed during OK PRE-STORM, *Mon. Weather. Rev.*, **116**, 1393-1408.

Sanders, F., 2000: Frontal focusing of a flooding rainstorm. *Mon. Wea. Rev.*, **128,** 4155–4159.

Saunders, C. P. R., and S. L. Peck, 1998: Laboratory studies of the influence of the rime accretion rate on charge transfer during crystal/graupel collisions. *J. Geophys. Res.*, **103**, 13949-13956.

Schumacher, R. S., R. H. Johnson, 2005: Organization and environmental properties of extreme-rain-producing mesoscale convective systems. *Mon. Wea. Rev.*, **133**, 961–976.

Schumacher, R. S., R. H. Johnson, 2006: Characteristics of U.S. extreme rain events during 1999–2003. *Wea. Forecasting*, **21**, 69–85.

Schumacher, R. S., and R. H. Johnson, 2008: Mesoscale processes contributing to extreme rainfall in a midlatitude warm-season flash flood. *Mon. Wea. Rev.*, **136,** 3964–3986.

Schumacher, R. S., R. H. Johnson, 2009: Quasi-stationary, extreme-rain-producing convective systems associated with midlevel cyclonic circulations. *Wea. Forecasting*, **24**, 555–574.

Seity, Y., S. Soula, and H. Sauvageot, 2001: Lightning and precipitation activities in coast thunderstorms, *J. Geophys. Res.*, 106 (D19), **22**,801-22,816.

Sheridan, S. C., J. F. Griffiths, and R. E. Orville, 1997: Warm season cloud-to-ground lightning-precipitation relationships in the south-central United States. *Wea. Forecasting.*, **12**, 449-458.

Shen, Y., A. Xiong, Y. Wang, and P. Xie, 2010: Performance of high-resolution satellite precipitation products over China. *J. Geophys. Res.*, **115**, doi:10.1029/2009JD012097, D02114.

Short, D. A., P. A. Kucera, B. S. Ferrier, J. C. Gerlach, S. A. Rutledge, and O. W. Thiele, 1997: Shipboard radar rainfall patterns within the TOGA COARE IFA. *Bull. Amer. Meteor. Soc.*, **78**, 2817-2836.

Simpson, J., 1992: Global circulation and tropical cloud activity. *The Global Role of Tropical Rainfall.* J. S. Theon et al., Eds., A. Deepak Publishing, 77–92.

Smith,R. B., and Coauthors, 1997: Local and remote effects of mountains on weather: Research needs and opportunities. *Bull. Amer. Meteor. Soc.*, **78**, 877-892.

Soriano, L. R., F. De Pablo, and E. G. Diez, 2001: Relationship between convective precipitation and cloud-to-ground lightning in the Iberian peninsula, *Mon. Weather Rev.*, **129**, 2998-3003.

Soriano, L. R., and F. De Pablo, 2003: Analysis of convective precipitation in the western Mediterranean Sea through the use of cloud-to-ground lightning, *Atmos. Res.*, **66**, 189-202.

Soula, S., and S. Chauzy, 2001: Some aspects of the correlation between lightning and rain activities in severe storms, *Atmos. Res.*, **56**, 355-373.

Spencer, R. W., H. G. Goodman, and R. E. Hood, 1989: Precipitation retrieval over land and ocean with the SSM/I: Identification and characteristics of the scattering signal. *J. Atmos. Oceanic Technol.*, **6**, 254-273.

Steiner, M., R. A. Houze, S. E. Yuter, 1995: Climatological characterization of three-dimensional storm structure from operational radar and rain gauge data. *J. Appl. Meteor.*, **34**, 1978–2007.

Straka, J. M., D. S. Zrnic, and A. V. Ryzhkov, 2000: Bulk hydrometeor classification and quantification using polarimetric radar data: Synthesis of relations. *J. Appl. Meteor.*, **39**:1341–1372.

Sun, W-Y., C. C. Wu, and W. R. Hsu, 1991: Numerical simulation of mesoscale circulation in Taiwan and surrounding area. *Mon. Wea. Rev.*, **119,** 2558–2573.

Szoke, E. J., E. J. Zipser, and D. P. Jorgensen, 1986: A radar study of convective cells in mesoscale systems in GATE. 1. Vertical profile statistics and comparison with hurricanes. *J. Atmos. Sci.*, **43,** 182-197.

Tapia, A., J. Smith, and M. Dixon, 1998: Estimation of convective rainfall from lightning observations, *J. App. Met.*, **37**, 1497-1509.

Takeda, T., and H. Iwaski, 1987: Some characteristics *of* meso-scale cloud clusters observed in East Asia between March *and* October 1980. *J. Meteor. Soc. Japan*, **3**, 507-513.

Tao, S., and L. Chen, 1987: A review of recent research on the East Asian summer monsoon in China. *Monsoon Meteorology*, C.-P. Change and T.N. Krishnamurti, Ed., Oxford University Press, 60-92.

Tao, S., and Y. Ding, 1998: Observational evidence of the influence of the Qinghai-Xizang (Tibet) Plateau on the occurrence of heavy rain and severe convective storms in China. *Bull. Amer. Meteor.*, **62**, 23-30.

Tao, W-K., J. Simpson, S. Lang, M. McCumber, R. Adler, and R. Penc, 1990: An algorithm to estimate the heating budget from vertical hydrometeor profiles. *J. Appl. Meteor*, **29**:1232–1244.

Toracinta, E. R., D. J. Cecil, E. J. Zipser, S. W. Nesbitt, 2002: Radar, passive microwave, and lightning characteristics of precipitating systems in the tropics. *Mon. Wea. Rev.*, **130**, 802–824.

Trenberth, K.E., Stepaniak, D.P., Caron, J.M., 2000: The global monsoon as seen through the divergent atmospheric circulation, *J. Climate*, **13**, 3969-3993.

Trenberth, K. E., A. Dai, R. M. Rasmussen, and D. B. Parsons, 2003: The changing character of precipitation. *Bull. Amer. Meteor. Soc.*, **84**, 1205-1217.

Trier, S. B., D. B. Parsons, and T. J. Matejka, 1990: Observations of a subtropical cold front in a region of complex terrain. *Mon. Wea. Rev.*, **118,** 2449–2470.

Tsai, K.-J., 2010: Comparisons of reflectivity and rain rate derived from the TRMM precipitation radar and the CWB Cigu radar over the southwestern area of Taiwan in 2008. M.S. Thesis, Graduate Institute of Atmospheric Physics, National Central University, Taiwan, 69 pp.

Ulbrich, C. W., and D. Atlas, 2007: Microphysics of raindrop size spectra: Tropical continental and maritime storms. *J. Appl. Meteor. Climatol.*, **46,** 1777–1791.

Uyeda, H., H. Yamada, J. Horikomi, R. Shirooka, S. Shimizu, L. P. Liu, K. Ueno, H. Fuji, and T. Koike, 2001: Characteristics of convective clouds observed by a Doppler radar at Naqu on Tibetan Plateau during the GAME-Tibet IOP. *J. Meteor. Soc. Japan.*, **79**, 463-474, 2001.

Vivekanandan, J., J. Turk, and V. N. Bringi, 1991: Ice water path estimation and characterization using passive microwave radiometry. *J. Appl. Meteorl.*, **30**, 1407-1421.

Vivekanandan, J., S. M. Ellis, R. Oye, D. S. Zrnic, A. V. Ryzhkov, J. Straka, 1999: Cloud microphysics retrieval using S-band dual-polarization radar measurements. *Bull. Amer. Meteor. Soc.*, **80**, 381–388.

Wang, C. C., G. T. J. Chen, and R. E. Carbone, 2004: A climatology of warm-season cloud patterns over East Asia on GMS infrared brightness temperatures observations. *Mon. Wea. Rev.*, **132**, 1606-1629.

Wang, C. C., G. T. J. Chen, and R. E. Carbone, 2005: Variability of warm season cloud episodes over East Asia based on GMS infrared brightness temperature observations. *Mon. Wea. Rev.,* **133**, 1478-1500.

Wallace, J. M., 1975: Diurnal variations in precipitation and thunderstorm frequency over the conterminous United States. *Mon. Wea. Rev.*, **103**, 406-419.

Wang, B., R. Wu, X. Fu, 2000: Pacific-East Asian teleconnection: How does ENSO affect East Asian Climate? *J. Climate*, **13**, 1517–1536.

Wang, B., and H. Lin, 2002: Rainy season of the Asian–Pacific summer monsoon. *J. Climate*, **15,** 386–398.

Wang, B., 2006: *The Asian Monsoon*. Praxis Publishing Ltd, Chichester, UK, 787 pp.

Wang, B., and Q. Ding, 2006: Changes in global monsoon precipitation over the past 56 years, *Geophys. Res. Lett.*, **33**, L06711, doi:10.1029/2005GL025347.

Wang, B., T. Li, Y. Ding, R. Zhang, and H. Wang, 2005: Eastern Asian–Western North Pacific monsoon: A distinctive component of the Asian–Australian monsoon system. *The global monsoon system: Research and forecast,* C.-P. Chang and B. Wang, N.-C. G. Lau, Eds., WMO/TD 1266, TMRP Rep. 70, 72–94.

Wang, J. J., 2004: Evolution and structure of the mesoscale convection and its environment: A case study during the early onset of the southeast Asian summer monsoon. *Mon. Wea. Rev.*, **132**, 1104-1120.

Wang, J. J., and L. D. Carey, 2005: The development and structure of an oceanic squall-line system during the South China Sea Monsoon Experiment. *Mon. Wea. Rev.*, **133,** 1544-1561.

Wang, T.-C. C., Y.-J. Lin, R. W. Pasken, and H. Shen, 1990: Characteristic of a subtropical squall line determined from TAMEX dual-Doppler data. Part I: Kinematic structure. J. Atmos. Sci., 47, 2357–2381.

Webster, P. J., and R. Lucas, 1992: TOGA COARE: The coupled ocean-atmosphere response experiment. *Bull. Amer. Meteor. Soc*., **73**, 1377-1416.

Williams, E. R., 1989: The tripole nature of thunderstorms. *J. Geophys. Res*., **94**, 13151-13167.

Williams, E. R., S. A. Rutledge, S. G. Geotis, N. Renno, E. Rasmussen, and T. Rickenbach, 1992: A radar and electrical study of tropical “hot towers”. *J. Atmos. Sci.*, **49**, 1386-1395.

Williams, E. R., and S. Stanfill, 2002: The physical origin of the land–ocean contrast in lightning activity. *Comp. Rendus Phys.*, **3,** 1277–1292.

Williams, E. R., and Coauthors, 2002: Contrasting convective regimes over the Amazon: Implications for cloud electrification. *J. Geophys. Res.*, **107.,** 8082, doi:10.1029/2001JD000380.

Wilson, J. W., R. D. Roberts, C. Kessinger, J. McCarthy, 1984: Microburst wind structure and evaluation of Doppler radar for airport wind shear detection. *J. Climate Appl. Meteor.*, **23**, 898–915.

Wu, G., Y. Zhang, 1998: Tibetan Plateau forcing and the timing of the monsoon onset over south Asia and the South China Sea. *Mon. Wea. Rev.*, **126**, 913–927.

Wu, R., 2002: A mid-latitude Asian circulation anomaly pattern in boreal summer and its connection with the Indian and East Asian summer monsoons. *Int. J. Climatol.*, **22**, 1879–1895.

Xu, W., E. J. Zipser, and C. Liu, 2009: Rainfall characteristics and convective properties of Mei-Yu precipitation systems over South China, Taiwan and the South China Sea Part I: TRMM observations. *Mon. Wea. Rev.*, **137**, 4261-4275.

Xu, W., E. J. Zipser, C. Liu, and H. Jiang, 2010: On the relationships between lightning frequency and thundercloud parameters of regional precipitation systems, *J. Geophys. Res.*, **115**, D12203, doi:10.1029/2009JD013385.

Xu, W., and E. J. Zipser, 2011: Diurnal variations of precipitation, deep convection and lightning over and east of eastern Tibetan Plateau. *J. Climate,* **24**, 448-465.

Yanai, M., C. Li, and Z. Song, 1992: Seasonal heating of the Tibetan Plateau and its effects on the evolution of the Asian summer monsoon. *J. Meteorol. Soc. Japan.*, **70**, 319-351.

Yanai, M., S. Esbensen, and J.-H. Chu, 1973: Determination of bulk properties of tropical cloud clusters from large-scale heat and moisture budgets. *J. Atmos. Sci.,* **30**, 611–627.

Yasunari, T., and Y. Seki, 1992: Role of the Asian Monsoon on the interannual variability of the global climate system. *J. Meteorol. Soc. Japan.*, **70**, 177-189.

Yeh, H.-C., and G. T.-J. Chen, 2004: Case study of an unusually heavy rain event over Eastern Taiwan during the Mei-Yu season. *Mon. Wea. Rev.*, **132**, 320-336.

Yeh, H.-C., Y.-L. Chen, 2002: The role of offshore convergence on coastal rainfall during TAMEX IOP 3. *Mon. Wea. Rev.*, **130**, 2709–2730.

Yu, R., T. Zhou, A. Xiong, Y. Zhu, and J. Li, 2007a: Diurnal variations of summer precipitation over contiguous China. *Geophys. Res. Lett.*, **34**, L01704, doi:10.1029/ 2006GL028129.

Yu, R., Y. Xu, T. Zhou, and J. Li, 2007b: Relation between rainfall duration and diurnal variation in the warm season precipitation over central eastern China. *Geophys. Res. Lett.*, **34**, L13703, doi:10.1029/ 2007GL030315.

Yu, R., Y. Yu, and M. Zhang, 2001: Comparing cloud radiative properties between the eastern China and the Indian monsoon region. *Adv. Atmos. Sci.*, **18,** 1090–1102.

Yu, R., J. Li, and H. Chen, 2009: Diurnal variation of surface wind over central eastern China. *Climate Dyn.* **33**, 1089-1097.

Yuan, T., and X. Qie, 2008: Study on lightning activity and precipitation characteristics before and after the onset of the South China Sea summer monsoon. *Geophys. Res. Lett.*, **113,** D14101, doi:10.1029/2007JD009382.

Yuter, S.E., R.A. Houze, E.A. Smith, T.T. Wilheit, E.J. Zipser, 2005: Physical characterization of tropical oceanic convection observed in KWAJEX. *J. Appl.*

Meteor., **44**, 385–415.

Zhang, B., 1990: A study of Meiyu rainstorms over the Yangtze Valley. China Meteorological Press, 269 pp.

Zhang, C.-Z., H. Uyeda, H. Yamada, B. Geng and Y. Ni, 2006: Characteristics of Mesoscale convective systems over the east part of continental China during the Meiyu from 2001 to 2003. *J. Meteor. Soc. Japan,* **84**, 763-782.

Zhang, J., and coauthors, 2009: High-resolution QPE system for Taiwan. *Data Assimilation for Atmospheric, Oceanic and Hydrologic Applications*. S. K. Park, L. Xu, Eds, Springer Publisher, Berlin, 147-165.

Zhang, Q., and S. Tao, 1998: Influence of Asian mid-high latitude circulation on East Asian summer rain fall. *Acta. Meteorol. Sinica.*, **56**, 199–211, (in Chinese).

Zhang, Q., K.-H. Lau, Y.-H. Kuo, and S. J. Chen, 2003: A numerical study of a mesoscale convective system over the Taiwan Strait. *Mon. Wea. Rev.*, **131**, 1150-1170.

Zhao, Z., L. R. Leung, and Y. Qian, 2005: Characteristics of diurnal variations of precipitation in China for the recent years. *Clim. Variability Exch.*, **10**, 24-26.

Zhou, T., R. Yu, H. Chen, A. Dai, and Y. Pan, 2008: Summer precipitation frequency, intensity, and diurnal cycle over China: A comparison of satellite data with rain gauge observations. *J. Clim.*, **21**, 3997-4010.

Zipser, E. J., 1969: The role of organized unsaturated convective downdrafts in the structure and rapid decay of an equatorial disturbance. *J. Appl. Meteor.*, **8**, 799-814.

Zipser, E. J., 1977: Mesoscale and convective scale downdrafts as distinct components of squall-line structure. *Mon. Wea. Rev.*, **105,** 1568-1589.

Zipser, E. J., 1994: Deep cumulonimbus cloud systems in the tropics with and without lightning. *Mon. Wea. Rev.*, **122**, 1837–1851.

Zipser, E. J., K. R. Lutz, 1994: The vertical profile of radar reflectivity of convective cells: A strong indicator of storm intensity and lightning probability? *Mon. Wea. Rev.*, **122**, 1751–1759.

Zipser, E. J., D. J. Cecil, C. Liu, S. W. Nesbitt, and D. P. Yorty, 2006: Where are the most intense thunderstorms on Earth? *Bull. Amer. Meteor. Soc.*, **87**, 1057-1071.

Zrnić, D. S., 1991: Complete polarimetric and Doppler measurements with a single receiver radar. *J. Atmos. Oceanic Technol.*, **8**, 159–165.

Zrnić, D. S., A. Ryzhkov, J. Straka, Y. Liu, J. Vivekanandan, 2001: Testing a procedure for automatic classification of hydrometeor types. *J. Atmos. Oceanic Technol.*, **18**, 892–913.